Mapping Local Manifestations of the Strain Mediated Magnetoelectric Effect in Composites

Faculty of Engineering, Institute of Materials Science of the

University of Duisburg-Essen

for award of the academic degree of

Doctor of Natural Sciences

Thesis submitted
by
Harsh Trivedi
M.Tech. Materials Science, IIT Kanpur
Born April 23, 1988
citizen of India

Date of defence:
09.12.2015

Chair: Prof. Dr. Ing. André Niemann

Examiner: Prof. Dr. rer. nat. habil. Doru C. Lupascu
Prof. Dr. Kathrin Dörr

Declaration

Herein, I declare that this thesis is a product of my authentic work, without any help from a third party or other aids, apart from those explicitly acknowledged, Thoughts, ideas, and information taken or used from others work or literature have been appropriately cited and listed in the reference section. Further, personals that have helped or guided me in realizing my research, by providing both, experimental and theoretical inputs, are duly acknowledged. Apart from those listed, no other person(s) was (were) involved in this work. In particular, I have neither obtained help from a PhD consultant nor have I paid a third party for accomplishing the entire or any selective part of the thesis.

This work has never been presented to any examining authority for an award of academic qualification, neither in this form nor in a modified form. Also it has not been published in this or any other form anywhere else.

I have never presented any other thesis of mine to an examining authority for an award of any kind of academic doctoral degree.

I confirm that I accept the doctoral guidelines of the Faculty of Engineering of he University of Duisburg-Essen.

Essen, den

Harshkumar Bhadreshkumar Trivedi

Acknowledgement

The presented thesis, in its best quality, has valuable contributions from persons who were actively, passively, directly, or indirectly associated with it. I would hereby like to extend my gratitude towards all those persons because of whom I was able to accomplish the quality of scientific work evident in this thesis. Firstly, I would like to thank Prof. Lupascu, my official advisor and a mentor, for providing me the opportunity to work as a part of the multifaceted EU wide consortium termed as NANOMOTION. His support and timely assessments throughout the span of my work are highly valuable. In addition, his continual nurturing and mentoring has not just improved the quality of my work, but also trained me as a responsible researcher in the concerned field of ferroic functional materials. I am extremely grateful to my supervisor Dr. habil. Vladimir Shvartsman for his omnipresent guidance, that drew me through the difficult labyrinths of the scientific world like a lighthouse. He not just taught me various important traits of dealing with experimental investigations, but also enriched my knowledge time to time, at the same time exposing me to the relevant scientific community. All this directly or indirectly contributed to my research work. No less than a mentor, Dr. Andrei Kholkin also played a pivotal role in my project, primarily by leading NANOMOTION from the front, and encouraging me towards important international scientific events and workshops. His timely suggestions and scientific input are also highly valued. The collaboration with the group of Prof. Vladimir Ya Shur was a major contributor to my work, which not just provided a new research direction but also stood as an opportunity for me to get exposed to the classical world of ferroelectrics. I am very grateful to Prof. Shur personally whose timely inputs were extremely valuable. It was an honor working with him. My special thanks to Dr. Pavel Zelenevoskiy, whose persistence allowed me to carry out productive measurements of Confocal Raman Microscopy in a very limited time. It is the encouragement and the work environment provided by Dr. Zlenovskiy and Prof. Shur, that have led me towards the development of some of the creative approaches adopted in context of the Raman Microscopy measurements. I am also thankful to Dr. Alex Belianov of ORNL (US) for his valuable help, without which some of the statistical analysis carried out in my work could not have been realized. It was he who first introduced me to the applications of multivariate data analysis in experimental science. At the twilight of my research span, I got the opportunity to visit and work at the NPL (UK) as a part of the NANOMOTION consortium, for which I would like to thank Rui Lopes and Dr. Markys Cain for overlooking my stay and exposing me to the key facilities at NPL.

Some of the valuable measurements, complimentary to my work, could not have been without the help of my colleagues and co-workers at University of Duisburg-Essen. I am thankful to Frau Dr. Priska Stemmer, who persistently assisted me in the electron back scattered diffraction (EBSD) acquisitions. I am also thankful to Soma Salamon, for the vibrating sample magnetometry (VSM) measurements. My colleagues at UDEMAT, Morad Etier, Yanling Gao,

and Naveed-Ul-Haq have helped me with setting up of various experiments and preparation procedures, for that I would like to thank them from the bottom of my heart. In addition, Patrick Dubray has persistently provided his technical logistic assistance, for which I am extremely grateful to him. I extend my gratitude collectively to all the group members who have at several points helped me in various aspects. The financial source provide by the EU commission to my project, as a part of the NANOMOTION consortium (grant no.290158), is deeply acknowledged. In addition, the travel opportunities provided as a part of the consortium are of immense importance, without which numerous valuable scientific contributions via various international conferences and workshops could not have been realized.

Lastly, I would specially like to convey the importance of my family, which always kept me anchored through the hurricanes of life, and always stood as source of encouragement for achieving my goals. I am thankful to all of them.

This thesis is dedicated to my grandfather

Late Ramanlal Trivedi

Abstract

The magnetoelectric effect has gained immense impetus in the last century, mainly due to its interesting potential applications into the technologies of the era. The fact that the two important space/matter permeating fields, the electric and the magnetic field, could be in a material, gives rise to key applications like high sensitivity magnetic field sensors, and voltage controlled non-volatile memory storage. As the various materials exhibiting magnetoelectric effect are being continually explored, the composites with combination of a ferroelectric and a ferro/ferrimagnetic material have emerged as favorite candidates with exceptional performance under ambient conditions. Quite often the magnetoelectric effect in composite is mediated via strain, requiring a complex constitutive model for their representation. Very recently, attempts have been made to construct robust models for understanding the strain mediated magnetoelectric effect in composites with various morphologies. However, such models lack the necessary experimental support. In general, there is a lack of proper understanding about the behavior of the strain mediation in the vicinity of the interface between the constituent phases.

The present study is aimed to tackle the lack of information surrounding the local manifestations of the magnetoelectric effect in composites, with a focus on pushing the boundaries of microscopic techniques like Scanning Probe Microscopy (SPM), and Confocal Raman Microscopy. Various SPM modes like Piezoresponse Force Microscopy (PFM), Magnetic Force Microscopy (MFM), and Kelvin-probe Force Microscopy (KPFM) were synergistically utilized. As a subject of study, bulk polycrystalline composites based on combinations of ferroelectric $BaTiO_3$ and various ferrimagnetic ferrites (viz. $BaFe_{12}O_{19}$, $SrFe_{12}O_{19}$, $CoFe_2O_4$, and $NiFe_2O_4$) were investigated. The choices of the magnetic components served as a wide spectrum of materials with different magnetocrystalline symmetries. In addition, the constituent morphologies favorably allowed longitudinal investigations in the vicinity of the ferroelectric-ferrimagnetic interface.

Both, direct and converse magnetoelectric effects were locally studied using in-situ MFM and PFM respectively. As a part of the converse effect the application of instantaneous electric poling under the SPM tip resulted in interesting micromagnetic fluctuations which were observed in MFM, and later analyzed using a self-developed image processing algorithm. The results suggest an intricate role of defects and microstructure in inducing the observed changes in magnetic domain configurations. As a part of the direct magnetoelectric effect, the in-situ application of magnetic field during PFM imaging results in a corresponding variation in PFM amplitude. This was rationalized as modulation of the local electromechanical coupling in $BaTiO_3$ by the magnetoelectrically induced stress via the magnetic phase. This was further studied in a systematical manner, using Principal Component Analysis (PCA) of PFM image sequences. The results revealed interesting magnetic field modulations of PFM amplitude, the extent of which followed a distinct spatial distribution. These patterns and their corresponding spatial distributions, indicated existence of various stress regimes which was mainly attributed to

the constituent morphologies. The distributions of the effect also suggested certain degrees of closeness to the classical micromechanical problem of inclusion in a matrix (Eshelby's solution). Later, the localized ferroelectric switching using the Switching Spectroscopy PFM (SSPFM) mode was also studied under and applied in-situ magnetic field. Maps of nucleation biases of the local switching were generated, suggesting presence of in-built electric fields localized at the interfaces. In addition, the application of magnetic field apparently modulated these fields, which could be attributed to the appearance of magnetoelectrically induced fields that could influence the balance of fields during the switching process. In order to corroborate the indirect observations of the effects of induced stress, a direct observation of the stress was carried out by the means of in-situ Confocal Raman Microscopy. A self-developed algorithm, based on a conjunction of PCA and Self Modeling Curve Resolution (SMCR) was utilized to generate 2D distributions of least-square fitted peak positions of $BaTiO_3$ Raman modes. On application of magnetic field the Raman modes manifest spatially consistent frequency shifts, which were considered as a direct consequence of the magnetoelectrically induced strain in the $BaTiO_3$ phase.

The outcomes, in totality, suggest a greater role of microstructure, as compared to that of the constituent material characteristics, in determining the persistence of the stress and hence the magnetoelectric effect within the composite.

Contents

List of Figures

List of Tables

List of Symbols

Symbol	Quantity	SI Unit
P_i	Polarization vector	C/m^2
α_{ij}	Magnetoelectric tensor	s/m
H_i	Magnetic field vector	A/m
M_i	Magnetization	A/m
P_i^S	Spontaneous polarization	C/m^2
M_i^S	Spontaneous magnetization	A/m
μ_0	Magnetic permeability of space	H/m
μ_{ij}	Magnetic permeability tensor	H/m
ε_0	Dielectric permittivity of space	F/m
ε_{ij}	Dielectric permittivity tensor	F/m
σ_{ij}	Stress tensor	N/m^2
σ	Domain wall energy density	J/m^2
ϵ_{ij}^S	Spontaneous strain	-
ϵ_{ij}	Strain tensor	-
C_{ijkl}	Elastic stiffness	N/m^2
S_{ijkl}	Elastic compliance	m^2/N
ω_S	Soft-phonon mode frequency	cm^{-1}
ω	Angular frequency	rad/s
T_c	Curie temperature	^oC
θ_c	Curie point	^oC
D_i	Electric Displacement	C/m^2
d_{ijk}	Piezoelectric coefficient	m/V
μ_B	Bohr Magneton	-
B	Magnetic flux	T
K_1	Magnetocrystalline anisotropy constant	J/m^3
K_M	Magnetomechanical anisotropy constant	J/m^3
q_{jjk}	Piezomagnetic coefficient	m/A
B_{ijk}	Magnetoelastic constant	N/m^2

List of Abbreviations

Abbrevation	Full form
MRAM	Magnetic Random Access Memoy
ME	Magnetoelectric
FE	Ferroelectric
FM	Ferro/Ferrimagnetic
BTO	$BaTiO_3$
CFO	$CoFe_2O_4$
NFO	$NiFe_2O_4$
PZT	$PbZr_xTi_{1-x}O_3$
PMN-PT	$PbMn_{0.33}Nb_{0.66}O_3 – PbTiO_3$
BaM	$BaFe_{12}O_{19}$
SrM	$SrFe_{12}O_{19}$
SPM	Scanning Probe Microscopy
PFM	Piezoresponse Force Microscopy
MFM	Magnetic Force Microscopy
KPFM	Kelvin Probe Force Microscopy
SSPFM	Switching Spectroscopy Piezoresponse Force Microscopy
NNB	Negative Nucleation Bias
PNB	Positive Nucleation Bias

1 Introduction

Materials are amongst the pillars of mankind's evolution into modern world. The versatility and performance of materials in applications ranging from concrete to Magnetic Random Access Memory (MRAM) are what drives design and innovation. This in a way necessitates invention of new classes of materials as well as understanding and optimizing the existing ones. The algorithm underlying the science of materials starts with the physical discovery of new phenomena in a material before ending up in the conventional materials paradigm. The relationship between structure property and processing governed by the merits, in turn forecast new possible discoveries. This concept can be summarized as shown in Figure 1.1.With increasing knowledge about various materials, a clear philosophical divide has arisen, which roughly classifies them into two broad categories [1]:

i) **Structural Materials**: These are the materials that play a passive role in applications, serving their purpose as mechanical entities; e.g. steel, concrete etc.
ii) **Functional Materials**: This class comprises of all those materials which are active and yield a specific function; e.g. piezoelectric actuators, or shape memory alloys.

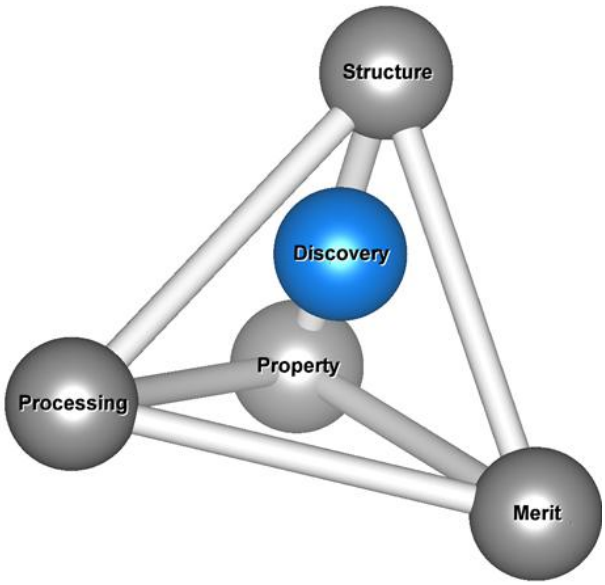

Figure 1.1 The Materials Science tetrahedron

The functional class of material is where majority of physics is concentrated, and where a vast potential exists to understand and engineer various phenomena. The motivation for functional

materials comes from their strategic importance to areas like energy harvesting (Solar cell [2, 3]), environment (Photocatalysis [4, 5]), and information technology (MRAM[6, 7]). This latter class of materials is what constitutes the broader interests underlying the present thesis.

Over time, with the development of new crystal-symmetry dominated functionalities [8, 9], a new trend of coupling multiple functionalities has emerged. This trend has its root in the foreseen technological applications where the materials are required reacting to multiple stimuli; this can be understood in the realm of magnetoelectricity, which in a broad sense means controlling of magnetic properties of the materials by electrical stimuli. The implications of this concept are illustrated in Figure 1.2.

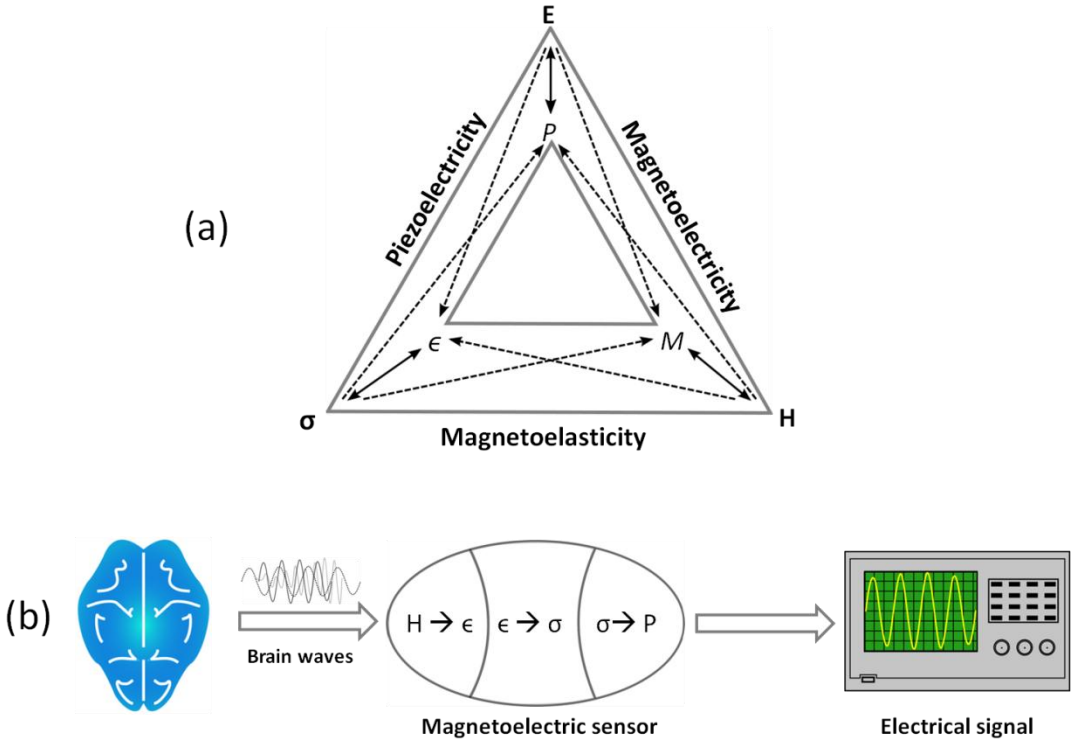

Figure 1.2 (a) A part of Heckmann diagram, emphasizing the coupling between the field parameters namely electric field {E}, magnetic field {H}, and mechanical stress {σ}; the bidirectional arrows relate the field parameters to the corresponding extensive variables namely polarization{P}, magnetization {M}, and strain {ϵ}, whereas the unidirectional arrows represent the cross couplings. (b) Schematics describing an important appliciation of the direct magnetoelectric effect in a composite based device for sensing physiological currents in human brain.

Out of all the possible couplings described in the Heckmann diagram (Figure 1.2a), magnetoelectricity is the most fascinating one, since it couples the two most important space permeating fields namely electric and magnetic. Also in terms of implications, this coupling has very important consequences (as shown in the Figure 1.2b). The magnetic signals generated by the human brain can have important contributions towards understanding of various

neurophysiological phenomena [10]. However, the sensing of such signals is a challenge since it demands high sensitivity, and the commonly used high sensitivity magnetometer, SQUID (Superconducting Quantum Interference Device; sensitivity ~ 10^{-12} Tesla), requires bulky cryogenic instrumentation [11]. On the other hand, a comparable sensitivity, in an easy to handle sensing device, can be realized by converting the magnetic signal to an electrical one, via a magnetoelectric element [12–15]; the sensing of an electrical signal with good sensitivity doesn't pose any challenge.

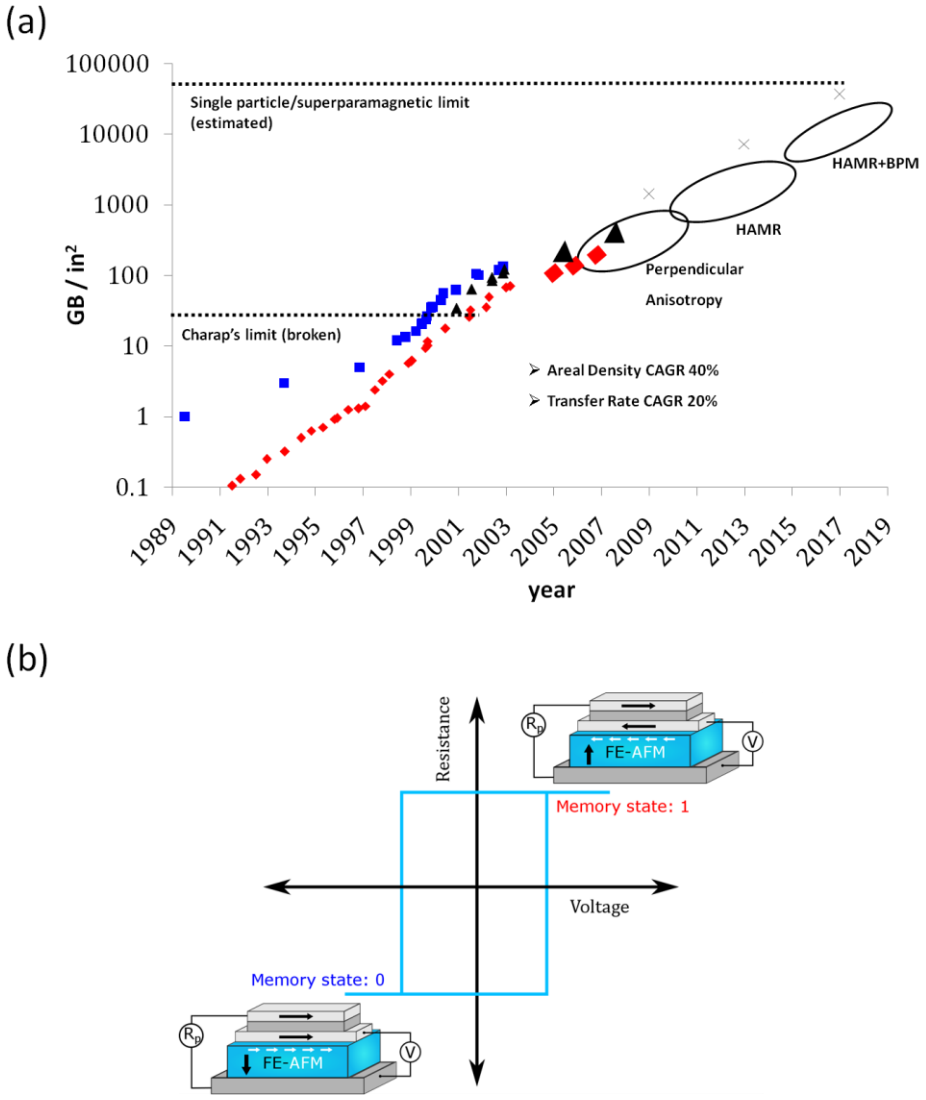

Figure 1.3 (a) A yearwise growth of the memory areal density, in terms of GB (gigabyte) of data storable per square inch [16]. The term CAGR refers to compound annual growth rate. The marked regions (black) represet the densities already achieved, pr to be achieved by the emerging technologies [17]. (b) A prototype of magnetoelectric random access memory (MeRAM) element, as proposed by Bibes et al. [18]. The cyan layer, which is the active component, is representative of the well-known room temperature magnetoelectric-multiferroic $BiFeO_3$.

It is not just the electrical sensing of magnetic field which constitutes the major interests surrounding the magnetoelectric (ME) effect, but also the converse implication, i.e. electrical control of magnetic properties. Figure 1.2b describes the concept of a magnetoelectric memory, where by electrically controlling the magnetic order by electric the magnetoelectric layer (cyan) the magnetic order in the adjacent layer can be controlled via an exchange bias. This concept is extremely useful in memory devices, since it allows energy efficient writing of magnetic bits using electrical voltage. Conventionally, an MRAM utilizes a current generated magnetic field to write the bits, which costs higher energy as compared to applying a voltage [17]. Although MRAM belongs to the niche market, it is expected to out run the current major market players like DRAM and flash memory [19], mainly due to its immense endurance and non-volatility (Table 1.1). However, apart from the higher write-energy, MRAM also suffers from the single particle (superparamagnetic) limit (Figure 1.3), in that the element can volatilize within nanoseconds by mere thermal excitation (Appendix-a). The present magnetic memory configurations have no provision to overcome these limitations, unless used in conjunction with a magnetoelectric element as first suggested by Bibes et al. [17] (Figure 1.3b).

Table 1.1 A comparision of various non-volatile memory technologies, in terms of their salient performance parameters [20].

Features	MRAM	SRAM	DRAM	Flash	FeRam
Read Speed	Fast	Fastest	Medium	Fast	Fast
Write Speed	Fast	Fastest	Medium	Low	Medium
Array Efficiency	Med/High	High	High	Med/Low	Medium
Future Scalability	Good	Good	Limited	Limited	Limited
Cell Density	Med/High	Low	High	Medium	Medium
Non-Volatility	Yes	No	No	Yes	Yes
Endurance	Infinite	Infinite	Infinite	Limited	Limited
Cell Leakage	Low	Low/High	High	Low	Low
Low Voltage	Yes	Yes	Limited	Limited	Limited
Complexity	Medium	Low	Medium	Medium	Medium

Since the first theoretical proposition of the existence of magnetoelectricity in an antiferromagnetic oxide (Cr_2O_3; [21]), followed by its first experimental observation [22], immense amount of work has followed up leading to a plethora of new classes of magnetoelectrics [23–29]. However certain symmetry requirements limit the availability of magnetoelectricity in materials. The first necessary condition states that the crystal has to have at least some magnetic order, so that a time-reversal, as well as a spatial inversion symmetry

operation should at least yield one non-zero coupling term in the coefficient matrix [8, 30, 31]. Another constraint that sets in an upper limit on the first order magnetoelectric coupling coefficient [32] states that the intrinsic linear ME coupling in any crystal cannot be greater than the square root of product of the electric and magnetic susceptibilities ($\sqrt{\varepsilon_{ij}\,\chi_{ij}}$). Now another constraint arises, which is the unavailability of simultaneously existence of magnetic (unfilled *d* bands) and electric (empty *d* bands) orders. Interestingly, these constraints are indeed met for certain special classes of crystal, that not just possess simultaneous electric and magnetic orders, but also manifest a direct (Type-1), or an indirect (Type-2) form of coupling between the two order parameters (magnetoelectric-multiferroics). The Type-1 and Type-2 multiferroics are generally termed as single phase magnetoelectric-multiferroics in order to differentiate them from their heterogeneous counterparts (composites). The coupling in Type-1 multiferroics (e.g. $BiFeO_3$) is rather weak, whereas for the Type-2 multiferroics (e.g. $TbMnO_3$) a direct and strong coupling exists only at cryogenic temperatures. In addition to these limitations, the rareness of single phase magnetoelectric-multiferroics itself poses a greater challenge for their technological integration. Evolving from the limitations of single phase magnetoelectric multiferroics, new approaches have been proposed, where either the available single phase materials are used to their best by integrating them into novel thin film heterosturctures [18, 33–36], or by combining two monoferroic materials to realize an indirect form of coupling at the interface. The composites that fall into the linear magnetoelectrics category, are a heterogeneous solution to the limitations suffered by the single phase magnetoelectric multiferroics, since it couples the two orders and their constitutive properties separately via a mediating property (e.g. strain), while decoupling the unique symmetry requirement and allowing the freedom of choice of the best suited constituent materials.

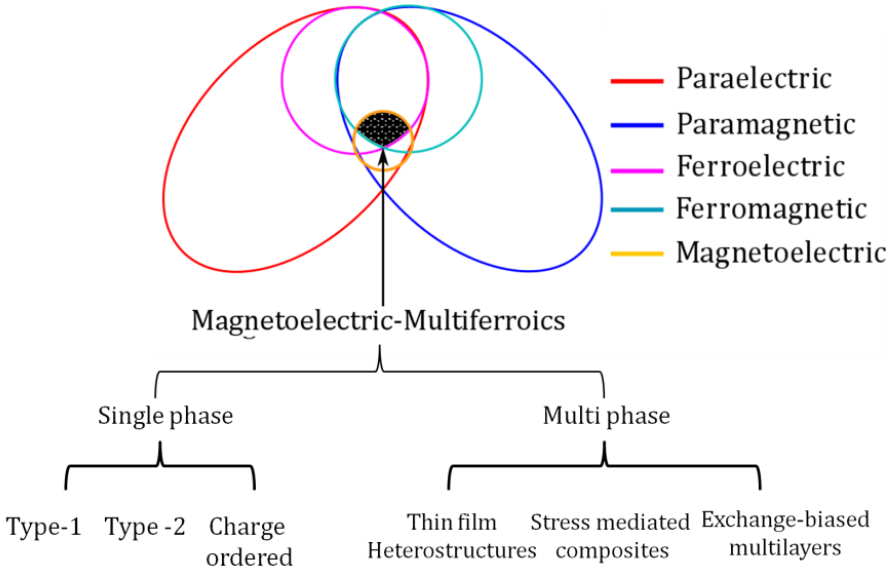

Figure 1.4 The classification of ferroic materials.

1.1 The Linear Magnetoelectric Effect and Magnetoelectric Composites

The ME effect, as described in the previous section, can be mathematically expressed as

$$\Delta P_i = \alpha_{ij} \Delta H_j \qquad \text{(Direct ME effect)} \tag{1.1}$$

$$\mu_0 \Delta M_i = \alpha_{ji} \Delta E_j \quad \text{(Converse ME effect)} \tag{1.2}$$

Einstein convention has been followed in the above expression as well as the other expressions hereafter unless specified otherwise. The direct ME effect equates an induced electric polarization (P_i) to the applied magnetic field (H_i), and similarly the converse ME effect displays generation of magnetization (M_i) under an applied electric field (E_j). The coefficient appearing in these equations (α_{ij}) is the tensor of the linear ME effect. α_{ij} is an important quantity, as it is a measure of the strength of the coupling. μ_0 is the magnetic susceptibility of vacuum.

The phenomenological expression of magnetoelectric coupling constant can be also derived thermodynamically. The Helmholtz free energy expression for a magnetoelectric-multiferroic system contains the following terms [29]:

$$F(E,H) = F_0 - P_i^s E_i - \mu_0 M_i^s H_i - \frac{\varepsilon_0}{2} \varepsilon_{ij} E_i E_j - \frac{1}{2} \mu_0 \mu_{ij} H_i H_j - \alpha_{ij} E_i H_j \tag{1.3}$$

Where P^s and M^s are the spontaneous polarization and magnetization respectively; E_i and H_i are the applied electric and magnetic field respectively; the coefficients ε_{ij}, μ_{ij}, and α_{ij} are the relative electric permittivity, relative magnetic permeability, and linear magnetoelectric coefficient tensors, respectively, with ε_0 being the dielectric permittivity of free space, and μ_0 is the magnetic permeability of free space. In order to deduce the explicit expression for magnetoelectric coupling {eqs. (1.1), and (1.2)}, it is necessary to consider the following Maxwell's differential pairs [37]:

$$P_i = P_i^s + \varepsilon_0 \varepsilon_{ij} E_j + \alpha_{ij} H_j \tag{1.4}$$

$$\mu_0 M_i = \mu_0 M_i^s + \mu_0 \mu_{ij} H_j + \alpha_{ji} E_j \tag{1.5}$$

$$\alpha_{ij} = \frac{\partial P_i}{\partial H_j} \qquad \text{(Dierect ME effect)} \tag{1.6}$$

$$\alpha_{ji} = \mu_0 \left(\frac{\partial M_i}{\partial E_j} \right) \quad \text{(Converse ME effect)} \tag{1.7}$$

Eq. (1.3) fully describes a single phase magnetoelectric multiferroic, and it relates to the net polarization as in parts due to the spontaneous polarization, the electrically and the magnetoelectrically induced polarization via the 1st, 2nd and 3rd terms, respectively. However we will shortly see that the terms in eq. (1.3) are not sufficient for an exhaustive description of a composite magnetoelectric.

Firstly, it is necessary to consider the philosophy of a composite magnetoelectric. As the name suggest, the end effect is achieved by combination of two different materials, whose individual properties multiply to give magnetoelectricity (product property). A more descriptive explanation of this philosophy can be put as follows: Material *A*, which exhibits a property *y* (stress under mechanical constraints) in response to stimulus *x* (magnetic field), related by the coefficient *dy/dx* (*q*; Piezomagnetism), when combined with a material *B*, which on the other hand exhibits property *z* (polarization) on application of *y* as related by the coefficient *dz/dy* (*d;* Piezoelectricity), than the resulting composite will have a property that will be the product of the two coefficients (*dz/dy*)·(*dy/dx*); in other words, on applying magnetic field, a corresponding polarization is generated in the material. Apparently, a converse effect also exists, which means appearance of magnetization on application of a corresponding electric field. This can be physically explained by considering a bi-layer ME composite (Figure 1.5). For the direct effect, application of magnetic field will produce a strain in the magnetic phase due to piezomagnetism, which will be converted to stress at the interface due to the elastic properties, ultimately inducing polarization inside the piezoelectric phase. A similar but opposite effect, termed as converse ME effect, also exists owing to the existence of symmetrical individual properties (Converse piezoelectricity + Villari effect).

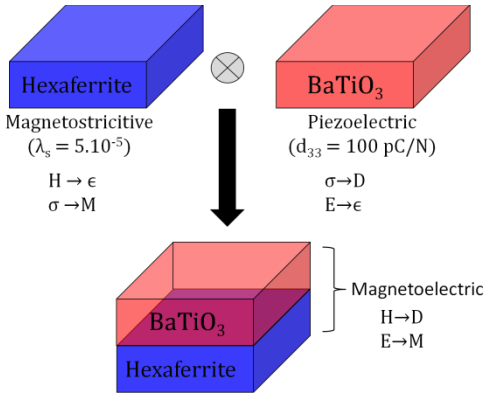

Figure 1.5 Schematics of a bilayered ME composite, out of the two individually piezoelectric and piezomagnetic phases. The values shown in bracket are typical for the key properties of the magnetic (saturation magnetostriction) and the piezoelectric (electromechanical coupling constant) phases.

Eq. (1.3) does not fully describe a composite system, since neither of the constituent phases in the composite exhibits the inherent coupling (α_{ij}). Rather, the coupling appears as an indirect manifestation via the mediating strain. In order to account for this strain mediated coupling, it is necessary to consider a combination of two monoferroic systems (bi-layers; Figure 1.5), viz. a piezomagnetic and a piezoelectric material. In this case, the two corresponding free energy expansion can be written as:

$$-F(E,\sigma) = P_s.E + \in_s.\sigma + \frac{\varepsilon_0}{2}\varepsilon^*_{ij}E_iE_j + C^{P*}_{ijkl}\sigma_{ij}\sigma_{kl} + d^*_{ijk}E_i\sigma_{jk} \quad \text{(Piezoelectric phase)} \qquad \textbf{(1.8)}$$

$$-F(B,\sigma) = M_s \cdot H + \in_s.\sigma + \mu^*_{ij}H_iH_j + S^{M*}_{ijkl}\sigma_{ij}\sigma_{kl} + q^*_{ijk}H_i\sigma_{jk} \quad \text{(Piezomagnetic phase)} \qquad \textbf{(1.9)}$$

$$P_i = P_s + \varepsilon_0 \varepsilon_{ij}^E E_j + d_{ijk}^P \sigma_{jk} \quad \textbf{(1.10)}$$

$$\epsilon_{ij}^E = \epsilon_s + S_{ijkl}^{P*} \sigma_{kl} + d_{kij}^* E_k \quad \textbf{(1.11)}$$

$$M_i = M_s + \mu_{ij}^* H_j + \frac{1}{\mu_0} q_{ijk}^* \sigma_{jk} \quad \textbf{(1.12)}$$

$$\epsilon_{ij}^m = \epsilon_s + S_{ijkl}^{M*} \sigma_{kl} + \frac{1}{\mu_0} q_{kij}^* H_k \quad \textbf{(1.13)}$$

The coefficients d_{kij}^* and q_{kij}^* are the piezoelectric and piezomagnetic coefficients of the respective phases, which are differentiated from their free phase counterparts (d_{ijk}, and q_{ijk}) by the use of '*' superscript. This modification is opted since both the phases are connected to each other, and do not exist freely. Similarly S_{ijkl}^{P*}, and S_{ijkl}^{M*} are the modified elastic compliances of the piezoelectric and piezomagnetic phases. These quasi-individual coefficients can be visualized as corresponding to measured while probing exactly one of the two layers, while the same being still in physical contact with the other. Had this probe been extended to cover both layers, then in effect a fully composite response would have been measured (to be discussed in section 1.4); on the other hand, if an extremely local spot on the composite is probed, then depending on its spatial location the exact free phase counterparts (either d_{ij} or q_{ij}) will be measured. Now the products, direct and converse magnetoelectric coupling, can be expressed as [38]:

$$\alpha_{ij}^* = \frac{\partial P_i}{\partial H_i} = \frac{\partial P_i}{\partial \sigma_i} \frac{\partial \sigma_i}{\partial \epsilon_i^P} \frac{\partial \epsilon_i^m}{\partial H_i} = \frac{1}{\mu_0} d_{imn}^* . C_{mnkl}^{P*} . q_{jkl}^* \quad \text{(Direct effect)} \quad \textbf{(1.14)}$$

$$\alpha_{ij}^* = \frac{\partial M_i}{\partial E_i} = \frac{\partial M_i}{\partial \sigma_i} \frac{\partial \sigma_i}{\partial \epsilon_i^M} \frac{\partial \epsilon_i^P}{\partial E_i} = \frac{1}{\mu_0} q_{imn}^* . C_{mnkl}^{M*} . d_{jkl}^* \quad \text{(Converse effect)} \quad \textbf{(1.15)}$$

Where C_{mnkl}^{P*} and C_{mnkl}^{M*} are the modified elastic stiffness of the piezoelectric and piezomagnetic component phases, respectively. The stress σ_{ij}, which acts as a mediator for the ME effect, is henceforth termed as ME stress. The asterisk superscript on the coupling constant in eq.(1.13) - (1.14) is meant to differentiate it from the experimentally measured value. Experimentally ME coupling is measured by measuring the magnetic field-generated macroscopic open circuit voltage on one of the faces of the composite, which might span either or both of the constituent faces. However, the scenario considered in the thermodynamical formulation presented above, represents the coupling values corresponding to just the component. This analysis basically highlights that in composites the direct and the converse ME effect can be different, and demonstrates the complexity associated with the microscopic contribution of the constituent properties to the macroscopic ME coupling; this aspect will be discussed in more details in section 1.4. Practically, a parameter called the open circuit ME voltage coefficient $\alpha_V = \Delta D/\Delta H$ *V/m.Oe* (D – electric displacement), or the ME flux co-efficient $\alpha_B = \Delta B/\Delta E$ *Gauss·m/V* (B – magnetic flux) are used, since they give a good measure of the more useful quantities (voltage/magnetic flux).

Apart from the bi-layer composites considered above, several other configurations are possible. Depending on the connect schemes within each constituent phase, different composite

configurations can be broadly classified as 0-3, 1-3, 2-2, or 3-3 type; here the numbers indicate dimensions in which the connectivity of the respective constituent phases persists; a physical description of these schemes can be classified as following:

- **Particulate composite (0-3/3-0):** Here one of the components, either the piezomagnetic (0-3) or the piezoelectric (3-0) phase, stays as particulates embedded inside a matrix of the other component (Figure 1.6c). Quite often these connectivity schemes are refereed to composites synthesized by conventional ceramic rout where the diffusion length of one phase is controlled in order to maintain an inclusion level connectivity, normally of the order of a few μm [39, 40].
- **Laminate composites (2-2):** Here the two components have 2-dimensional connectivity and are separated by a planar interface (Figure 1.6a). A union of the two components can be realized with different degrees of precision, e.g. heteroepitaxy, tape-casting, or lamination. Common examples range from tape casted PZT–$Co_{0.6}Zn_{0.4}Fe_2O_4$[41] to heteroepitaxially grown $BaTiO_3$ – $CoFe_2O_4$ thin films[42].
- **Columnar composites (1-3/3-1):** In such a connectivity scheme one of the components, either piezomagnetic (1-3) or piezoelectric (3-1) phase exists in the form of columns embedded inside a matrix of the other component (Figure 1.6b). More commonly such structures are realized using thin film technology where a self-assembly mechanism involving $BaTiO_3$/$PbTiO_3$/$BiFeO_3$–$CoFe_2O_4$ [43] systems is employed. However, possibilities to synthesize bulk columnar composites, using electrospinned fibers also exist [44, 45].
- **Mixed phase composites (3-3):** This is the most complex connectivity scheme possible, in which the two phases are continuously connected in all the dimensions, and yet are in intimate contact with each other. Such schemes are often found in ceramics as a consequence of uncontrolled processing parameters. A precise comprehension of bulk ME coupling is often difficult, and can only be approximated up to some extent.

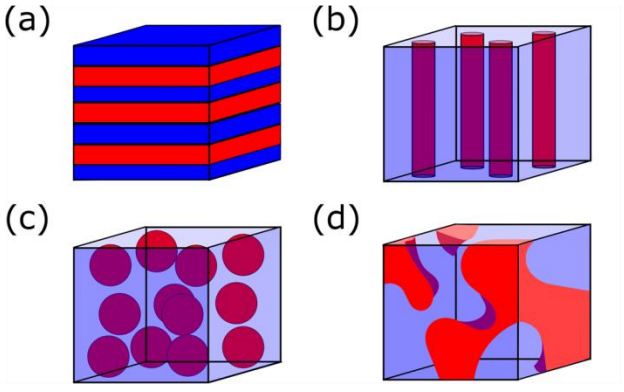

Figure 1.6 (a) The 2-2, (b) 1-3, (c) 0-3, and (d) 3-3 types of phase connectivity schemes found in ME composites.

The motivation behind magnetoelectric composites comes from the fact that there are no material specific limiting constraints, as is the case with single phase magnetoelectric-multiferroics. This

allows the freedom of choice for the best constituent materials with ideal properties, out of a large spectrum of materials available. The best choice is basically dictated by a primary aspect of the constituent phases, which is their phase transition temperature. From performance point of view the constituents should be active at ambient temperatures for most of the applications; this is something hardly achievable in the single phase counterparts. Considering the choices of ideal pairs of constituent materials, there are four important factors identified:

- Piezomagnetic coefficient
- Piezoelectric coefficient
- Mechanical impedance
- Chemical stability

Over time, several composite systems have been explored. Out of those, combinations of ferroelectric/piezoelectric oxide and a ferrimagnetic ferrite have emerged as the most practical and well performing candidates. Interestingly, even though the presence of a ferroic order in the constituent phase is not a requirement, the above mentioned factors are well met for such combinations. Table 1.2/Table 1.3 summarizes the key combinations that are heuristically developed and optimized over time. $BaTiO_3$ – $CoFe_2O_4$ (BTO-CFO) was the first ever composition to be studied for magnetoelectric effect [46]. Until now, BTO-CFO stays by far the most chemically stable pair, in that they do not form any intermediate phases when co-synthesized. However parallel to the studies in BTO-CFO, several other compositions were developed; first amongst them was $BaTiO_3$ – $Ni(Co, Mn)Fe_2O_4$, where it was found that the magnetic phase (modified $NiFe_2O_4$), even though loosing on magnetostriction to $CoFe_2O_4$, possesses superior electrical resistivity which is also an important factor affecting the end coupling. Apart from this, attempts have been made to improve the electrical resistivity of $NiFe_2O_4$ (NFO) in the composites, by substituting A site ions with zinc resulting in optimized coupling [47]. Composite systems based on PZT ($PbZr_xTi_{1-x}O_3$) are also extensively studied owing to their superior piezoelectric properties. However it can be inferred from Table 1.2 that those PZT based compositions, where CFO is a magnetic constituent, are not any different as compared to their counterparts based on BTO (especially in 0-3 configuration). This once again reflects the poor electrical characteristics of CFO. On the other hand those compositions with NFO as a magnetic component show much higher coupling. Overall, however, PZT based systems are not much studied in particulate configuration (0-3), which can be associated with its poor chemical stability in comparision to BTO based systems. Later on, Srinivasan et al. proposed that the optimal choice of materials for a magnetoelectric composite are a highly magnetostrictive rare-earth compounds (Terfenol-D) in combination with a relaxor based piezoelectric material [48]. Followed by this, several systems based on PMN-PT ($PbMn_{0.33}Nb_{0.66}O_3$ – $PbTiO_3$) were studied and found to be having high coupling values. Due to a higher freedom of choice for materials, and the possibility to better control the interface, layered configurations (2-2), centered on PZT and PMN-PT based systems, were highly studied. Later on such systems were found to be executing a Giant magnetoelectric effect when operated at

mechanical resonance [49]. This opened up new opportunities for magnetoelectric composites and lead to a quest for optimization of the individual components to achieve maximum sensitivity at mechanical resonance [50, 51].

Table 1.2 A summary of various ME composite systems, classified in terms of the constituent piezoelectric component.

System	Composition	Connectivity scheme/Method	α_E (mV/cm.Oe)	Method of measurement	Ref.
$BaTiO_3$ Based	$0.62BaTiO_3 – 0.38CoFe_2O_4$ + 1.5Wt% TiO_2	Eutectic/Unidirectional growth	50	Lock-in (f=1 kHz)	[52]
	$0.8BaTiO_3 – 0.2CoFe_2O_4$	0-3/Sintering	10	Lock-in (f=1 kHz)	[53]
	$0.8BaTiO_3 – 0.2CoFe_2O_4$	0-3/Sintering	0.25	Pulsed magnetic field technique	[54]
	$0.6BaTiO_3 – 0.4CoFe_2O_4$	0-3/Sintering	0.8	Pulse magnetic field technique	[54]
	$0.25BaTiO_3 – 0.75CoFe_2O_4$	0-3/Sintering	2	Lock-in	[55]
	$BaTiO_3 – CoFe_2O_4$	1-3/Self Assembled	1×10^3(Locally measured)	Magnetic force Microscopy	[56, 57]
	$BaTiO_3 – CoFe_2O_4$	2-2/Hetroepitaxy	104	Lock-in	[58]
	$0.6BaTi_{1.01}O_{3.01} – 0.4Ni_{0.97}Co_{0.03}Mn_{0.1}Fe_{1.9}O_4$	0-3/Sintering	21	Lock-in	[59]
	$0.6BaTiO_3 – 0.4NiFe_{1.98}O_4$	0-3/Sintering	252	Lock-in	[60]
	$0.7BaTi_{1.01}O_{3.01} – 0.3Ni_{0.92}Co_{0.03}Cu_{0.05}Fe_2O_4$	0-3/Sintering	0.59	Lock-in	[61]
	$BaTiO_3 – NiFe_2O_4$	2-2/Hetroepitaxy	12	Lock-in	[42]

Table 1.3 A summary of various ME composite systems, classified in terms of the constituent piezoelectric component.

System	Composition	Connectivity scheme/Method	α_E (mV/cm.Oe)	Method of measurement	Ref.
$BaTiO_3$ Based	$0.9BaTiO_3$ –0.1 $NiFe_2O_4$	0-3/Sintering	12	Lock-in	[62]
	$[(Bi_{0.5}Na_{0.5})TiO_3$ – $(Bi_{0.5}K_{0.5})TiO_3$ – $BaTiO_3]$ – Terfenol-D	2-2 trilayer/ epoxy bonded	40.7	Lock-in (1 kHz)	[63]
PZT Based	$0.8PZT– 0.2CoFe_2O_4$	0-3/Sintering	30.1	Lock-in (80 kHz)	[64]
	$PZT– CoFe_2O_4$	2-2/Heteroepitaxy	27	Lock-in (1 kHz)	[65]
	$0.5PZT– 0.5CoFe_2O_4$	0-3/Sintering	2.5	Lock-in (1 kHz)	[66]
	PZT	1-1(Nanofibres)/Electrospinning	2.5×10^4	Piezoresponse force microscopy (locally)	[45]
	$PbZr_{0.52}Ti_{0.48}O_3$– $CoFe_2O_4$	2-2 (Multilayer)/Sol-gel	350	Lock-in (1kHz)	[67]
	$PZT– Co_{0.6}Zn_{0.4}Fe_2O_4$	2-2(Multilayer)/tape casting	280	Lock-in (100KHz)	[41]
	0.55PZT – 0.45NiFe2O4	0-3/Sintering	6700	Lock-in 132.6 KHz (Resonance)	[68]
	0.8PZT – 0.2NiFe2O4	0-3/Sintering	195	Lock-in 1 kHz	[69]
	0.2PZT – 0.8(Ni0.8Zn0.2Fe2O4)				
	PZT - NFO	2-2/Tape casting	460	d.c. method	[70]
	PZT - NFO	2-2 (multilayer)/Tape casting	1500	d.c. method	[70]
	PZT – Terfenol-D	2-2/Epoxy Bonding	4700	Lock-in (1 kHz)	[48]
	PZT – PVDF – Terfenol-D	2-2/ Binding + Bonding	3000	Lock-in (100 kHz)	[50]
PMN-PT Based	PMN-PT – Terfenol-D	2-2/ Epoxy bonding	740	Lock-in (1 kHz)	[71]
	PMN-PT – Terfenol-D	2-2/ modified layers/bonded	3300	Lock-in (1 kHz)	[51]

Apart from serving as a literature survey, Table 1.2/Table 1.3 also reflects the fact that within a particular system, with a particular connectivity scheme, there exist a large scatter in the coupling values. These large deviations point towards the fact that the ME coupling is highly critical to the relative microstructures of the constituent phases, which under different processing conditions, might assume highly scattered morphologies. This partly constitutes the motivation for the present thesis. Attempts are made to unravel the local dynamics in the oxide/ferrite composite systems, which might impart an understanding about the microstructure dependency of overall ME coupling.

For the local ME investigations, the constituent phases are considered individually, and the resultant effects of the ME stress are studied. Interestingly, aspects surrounding ferroicity of the individual phases (ferroelectric/ferrimagnetic) form the core of the local ME investigations presented in this thesis. In the next sections, relevant aspects of ferroelectricity and magnetism are reviewed.

1.2 Ferroelectricity

By definition, ferroelectricity means possession of a spontaneous dipole order in a crystal, which can switch its orientation between two or more states on application of an electric field. The consequence of such a polar order is the appearance of a large measurable surface charge density at the electrodes in a capacitor arrangement (Figure 1.11).

Origin of ferroelectricity in certain specific cases lies in structural transitions triggered by

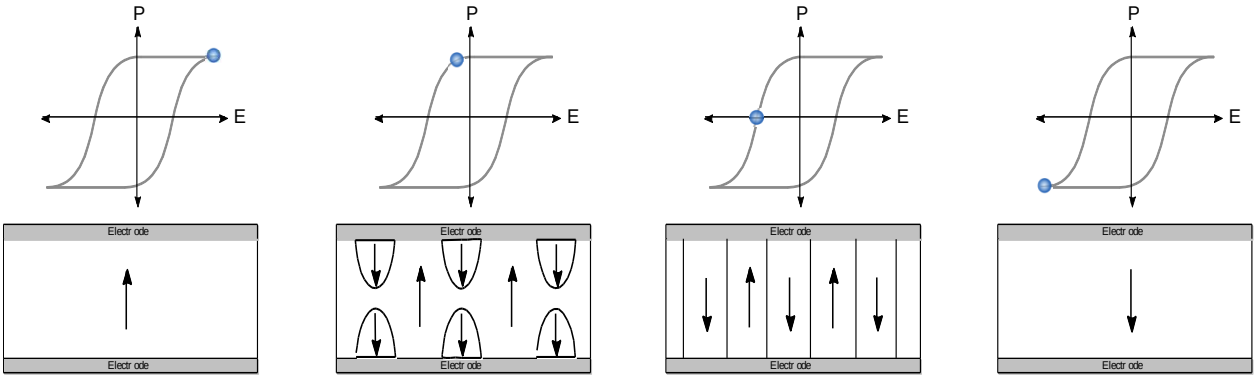

Figure 1.7 The evolution of ferroelectric switching on application of external electric field in a closed circuit configuration (Bottom row), and a corresponding change in the polarization (Top row).

condensation of a low frequency phonon mode (Soft-mode). Such modes, which on condensation lead to shifting of charge centres in the lattice, are hence termed as *ferrodistortive*. The structural transition is usually (first order) marked by a discontinuity in electrical and other related properties across a critical transition temperature (T_c), with a high temperature centrosymmetric phase transforming to a non-centrosymmetric polar phase as temperature decreases. The mode that triggers the non-polar to polar transition is termed as *ferrodistortive*, and in most crystals,

where the condensed mode is necessarily polar (optically active), the set in spontaneous polarization $(P \neq 0; E = 0)$is reversible leading to ferroelectricity. Figure 1.8shows experimentally observed divergence of dielectric constant on approaching T_c (120°C), along with the discontinuous change in polarization (Figure 1.8a); this is typically taken as a sign of the first order non-polar to polar transition. The link between the observed electrical anomalies, and the established role of soft mode induced polar transition, were first proposed and formulated by Cochran [72]. This formulation is so far the most successful one, and has been authenticated by experimental findings. According to Cochran's treatment the frequency of a soft phonon mode, always centred at the zone centre of the respective Brillouin zones, is a function of temperature *T*, given as

$$\omega_s(k = 0) = \sqrt{C(T - \theta_c)} \tag{1.16}$$

where *C* is a constant, and θ_c is the curie-point. Eq. (1.16) combined with the *Lyddane-Sachs-Teller* (LST) relation [73] results into

$$\varepsilon' \propto {}^{1}/_{\omega_s^2} \tag{1.17}$$

Eq.(1.17) gives a clear picture of the variation of dielectric properties as a function of temperature. According to eq.(1.16)-(1.17), as the temperature approaches the transition temperature T_c the transverse optical soft phonon mode tend to zero leading to a divergence in the dielectric constant. In other words, a zero frequency polar mode at transition temperature means no effective force constant to hold back the polarized ions and hence a large dielectric constant (Figure 1.11).

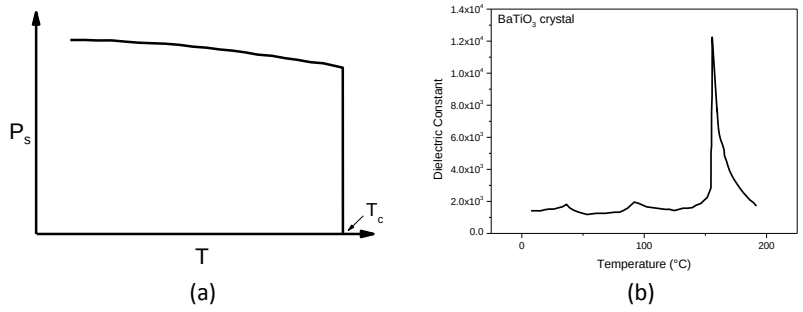

Figure 1.8 The temperature variation of polarization (a), and the dielectric permittivity [74] (b) spanning across the first order phase transitions for a typical ferroelectric [16].

Since the dielectric properties are linked to the lattice dynamics, the crystal symmetry has a vital role to play in determining ferroelectricity in crystals. Only certain class of crystals can be classified as ferroelectrics due to such symmetry constraints. Table 1.4 classifies the different crystal classes based on their centro-symmetry which is a necessary ingredient determining ferroelectricity. Simultaneously, Table 1.4 also highlights the fact that absence of

centrosymmetry is not a sufficient condition for polar order, as the basis of certain lattice positions has to have opposite charges in order to have a net dipole moment.

Table 1.4 Classification of crystal symmetries in terms of electrical polarity [16].

Polarity	**Crystal system**										
	Cubic		Hexagonal		Tetragonal		Rhomboh-edral		Orthor-hombic	Monoclinic	Triclinic
Non-Polar	m3m	m3	6/mmm	6/m	4/mmm	4/m	$\bar{3}$m	$\bar{3}$	mmm	2/m	
	432 $\bar{4}$3m	23	622 $\bar{6}$m2	$\bar{6}$	422 $\bar{4}$2m	$\bar{4}$	32		222	–	–
Polar (Pyroelectric)			6mm	6	4mm	4	3m	3	mm2	2m	1

Among most of the non-centro symmetric classes, however, piezoelectricity (the appearance of charges at the surface in response to an applied stress) is in common. Only a subset of the 10 crystal class (Table 1.4) exhibit a coupling between the acoustic mode and the polar mode, resulting in co-existence of a spontaneous polar order (pyroelectricity) and piezoelectricity. A sub-subset of this pyro-piezoelectric crystals exist, in which a complete mode condensation takes place, and the induced order is reversible are the ones that exhibits ferroelectricity as well. From this coupling, it can be inferred that ferroelectrics also universally possess a spontaneous strain, which in some cases (BTO) can also be switched by application of mechanical stress (Ferroelasticity). The net electrical displacement (D_i) in such a ferro-elasto-electric material can be described by following relation [75]:

$$D_i = P_S + d_{ijk}^{T,E}\sigma_{jk} + \varepsilon_0\varepsilon_{im}E_m \qquad \textbf{(1.18)}$$

where d_{ijk} and ε_{im} are the piezoelectric coefficient. The first term indicates the contribution from the spontaneous polarization, whereas the last term is the electric field induced displacement. The central term in the r.h.s. of eq.(1.18) is the direct piezoelectric effect, which relates the applied stress and the induced displacement contribution via the piezoelectric tensor. Here both the piezoelectric tensor and stress tensor are given in the Voigt notation for sake of simplicity. The intrinsic direct piezoelectric coefficient has to be measured at a constant (or zero)

temperature and electric field, as indicated by the superscripts T and E in the central term of eq.(1.18) [75].

$$D_i = d_{ijk}^{T,E}\sigma_{jk} \qquad \text{(Direct piezoelectricity)} \tag{1.19}$$

Thermodynamically, the free energy (G) contribution of the net electrical displacement is formulated by the extensive/intensive pair product, $D_i \cdot dE_i$, and hence the direct piezoelectric effect is thermodynamically expressed as [75]:

$$d_{ijk}^{T,E} = \left(\frac{\partial D_i}{\partial \sigma_{jk}}\right) = -\left(\frac{\partial^2 G}{\partial \sigma_{jk}\,\partial E_i}\right) = -\left(\frac{\partial^2 G}{\partial E_i\,\partial \sigma_{jk}}\right) = \left(\frac{\partial \epsilon_{jk}}{\partial E_i}\right) = d_{ijk}^{T,\sigma} \tag{1.20}$$

$$\epsilon_{ij} = d_{kij}^{T,\sigma} E_k \qquad \text{(Converse piezoelectricity)} \tag{1.21}$$

where the term $d_{kij}^{T,\sigma}$ relates to the converse piezoelectric effect; appearance of a strain on application of electric field. Also eq.(1.20) shows that the converse and the direct piezoelectric coefficients are thermodynamically equivalent, with the only distinction that unlike the direct effect, stress along with temperature has to be constant (or zero) while measuring the converse effect.

1.2.1 Domain Walls in Ferroelectrics

Now, due to the presence of imperfections and surfaces in a crystal where polarization induced bound charges are uncompensated, a large depolarization field is created which can possibly suppress polarization. In order to maintain the ferroelectric state, a crystal upon cooling below Curie temperature, tends to form domains with polarization pointing in two or more equivalent directions, this leads to minimization of the total free energy. The stable configuration is hence decided by an equilibrium between domain wall energy and depolarization energy. The width of a domain d for a stable periodic configuration can be expressed as:

$$d = \sqrt{\frac{\sigma t}{\varepsilon^* P_s^2}} \tag{1.22}$$

Where σ is the domain wall energy density, P_s is the domain polarization, t is the thickness of the crystal slab, and ε^* is an equivalent dielectric constant. The domain wall energy holds contributions from depolarization energy due to $div \cdot P$ at domain boundaries, in addition to the electrostatic and the elastic energy. In absence of high conductivity to neutralize the depolarization, the minimization of energy is allowed by 180^o and 90^o domain configurations for perovskites with tetragonal symmetry.

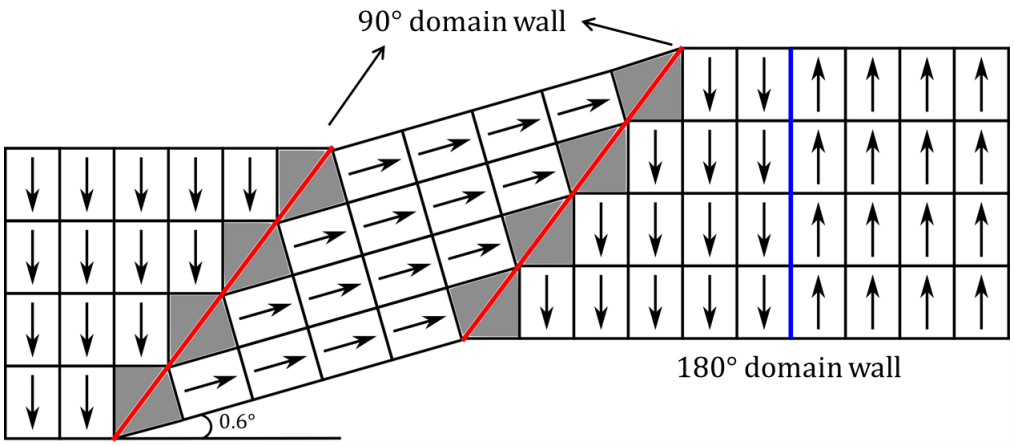

Figure 1.9 Schematics of the 90°, and the 180° domain walls existing in the commonly studied ferro-elasto-electric materials like $BaTiO_3$, and $PbTiO_3$. The arrows in the exaggerated tetragonal cells represent the corresponding polarization directions. In $BaTiO_3$, the 90° domain walls deviate by a value of 0.6^0, which is exaggerated here.

Since the polarization is accompanied by a spontaneous strain, the 90° domains walls exhibit a misfit strain (Figure 1.9), and are also ferroelastic walls.

Amongst the various available ferroelectric materials, $BaTiO_3$ is a classical compound that has been widely studied. Ferroelectricity in $BaTiO_3$ is very well understood [74]; it manifests a displacive type of ferroelectricity, along with the appearance a spontaneous switchable strain (Ferroelasticity). In addition to superior ferro-elasto-electric properties, $BaTiO_3$ is also a chemically stable compound, which makes it an evergreen compound for technological applications.

1.2.2 $BaTiO_3$

$BaTiO_3$ is a ferroelectric with multiple structural symmetries appearing within different ranges of temperature. Above 120° C it is cubic (m3m); ferroelectricity is triggered on cooling down as the phase evolve to tetragonal symmetry (4mm) with the polarization pointing along ⟨001⟩ directions. Ferroelectricity is then maintained until absolute zero accompanied by two successive transitions; tetragonal – orthorhombic (mm2; 5 °C), and orthorhombic – rhombohedral (3m; -95 °C) with the polarization pointing in ⟨011⟩ and ⟨111⟩ equivalent directions respectively. Ferroelectricity in the room temperature phase (tetragonal), is characterized by a displacive transition triggered by a soft phonon mode as shown in Figure 1.8.

The tetragonal phase has six possible polarization directions. This results into antiparallel as well as orthogonally juxtaposed domains. The domains with polarization parallel to [001] direction are for evident reason termed as c-domains while those with polarization parallel to [100] or [010] are for the same reason called a-domains. The wall between same type of domains are called 180° walls whereas those between the two types i.e. c/a, are termed 90° walls. For a 90° wall, domains are not actually oriented exactly at 90° to each other rather at 90.6°, rendering the

surface over in-plane domains ([100] and [010]) to tilt at 0.6° as shown in Figure. These walls are also termed ferroelastic walls since they separate two elastically switchable states.

Piezoelectricity in $BaTiO_3$ is characterized by a third rank polar tensor that can be represented in the following matrix [8].

$$d_{ijk}^{T,E} = \begin{pmatrix} 0 & 0 & 0 & 0 & d_{15} & 0 \\ 0 & 0 & 0 & d_{15} & 0 & 0 \\ d_{31} & d_{31} & d_{33} & 0 & 0 & 0 \end{pmatrix} \quad \textbf{(1.23)}$$

The measured coefficients for $BaTiO_3$crystals and ceramics, along with the predictions from Devonshire theory, are listed as below.

Table 1.5 Open circuit piezoelectric coefficients (pC/N) of $BaTiO_3$, measured at 25°C [76].

Components	Crystal	Ceramic	Devonshire crystal values
d_{15}	392	270	1160
d_{31}	-34.5	-79	-63
d_{33}	85.6	191	165
g_{15}	15.2	19.8	-
g_{31}	-23.0	-4.7	-
g_{33}	57.5	11.4	-

The piezoelectric coefficients exhibit an anisotropic nature, w.r.t different crystallographic directions. Figure 1.10 shows the angular dependence of d_{33} component for $BaTiO_3$. Interestingly, the maximum longitudinal co-efficient (d_{33}) is achieved not along the polarization directions ⟨001⟩, rather the ⟨111⟩ directions.

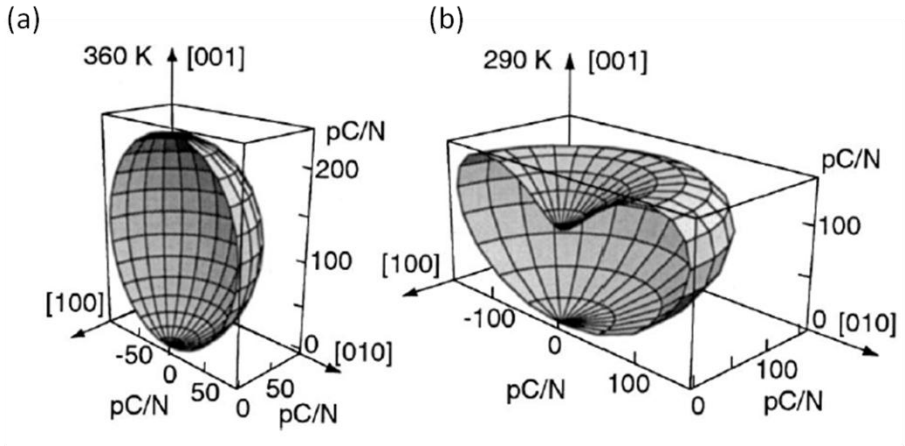

Figure 1.10 Angular dependence of the longitudinal piezoelectric coefficient in $BaTiO_3$, theoretically calculated at (a) 360 K, and (b) 290 K [77, 78].

1.3 Magnetism: Origins and Related Phenomena

The modern electromagnetic formalism has come a long way; its initial discovery roots in its manifestations out of solids (ferromagnets). The first material known to mankind (2500 years ago) to be attracting another objects was a ferrimagnet, which we know today as ferrite (Fe_3O_4). The interplay between atomic/ionic spin states and their arrangement in crystals give rise to the various forms of magnetism. The basic units of all kinds of magnetism are atomic/ionic magnetic moments. The atomic unit of such magnetic moments is a Bohr magneton ($1\ \mu_B \sim 0.93 \times 10^{-23}$ $A{\cdot}m^2$), which also happens to be the value of a single electron spin magnetic moment. Net magnetic moment for an ion/atom is derived from a combination of the total-orbital angular momentum (*L*) and the total spin-angular (*S*) momentum of the outermost electrons. For most of the magnets, the latter has been found to have larger contribution, since the angular momentums of the concerned orbitals are almost quenched due to the presence of crystal field. As an example consider the Mn^{+4} ion with three unpaired electrons in the outermost shell ($[Ar]2p^0 3d^3$) has a net moment observed as 3.90 μ_B which is approximately equal to the spin only contribution of the three electrons with slight deviations due to spin orbit-coupling.

The overall magnetic character of a material can be categorized based on its response to an applied magnetic field *H*. Those materials that tend to attract towards the stronger part of an inhomogeneous magnetic field are termed as paramagnetic and those which tend to drift towards the weaker part of it are called diamagnetic. The general formulation relates magnetic flux (*B*) to the applied magnetic field (*H*) and the magnetization (magnetic moment per unit volume of the material; *M*) [79]:

$$B = \mu_0 (H + M) \tag{1.24}$$

where μ_0 represents the permeability of space. Now, in order to conveniently express the effect of material induced fields it is common to represent an external induction as $B_0 = \mu_0 H$**.** Secondly the relation between the applied field and the magnetization induced thereof is expressed as [79]

$$M = \chi H \tag{1.25}$$

where χ is termed as the magnetic susceptibility. For the paramagnetic class χ is positively linear, whereas for the diamagnetic class it is negatively linear. Now within the paramagnetic class, a sub-class of materials exists where this relation is non-linear, and the non-linearity is attributed to the existence of spontaneously magnetized regions in the absence of magnetic field. Such regions appear after cooling down a material below a specific transition temperature called Curie-temperature (T_c); they are usually oriented opposite to each other canceling the net magnetization of the material. However on application of magnetic field they rotate and orient themselves along the magnetic field direction before saturating at some point, hence giving rise to the non-linearity. The magnetization order within a domain can lead to a (i) non-zero net magnetization in one direction (Ferromagnetism), (ii) zero net magnetization due to mutual

cancelation (Anti-ferromagnetism), (iii) or a non-zero net magnetization due to partial cancellation (Ferrimagnetism).

The action of spontaneous alignment of the moments is similar, as if an additional mean field is acting upon each moment. This mean field proposed by Weiss is termed as Weiss's mean field and it is related to magnetization. It turns out that the typical Weiss field values for ferromagnets, calculated from magnetostatics, are of the order of 10^3 T, a value that is four order of magnitude higher than the field produced in the vicinity of a magnetic ion ($\mu_0\mu_B/4\pi a^3$). This signifies that Weiss's mean field theory cannot be the basis for explaining the coupling of ionic moments.

The actual interaction which gives rise to such ordering of moments can only be explained in quantum mechanics. To understand this, one considers the total eigen (wave) function of a system of electrons α and β (fermions), which according to Pauli's principle has to have an asymmetric form. For a two electron system, the total eigen function can be expressed as a combination of spatial and spin eigen functions [80].

$$\psi_A = \frac{1}{\sqrt{2}}[\psi_\alpha(1)\psi_\beta(2) + \psi_\beta(1)\psi_\alpha(2)] \quad \textbf{(1.26)}$$

$$\psi_A(\text{total}) = \psi_A\{\text{Spatial}\} \cdot \psi_S\{\text{Spin}\} \ (\text{Parallel spins}) \quad \textbf{(1.27)}$$

Or

$$\psi_A(\text{total}) = \psi_S\{\text{Spatial}\} \cdot \psi_A\{(\text{Spin})\} (\text{Antiparallel spins}) \quad \textbf{(1.28)}$$

where the subscripts *A* and *S* denotes the anti-symmetric and symmetric wave functions, respectively. Out of the two possible representations of the total eigen functions, the one with an anti-symmetric spatial function has an interesting consequence, in that if the co-ordinates of the two electrons, with quantum states *a* and *b*, are very close than the anti-symmetric spatial eigen function vanishes [80].

$$\frac{1}{\sqrt{2}}[\psi_a(1)\psi_b(2) - \psi_b(1)\psi_a(2)] \cong \frac{1}{\sqrt{2}}[\psi_a(1)\psi_b(2) - \psi_a(1)\psi_b(2)] \cong 0 \quad \textbf{(1.29)}$$

here the subscripts denote the quantum state. In other words, if the spins of the two electrons for this case are parallel then they will tend to stay far apart, as closeness would result into vanishing probability. On the other hand for the second case it can be inferred in similar fashion that the antiparallel alignment of the spins results in a close association of the otherwise repulsive electrons. Such an interaction is hence termed as an exchange interaction and the virtual force tending to bind the particles is termed as exchange force. In this particular case of overlap between the two electrons wave functions, the arrangement with mutually parallel spins marks the lowest energy state as the electrostatic repulsion is minimal in this case. However depending on various different types of overlaps between different excited states and specifically in solids where the ions are surrounded by other ions/ligands, different spin arrangements are possible that

practically depends on the effective interatomic distance (Figure 1.11). For crystals the energy associated with exchange interaction can be expressed as [79]:

$$H_{spin} = -2J_{ex} S_1 . S_2 \cos \emptyset \quad \textbf{(1.30)}$$

where *ø* is the angle between S_1 and S_2 (the quantum mechanical spin tensors). Ferromagnetism appears for positive values of J_{ex}, whereas a negative J_{ex} leads to Anti-ferromagnetism. Eq.(1.30) governs the nearest neighbour interactions in metals which vary depending on the ratio of the atomic radii and the radius of 3d shells (Figure 1.11). It can be easily inferred quantum mechanically that as the atoms come closer a singlet state i.e. asymmetric spin function is favored. However this direct exchange is not feasible in case of oxides where the metal ions are separated by oxygen ions at larger distances. The ferrimagnetism that still exists in oxide is a consequence of an indirect form of exchange termed as superexchange (Figure 1.12). A generalized explanation can be that the closeness of the metal ions to the oxygen ion itself leads to an overlap of various orbitals resulting in sharing of electrons between the oxygen and the metal ions (covalent bond). Now due to this sharing, the permanent electrons in the outermost shell of the metal ions (3d shell for transition metals) are bound to the spins of incoming 2p oxygen electrons (Hund's rule) that are already bound antiparallel to each other inside the oxygen atom (Pauli's principle). As a result an indirect antiferromagnetic interaction occurs between the two metal ions. This general scenario actually comprises of several different mechanisms [81–84], that explain antiferromagnetic as well ferromagnetic interaction in metal-complex systems.

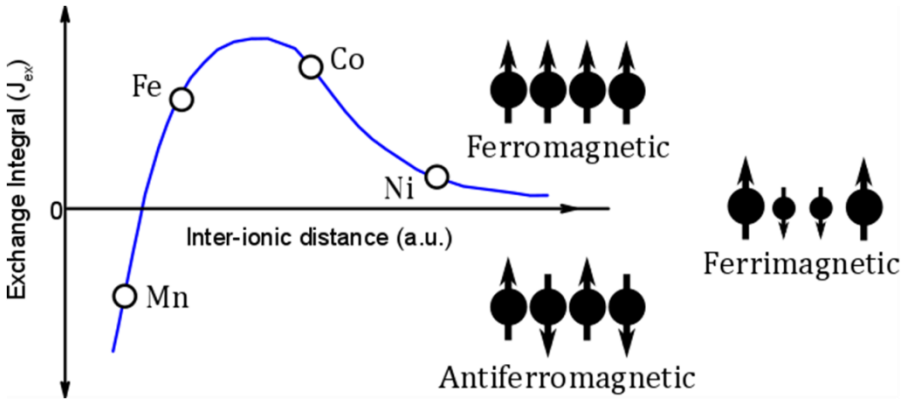

Figure 1.11 Dependence of exchange integral on inter-ionic distance in commonly used metallic ferromagnets [85].

However in general the interactions are sensitive to the distance of the metal ions from the anions as well as the bond angle between the two metal ions which determines the intensity as well as the type of orbital overlap. As an example a 180° interaction between two Ni^{+2} ions results in an antiferromagnetic state, whereas a 90° interaction between the same results in a ferromagnetic interaction.

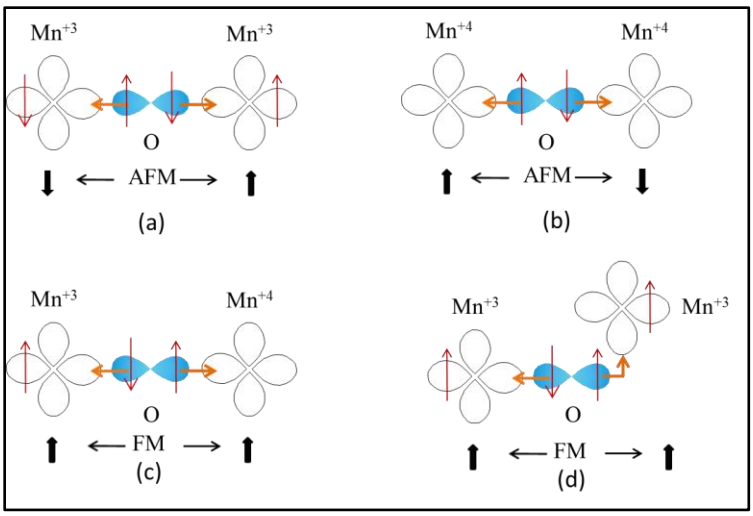

Figure 1.12 Different antiferromagnetic (a-b), and ferromagnetic (c-d) superexchange interactions possible in Mn.

Another important characteristic of a magnetic crystal is found to be its variability in magnetizability w.r.t. the direction of the applied magnetic field, in other words the magnetization properties in most magnetic crystal are anisotropic. Based on their origin different anisotropies can be classified as:

i) Crystal/Magnetocrystalline anisotropy
ii) Shape anisotropy
iii) Stress anisotropy
iv) Anisotropy induced by
    a. Magnetic annealing
    b. Plastic deformation
    c. Irradiation
v) Exchange anisotropy

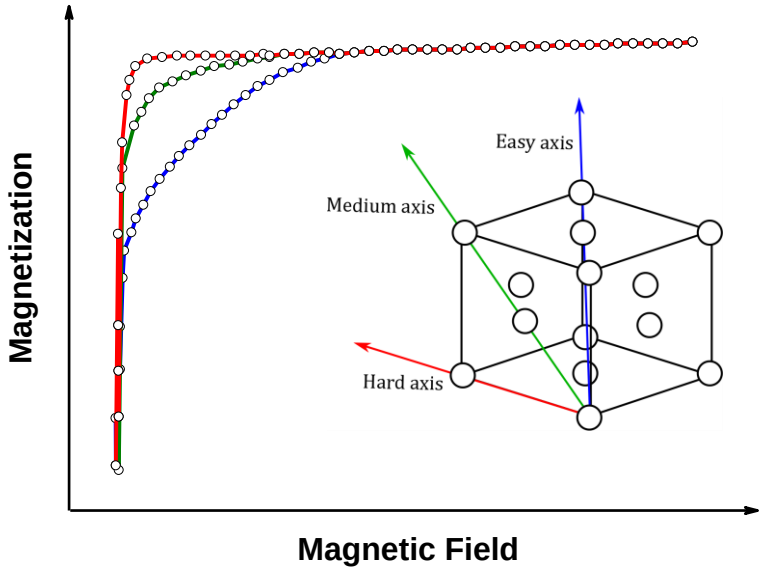

Figure 1.13 Magnetization vs magnetic curves for Fe single crystal, along crystallographic axes with different degrees of freedom. The red curve represents the easiest axis, along which the magnetization is oriented in the zero-field cooled condition [85].

Out of these anisotropies, only the crystal anisotropy is relevant in the context of the present thesis, since it is intimately related to the magnetostriction phenomena. Such an anisotropy originates from the directional nature of the spin-orbit coupling leading to degeneracy of crystal axis with different degree of easiness in terms of saturating the magnetization in those directions (Figure 1.13). Hence it can be easily realized that there is some energy associated with each axis and the difference between them decides the easiness of these axes. Basically the mgnetocrystalline anisotropy energy can be characterized in terms of the angle made by the magnetization vector to the crystal axis under consideration. The general form can be given as [85]:

$$E_{MS\,(Cubic\ )} = K_0 + K_1(\alpha_1^2\alpha_2^2 + \alpha_2^2\alpha_3^2 + \alpha_3^2\alpha_1^2)\ldots\ldots \quad \textbf{(1.31)}$$

$$E_{MS\,(Uniaxial\ )} = K_0 + K_1 \sin^2\theta\ldots\ldots \quad \textbf{(1.32)}$$

where the constants K_0 and K_1 are material properties, with the insignificant higher order coefficients being neglected for the sake of simplicity; α_1, α_2, and α_3 are the direction cosines of the angles made by the magnetization vector with the crystal axes, whereas θ is the angle between the magnetization vector and the principal axes (the c-axis for hexagonal crystals). Since more than E_{MS}, it is the total difference between the energies of two different axes (ΔE) that matters; it can be shown the K_1 is then more decisive in determining the characteristics of the material. Table 1.6 shows a comparison for two magnetic nanoparticles of $CoFe_2O_4$ and Fe_2O_3

(radius ~ 5nm) in terms of their easy axis based on the sign of the ΔE between [110] and [010] axis.

Table 1.6 Magnetocrystalline anisotropy characteristics for two important ferrite magnets [86].

Material	K_1 (J/m^3)	$\Delta E\{110-010\}=\frac{K_1}{4}.V$ (J)	Easy axis
$CoFe_2O_4$	90×10^3	1.17×10^{-20}	[010]
Fe_2O_3	-11×10^3	-0.144×10^{-20}	[110]

In case of hexagonal symmetry which is a uniaxial system, if K_1 is positive then the minimum energy occurs at $\theta = 0$, i.e. parallel to the c-axis, and in case if it is negative then the basal plane becomes a plane of easy axis orientation. Basically what this means is that in each case depending on the values and sign of K_1 the spontaneous magnetization will align along the easy axis which for the cubic system in general are $\langle 001 \rangle$ and that for hexagonal systems is either along the C-axis or within the basal plane.

The origin of crystal anisotropy is largely spin-orbit coupling. The spin-orbit coupling as the name suggests is essentially a coupling of the electronic orbits or the electron cloud with the orientation of spin by the means of the intense relativistic magnetic field felt by the electrons. In other words a reorientation of the spins would require a reorientation of the orbitals which on the other hand are coupled with the lattice via the crystal field. As a result there exists directions in the lattice where the spins are preferably oriented and a reorientation from those directions will cost energy. This energy can be expressed in terms of the spin and the angular momentum as :

$$\Delta E = \frac{1}{2m^2c^2r}\frac{dV(r)}{dr}S.L \qquad \textbf{(1.33)}$$

Where *m*, *V*, and *r* are the electron mass, electric potential, and distance from nucleus respectively. For a typical excited state of a hydrogen electron this energy can be of the order of 10^{-4} ev which is 4 orders of magnitude lower than a typical binding energy itself. Hence these interactions are very weak and the spins can indeed be oriented in a non-easy direction by application of a modicum of field.

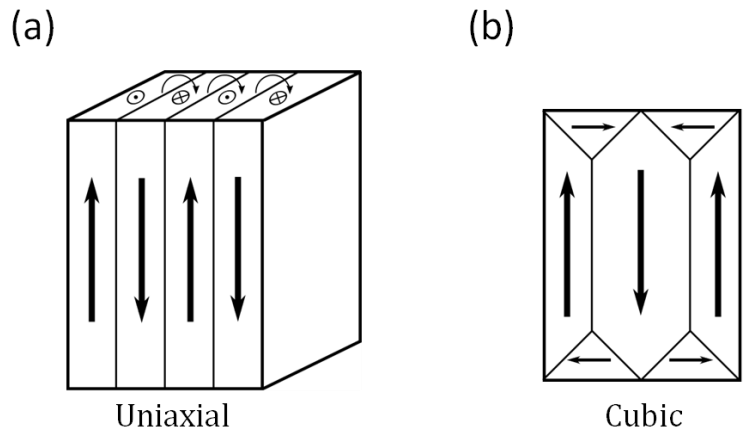

Figure 1.14 (a) The 180° degree (uniaxial), and (b) 90° (cubic) configurations of magnetic domains. Domain configuration in (b) is also termed as the closure domains.

Owing to the magnetocrystalline or any other form of anisotropy, in a demagnetized state, the microscopic moments can align themselves along any one of the equivalent easy directions. However a scenario where a large amount of crystal aligns in the same direction is energetically not feasible, since in that case a huge amount of field lines will permeate the space necessitating storage of huge magnetostatic energy inside the crystal. As a result, every time upon cooling below the Curie temperature, a magnetic crystal forms small domains aligned along all possible equivalent easy axes, in such a way that the intensity of permeating space is minimized. Figure 1.14 shows two such configurations of domains for a cubic and a uniaxial system. The interface separating two spontaneously magnetized domains are termed as domain walls, which encompasses the gradually changing magnetization owing to an energy bargain between the exchange energy and the anisotropy energy. Ideally, the gradual change of magnetization takes place in the form of a Bloch-wall, where magnetic moments rotate perpendicular to the plane of domain magnetization. The thickness of the wall (δ) in such a case will depend on the exchange stiffness A, and the magnetocrystalline energy K_1 [85]:

$$\delta = \pi\sqrt{\frac{A}{K_1}} \qquad \textbf{(1.34)}$$

In order to estimate the thickness of a wall it is crucial to accurately determine A, which is not trivial as A is proportional to an incommensurate factor J_{ex} (Exchange interaction constant). However rough estimation of J_{ex} from the transition temperature allows to calculate A. Typically, the domain wall thickness so calculated falls in the range of a few tens of nanometers.

Under an applied magnetic field the reorientation of the domains takes place as shown in Figure 1.15. For an applied magnetic field in an arbitrary direction the process of reorientation begins by domain wall motion, as shown in the figure this means that the domains with minimum energy (determined by the small-angle w.r.t the direction of applied field) will grow at the cost of those having larger energy. After complete disappearance of the higher energy domains the

remainder domains will have to rotate in the direction of the applied magnetic field in order to minimize the magnetostatic energy given by $M_S.H$. It is self-explanatory that when the applied field is parallel to any of the easy axis than the process of reorientation will only be void of any magnetization rotation. This also explains the step magnetization curves in the easy directions (Figure 1.13).

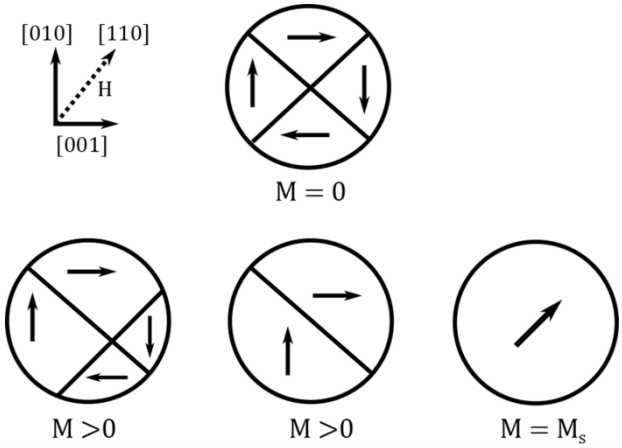

Figure 1.15 The evolution of closure type magnetic domains in a typical cubic anisotropic system. The magnetic field is applied along [110] direction.

1.3.1 Magnetostriction

Magnetic crystals also undergo a dimensional change when subjected to magnetic field, termed as magnetostriction. It is often characterized by the strain level at the saturation λ_s, often of the order to 10^{-6} but can be as high as 10^{-4} in ferrites. The origin of magnetostriction again lies in the spin-orbit coupling and hence is interlinked to the magnetocrystalline anisotropy. This can be roughly visualized as shown in Figure 1.16. The spin-orbit interaction makes a spherical electron distribution slightly elliptic; a reorientation of the spin thus reorients the charge cloud resulting in an effective dimension change. The interrelation of magnetostriction and anisotropy confers that the magnetocrystalline anisotropy constant K_1 that characterize the strength of anisotropy also is a measure for magnetostriction. For an example hexagonal systems often have a higher K_1 and also possess a higher magnetostriction.

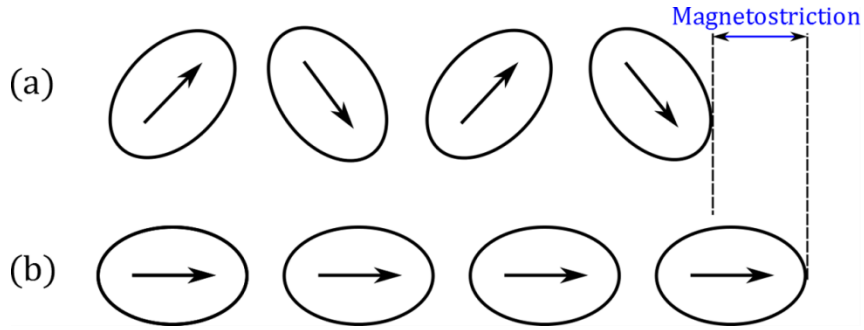

Figure 1.16 Schematic representation of the atomic origin of magnetostriction. The electron cloud (ellipse), upon magnetizing the material (spontaneously or by applying field), rearranges from (a) to (b), generating a net strain (magnetostricrtion).

In case of ferromagnetic crystals, on cooling below the Curie temperature a dimensional change, termed as the magnetostriction, takes place in addition to thermal expansion,. This can be explained e.g. in a cubic system, by appearance of magnetic domains which are spontaneously strained to a bit of tetragonality along the easy directions of magnetization. This phenomena is commonly termed as magnetostriction; within a linear regime (Piezomagnetism) of magnetoelasticity is expressed by the following relation

$$\epsilon_{ij} = q_{kij} M_k \tag{1.35}$$

Where q_{kij} is a 3rd rank tensor, relating the magnetization to the resultant strain. On reorientation of the magnetic domains under an applied magnetic field, the canceling spontaneous strains realign to give a net dimensional change. From this it can be inferred that for a hexagonal system where only 180° domains exists a simple reorientation along the easy axis or in other words domain wall motion will not result into any effective strain, rather only a domain rotation will give rise to a resultant strain. A general expression for saturation strain in any arbitrary direction with direction cosines $\beta_1, \beta_2, \beta_3$ w.r.t to the crystal axes, resulting from a magnetization reorientation in a direction with direction cosines for a cubic system can be given as [85]:

$$\lambda_s = \frac{3}{2}\lambda_{100}\left(\alpha_1\alpha_2 + \alpha_2\alpha_3 + \alpha_3\alpha_1 - \frac{1}{3}\right) + 3\lambda_{111}(\alpha_1\alpha_2\beta_1\beta_2 + \alpha_2\alpha_3\beta_2\beta_3 + \alpha_3\alpha_1\beta_3\beta_1) \tag{1.36}$$

Here λ_{100}, and λ_{111} are the saturation strains for domains oriented in [100] and [111] directions respectively, and the α_i's are the magnetization direction cosines as described for eq.(1.31). A similar expression for hexagonal crystals can be given as per the alternative notations proposed by Callen et al. [87, 88]:

$$\lambda_s = \frac{1}{3}\lambda_\alpha^z\left(\alpha_3^2 - \frac{1}{3}\right) + \lambda_{\alpha\beta}^z\left(\beta_3^2 - \frac{1}{3}\right)\left(\alpha_3^2 - \frac{1}{3}\right) + \lambda_{\alpha\beta}^{xy}\left[\frac{1}{2}(\beta_1^2 - \beta_2^2)(\alpha_1^2 - \alpha_2^2) + 2\alpha_1\alpha_2\beta_1\beta_2\right] + 2\lambda_{\alpha\beta}^{xyz}(\alpha_1\alpha_3\beta_1\beta_3 + \alpha_2\alpha_3\beta_2\beta_3) \tag{1.37}$$

where the λ's are material specific magnetostriction constants. As already discussed before, for a hexagonal crystal a 180° magnetization reorientation does not amount to any strain hence the key part of the equation can be deduced by only considering the 90° rotation case i.e. a reorientation

from C-axis to basal plane or vice versa. It can be seen, that for such a situation the net strain is nothing else but the coefficient (magnetostriction constant) for the third term in eq.

$$\lambda_s(90°) = \lambda_s(\alpha_1 = \beta_1 = 1) - \lambda_s(\alpha_2 = \beta_1 = 1) = \lambda_{\alpha\beta}^{xy} \quad \textbf{(1.38)}$$

Figure 1.17 shows the typical magnetostriction for cubic as well as hexagonal system measured along their respective crystal axis. Amongst all, the anomalous behavior along cubic [110] is worth noting. In this case the magnetostriction initially increases under the influence of magnetic field in [110] direction, as the [001] and [00$\bar{1}$] diminish resulting in a net expansion in the [110] direction. Later on rotation of the lowest energy remainder domains ([100] and [010]) takes place resulting into a *¾ λ_{111}* strain, which as can be seen from the curve for [111] direction, is negative. Hence after a maximum, the magnetostriction in [110] directions undergoes a contraction. Following from this example it could be realized that there may exist, similar more complicated domain reorientation conditions where a non-monotonous magnetostriction can take place.

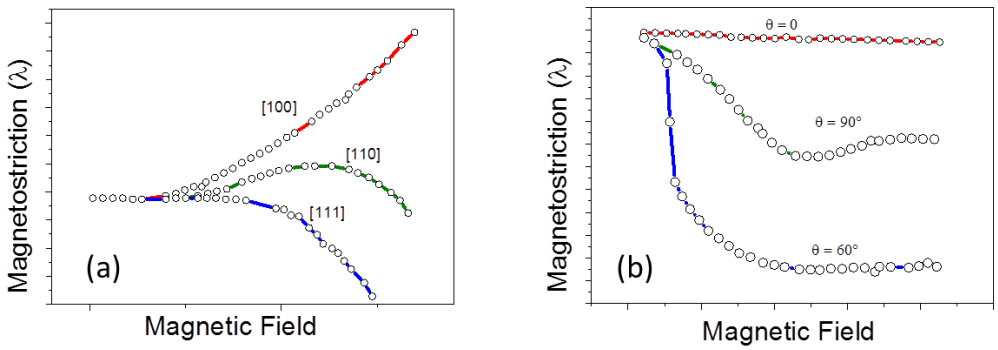

Figure 1.17 Magnetostriction along different crystallographic directions for systems with (a) cubic (Iron), and (b) uniaxial/hexagonal (Cobalt) magnetocrystalline anisotropy [85].

Now since the alignment of magnetization along the easy direction owing to an anisotropy energy minimization leads to dimensional change (strain), it can be conveniently imagined that there exists a separate magnetoelastic anisotropy energy term in the total anisotropy equation. Which means that just like a spontaneous alignment of domains owing to minimization of total anisotropy energy leads to a dimension change, application of stress can add additional contribution to the total energy hence necessitating a reorientation of magnetization. This effect is nothing else but the converse magnetostrictive effect or the Villari effect. The magnetoelastic energy term comprises of a product of applied stress and the existing strain. In the present work for the sake of simplicity we will assume the isotropic case, hence the expression for the magnetoelastic energy term reduces to:

$$E_{me} = \frac{3}{2}\lambda_{si}\,\sigma \sin^2\theta \quad \textbf{(1.39)}$$

Where λ_{si} is the isotropic magnetostriction, σ is the applied stress, and the θ is the angle between the direction of magnetization and the applied stress. The consequence of Villari effect is that under an applied stress, depending on whether the constant term in eq.(1.39) is positive or negative, the direction of easy axis shifts to those either parallel or perpendicular to the applied stress respectively. Another important consequence is that under the influence of stress the domain configurations can change after an apparent domain wall motion (Figure 1.18).

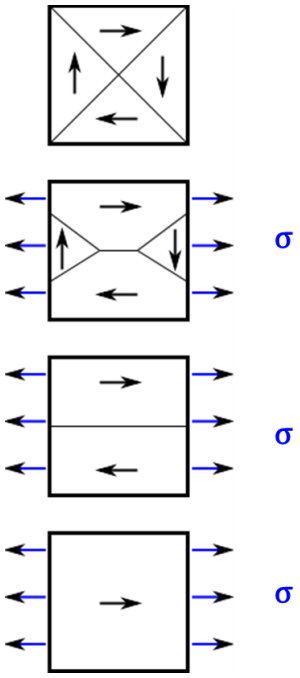

Figure 1.18 Evolution of closure magnetic domains, upon application of a uniaxial tensile stress (blue arrow) along the easy axis.

Among the various magnetic materials, identified for a high magnetostriction, the ferrites are the most prominent candidates exhibiting good magnetostrictive characteristics.

1.3.2 $CoFe_2O_4$

Cobalt ferrite is a ferrimagnetic oxide with cubic symmetry. The crystal structure of CFO belongs to the spinels class (AB_2O_4; Fd3m) which can be understood by considering the oxygen ions forming a FCC closed pack structure with 1/8 of the tetrahedral interstitial sites filled with A ions whereas ½ of the octahedral interstitial sites are occupied by B ions in a normal spinel [89]. However for CFO the filling is inversed, i.e. 8 of the divalent A ions occupy the 16 available octahedral sites whereas the 16 trivalent B ions occupy the remaining octahedral sites as well as all of the tetrahedral sites, and form a structure called *inverse spinels*. The resultant unit cell with origin at cobalt ion is shown in Figure 1.19.

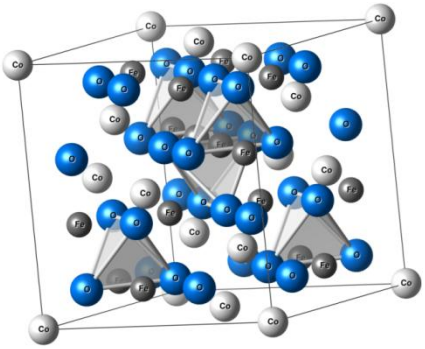

Figure 1.19 Atomic arrangement of a $CoFe_2O_4$ unit cell, based on the inverse spinel structure. The empty tetrahedral sites are emphasized by the polygons [89].

The oxygen parameter for cobalt ferrite, which accounts for the expansion of the tetrahedral sites in ferrites, is typically greater than 3/8. As a result, some of the Fe-O-Co antiferromagnetic exchange interactions are weakened due to an increased Co-O distance and a decreased bond angle as a result the 90^o Fe-O-Fe ferromagnetic interaction dominates resulting in a ferrimagnetic lattice structure. As a result of such a lattice structure the contribution of tetrahedral ions (Fe^{+3}; 5 μ_B) and octahedral ions (Fe^{+3} + Co^{+2}; 5 μ_B + 3 μ_B) yields a theoretical net moment of 3μ_B per unit cell. However, experimentally often a different value is observed (~3.7 μ_B) owing mainly due to local canting of the moments [90]. Apart from this however the cause of experimentally observed discrepancy is also associated with a different ion distribution due to mixed valency. The single crystal saturation magnetization of CFO is about 37.8 kA/m, below 520 °C (Curie temperature).

CFO possesses a cubic anisotropy with ⟨100⟩{100} being the easy axes. The anisotropy constant K_1 measured for CFO is about 1.8 – 3.9 × 10^5 J/m^3[91]. Associated with such a high anisotropy energy is an equivalently high magnetostriction. For CFO λ_{100} = -590 × 10^{-6} and λ_{111} = 120 × 10^{-6} [92], suggesting a high negative magnetostriction at least along the easy axes. For that matter it should be also noted that this is by far the highest value of magnetostriction obtained for any undoped ferrite crystal.

1.3.3 $NiFe_2O_4$

NFO which is another ferrimagnetic ferrite belongs to the identical class of spinel based ferrites, and possesses a lattice and spin structure equivalent to CFO.

Unlike CFO, however, the ion distribution of NFO (tetrahedral: Fe^{+3}, 5 μ_B; octahedral: Fe^{+3}+Ni^{+2}, 5 μ_B+2 μ_B) results in a net theoretical moment per formula unit of 2 μ_B, which experimentally is often found to be around 2.3 μ_B. The lower discrepancy between experimental and theoretical values of moment per formula unit can be associated with a relatively lower canting of Fe moments w.r.t. those in CFO. This results in a single crystal saturation magnetization of about 23.8 kA/m with a transition temperature of 585 °C.

Equivalent to CFO, NFO also possesses a cubic anisotropy with ⟨110⟩{1 being the easy axes. The crystal anisotropy constant K_1 for NFO is about 3.9 – 5.1 × 10^3 J/m^3. With such small anisotropy energy, NFO evidently shows a magnetostriction smaller as compared to CFO. The magnetostriction constants for NFO are λ_{100} = -36 × 10^{-6}, λ_{111} = -4 × 10^{-6}.

1.3.4 M-Type Hexaferrites

The M-Type hexaferrite ($MeFe_{12}O_{19}$) belongs to the large family of hexaferrites. Quite often, they are referred to in literature acronym *M* (following the mineral class magnetoplumbite) preceded by the symbol of Me ion (e.g. $BaFe_{12}O_{19}$ is referred to as BaM). The crystal structure of M-Type hexaferrite belongs to the hexagonal symmetry class ($P6_3/mmc$). The detailed structure can be understood based on the spinel structure, thought of in terms of the layered close packed stacking of oxygen ions, with metal ions occupying the interstitial sites. In M-hexaferrites the stacking sequence is of the type $BAB_{MeO}ABCAC_{MeO}AC$….which forms an alternating sequence of a hexagonally-stacked and a cubically-stacked block [89]. The only difference in the layers in a hexaferrite is that in the layers that are centered in the hexagonal block ($AC_{MeO}A$) some oxygen ions are replaced by Me ions. The unit cell hence formed by the10 layers, overall possesses a hexagonal symmetry (Figure 1.20).

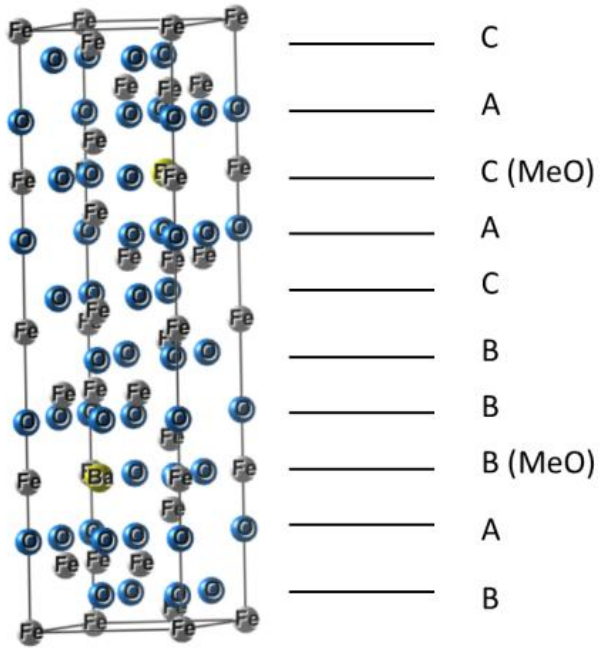

Figure 1.20 Atomic arrangement of a $MeFe_{12}O_{19}$(Me=Ba)unit cell, based on the magnetoplumbite crystal structure [89].

As a result of such a stacking configuration the Fe^{+3} ions are now distributed into tetrahedral, octahedral as well as bipyramidal (co-ordination = 5) sites. The predominant superexchange responsible for ferrimagnetism is associated with a 140° Fe-O-Fe interaction across the MeO layer (within the hexagonal block). Across a hexagonal and a cubic block there exists a

dominating 130° interaction between two octahedrally situated Fe ions which aligns the interfacial Fe ion in a direction parallel to the net dipole moment of the adjacent hexagonal block. Even though all of these interactions are antiferromagentic, owing to the distribution of ions, a net theoretical moment per formula unit of 20 μ_B survives. This results into a single crystal saturation magnetization of about 30.2 kA/m below a Curie temperature of 450°C.

As evident from the structure of M-type hexaferrite, they possess a hexagonal magnetocrystalline anisotropy with a typical anisotropy constant (K_1) of 3.3 – 3.5 × 10^5 J/m^3 [93]. Associated with such a high anisotropy, is an equally high saturation magnetostriction of about 13 × 10^{-6}, though slightly lower as compared to that of CFO. Two identical members of the M-type hexaferrite family, namely $BaFe_{12}O_{19}$ (BaM) and $SrFe_{12}O_{19}$, are studied within the present thesis.

1.4 Modeling Magnetoelectricity

The phenomenological description of composites described in section 1.1, highlighted the fact that the properties of the constituent phases are actually interactive. Firstly the applied magnetic/electric fields are differently distributed in the composites as compared to that in the freely existing component phases, merely due to the fact that the closely placed components have each magnetic as well as dielectric properties. In addition, the mediating parameter, stress, is not trivially transferred to the passive component, since the elastic constants are modified, even at the interface. This can be understood more clearly by considering the fact that a randomly selected macro point from the material is supposed to be microscopically inhomogeneous. As a result the response observed at the macro scale is an effective outcome of the individual microscopic properties. Finding the complex relation between the coefficients of the free existing constituent phases and the effective macroscopic response is what constitutes the problem of modeling magnetoelectricity. An analytical solution for such a problem was first provided by Harshe et al. [53] For the simplest case of a clamped bilayer 2-2 (Figure 1.5), with a perfectly bonded interface; the longitudinal ME coupling was evaluated as.

$$\alpha_{33}^{E} = \frac{E_3}{H_3}$$

$$= \frac{[\{-(S_{11}^{m}+S_{12}^{m})q_{33}V^{m}+(S_{31}^{m}+S_{32}^{m})q_{31}V^{m}\}\cdot\{d_{33}(S_{11}^{p}+S_{12}^{p})-2d_{31}S_{13}^{p}\}(S_{11}^{p}+S_{12}^{p})]}{\left[\begin{array}{l}\{-(S_{31}^{m}+S_{32}^{m})(S_{11}^{m}+S_{12}^{m})S_{13}^{m}V^{m}-(S_{31}^{p}+S_{32}^{p})(S_{11}^{m}+S_{12}^{m})S_{13}^{p}V^{p}+(S_{33}^{m}V^{m}+S_{33}^{p}V^{p})(S_{11}^{m}+S_{12}^{m})(S_{11}^{p}+S_{12}^{p})\}\cdot \\ \{2(d_{31})^2-\varepsilon_{33}^{T}(S_{11}^{m}+S_{12}^{p})\}+\{(S_{11}^{m}+S_{12}^{m})(S_{11}^{p}+S_{12}^{p})d_{33}\}+\{(S_{11}^{m}+S_{12}^{m})(S_{11}^{p}+S_{12}^{p})d_{33}V^{p}-(S_{31}^{p}+S_{32}^{p})(S_{11}^{m}+S_{12}^{m})d_{33}V^{p}\}\{d_{33}(S_{11}^{p}+S_{12}^{p})-2d_{31}S_{13}^{p}\}\end{array}\right]} \quad \textbf{(1.40)}$$

Eq.(1.40) expresses the induced magnetoelectric coupling α_{33} in terms of the individual material properties (S, ε, μ, d, d^T). Hypothetically, a rigorous factorization of eq.(1.38) might yield a product of three distinct terms, that can be equated to the three quasi-microscopic coefficients appearing in the thermodynamically derived relation for ME coupling {Eq.(1.14)}. The same analysis was extrapolated to 0-3 connectivity scheme with different boundary conditions, by expressing the inclusion-in-matrix geometry in terms of juxtaposed bars (*cube model*).

The relation also tells that a direct ME coupling for composites would be higher for a higher dielectric constant in the piezoelectric component. This means that a ferroelectric piezoelectric phase would still be a best candidate despite of the same not being a necessary requirement.

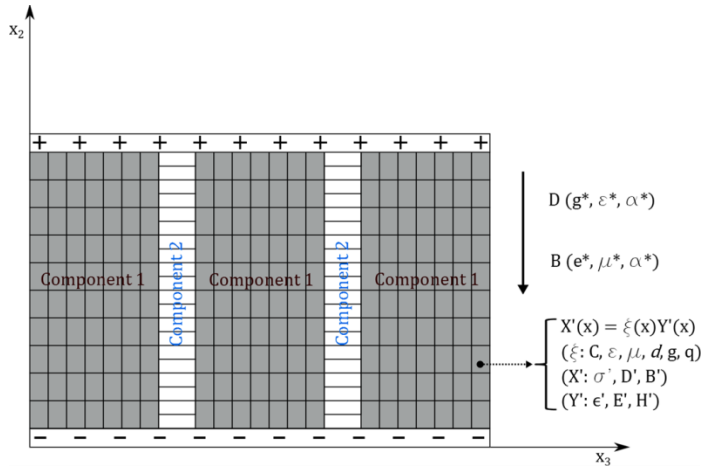

Figure 1.21 A schematic representation of the Greens function approach.

A similar set of equations were arrived at by Nan et al.[94] using a Green's function based approach. In their approach they considered a composite constitutive formulation as

$$\sigma_{ij} = C^*_{ijkl}\epsilon_{kl} + d^*_{kij}E_k + q^*_{kij}H_k \quad \textbf{(1.41)}$$

$$D_i = d^{T*}_{ijk}\epsilon_{jk} + \varepsilon^*_{ij}E_j + \alpha^E_{ij}H_j \quad \textbf{(1.42)}$$

$$B_i = q^{T*}_{ijk}.\epsilon_{jk} + \mu^*_{ij}H_j + \alpha^M_{ji}E_j \quad \textbf{(1.43)}$$

$$\begin{bmatrix}\sigma\\ D\\ B\end{bmatrix} = \begin{bmatrix}C^* & d^* & q^*\\ d^{T*} & \varepsilon^* & \alpha^E\\ q^{T*} & \alpha^M & \mu^*\end{bmatrix}\begin{bmatrix}\epsilon\\ E\\ H\end{bmatrix} \quad \textbf{(1.44)}$$

The 12 × 12 coefficient matrix relating the intensive variables to the extensive ones are the effective coefficients (as indicated by the asterisk). For the sake of simplicity, the magnetoelectric effect was captured within the coefficient α, overlooking the indirect manifestation of the stress generated by the individual coupling properties of the components. In order to relate this macroscopic coefficient with the seemingly homogeneous microscopic ones, Nan et al. used the following approach [94]:

- Estimation of local field parameters X (ϵ, E, H) using a space dependent Greens function based solution of the boundary condition on the field variables *Y'*:

$$\vec{\nabla}Y' = 0 \text{ (Boundary condition)} \quad \textbf{(1.45)}$$

Followed by constituting a solution for the field parameters X, as follow:

$$X(x) = X^0 + \int G(x,x')F(x')dx' \text{ (Solution)} \quad \textbf{(1.46)}$$

Where *F(X')* are the functions of the local constitutive coefficients ξ (Figure 1.21), and *G(x, x')* are the potential Green's functions for a homogeneous comparison media.

- Later on the local fields are substituted in the formulation (Eq.(1.46)), followed by an averaging of the resulting local identities over the entire macro point. The final expression will relate the average intensive variables with the average extensive ones as in Eq.(1.41), however the coefficient now being expanded in terms of the homogeneous material coefficients.

$$\alpha^{E} = f(C, \varepsilon, \mu, q, q^{T}, d, d^{T}) \quad \textbf{(1.47)}$$

- The validity of the formulation lies in the fact that in the absence of any cross coupling, the expressions relating the effective coefficients reduce to those in the case of the individual component.

Using above mentioned approach, Nan et al. evaluated the coupling constant for a bilayer system similar to the case of Harshe et al., however by considering different contents of the constituent phases, represented by the volume fraction of the piezoelectric phase.

$$\alpha_{33}^{E} = \frac{E_3}{H_3} = \frac{2f(1-f)d_{31}q_{31}\mu_0\bar{s}}{(2fd_{31}^2-\varepsilon_{33}\bar{s})[\bar{\mu}\bar{s}+2q_{31}(1-f)^2]} \quad \textbf{(1.48)}$$

$$\alpha_{31}^{E} = \frac{E_3}{H_1} = \frac{-f(1-f)(q_{11}+q_{21})d_{31}}{\varepsilon_{33}\bar{s}-2fd_{31}^2} \quad \textbf{(1.49)}$$

Where $\bar{s} = f\left(S_{11}^{p} + S_{12}^{p}\right) + (1-f)(S_{11}^{m} + S_{12}^{m})$ and $\bar{\mu} = f\mu_0 + (1-f)\mu_{33}$. As can be seen, the expression is not very different from eq.(1.38). Apart from this, Nan et al also demonstrated a dependence of the coupling on the volume fraction (*f*) as well as the aspect ratio of the one dimensional constituent which then simulated a transition from 2-2 to 1-3 schemes through 0-3 scheme as shown in Figure 1.22. Also Figure 1.22 reveals the success in addressing the complexity of phase distribution as compared to the simplified cube model adopted by Harshe et al.

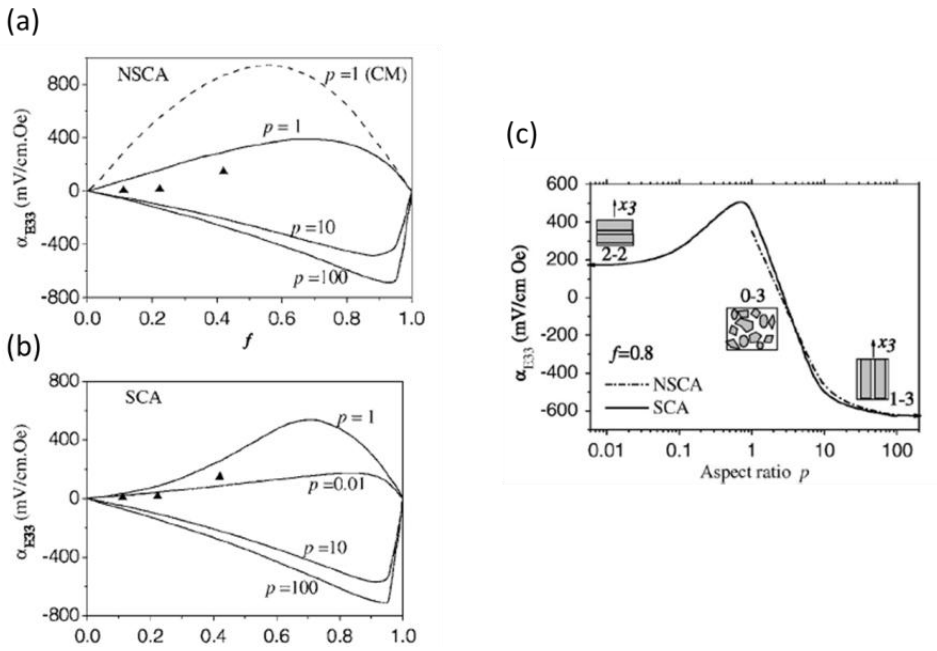

Figure 1.22 (a-b)The variation of longitudinal magnetoelectric coupling w.r.t. the component volume fraction for different aspect ratios/connectivity schemes, and (c) the same for a particular volume fraction of 0.8 w.r.t. to aspect ratio. The terms NSCA and SCA refers to non self-consistent analysis and self-consistent analysis respectively [94].

The seminal work of Bichurin et al. and Srinivasan et al. [95, 96] also deals with similar expressions, that took into account not just the volume fraction of the constituent phases rather also the degree of bonding between the phases by introducing an interface coupling parameter.

Very recently attempts have been made to quantitatively determine the coupling in composites using micromechanical approaches (Labuschet al. [97]) that rely on a two scale homogenization method [98].The approach aims at finding the effective coupling at a macroscale defined with certain boundary condition based on a suitable volume average of an appropriately chosen Representative Volume Element (RVE) comprising of essential microelements. The approach is based on the *principle of ergodicity* as accepted in classical formulation for mechanical homogenization. The principle states that an average of an event (which in micromechanical terms refers to microstructural inhomogenities or a combination of them e.g. inclusions, quenched phases, cracks, or dislocations) evolving over time is identical to an average of all the possible events over an infinite volume. In the context of the micromechanical approach taken by Labusch et al., the *principle of ergodicity* is expressed as:

$$\langle f(\xi, X)\rangle_V = \frac{1}{V^{RVE}} \int_{RVE} f(\xi, X')dX'^3 \; (\xi = \sigma, \epsilon, D, E, B, H) = \langle f(\xi, X)\rangle_T \qquad \textbf{(1.50)}$$

In this approach the local constitutive relations defined are similar to those in eq.(1.41) - (1.44), followed by a homogenization step. Apart from adopting the conventional micromechanical approach to calculate the coupling constant for an ideal RVE, Labusch et al. further

demonstrated calculations for a realistic case by adopting an electron microscope image of $BaTiO_3 – CoFe_2O_4$ ceramic. They also displayed the effect of poling the ceramic on the resultant magnetoelectric coupling in that they simulated a pre-poling step. Here they applied an electric field in absence of any constitutive coupling (piezoelectric) and locally determined the distribution of electric field, from which they calculated polarization and later on the piezoelectric coupling constant. Followed by this they estimated the effective magnetoelectric coupling as a function of different poling voltage and suggested an increase in the longitudinal coefficient. This approach is extremely useful for materials with inhomogeneous microstructure, such as 3-3/0-3 ceramic composites, which not only have dispersive microelements but also stochastically distributed property matrices. This is basically the sole purpose of mechanical homogenization; to represent the effective material properties based on the known microscopical properties.

The approaches mentioned above, constitute an exhaustive formulation for magnetoelectricity in composites that exists so far. A flying comparison of these models, suggests that they can be divided into the following categories:

1) Analytical approach
2) Green's function based approach
3) Micromechanical (FEM based) approach

All of the developed models reflect the importance of local (individual component) properties, in determining the macroscopic ME coupling. However, as far as the distributions of these local properties are concerned (phase distribution), it is only the micromechanical approach that projects capabilities of comprehending a more complex microstructure.

1.5 Motivation

As evident from the preceding section, the knowledge about local distributions of ME response is key for tailoring the same. However, when it comes to polycrystalline materials, which constitute a large portion of the currently studied ME composites (e.g. polycrystalline films, laminates, ceramic composites etc.), just the type of connectivity scheme or the interface quality are not sufficient to determine these local contributions. Rather, the material texture, namely the relative crystallographic orientations of the constituent phases, as well as the inclusion shape, size, or the phase morphologies (e.g. lamellar, polygonal, spherical etc.) have to be taken into account. This will also provide a powerful tool to predict or differentiate the ME response amongst identical compositions with varying microstructures (Table 1.2 and

Table 1.3). The micromechanical approach, as conveyed in the previous section, is capable of handling complex microstructure. However, unlike the other approaches, the micromechanical approach will specifically need to be corroborated with local experimental investigations.

At this juncture, it is not possible to comprehend a detailed theoretical framework, involving all the microstructural aspect. However it is worthwhile to consider a simple example of Eshelby's solution for a dilating inclusion within an elastic matrix. According to this solution, the eigen strain (strain without stress) of a dilating ellipsoidal inclusion is balanced by an imaginary surface traction exerted by the matrix at the interface. This in effect provides the solution for the resultant stress distribution in the matrix, termed as Eshelby's exterior solution. As per this solution, a strain discontinuity occurs at the matrix-inclusion interface resulting in a position dependent strain/stress inside the matrix

$$\epsilon_{ij}(x) = S^{E}_{ijmn}(x)\epsilon^{*}_{mn} \quad \textbf{(1.51)}$$

Where $S^{E}_{ijmn}(x)$ is the position dependent Eshelby tensor. The strain $\in^{*}_{mn}$ is the eigen strain or the dilation strain of the inclusion, differentiated from the stress induced strain by the use of asterisk. On the other hand, Eshelby's interior solution predicts that for a perfectly ellipsoidal inclusion, the strain/stress field within the inclusion will be constant. In the context of ME composite, Eshelby's solution dictates that the dilating component, either the piezoelectric (converse ME effect) or the magnetic (direct ME effect) phase, will exert a stress field inside the other component, such that the interfaces will be sites of high stress concentration. As a natural argument, one can hence think of increasing the number of interfaces by reducing the phase dimensions to the nanoscale, however the reports on ME coupling in such nanostructured systems is found to be ambiguous. To throw more light into such ambiguities, in the light of Eshelby's solution, localized experimental investigations stand once again as a need of the hour. In conjunction with this, the distribution and morphologies of the dilating phase are expected to play a critical role in determining the ME response distribution. Figure 1.23a-b shows the result of 2D FEM modeling carried out in a parallel work [99], for different distribution of dilating CFO inclusions in a BTO matrix. The nuances in the stress distributions between the ordered and randomly distributed inclusions are clearly visible. Within the framework of this modeling work, a realistic case was also modeled (Figure 1.23c), where two polycrystalline phases separated by a sharp interface were considered. The grains were modeled to manifest a random orientation of their constituent elastic properties as in a realistic scenario. The stress generated by the equally dilating grains of one phase is exerted onto the other phase in a manner very distinct from that in the case of the isotropic inclusions (Figure 1.23a-b). Apparently, the stress distribution seems to be dependent on factors like the nature and span of the neighboring grain interfaces, as well as the orientation of the grains on either side. Although the modeling lacked the level of sophistication necessary to achieve self-consistency, it does provide a logical outcome. The hypothesized aspects, surrounding the role of microstructure also needs to be experimentally

reflected. The neccesarry local characterization is only pripherially investigated in literature [43, 100–104].

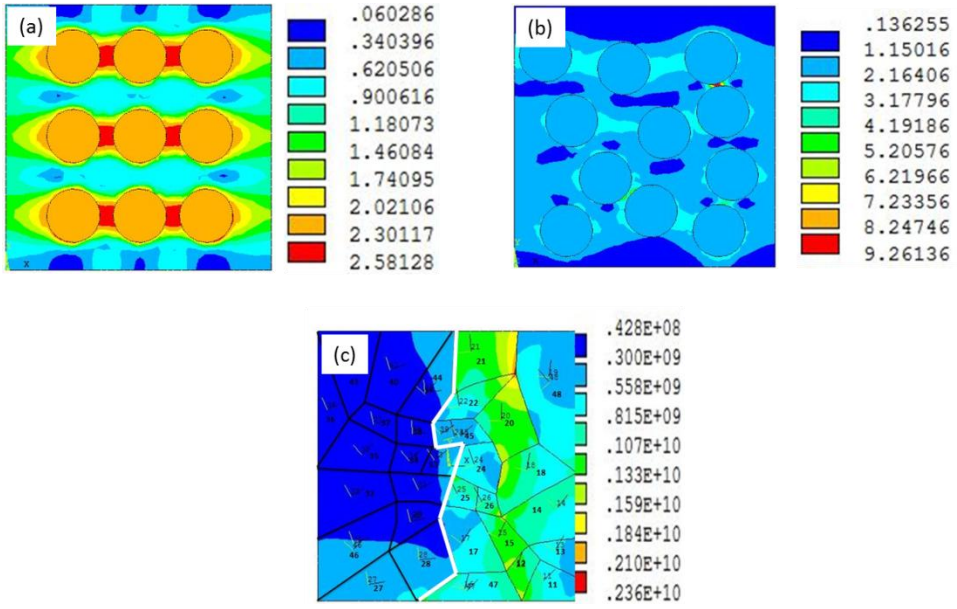

Figure 1.23 Von Misses stress calculated by thermoelasticity based FEM modeling for: (a) ordered & (b) randomly distributed circular inclusions, and (c) for a realistic case of an ensemble of randomly oriented grains (elastic properties) of two different phases (BTO & CFO, situated left & right of the white line respectively) [99].

The focus of the present thesis, is to explore near field microscopic (probe based as well as optical) techniques for probing the local manifestations of the ME effect in composites, especially in the context of the above mentioned factors. As a matter of subject, bulk polycrystalline composites out of the classical ferrite-BTO (CFO-BTO, NFO-BTO, Hexaferrite-BTO) pairs were studied. The choice of the bulk polycrystalline form of these systems is dictated by three major advantages:

i) Easy synthesizability.
ii) Existence of sharp longitudinally observable interface.
iii) Rich microstructure.

On the other hand the choice of the material systems is based on the goal of exploring a rich variety of magnetic anisotropy, which could actually provide variable stress distributions. In the next section, the opted techniques are reviewed and described in detail.

2 Experimental and Analytical Techniques

As evident from the motivation (Section 1.5), the centre of investigation in the present thesis is spatial mapping of the ME coupling. This implicitly means that any employed experimental techniques should be able to map parameters that are directly or indirectly dependent on the concerned variables (Viz. magnetization, stress, and polarization). The spatial mapping of these variables as such is not a challenge, as there are ample amount of techniques that can realize it; they can be broadly classified into following categories:

i) Optical techniques (Electron-Emission/Non-Linear Optics)
ii) Ultrasound techniques
iii) Scanning probe techniques

It is worthwhile to review some of the techniques belonging to each of the classes, which have been successfully used in context of multiferroics and magnetoelectric materials. Among the optical techniques, the Photoelectron Emission Microscopy (PEEM) has shown interesting implications in simultaneous mapping of ferromagnetic/antiferromagentic domains in multiferroics [105–107]. As an example, L-edge (2p to 3d transition) spectra of $BiFeO_3$ heterostructures detected by PEEM are sensitive to the relative orientations of the incident X-ray polarization and the sample magnetic axis, which can be mapped into a high resolution image of the magnetic domain arrangements. Such a technique, that is in general sensitive to any kind of spin/charge anisotropy, is therefore also used to map the constituent ferroelectric domains [107]. Unlike PEEM, Second Harmonic Generation (SHG/Non-Linear Optics), another technique successfully utilized in multiferroics [108–112], is relatively simple and does not require large scale instrumentation (synchrotron). SHG is sensitive to the structural aspects viz. broken time (magnetic) and space (ferroelectrics) inversion symmetry of the crystal, and hence can spatially map both ferroelectric and magnetic domains. It is evident that both of these (PEEM and SHG) optical techniques are capable of mapping in-situ interactions of magnetic and ferroelectric domains. However, the obtained results serve only the qualitative purpose of characterizing the ME coupling, and are limited when it comes to understanding the intermediatory mechanisms. Moreover, application of these techniques to bulk-polycrystalline ME composite is limited by two main factors: (i) poor sensitivity to weak stress induced changes, and (ii) lack of robustness towards the rich (polycrystalline) microstructures. Unlike PEEM and SHG, Raman spectroscopy is extremely sensitive to stress/strain, which are the key intermediating parameters of the ME coupling in composites. In addition, Raman spectroscopy has the capability to differentiate between the nature of stresses (tensile, shear,etc). These advantages, coupled with the developments in confocal Raman microscopy, provide a distinct opportunity in the present context.

Scanning probe microscopy (SPM) on the other hand, has emerged as a robust technique with unprecedented detection capabilities. Originally developed with a vision of exploring a limited

range of surface properties in materials (1980's [113]), SPM has expanded its regime into diverse applications over the course of time [114–123]. This has to do with the mere ability of an SPM probe (conducting cantilever-tip assembly) to adapt into different configurations and measure various type of surface emanating electromagnetic forces (simultaneously or independently) with high out of-plane resolution. In addition, its ability to go ultra near-field (contact), in a way bridges the gap that existed between the high-resolution optical/electron microscopic techniques and the contact based macroscopic measurement setups. As a relevant example, a ferromagnetic SPM tip, which is also conductive, cannot just map micromagnetic configurations (domains) of a magnetic phase, but under the same experimental conditions can also map the local electrical characteristics (domains, switching) of a ferroelectric phase. It is this very characteristic that leads to suitability of SPM techniques in the present work. In particular, the Piezoresponse Force Microscopy (PFM) plays a central role in the present thesis.

Owing to their potential in probing/imaging comprehensible ME parameters, both SPM as and confocal Raman microscopy have been exhaustively utilized in the present thesis. In addition, these techniques also provide complementary information about the mechanisms of interest.

2.1 Scanning Probe Microscopy

The SPM modes, used in the present work, are variants of Atomic Force Microscopy. In all the cases, forces of different originsare sensed by a static or dynamically driven microscopic cantilever. Out of these forces, the atomic level forces namely Van-der-Waals (attractive) and the covalent (repulsive) forces are primary. Figure 2.1 shows the standard Lennard-Jones type force curve, differentiating the regimes of dominance of the attractive and the repulsive forces as the microscopic cantilever approaches the sample surface. Depending on the experimental conditions both types of forces can be sensed.

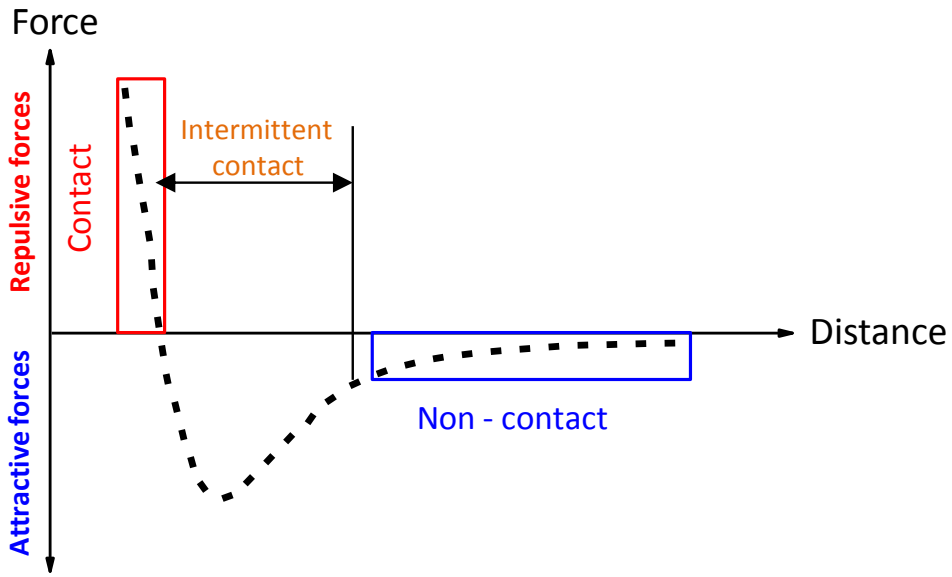

Figure 2.1 Lennard-Jones type curve for the force acting on an AFM cantilever, as it approaches the surface. The abscissa represents the tip-surface separation.

Typical AFM operation involves maintaining a constant force on the tip while scanning it on the sample surface. This is realized by a feedback mechanism, which drives the tip-sample separation. A feedback typically controls the tip z-height, and an image of this height difference is what serves as a measure of the sample topography or the forces in general. As part of the core sensing assembly, the tip deflections in static (dynamic) mode caused (changed) by the force (force gradient) acting on it is sensed by the changing angle of a laser beam, reflected from the backside of the tip onto a photodetector. Depending on whether the force is sensed by a static or a dynamically driven cantilever, two key modes of AFM operation are defined as follows:

Non-Contact Mode: In this mode, the cantilever is typically oscillated at a particular equilibrium height *c* above the sample surface, and hence the mode is also referred to as dynamic mode. Interaction between the surface and the oscillating tip are evaluated by modeling the tip as a forced oscillator. The tip displacement z at any moment of time satisfies the following equation

$$\ddot{z} + 2\delta\dot{z} + \omega_0 z = A\cos\omega t \qquad \textbf{(2.1)}$$

Where A and ω_0 are the amplitude and resonance frequency of the force oscillator, δ is the system damping coefficient, whereas ω is the frequency of the oscillating force (piezoactuator). Under the influence of additional surface forces $F_s(z)$ acting on the oscillator, eq.(2.1) changes to

$$\ddot{z} + 2\delta\dot{z} + \omega_0 z = A\cos\omega t + F_s(z)/m_{eff} \quad \textbf{(2.2)}$$

where m_{eff} is the cantilever effective mass. For small oscillations the surface force term $F_s(z)$ can be expanded as a Taylor series around c (equilibrium position), followed by a substitution into eq.(2.2). In this way, eq.(2.2) can be transformed in terms of the new variable z' such that it looks identical to the case of a forced oscillator in absence of any additional forces {eq.(2.1)}

$$\ddot{z}' + 2\delta\dot{z}' + \omega_0' z' = A\cos\omega t \quad \textbf{(2.3)}$$

$$\omega_0' = \omega_0\sqrt{1 - \frac{F_s'}{k}} \quad \textbf{(2.4)}$$

where k is the free air spring constant and $\omega_0'\omega'$ is the new resonance frequency of the system, proportional to the gradient of the surface force. The end effect of surface force acting on the cantilever is hence a shift of the natural resonance of the system. This has a direct consequence on the amplitude-frequency and phase-frequency curves (Figure 2.2). The resonance frequency shifts either to left or to right under the influence of an attractive or a repulsive surface force, respectively. As a result of this, the amplitude as well as the phase change (Figure 2.2a). These changes in resonance frequency, phase, and amplitude are formulated within linear approximation of the surface forces, and assuming that the free air phase (inflection point in Figure 2.2b) is set to 90°.

$$\Delta\omega_0 = -\frac{1}{2k}\frac{\partial F}{\partial Z}\omega_0 \quad \textbf{(2.5)}$$

$$\Delta A = \left(\frac{2A_0Q}{3\sqrt{3}k}\right)\frac{\partial F}{\partial Z} \quad \textbf{(2.6)}$$

$$\Delta\phi = \frac{Q}{k}\frac{\partial F}{\partial Z} \quad \textbf{(2.7)}$$

These changes in phase and amplitude of the cantilever are exploited in the non-contact mode of AFM operation. The normal procedure involves vibrating cantilever at a frequency close to the resonance, such that any influence of the surface force will result into a change in the amplitude and phase channels, which are then used as a feedback to maintain a constant force gradient on the tip. A fixed amplitude/phase, termed as set-point, is used as a reference for maintaining constant force. The choice of the set-point will decide the tip-sample separation, and hence also the type of force regime (attractive, repulsive, or electromagnetic). Since the tip being operated at away from the sample surface, the inherent sensitivity of the non-contact mode is lower (10^{-5} N/m).

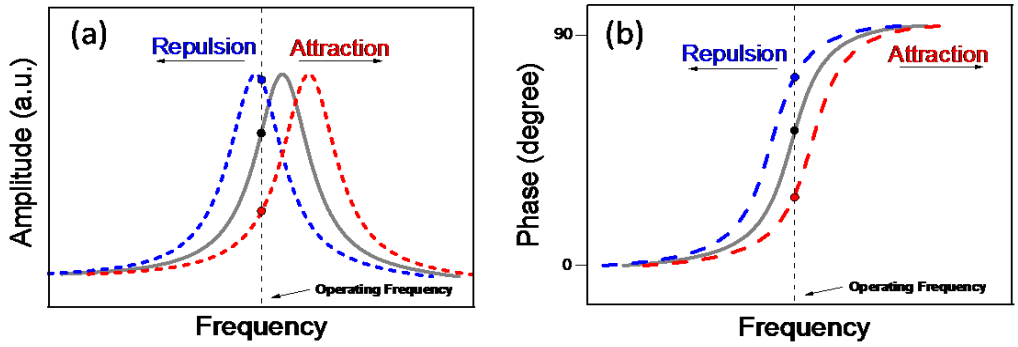

Figure 2.2 Schematics of force modulation (shifts) of the (a) cantilever resonance frequency, as well as (b) phase. The locations of dots signify that under the influence of an attractive (repulsive) force the resonance shifts to higher (lower) frequency, leading to a decrease (increase) in amplitude as well as phase at the operating frequency.

Contact Mode: In contrast to the non-contact mode, in contact mode the tip is brought into physical contact with the sample surface, and the dominating short-range repulsive interatomic force leads to a static cantilever deflection. This deflection is then used as a feedback to map the surface topography. For the contact mode, a relatively higher sensitivity is achieved (10^{-18} N), along with a higher resolution. Unlike the non-contact mode, a fixed cantilever deflection termed as the set-point, is used as a reference for maintaining the constant force in contact mode; the amount of force exerted by the tip, and hence the state of the tip-sample contact is controlled by the set-point. A higher set-point means a harder contact and vice-versa.

Next the applications of these general modes are discussed in the context of various SPM techniques used in the present thesis. It has to be kept in mind that for all the techniques to be discussed, the basic underlying parameter is force.

2.1.1. Topography

Typically, operation of the AFM cantilever close to the surface (<20 nm) will have the Van-der-Waals and the repulsive interatomic forces dominate. These forces, when mapped in the non-contact or contact mode, respectively, provide identical information about the surface topography. In case of contact mode, interpretation of the obtained cantilever deflection map is straightforward, with the hills and valleys of the surface corresponding to bright and dark regions in the map, respectively. Whereas in non-contact mode a differentiating contrast related to spatial shifts in amplitude/phase, needs a proper optimization of the key parameters (viz. tip height and amplitude) depending on the topography of the studied sample. However, in both cases the map of z-height signal, which is nothing but a reversed feedback signal, is conventionally used as a measure of the surface topography. Figure 2.6 shows a typical topography of the studied ME composite surface. The bright and the dark regions in this image correspond to the hills and valleys of the sample surface respectively.

2.1.2. Magnetic Force Microscopy

The magnetic stray field emanating from the surface of a magnetic material can be mapped based on the interaction of this field with a magnetic tip. This interaction is typically sensed in a non-contact mode by operating the tip at a distance large enough for the magnetic force to dominate over the short range atomic forces (>20 nm). As explained in the above section, in the non-contact mode of operation the magnetic force acting on the tip will alter dynamic properties of the cantilever (resonance frequency, phase and amplitude). In this case, eq.(2.5) - (2.7) represent the effect of the magnetic force-gradient acting on the tip.

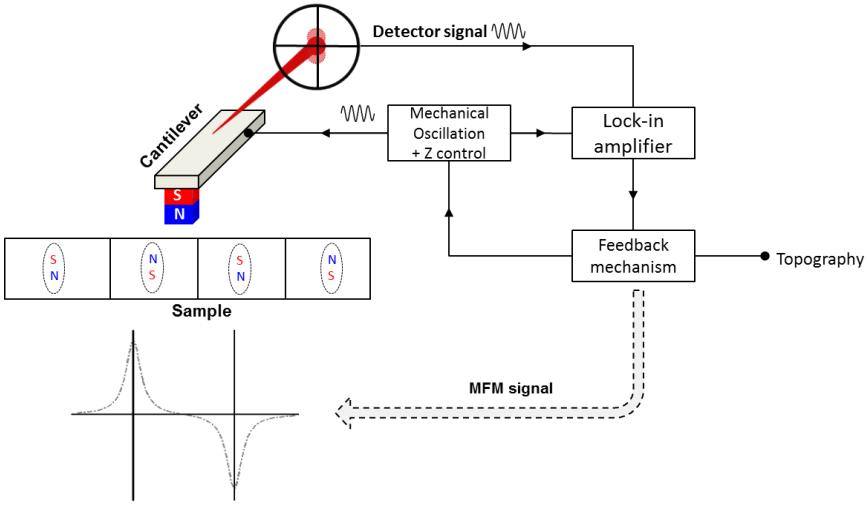

Figure 2.3 Schematic representation of the operation of MFM. Practically, magnetic tip is realized by coating a metallic ferromagnetic layer (Co/Fe) of about a few tens of nanometres in thickness. The block diagram on the right hand side is typical set-up of an AFM.

Typically, the force gradient distribution over the sample surface is correlated to the distribution of the magnetic stray field (section 4.2). As a result the force gradient mapped in MFM is in a sense a depiction of the surface micromagnetic characteristics namely domains and domain walls [124–126]. A detailed explanation about the interplay of micromagnetics and the observed contrast is provided in section 4.2.

2.1.3. Electrostatic Forces: Kelvin Probe Force Microscopy

If a potential difference exists between the tip and the sample, a capacitive electrostatic force acts between them, given as

$$F_c = \frac{1}{2}\frac{dC}{dz}V_{ts}^2 \qquad \textbf{(2.8)}$$

Where C is the system capacitance, which accounts for the combined dielectric polarization partly in the pocketed air, and the sample [127]. On the r.h.s. of eq.(2.8), V_{ts} represents the potential difference between the tip and the sample. Even in the absence of any applied potential to the tip, there exists a built in potential between the tip and sample surface (contact potential). The key factor is the difference in the work function of the tip and the sample. Hence, the tip-

sample potential difference is termed as contact potential V_{CP}. In Kelvin probe force Microscopy (KPFM), this contact potential is measured by means of applying a combination of DC and AC voltages to the tip while operating in a non-contact mode,

$$V_{tip} = V_{CP} + V_{DC} + V_{ac}\cos\omega t \tag{2.9}$$

Substitution of eq.(2.9) into eq.(2.8), followed by rearrangement, results into a first harmonic oscillation term which depends on the difference between the contact potential and the tip DC potential, given as

$$F_C^{1\omega}(z) = (V_{DC} - V_{CP})V_{ac}\frac{\partial C}{\partial z} \tag{2.10}$$

A feedback loop is used to nullify the first harmonics of this force by adjusting V_{dc}=-V_{CP}. Thus, mapping of the nullifying potential, V_{DC}, yields a distribution of the surface potential [128]. It has to be noted that unlike a typical non-contact mode, the cantilever in KPFM is not externally excited (oscillated), rather it's the ac voltage that induces the forced tip oscillation.

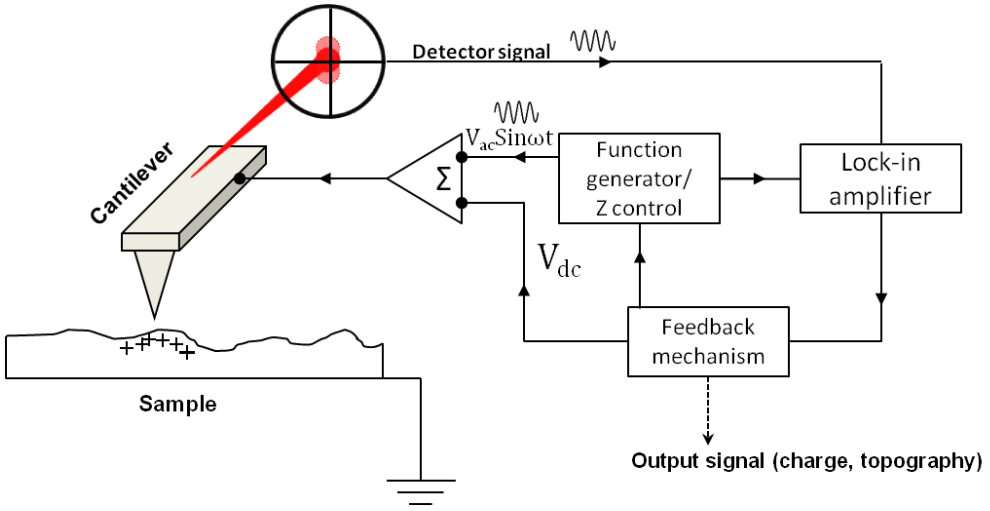

Figure 2.4 Schematic representation of a typical KPFM set-up. The block diagram on the right hand side is typical set-up of an AFM.

The mapped potential in KPFM is not absolute, but a superimposition of several physical sources [129], like work function difference, surface charges, doping profiles etc. Though the technique remains mainly qualitative, in many cases phases with different work function or dielectric properties can be distinguished by KPFM.

2.1.4. Electromechanical Regime: Piezoresponse Force Microscopy

If the sample is ferroelectric, then an electric field applied through the tip being in contact with the sample (contact mode) will lead to electromechanically induced deformation of the latter. The deformation of an extremely localized volume beneath the tip surface (1.5 × tip-radius [130]) dominantly contributes to tip deflection [131, 132], in addition to the presence of the

capacitive forces. Hence, the deformation (in the absence of any external mechanical stress) can be expressed using the constitutive relation for piezoelectrics.

$$\Delta z = d_{33}^{eff} V \tag{2.11}$$

where the use of d_{33} signifies that the axes of applied field and the measured displacement coincide, and that both are along the z-axis corresponding to the macroscopic sample reference frame (system reference frame). However, in the context of polycrystalline samples, the individual grains under the probe, at a time have their respective crystal axes aligned randomly w.r.t. the macroscopic sample reference frame. Hence the response to the vertically applied field does not correspond to the actual d_{33}. For that matter, the use of the superscript *eff* (effective) in eq.(2.11) is followed in the thesis in order to represent the so called effective longitudinal piezoelectric coefficient.

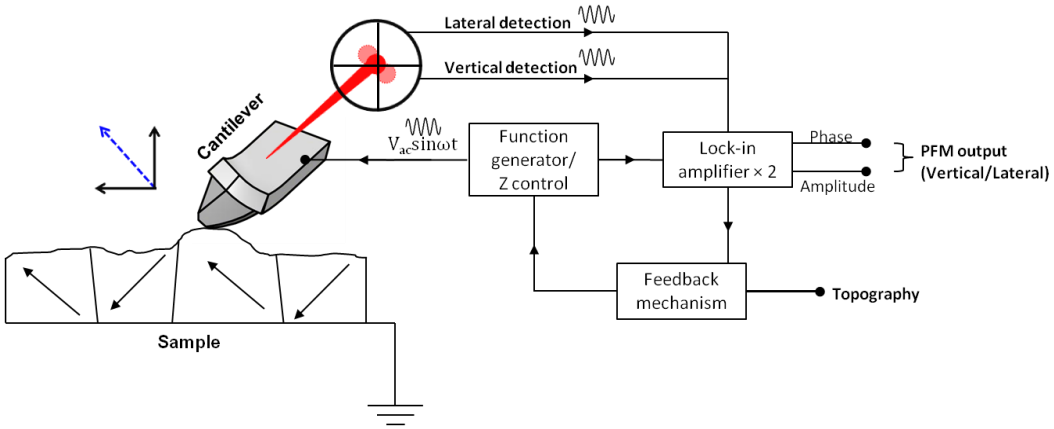

Figure 2.5 Schematic representation of the operation of PFM. The arrows inside the sample indicates the polarization orientation. The block diagram on the right hand side is typical set-up of an AFM, and has no special exceptions as far as PFM is concerned, except that occasionally additional lock-in amplifiers are connected for simultaneously mapping lateral and vertical piezoresponse.

In addition to the local crystal axes, the piezoelectric coefficient d_{ij} is also related to the local polarization state, expressed as [37]:

$$d_{kij}^{T,\sigma} = \varepsilon_{km} Q_{ijml} P_l \tag{2.12}$$

where Q_{ij} is the electrostriction tensor. This means that the displacements over domains with opposite polarity will hence display opposite signs (Figure 2.6). Now a common strategy in PFM is to operate the tip in contact mode, with an AC voltage $V_o sin\omega t$ being applied to it, inducing an AC surface displacement. This resultant AC tip-deflection is then measured using a lock-in amplifier. The purpose of this strategy is two-fold: (i) achieving higher detection sensitivity, taking advantage of lock-in amplifier, and (ii) resolving domains with different polarization orientations. The latter is achieved by observing the phase of the measured AC displacement w.r.t. to the applied AC voltage (excitation). As shown in Figure 2.6 for a domain with polarization along the system –z axis, the sample displacement will be in phase with the applied

field. Whereas for a domain with polarization along the system +z axis an out of phase AC displacement occurs. Consequently, mapping the phase will essentially map the polarization orientations. The amplitude signal, on the other hand, does not differentiate itself between exactly opposite domains (180^0), rather it undergoes significant clamping at domain walls where the mutually opposing surface displacement on either side in effect nullifies the net amplitude. The measured signals in PFM, comprising of both phase and amplitude, are in practice combined within the lock-in amplifier itself to give a signal that is either of the following channels commonly termed as *piezoresponse* ($X = A\cos\theta$, and $Y = A\sin\theta$).

In the case that the polarization lies parallel to the sample surface plane, a dominant in plane displacement takes place under the influence of the tip applied field. This in-plane displacement/shear results in torsion of the cantilever, which contributes to the tip deflection in terms of lateral motion of the laser reflected onto the photodetector. This contribution is measured as lateral PFM signal (LPFM) and gives an idea of the in-plane polarization components (Figure 2.6). The vertical and the lateral PFM signals are acquired either simultaneously using two different lock-ins (Figure 2.5), or are measured with one lock-in in two consecutive passes. With this, the 3D orientation of polarization can be partially estimated, and hence the technique of operating the lateral and vertical PFM is termed as the vector PFM.

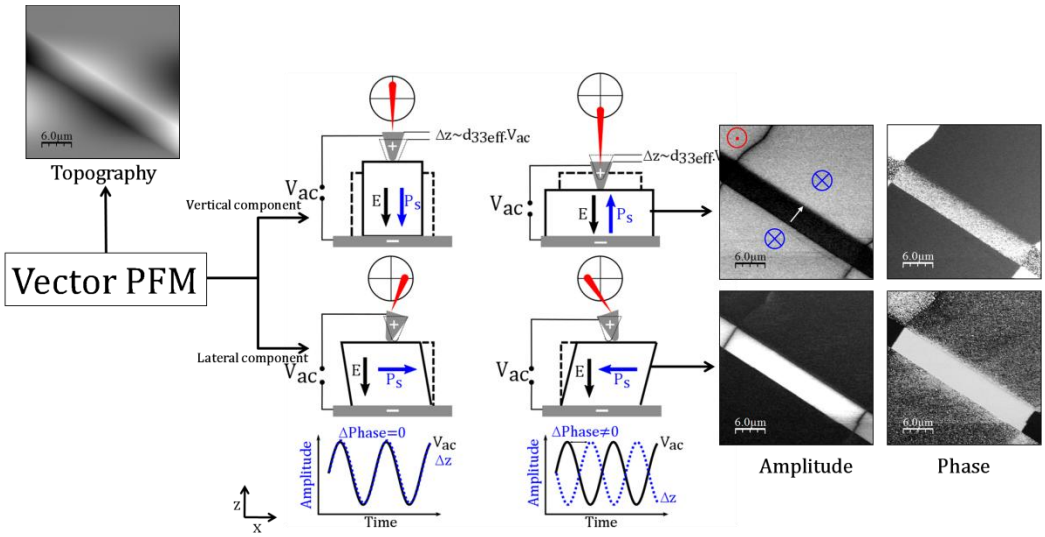

Figure 2.6 A schematic representation of the concept of vector PFM. The central cartoon exaggeratedly shows the modes of displacement under the vertically applied electric field, along with the phase differences between the excitation voltage and the induced surface displacements. The images on the right correspond to the c (top) and the a (bottom) domains in a $PbTiO_3$ single crystal (001).

The dynamic tip response in PFM is identical to that of a forced oscillator, where the combined oscillation of the tip and sample (contact) is considered. The response, as a result, is highly dependent on the mechanical properties of the contact, and like any other oscillatory system shows a resonance. This resonance is commonly utilized in PFM, to bosst the inherently weak piezoresponse. However, as will be discussed in chapter 5, the resonance frequency varies over

the surface, owing to the varying contact mechanics. As a result, several strategies are suggested in literature, for either tracking the resonance while imaging [133], or to use a band of excitation frequencies[134] and obtain the complete dynamic response at each data point. In the present thesis, tracking of resonance was realized using a built-in routine, termed as *dual-frequency AC resonance tracking* (DART)[135]. As the name suggest, DART utilizes dual frequencies across the contact resonance to operate the tip, and the difference in the amplitude at both the frequencies is used as a feedback for tracking the resonance frequency. In this way, depending on the feedback efficiency, at each pixel the operating frequency is as close to resonance as possible. Most of the PFM image acquisition in the present thesis, that are mainly utilized for semi-quantitative data analysis, were carried out in DART mode. Whereas the PFM images meant for qualitative analysis were acquired at a single frequency (50 kHz), far below the contact resonance.

2.1.5. Switching Spectroscopy PFM

The conductive AFM tip can be used not only for visualization but also for investigation and manipulation of ferroelectric polarization switching in an extremely localized volume. In particular, due to a very small tip apex radius, even a moderate DC voltage applied between the tip and the bottom electrode generates an electric field of several hundred kilovolts per centimeter in the vicinity of the tip apex. Such a field easily exceeds the threshold field (~10^9 V/cm) necessary for nucleation of a new domain with reversed polarization.

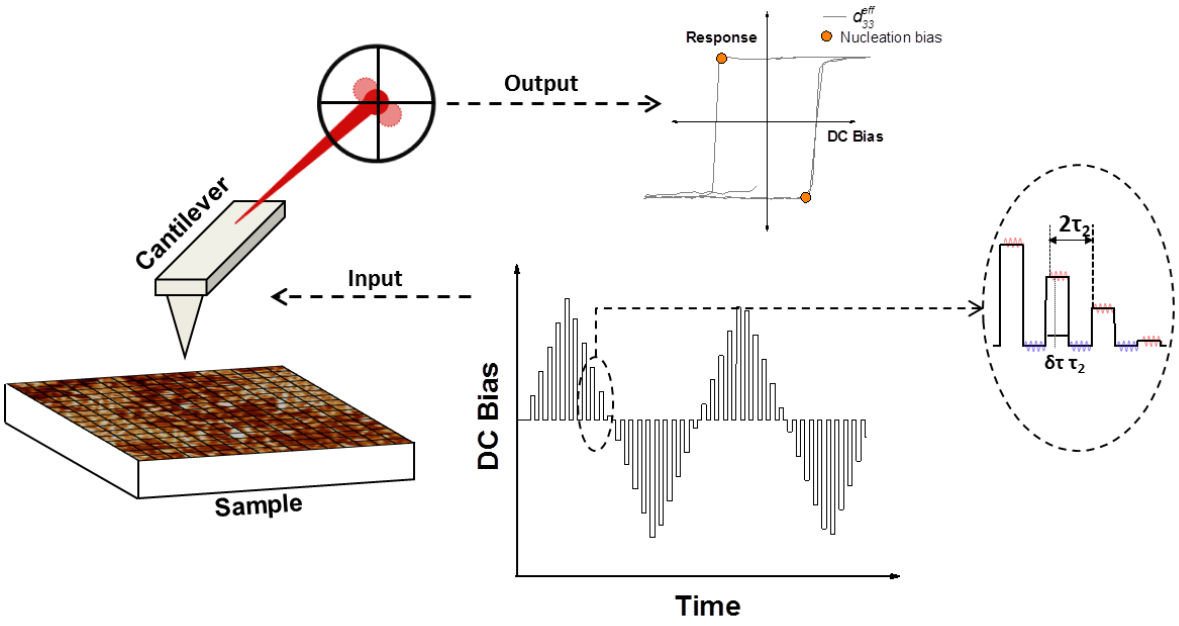

Figure 2.7 Schematic representation of SSPFM operations. (left) DC voltage dependences of the PFM signal (local hysteresis loops) are measured in each point of a 2D spatial grid. The bottom right waveform represents cycling DC bias steps applied to the tip. Whereas the top right frame is typical SSPFM phase signal, with the key parameter of interest, the nucleation biases, marked by the orange circles.

One of the approaches to study processes of polarization switching in ferroelectrics is to use PFM in a voltage spectroscopy mode [136, 137], where the measurements are done on a point by point basis (identical to the force-distance curve measurements), with a DC voltage swept in a cyclic manner. The obtained dependence of the local piezoresponse on the applied bias is referred to as a local piezoelectric hysteresis loop. Figure 2.7 shows the operation of SSPFM, where the DC bias is applied as a chopped saw-tooth waveform, with small AC probing voltage applied during the on and off steps. The small AC voltage works by measuring the instantaneous piezoresponse, which increases with increasing DC bias, as a nano-sized domain nucleated under the tip expands. This increase/decrease in piezoresponse has two underlying components; (i) changing amplitude due to changing contributions of the switched area, and (ii) changing phase associated with the changing polarization orientations under the tip (Figure 2.8). In the present thesis, rather than piezoresponse loops, those corresponding to amplitude and phase are separately addressed.

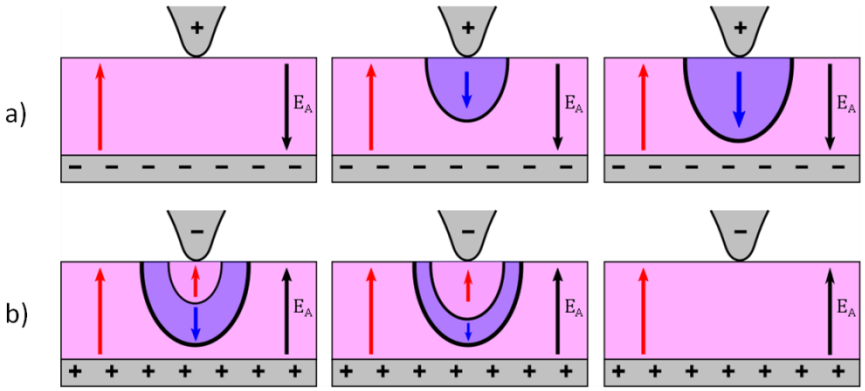

Figure 2.8 Schematic representation of the domain nucleation and growth process, for (a) the forward, and (b) the reverse switching cycles. The reverse switching process (b) signifies presence of domain pinning.

2.1.6. The Philosophy of Scanning

The imaging in SPM is realized by scanning the tip over a fixed sample area, using a piezoactuator based *xy* scanner stage. The scan trajectories generally comprise of movement along two axes namely the fast axis and the slow axis. These axes, as their names suggest, correspond to back and forth motion (fast axis) that slowly (raster-scan) or stepwise (ortho-scan) proceeds along the slow axis (Figure 2.9). Each forward and backward stroke along the fast axis corresponds to a trace and a retrace scan, respectively, along which data (viz. deflection, phase, amplitude etc) are sampled at specific step size (pixel weight). Commonly, either the trace or retrace sampled arrays are utilized for image compilation. The number of lines per scan (M), also referred to as the total number of trace/retrace strokes within the scanned area, along with the number of sampled data points/pixels per line (N) constitutes the scan size (M x N) and hence the image-resolution (to be differentiated from true SPM resolution). Choice of the scan size parameters, along with the choice of scan axes orientation w.r.t. to the imaged sample plane, can be arbitrary, as per the experimental requirements. Within the present thesis, typical scan sizes used are either 256 × 256 or 512 × 512, and the scan trajectory used is of ortho-type.

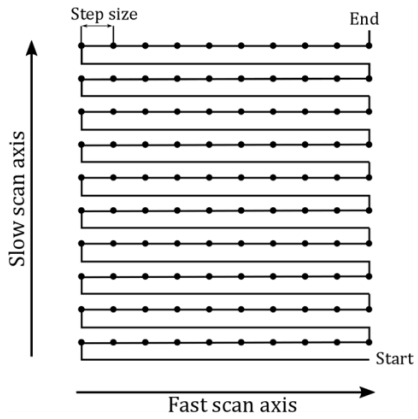

Figure 2.9 The ortho type scanning trajectory. The acquired points are shown for the retrace stroke, that basically refers to the backward motion of the cantilever. A similar acquisition can also be made during the trace strokes.

In all of the SPM techniques discussed above, the scan process involves more than one pass (trace and retrace strokes). In each case, the first pass collects topographic information, whereas the second pass is allocated for realizing the core information related to the technique in concern. Based on the manner in which the second pass is executed, two categories exist:

The NAP Mode: In this mode, during the second pass, the tip is lifted in order to probe the long range forces. This mode is hence specifically used for techniques like MFM and KPFM, where the long range magnetostatic and electrostatic forces need to be probed.

The Parm Swap Mode: This mode is specifically employed in PFM, where by the consecutive passes the photodetector channel is switched between the vertical and lateral deflection, thus realizing both, vertical and lateral PFM.

The SPM measurements in the present thesis were carried out on different commercial SPM set-ups (MFP-3D/Asylum Research, and Ntegra-Prima/NT-MDT). The PFM measurements were performed either in single frequency mode or in DART-PFM mode. In the first case, unless if otherwise specified, an AC voltage with amplitude V_{ac} = 5 V- 8V, and a frequency of f = 50 kHz was applied to the tip. In the second case, the PFM signal was collected at two frequencies, below and above the contact cantilever resonance frequency (~ 600 kHz). In the SSPFM measurements, a train of DC voltage pulses with a constant duration τ_p = 25 ms, and amplitude changing stepwise from 0 to $+V_{max}$, then from $+V_{max}$ to $-V_{max}$and back to 0 was applied to the tip. Between the pulses, a small probing AC-voltage of about 5 – 8 V was applied to induce the instantaneous PFM (DART) signal. Fresh uncoated doped silicon cantilevers (Nanosensors SEIHR) with a spring constant k = 15 N/m and free air resonance of f = 130 - 250 kHz were used for all PFM/SSPFM measurements. The choice of cantilever was optimized after several trial and error steps, in order to provide an optimal tradeoff between electromechanical contributions and the signal intensity. For MFM imaging commercial cantilevers (Asylum Research ASYMFMHC), coated with a thin magnetic layer

of Co/Fe (tip apex radius 45nm; H_c> 5 kOe), were utilized. A commercial variable magnetic field module (VFM2, Asylum Research) was used to apply in-plane magnetic field up to 8 kOe (Figure 2.10).

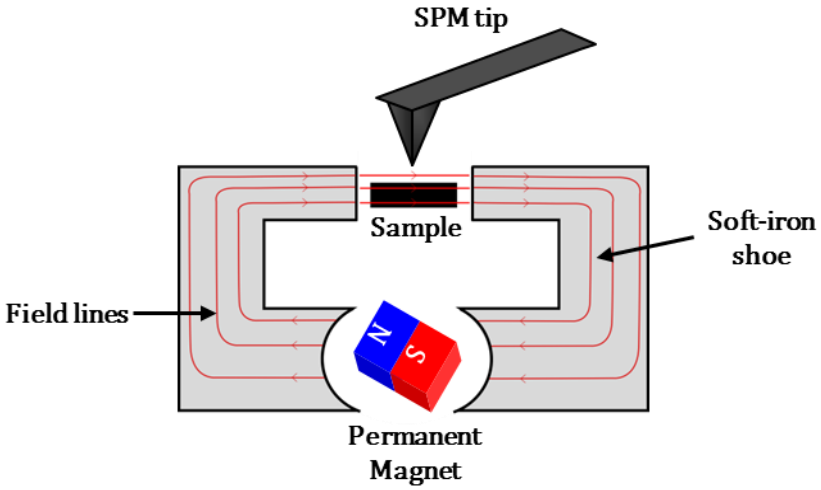

Figure 2.10 Schematic representation of the commercial sample stage, used to apply in-situ magnetic fields.

2.2 Confocal Raman Microscopy

2.2.1 The Raman Effect

The light (electromagnetic radiation) scattered from matter consists of two components: one is called Rayleigh scattering, which is strong and has the same frequency as the incident beam (ω_0), and the other is called Raman scattering, which is very weak (~ 10^{-5} of the incident beam)and has frequencies $\omega_0 \pm \omega_m$, where ω_m is a vibration frequency of a molecule/lattice [138, 139]. The scattering at $\omega_0 - \omega_m$ and $\omega_0 + \omega_m$ result in the stokes and anti-stoke lines, respectively. Raman spectroscopy essentially gauges the vibration frequency (ω_m) of the molecules/lattice (phonons), that are either excited (stokes) or damped (anti-stokes) by the incident beam frequency (ω_0).

Classically, the Raman effect is explained in terms of the interaction between electric field of an electromagnetic wave, $E = E_0 cos(2\pi\omega_0 t)$, and a dipole entity (a molecule or a unit cell), vibrating at a frequency ω_m. In such phenomena, the variable polarizability α of the vibrating dipole results into the following expression of the resultant polarization

$$P = \alpha_0 E_0 \cos 2\pi\omega_0 t + \frac{1}{2}\left(\frac{\partial\alpha}{\partial x}\right) q_0 E_0 [\cos\{2\pi(\omega_0 + \omega_m)t\} + \cos\{2\pi(\omega_0 - \omega_m)t\}] \quad (2.13)$$

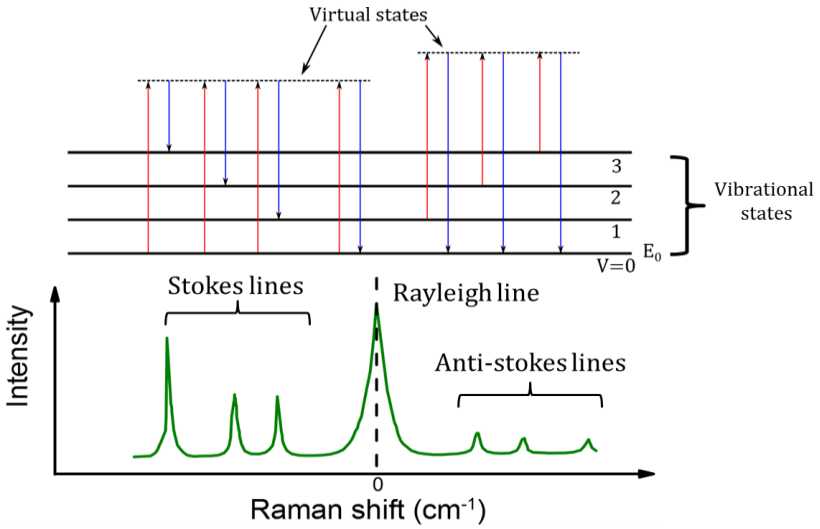

Figure 2.11 (top) Schematic representation of the types of transitions involved in the Raman lines. The process of destruction or creation of a phonon is represented by virtual states.

Here the first term represents an oscillating dipole, which radiates light of frequency ω_0 (Rayleigh scattering), while the second term corresponds to the Raman scattering of frequency $\omega_0 - \omega_m$ (anti-Stokes) and$\omega_0 + \omega_m$ (Stokes). The derivative of polarizability is taken over the spatial co-ordinate *x*. If $\left(\frac{\partial \alpha}{\partial x}\right)$ is zero, then the corresponding vibration mode is not Raman-active. In other words, for a vibrating entity to be Raman-active, the rate of change of its polarizability (α) must not be zero (selection rule). In case of solid crystals, these vibrating entities are nothing but the co-operative lattice vibrations termed as phonons. As a result, the anti-stokes Raman spectra of solids actually represent a loss in energy that a phonon undergoes upon interaction with incident light, providing information about the intrinsic phonon modes. Theoretically, for a crystal with *n* atoms per unit cell, a total of 3*n*-3 vibration modes can exist, however not all of them are Raman active. As evident from the selection-rule, that the polarizability should vary for the vibration mode to be Raman active, the crystal symmetry is hence decisive to the total number of Raman active modes in a particular crystal. Classical group theory for Raman modes takes into account the crystal symmetry under consideration and predicts Raman active modes, which are then heuristically assigned to the experimentally observed Raman anti-stokes spectra. Once the Raman modes are deduced, the spectral intensity of each Raman mode can be given as:

$$I \propto |e_i R e_s|^2 \qquad \textbf{(2.14)}$$

where e_i and e_s are the polarization vector for the electric field corresponding to incident and scattered light, respectively. *R* represents the Raman scattering tensor of the particular vibration mode under consideration. *R* strongly depends on the particular symmetry under consideration, and hence accounts for the various nuances in Raman spectra that provide experimental information about crystal symmetry. The observed Raman spectrum is also critical to the polarization of the incident and scattered light implemented. In our case, the polarization of incident light used was parallel to the sample plane whereas the scattered light from all the possible polarization directions was collected. However, since the sample under consideration has a random grain orientation, the corresponding random variation of *R* nullifies any

preferences to a particular spectral envelope, in effect generating a fixed spectral envelope over each individual grain.

2.2.2 Confocal Microscopy and Raman Effect

Confocal Raman Microscopy stands for observation of Raman spectra in a Confocal Microscope mode of operation. The main advantage of Confocal Microscopy lies in its ability to focus a point-like light source (laser) onto a sample surface and to detect only part of the reflected light corresponding to a specific focal plane [140–142]. The schematic arrangement of Confocal Microscopy, as shown in Fig, displays selectivity of Confocal Microscopy as far as the focal plane is concerned. The image, which is focused through an aperture (pinhole) in front of the detector, only comprises of reflections from the particular focal plane, as well as particular lateral range (Figure 2.12), which can be controlled by the size of aperture. Because the image plane collects the reflection that corresponds to incident focus, it is termed as confocal w.r.t. the incident light.

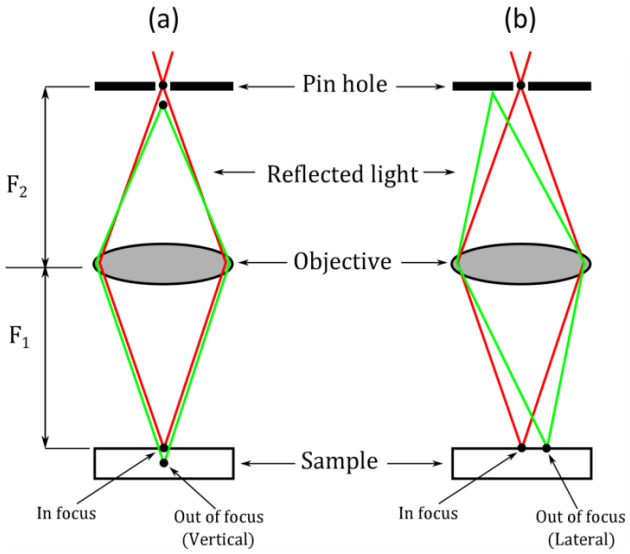

Figure 2.12 Schematic arrangement of a confocal microscope, showing the out of plane (right) and in-plane (left) focusing

The lateral resolution in confocal microscopy as per the Rayleigh criterion can be given as,

$$\mathbf{R_{x,y}} = \frac{\alpha\lambda_I}{\mathbf{NA}} \qquad \textbf{(2.15)}$$

Where α is a factor that ranges from 0.37-0.51 depending on the choice of pinhole diameter, λ_I is the incident light wavelength, and NA is the numerical aperture which is a measure of the light collecting capacity of the objective. Although the resolution can be improved by increasing the NA, there exists a lower limit determined by the wavelength of the incident light. In addition, the vertical spread of the incident beam also brings into play a vertical resolution, which is of less importance in the present context where only images from the apparent sample plane have been

obtained. The vertical spread of the image is only crucial in that it determines the sample depth up to which the Raman signal will be significant.

Conventionally, in rigorous optical studies the spread of the focused beam is considered in terms of a spread in the corresponding electrical or magnetic energy density, also termed as the point spread function (PSF). In any form of confocal microscopy, before forming an image, the incident light which has a certain PSF h_1, is modified by the sample (e.g. by Raman scattering). Since the detector is also point-like, it has its own contribution of convolution h_2 to the formed image

$$I = |h_1 h_2|^2 \otimes f(x, y, z) \quad \textbf{(2.16)}$$

Where f represents the Raman generation function. In practice the function h_2, which depends on the emitted wavelength, introduces complicacy for getting an exact estimation of the produced image, since in Raman scattering the emitted light has certain wavelength distribution, requiring integration over all of them. However, in experiment, it is a common practice to presume a Gaussian distribution of the confocal Raman image of a point like source and use it as a model to fit an observed experimental image across a suitable sharp interface in order to predict parameters that will determine the convolution of the system PSF ($h_1 \cdot h_2$). This aspect is necessary in facilitating deconvolution of the observed image, especially when sharp interfaces are involved; this will be discussed in detail in chapter 5.

The key feature of CRM in a nutshell, that makes it suitable for the task at hand, is its ability to focus a point like beam onto a specific surface plane and to collect the light reflected only from the point-like area illuminated. This makes it possible to scan the laser beam on the sample surface in order to acquire a distribution of the Raman spectra with high spatial resolution.

2.2.3 Instrumentation

Figure 2.13 schematically shows a typical Confocal Raman microscope set-up, where the most important component that is critical to observation of Raman spectra is the detector system in conjunction with a confocal microscope set-up. The reflected light, which comprises of Raman bands of different wavelengths, is firstly separated using a suitable grating within the spectrometer (Figure 2.13). For the acquisition presented in the thesis, a commercial microscope (Alpha 300AR; WiTec GmbH) was used. The incident light source is a green laser (633 nm). The light was polarized along the horizontal (x) direction within the sample frame of reference. The spectrometer comprises of a grating with 600 grooves/mm, which provides a spectral resolution of 1.9 cm^{-1} for the incident light used. The laser was focused by an objective of100x magnification with the numerical aperture of 0.75, providing a beam with 290 nm waist (xy plane) and a 550 nm depth (along z direction). The imaging is realized by ortho-type scanning of the sample, using an xy-piezo scanner underneath (Figure 2.13). The scanned area is divided into a grid of points; at each point, the Raman acquisition is done for a fixed interval of time, also

termed as the rate of acquisition. In the present case the acquisition rate ranges from 0.5 to 5 seconds, depending on the required quality of the spectra.

In order to apply an in-situ magnetic field, a home-built module (Figure 2.13a) was used. The module essentially supports two strong NdFeB magnets (commercial) within the fixtures of the two independently movable arms, facing each other with opposing poles. The samples were placed between these arms, elevated using custom supports, such that their position lies exactly collinear with the central axis of the magnetic poles. The frame of the module was so designed that it fixes the entire module on the scanning stage of the microscope. The sample elevation was adjusted such that any tolerance between the magnet arms and the objective is avoided during focusing. The variation of magnetic field was realized by varying the distance between the magnet poles, such that at each time they stay equidistant from the sample, in order to maintain a homogeneous magnetic field on the sample. All the Confocal Raman acquisitions were carried out with the help of Dr. Pavel Zelenovskiy.

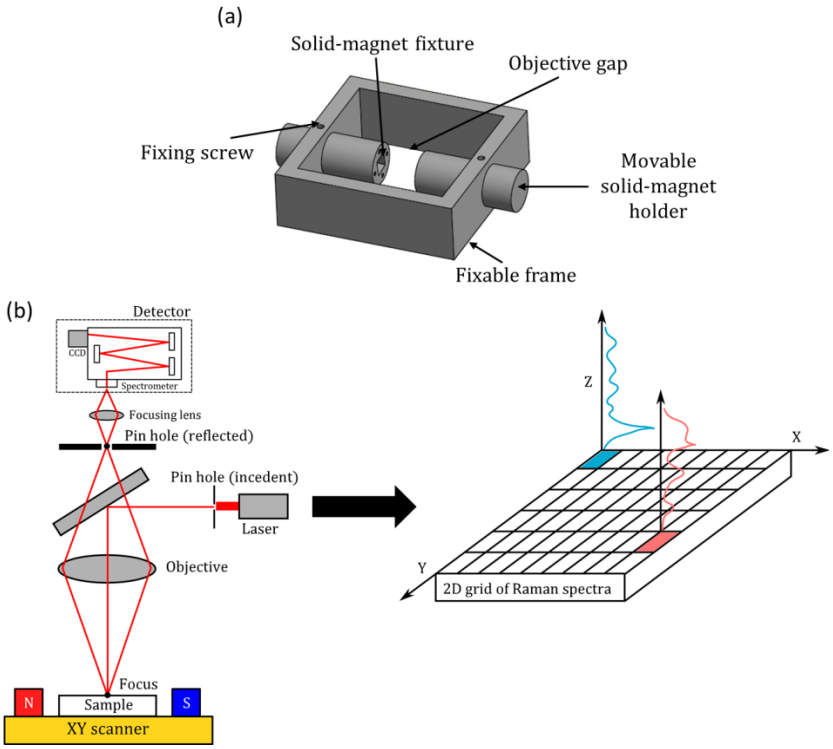

Figure 2.13 (a) The design of the module developed for applying in-situ magnetic field. (b) A schematic representation of the CRM set-up

2.3 Sample Preparation

All the composite samples studied in the present thesis are bulk ceramics synthesized by conventional powder processing method. Although the individual processing parameters and raw materials for the studied samples are different [39, 143, 144], the entire process can be generalized as shown in Figure 2.14. In most cases, starting powders of the individual phases

namely BTO and ferrites (BaM, CFO, NFO) are separately synthesized using appropriate raw materials, which are then mixed together. The mixture is then formed into pellets and sintered at high temperature (1000 – 1200 ^{0}C). The sintering step not just induces binding within and between the constituent phases, but also leads to agglomeration amongst the individual component phases. The degree of mixing and the sintering temperature, which critically decides the extent of agglomeration, has not been specifically controlled. As a result, the studied samples possess distinct morphologies.

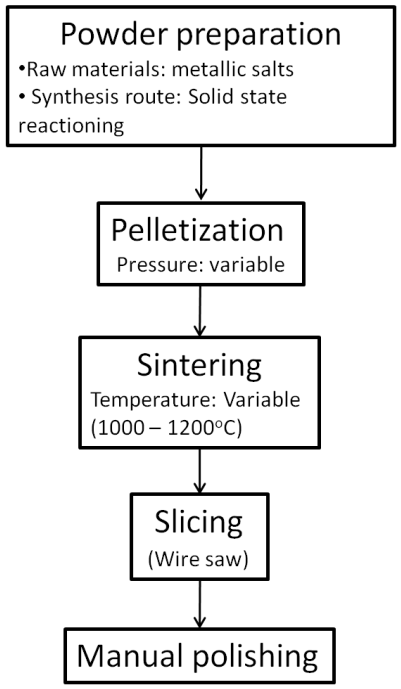

Figure 2.14 Schematic representation of the process of sample preparation.

Both surface analysis techniques utilized, namely SPM and CRM, are extremely critical to the surface conditions. The preliminary requirement for good imaging is minimal surface roughness. As already discussed, in SPM the feedback mechanism has a limited z range within which it can efficiently operate. In addition, an extremely rough surface can result into instabilities in the tip motion leading to a crosstalk between the topographic and non-topographic (MFM, PFM) images. For that matter, it is a norm to implement rigorous polishing steps to fine polish the surface up to a roughness of few tens of nanometres. For that matter a commercial automated polishing set-up (Streuers) was utilized in conjunction with diamond pastes as polishing material on a special polishing paper. Several polishing step in a sequence of grit sizes 15 μm, 9 μm, 6 μm, 3 μm, 1 μm, and 0.25 μm were carried out, each followed by a thorough ultrasonic cleaning. Diamond polishing serves an excellent purpose of polishing the sample surface without causing unnecessary damage (grain pull out). The manual (hold by hand) polishing approach avoids uneven sample polishing and formation of terraces due to the stochastic hand movement involved. Before the polishing step, the samples were sliced using a high-precision wire saw (K. D. Unipress WS22, with a 30 μm tungsten spool), followed by grinding, such that the thickness

(1-3 mm) of the pellets achieve dimensions appropriate for the in-situ measurements. In addition, the grounding step is also necessary to remove any low dielectric constant glassy phases that often segregate at the sample surface during the sintering process.

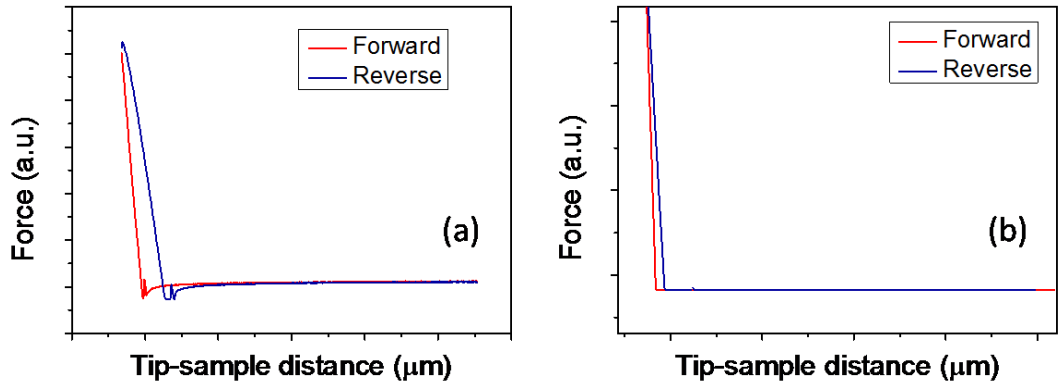

Figure 2.15 Force distance curves on an (a) unclean, and a (b) cleaned sample surface. For the unclean sample, the slopes of the repulsive regions for the forward and reverse branches are different, along with a sign of interaction with a liquid meniscus clear at the minima point. Apparently the same features are absent for the cleaned surface, indicating a significant removal of any adsorbed liquid layer.

Next, it is crucial to thoroughly clean the sample surface to make it devoid of any surface adsorbates like organic layers etc. Presence of such adsorbates can lead to capillary forces on the SPM tip, leading to ambiguities in the obtained images. Such forces can also destabilize the tip dynamics leading to artefacts. Figure 2.15 shows how capillary forces influence the tip deflection, leading to a dip at the equilibrium point of the force distance-curve. In order to realize a clean sample, high contact angle substances like isopropanol were used before every measurement, after which the samples were left to dry in air for a few minutes. Figure 2.15 shows a typical force-distance curve acquired on a composite sample after such a cleaning process. It can be seen that the curve shows no significant dip at the inflexion point, signifying a good cleaning step. Henceforth, it has been assumed that the nature of these forces is purely atomic, and that the existence of any other type of forces like capillary forces can be ignored.

2.4 General Characterization Methods

In addition to the investigation carried out using the core techniques (SPM, and CRM), the studied samples were comprehensively characterized for their essential properties like structure, electrical and magnetic properties.

The crystal structure/phase homogeneity of the samples was primarily characterized using a standard powder X-ray diffraction system (Siemens D5000). The reflection angle (2θ) was slowly varied (0.1^{o} per second) from 20^{o} – 80^{o}, which covers the majority of characteristic diffraction peaks. The XRD measurements were carried out with the help of Dr. Irinia Anusca, and Dr. Morad Etier. The microstructural characteristics like grain size distribution, and grain

orientations were observed using the Electron Backscatter Diffraction (EBSD) method, performed using an integrated EBSD detector in a Scanning Electron Microscope (SEM; LEO 1530 Gemini). The field emission was created at an acceleration voltage of 20 kV; the studied samples were inclined at 70^{o} w.r.t. the gun, in order to get better diffraction contrast. The underlying working principle of EBSD is similar to X-ray diffraction, where instead of the X-rays the electrons are diffracted by the periodic lattice, obeying Bragg's law [145]. The EBSD measurements wre carried out by Frau Dr. Priska Stemmer.

For the electrical characterization, Pt/Pd electrodes were sputter coated onto the samples, followed by adhesion of copper wires using silver paint. Each time, the paint was left to dry for one day before starting the measurements. The electrical resistivity was measured on a KEITHLEY 6585 Picoammeter. Whereas the dielectric properties were measured using a SOLARTON 1260 impedance analyzer with the dielectric interface system 1296. A small voltage of 0.1 V was applied while measuring the impedance. The sample thicknesses and electrode diameters were taken into account for each sample individually. The ME voltage coefficients were measured using a home built set-up based on the lock-in technique [146]. The electrical, dielectric, and magnetoelectric measurements were carried out with the help of Dr. Habil. Vladimir Shvartsman, Dr. Morad Etier, Dr. Yanling Gao, and Naveed-Ul-Haq. The magnetic measurements were performed on two different Vibrating Sample Magnetometers (VSM). In one case an assembled VSM (Princeton Instruments) with an electromagnet, whereas in other case the VSM option in a Physical Property Measurement System (PPMS DynaCool) weres utilized. These magnetic measurements are courtesy to my colleagues Ahmadshah Nazrabi, and Soma Salamon.

2.5 Tools of Data Analysis and Image Processing

In the present context, where the central theme necessitates mining of useful information from the acquired data-sets and presenting the same as images, it becomes inevitable to utilize *ad hoc* tools/algorithms for data transformation and analysis. The data-sets under consideration are multidimensional, in other words unlike a conventional graph they have more than 2 independent variables involved. A normal map of an image, which has a single value associated with each of the M×N pixels is a 2D data-set. Whereas if at each of those M×N pixels a quantity is measured either w.r.t. voltage (SSPFM), magnetic field, or wavelength (CRM) the resulting data set will be 3D, comprising of 3 variables; 2 spatial co-ordinates (x_i, y_i), and the variable swept (e.g. voltage or wavelength) at each of the spatial co-ordinates. In some cases, especially in SSPFM, there are more than one quantity (phase, amplitude and frequency) is measured simultaneously. However, in contrast to the reference made to such data-sets in literature, they are still considered as 3D in the present thesis, since there are still 3 independent variables.

Table 2.1 Types of data-sets, and their dimensions typically encountered in the present thesis.

Technique	Data-set	Independent variables
SPM imaging	2D	2 X spatial co-ordinates
SSPFM	3D	2 X spatial co-ordinates, voltage
In-situ magnetic field PFM	3D	2 X spatial co-ordinates, magnetic field
Raman spectroscopy	1D	Wavenumber (Raman shift)
CRM	3D	2 X spatial co-ordinates, wavenumber

As evident, either of the 3D data-sets will comprise of arrays that correspond to inhomogeneous spatial regions. Although for a 2D data-set, the identification and analysis of the quantities corresponding to different phases is simple (in terms of the image contrast), the case with a 3D data set is not so trivial. For that matter, various commonly accessible statistical data-analysis techniques are employed. Various data transformation strategies are opted in order to prepare or identify data-sets for the data-analysis step.

2.4.1 Data Transformation

Data transformation stands for reshaping and/or normalizing the data arrays as either a pre-processing step for the final data-analysis or representation of the obtained results into a visually perceptible form. These steps that are commonly used throughout the thesis are defined in this section as following:

Reshaping data-set: The process of transforming a data-set from 3D to 2D or 2D to 1D is termed reshaping. The 2D to 1D conversion is extensively utilized in cases where a sequence of images acquired under different external conditions need to be converted into arrays. These arrays can be stacked as columns or rows in the same sequence so as forming a data-matrix usable for the data-analysis step. A 2D data-set which is basically a matrix can be reshaped into a 1D form by sequencing each subsequent row back to back as shown in the following example.

$$\begin{bmatrix} 9 & 5 & 3 \\ 7 & 2 & 0 \\ 6 & 8 & 1 \end{bmatrix} \leftrightarrow [9 \quad 5 \quad 3 \quad 7 \quad 2 \quad 0 \quad 6 \quad 8 \quad 1]^T \tag{2.17}$$

Here, the subscript T on the r.h.s of eq.(2.17) stands for transpose. As can be seen from eq.(2.17), if the 1D data-set is reverse reshaped, it exactly turns into the original 2D data-set.

On the other hand, the 3D to 2D reshaping refers to spatially representing the measured quantity corresponding to a particular value of the swept variable. This type of representation

serves visually perceptible images, which bring out the key quantities of interest out of the 3D data-set.

Normalization: Data arrays that represent a continuously changing quantity w.r.t. the swept variable, need to be standardized so as to have a comparable form. In the present context, this standardization is carried out by normalizing each array using the area under the curve (the plot of array values against their co-ordinates). By doing this, one essentially preserves only the arbitrary qualitative nature of an array that is than comparable with other normalized arrays. In case of 2D PFM data-sets, line wise normalization has been adopted in that each scan line has been individually normalized, removing any artifactual line shifts. On the other hand, in a 3D data-set of CRM Raman spectra corresponding to each grid point have been area normalized.

2.4.2 Drift Correction

Images acquired in a sequence at different values of a sweeping quantity (e.g. magnetic field) are often drifted w.r.t. each other, mainly due to thermal drifts of the xy-piezostage. In order to achieve the drift correction in the present thesis, the drifts were initially determined using method based on topography correlation [20]. The relative drifts δ_x *and* δ_y were determined in each image with reference to a heuristically chosen central image, and based on these drifts the lateral dimensions were reduced such that all the images achieve maximum correlation with each other.

$$M' = M - [\max(\delta_y) - \min(\delta_y)] \quad \textbf{(2.18)}$$

$$\mathrm{N}' = \mathrm{N} - [\max(\delta_x) - \min(\delta_x)] \quad \textbf{(2.19)}$$

where M' and N' are the new dimensions of the images. The drift determined and corrected for topography images is than applied to the other image channels.

2.4.3 Principal Component Analysis

Coming to the core statistical data-analysis techniques utilized in this work it is essential to review the features of the data in concern. The 3D data-sets often hide important trends within them which could not be predicted beforehand. In addition, since in the present case the data-sets comprise of two different sets of distribution, each corresponding to the constituent phases, a technique is required that can tackle the whole data-set at once. Principal Component Analysis (PCA), which is a popular feature detection technique, comes by as a convenient tool for operating the experimental data-in concern. Following are the salient features of PCA that explain its suitability in present context [147–152].

- Unlike other statistical techniques, PCA is best suited for correlations within the data set.
- Less amount of pre-processing (whitening) of data is needed.
- PCA can be applied to an arbitrary distribution of data.

A brief understanding about the working principle of PCA can be achieved by considering a simple example of two independent 3-point features (Figure 2.16; left). A fictitious data set can be constructed by adding white noise to these features together with a baseline, and arranging them randomly as rows of a matrix. Such a matrix is termed as a data matrix, and the rows that comprise the feature are commonly termed as data vectors. The columns of the matrix are the vector components, which if plotted in a three dimensional Cartesian system would appear as an irregular swarm of points (Figure 2.16 bottom). It can be inferred that the major and the minor axis of the data swarm actually correspond to the original features. Now, useful statistical properties of the data set can be defined as following:

Non-central univariate second moment: This is the non-central (no mean subtracted) counterpart of what is commonly known in statistics as variance. Here the univariate moments within each row are referred as:

$$\boldsymbol{univariate\ second\ moment} = \sum_{i=1}^{3} x_i^2 \tag{2.20}$$

Non-central multivariate second moment: This is the non-central of what is commonly known in statistics as covariance**.** Here the multivariate moments amongst the rows are referred.

$$\boldsymbol{multivariate\ second\ moment} = \sum_{i=1,j=1}^{3} x_{ij}^2 \tag{2.21}$$

According to the definition of statistics the feature directions are associated with a high univariate second moment, whereas the orientation of the swarm of points around the origin is accounted by the multivariate second moment. Hence the task is now to trace these directions of high univariate second moment, which can be done by rotating the swarm of point in such a way that these directions which also happen to be orthogonal to each other, coincide with the axes of the co-ordinate system. This rotation statistically amounts to maximizing the univariate moment while minimizing the multivariate moment. In terms of linear algebra this rotation of data matrix X giving a new data matrix Y can be expressed as

$$VX = Y \tag{2.22}$$

$$X = YV^T \tag{2.23}$$

$$X = U[DV^T] \tag{2.24}$$

Where V is the orthogonal rotation matrix, and D is the matrix of second moments for the transformed data matrix (Y), with diagonal elements as univariate moments and the off diagonal elements as the multivariate moments. Eq.(2.24) represents the singular value decomposition (SVD), where D is diagonalized. It is the choice of V integrated within the SVD that diagonalizes the second moment matrix, hence the quantity DV' essentially traces the amount by which each vector component had to be moved. In effect DV' traces the principal components (original features), which the 1st row (1st component) being the most prominent feature, whereas the 2nd row being the next prominent feature. The multiplicative matrix U is termed as the score

matrix as its columns represent the extent of each components present in the original data-set. For example, rows of the first column of U essentially represent the scores of the 1st component in the corresponding rows (features) recorded in the original data set.

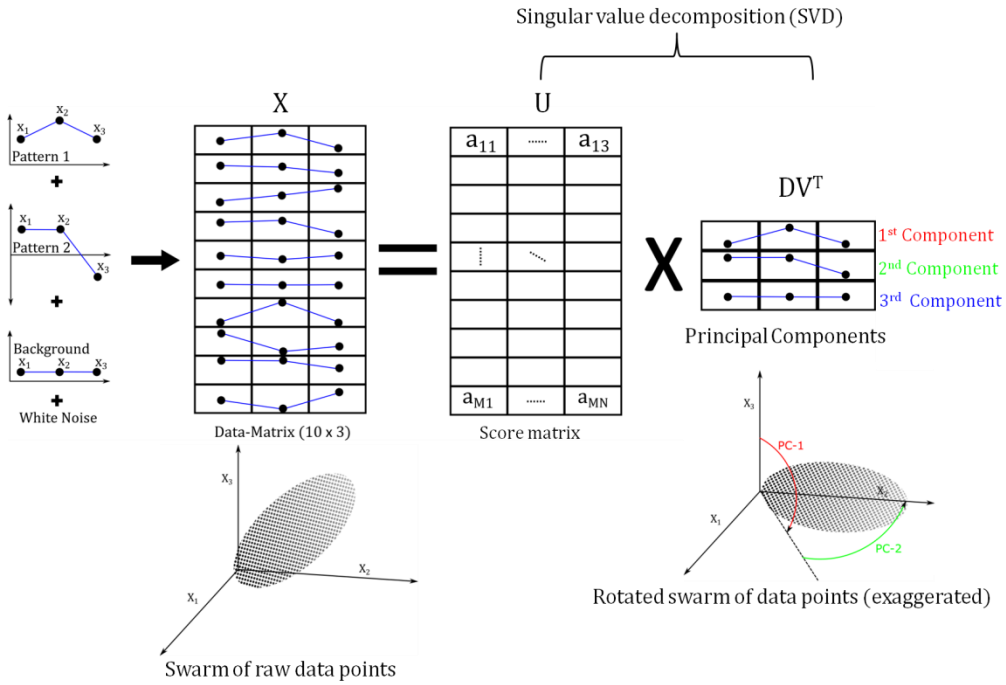

Figure 2.16 (from left to right) the example patterns, formed into a 10 × 3 data-matrix, followed by its decomposition into product of the score matrix and the principal component matrix. It can be inferred from the distribution of patterns in the raw data-matrix that $a_{11}>a_{12}>a_{13}$. At the bottom, the swarm of data points for the raw data (left) as well as the rotated data (right) are shown; the rotated data-swarm is exaggerated, as normally the number of data-points reduces due to the dimension reduction property of PCA.

This approach of PCA is not conventional, since the non-centered moments are used. Conventionally the means of the data arrays are subtracted (whitening) before carrying out PCA, this way the central moments (variances and co-variances) are operated. However, recently it has been heuristically established that a non-central PCA is more suitable for data-sets that comprise of certain patterns, overlaid on a constant noise background [153].

A limitation of PCA, which was overlooked in the considered example, is that the principal components have to be mutually orthogonal. This limitation can lead to significant consequences for a specific type of data-set, where the actual feature directions are not mutually orthogonal. Such a data set can be schematically represented by a swarm of data points of the shape of a heart (Figure 2.17). Hence, such a problem is termed as the *broken heart problem*. As shown in Fig.2.17, the limited rotation of data swarm realized in PCA leads to tracing of features that slightly depart from the original features. This problem is often encountered in the application of PCA throughout the thesis, and will be duly taken into consideration.

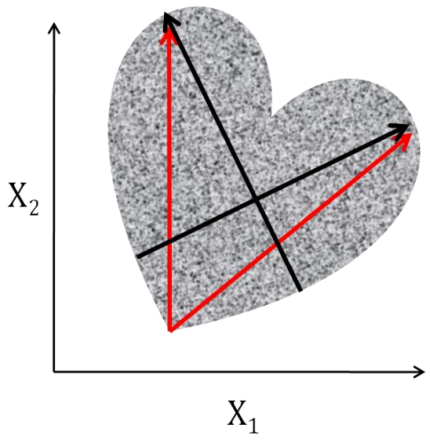

Figure 2.17 A schematic description of the *broken heart* anomaly. The textured heart shape represents the data swarm, with the red arrows representing the actual features, and the black arrows representing the features resolved in PCA.

In the present context, utilization of PCA for various experimental data-sets will necessitate two main conditions: (i) The features to be extracted have to be distinct, and (ii) they should be arranged as rows of the data matrix. In most cases, as will be seen, the data vectors have more than three components, making it a bit complex version of the rather simple example provided here. However, the main essence of the technique is not altered.

2.4.4 Self-Modelling Curve Resolution

As mentioned in section 2.2.3., the 2D CRM acquisition is expected to comprise of different spectra associated with the different phases along with their convolution. This necessitates utilization of a technique that can identify the underlying individual spectral components by taking reference from initial spectra provided. This is exactly what self modelling curve resolution (SMCR) realizes [154, 155]. It utilizes advanced algorithms to alternatively regress the initial spectra and their respective weights at each grid point. As a first step, the data matrix X is formed by arranging the spectra corresponding to each grid point as rows in a sequence identical to that of the 2D to 1D reshaped spatial co-ordinates. The data matrix can be factorized in terms of the weight matrix W and the initial spectra matrix S

$$X = WS + E \tag{2.25}$$

where the initial spectra are arranged as rows in S, and the columns of W correspond to the weights that relate the respective spectra to the original data. E is an error matrix that represents the residual remained after the regressive iterations. Hence, the general approach in SMCR is to achieve minimal E. After an optimal regression, the matrix S will represent the average of the individual spectral component existing in the data-set, whereas W will consist of the weight of those spectra. Hence, by 1D to 2D reshaping the columns of W will actually provide spatial distribution of the corresponding spectrum, or in other words a concentration map for the phase to which the spectrum belongs.

3 Characterizing Bulk Magnetoelectric Composite Systems: From Macro to Micro Scale

The macroscopic characteristics of the studied composite systems are collectively critical to the end ME performance. On the other hand, these characteristics, which although are an aggregate of the microscopic contributions, still rely on the specific distribution of local properties (Section 1.5) to some degree. This is what chiefly accounts for the large statistical variations of the ME coupling within identical compositions (Table 1.2 and Table 1.3). These large variations also reflect the fact that the microscopic distribution of the properties plays a major role in determining the macroscopic end properties. The distribution of phases as well as the respective grain sizes are a good measure of these microscopic property variations (Figure 1.23c). Different synthesis parameters lead to different microstructures, and hence different macroscopic behavior. In the context of ME composites, this means that corresponding to a specific microstructure there exists a specific distribution of stresses and charges generated during the ME coupling process, which ultimately enter into a corresponding macroscopic coupling value. The local investigations presented in this thesis, precisely explores these aspects of composite magnetoelectrics. Hence, as far as justification of the observed local phenomena is concerned, it becomes essential to acquire information about the microscopic as well as the macroscopic characteristics of the studied systems.

In the case of ME composites, where the two constituent phases possess not just different structural and chemical properties, but also different electrical and magnetic properties, it becomes necessary to measure the macroscopic reflections of their individual constituent properties. As a simple example, it needs to be examined whether any impurity phases exist, as the amount of the same will determine parasitic losses of the foreseen properties. Differences in electrical properties of the two constituent phases need to be specially addressed, as there exist a huge gap between the charge mobility between both the phases. As a result any electrical process will always encounter a short circuit configuration in that any generated or applied charge/potential will lead to conduction via the high conductivity phase. This chapter covers various macroscopic characterizations of the studied systems, starting with crystal and microstructural cross-investigations, followed by a correlation to the resultant electrical and magnetic properties.

3.1 Structural Characterization

The powder diffraction patterns acquired on the composite systems basically reflect a convolution of two constituent phases. In cases where the microstructure is homogeneous (a random and segregation free distribution of the two constituent phases), the resultant powder pattern will have the peak intensity distribution proportional only to the content of the constituents. Any significant variation from such a behavior XRD-pattern would indicate a microstructural inhomogeneity. In addition to this, a scenario where the cross-section

corresponding to each phase might not be statistically random enough to resemble a powder diffraction pattern, also needs to be taken into consideration. The observed XRD patterns are hence analyzed in context of the phase distribution, along with the qualitative tracing of any impurity phases on the premises of heuristic arguments based on literature.

3.1.1 $BaFe_{12}O_{19}$-$BaTiO_3$

Figure 3.1 shows the X-ray diffraction pattern of a BaM-BTO (35-65) sample, along with the observed planes marked individually in the pure BaM and BTO standard patterns (Figure 3.1b, c). A comparison of the intensity ratios for the BaM peaks in the observed pattern (taking BaM (114) plane as reference) makes it clear that BaM has a weaker diffraction cross-section as compared to the BTO one. This simply reflects the fact that BaM has lower volume fraction as compared to BTO. Apart from this no impurity phase could be traced from the diffraction pattern. However taking into consideration the quality of the diffraction pattern any presence of impurity phases cannot be completely excluded. Samples belonging to an identical batch with identical processing parameters, have been reported in literature with a 3% of $BaFe_2O_4$ impurity phase, which was not present in the starting material, and acts as an intermediate precursor phase for BaM [144, 156]. The split observed in the peaks corresponding to (002) and (200) planes is a sign of tetragonality in BTO. Additionally, despite of the close association of the BaM (107) peak, the split in the 101 and 110, also associated with tetragonality in BTO, was clearly visible.

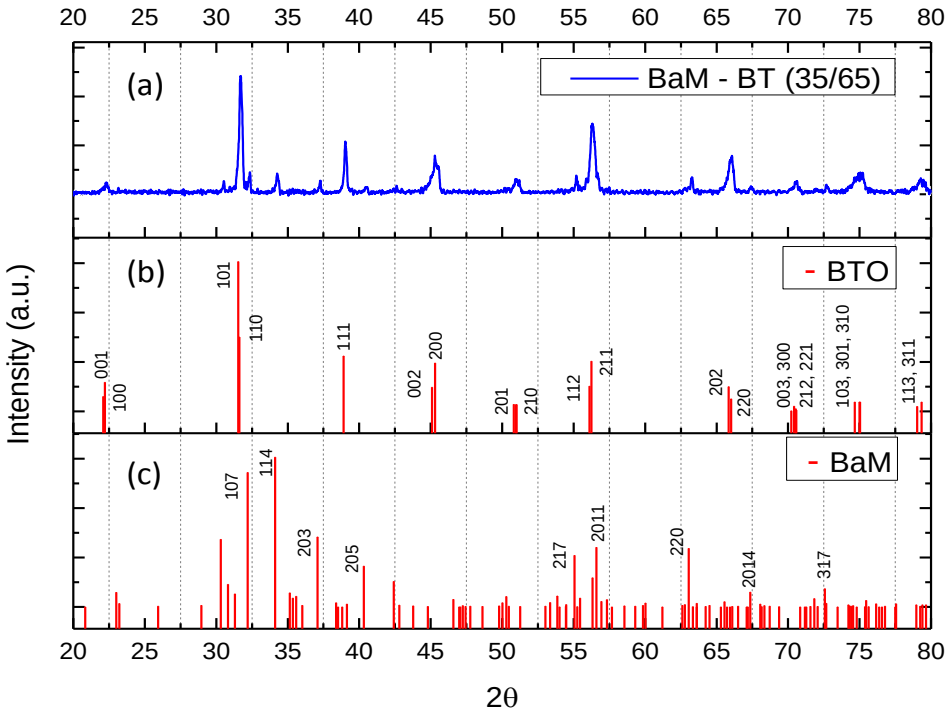

Figure 3.1 XRD pattern (a) corresponding to BaM-BTO (35/65) sample, along with standard peaks for (b) BTO [157], and (c) BaM [158].

3.1.2 $SrFe_{12}O_{19}$-$BaTiO_3$

Figure 3.2 shows the diffraction pattern of SrM-BTO (30/70) sample. Apparently there is no large difference in the patterns for SrM-BTO the BaM-BTO samples, which is expected, as structurally the hexaferrite constituents are identical, and there is not big difference in the scattering factor of Ba and Sr lattice sites. However, there exists a small difference between these two samples, as far as the distribution of peak intensities corresponding to the FE and FM phase is concerned. The peaks corresponding to SrM phase are slightly stronger as compared to those for the BaM phase; this anomaly will be addressed in a later section. No impurity phases could be traced from the observed pattern. Also there are no reports in literature, concerning any possible impurity phases for this particular system. Signs of tetragonality in BTO phase were visible in the form of slight splitting of the peaks corresponding to (101)/(110), and (002)/(200) set of planes.

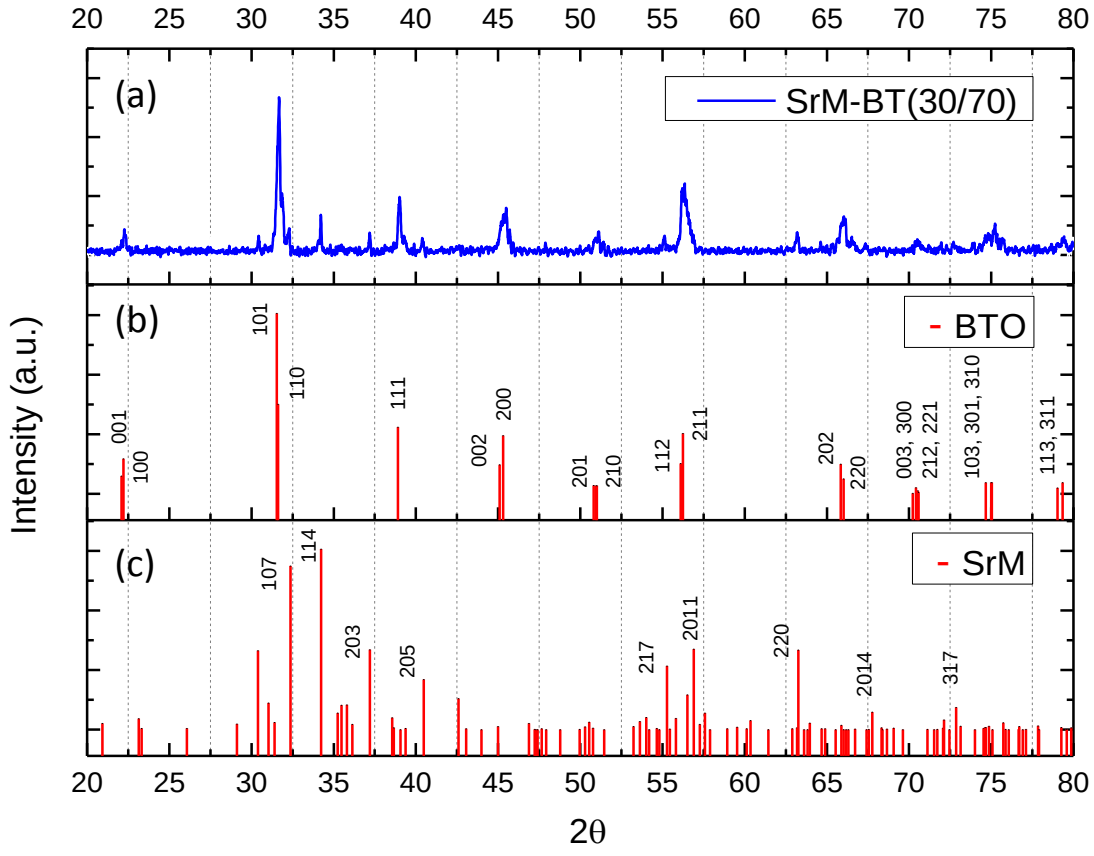

Figure 3.2 XRD pattern (a) corresponding to SaM-BTO (30/70) sample, along with standard peaks for (b) BTO [157], and (c) SrM [159].

3.1.3 $CoFe_2O_4$-$BaTiO_3$

The CFO-BTO (40/60) diffraction pattern (Figure 3.3) reveals a distribution of peak intensities corresponding to CFO and BTO phases, which is apparently in accordance with their volume fractions. As compared to the BaM-BTO/SrM-BTO samples, in the case of the CFO-BTO the ratio of peak intensities of BTO and CFO is smaller. Especially the peak corresponding to CFO (113)/(11$\bar{3}$) planes is more prominent in the composite diffraction pattern as compared to that for the BaM (114) planes in the BaM-BTO sample. This simply reflects the higher scattering power of the cubic lattice of CFO as compared to the BaM hexagonal lattice.

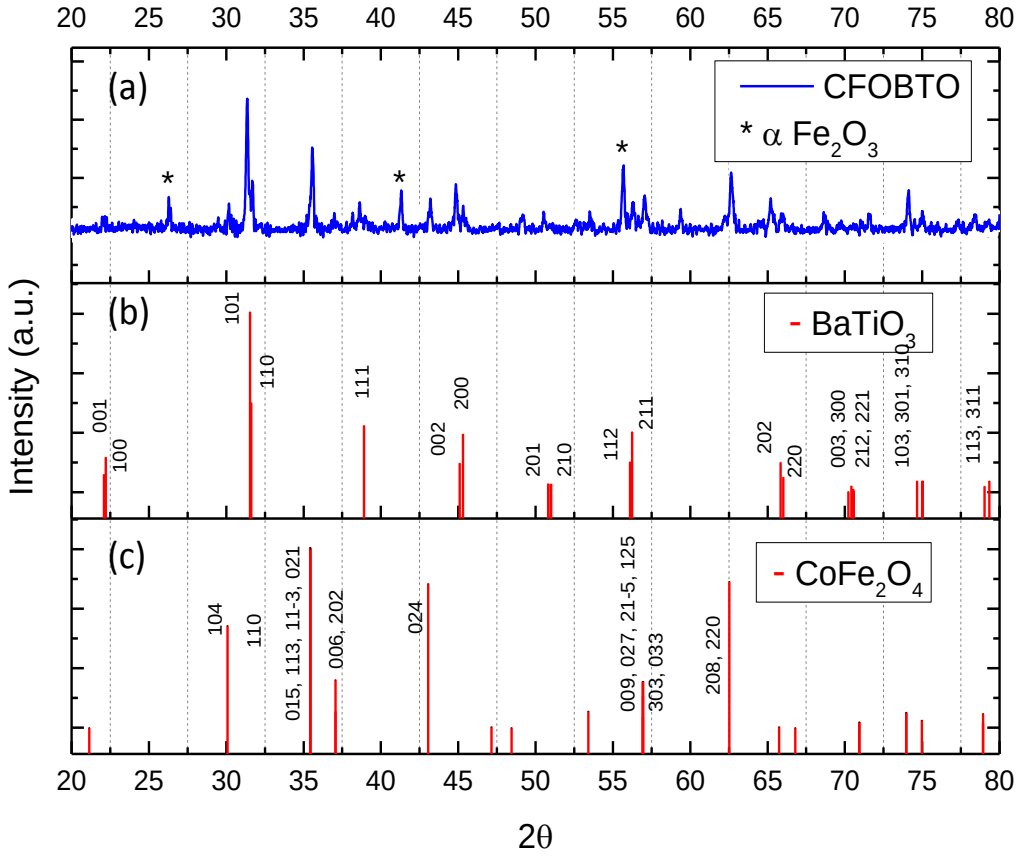

Figure 3.3 XRD pattern (a) corresponding to CFO – BTO (40/60) sample, along with standard peaks for (b) BTO [157], and (c) CFO [160].

Apart from this, the diffraction pattern showed traces of impurity phases which could only be associated to α-Fe_2O_3 which is likely to have been incurred from the starting material. α -Fe_2O_3 as an impurity phase is often found in several ferrite systems, synthesized via conventional ceramic processing route [91, 93].

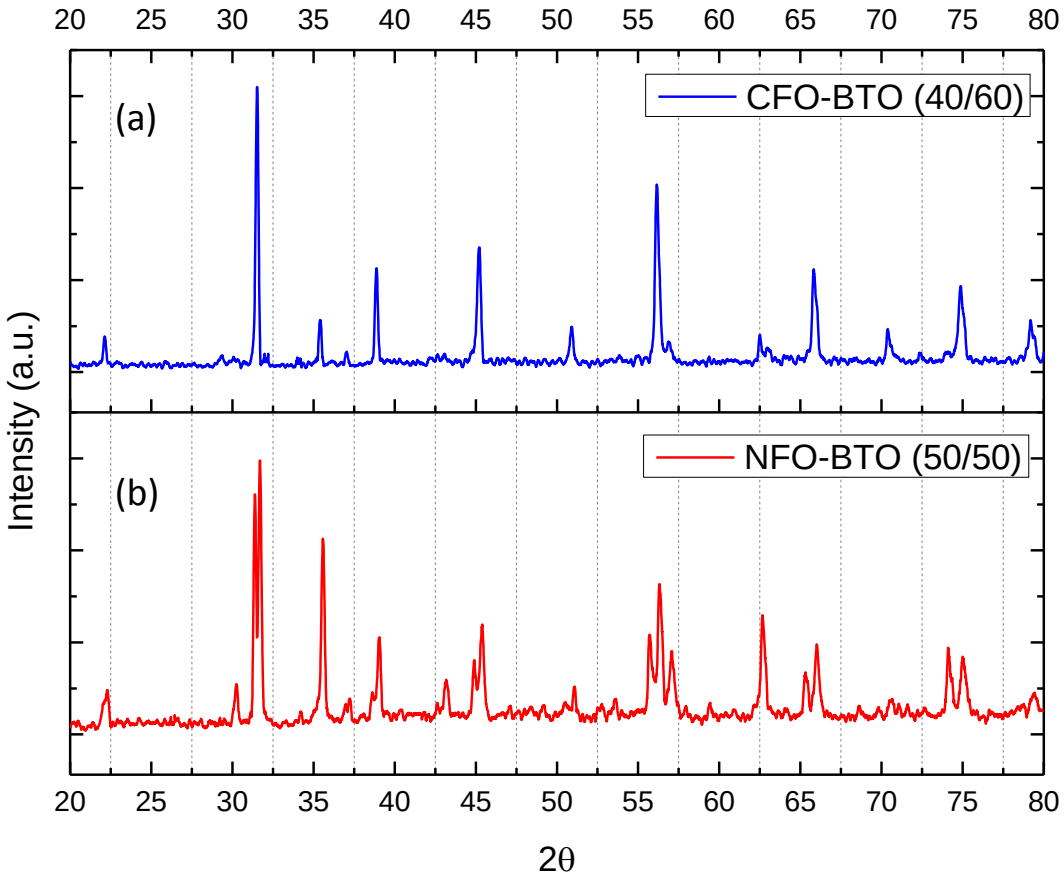

Figure 3.4 XRD patterns corresponding to (a) CFO – BTO (40/60) and (b) NFO – BTO (50/50) samples synthesized via organosol route.

In addition to this particular CFO-BTO sample, which is rigorously studied in the current thesis, two other CFO based compositions are peripherally studied, which were synthesized via a different route (organosol process), and have already been well characterized as reported in literature [39]. Figure 3.4 shows the diffraction patterns related to the organosol synthesized compositions. It can be seen that as the CFO volume fraction increases from the 40/60 to 50/50 composition, the peak intensity distribution also changes proportionally. As compared to the pattern related to the powder processed CFO-BTO sample (Figure 3.3), those corresponding to the organosol based CFO-BTO systems show a stark difference in their peak intensity distribution. As an example, the peak corresponding to the CFO 208/220 planes is stronger in the powder processed CFO-BTO (40/60) systems as compared to the same in organosol processed (40/60) sample. This cannot just be associated with any possible variation in volume fraction; rather it has to do with the differences in the statistical distribution of the grains, which effectively contributes to the diffraction cross section. In other words, the samples which are a priori expected to be having a homogeneous microstructure are found to be having different microscopic morphologies within a common macroscopic boundary. Different parts of the sample may possess different distributions of the phases coupled with certain preferences in

grain orientation, hence slightly deviating from the presumption of a completely random microstructure. This scenario will be here onwards addressed in the following text by the term *partially random microstructure.* The observed differences in the peak intensity distribution of the magnetic phase in BaM and SrM based samples (Figure 3.1 and Figure 3.2) also point towards a relatively more partial random microstructure for the BaM based sample as compared to that in the SrM based sample.

3.1.4 $NiFe_2O_4$-$BaTiO_3$

The NFO-BTO (50/50) diffraction pattern (Figure 3.5) reveals a distribution of peak intensity corresponding to BTO and NFO phases which is apparently proportional to their respective volume fraction. Similar to the diffraction pattern of the powder processed CFO-BTO, in the case of NFO-BTO also the ratio of peak intensities of BTO and CFO is smaller as compared to that in the BaM-BT/SrM-BT samples. However since the proportion of the NFO and BTO is different as compared to the CFO-BTO sample, the diffraction pattern (Figure 3.5) reflects an even distribution of the peak intensity corresponding to the NFO and BTO phase. Similar to the powder processed CFO-BTO (40/60) sample, diffraction patterns of the NFO-BTO (50/50) sample also showed traces of impurity phases which could only be associated to α-Fe_2O_3, likely to have been incurred from the starting material.

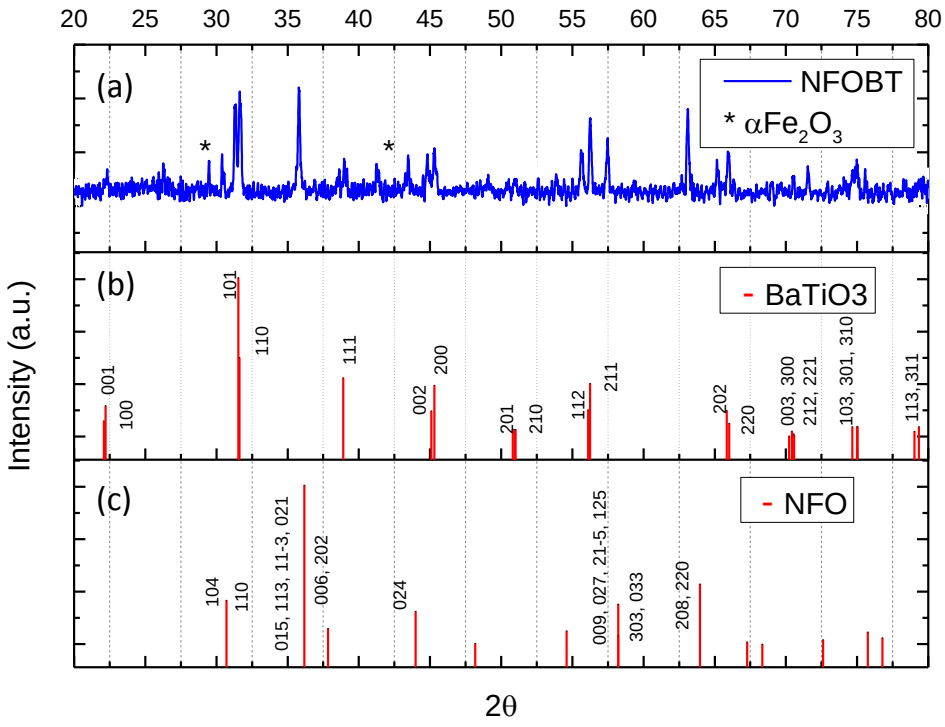

Figure 3.5 XRD pattern (a) corresponding to NFO-BTO (50/50) sample, along with standard peaks for (b) BTO [157], and (c) NFO [161].

3.2 Microstructural Characterization

The microstructural features of interest in the present case of magnetoelectric composites are the distributions of their constituent ferroelectric/ferrimagnetic phases along with their corresponding grain size distributions. Microstructural characterization can also give an idea of the connectivity schemes of the constituent phases. All these aspects are crucial in determining not just the macroscopic ME-effect but also the local manifestations of the same, as will be discussed in the next chapters. The studied samples were initially investigated by SPM, to get an idea of the distributions of the ferroic domains and hence a first glance at the phase distributions. Some of the samples were more rigorously characterized by mapping local chemical characteristics via correlated Scanning Confocal Raman Microscopy and SPM. The key compositions were also studied for their grain size distribution using the EBSD technique.

3.2.1 Scanning Probe Microscopy Characterization

Correlated PFM and MFM imaging, along with simultaneous topography acquisitions were performed on all the studied samples. The almost mutually conjugative nature of PFM and MFM active regions corresponding to identical spots on various compositions, is considered as a necessary condition for distinction between the ferroelectric and ferrimagnetic phases, since the ferrimagnetic phase is not expected to show any local displacements in response to the tip induced AC electric field, and likewise the ferroelectric phase cannot show any magnetic interactions in MFM images.

SPM images corresponding to the BaM-BTO and SrM-BTO compositions (Figure 3.6), clearly reveals the juxtaposition of the MFM and PFM active regions, simultaneously correlated with topography (as referenced by the marked regions). This suggests a microstructure where partial agglomerates of the ferroelectric and ferrimagnetic phases are randomly distributed, with a sharp interface dividing them. As can be seen in Figure 3.6, the phase distribution is stochastic with both phases exhibiting partly landlocked (0-3) as well as continuous (3-3) connectivity scheme. Hence it is difficult to generalize the phase distribution under a single connectivity schemes, hence it will be termed as a mix of 3-3 and 0-3 schemes. Simultaneously, it can be seen that the BaM-BTO sample shows a higher degree of agglomeration as compared to the SrM – BTO sample, which in other words means that the BaM-BTO sample has more of a partially random microstructure as compared to the SrM-BTO sample. This is also corroborating the corresponding arguments made from the XRD patterns (section 3.1.3).

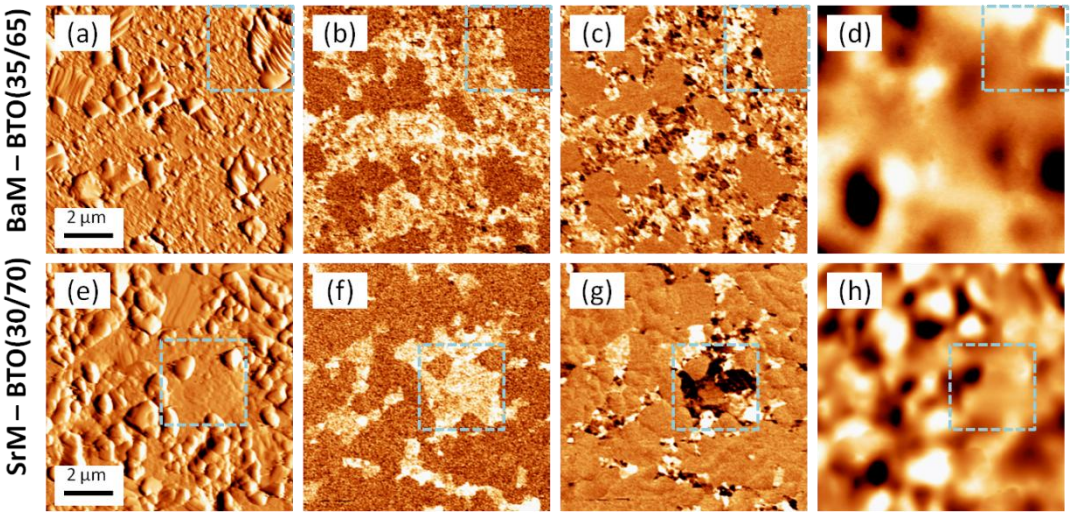

Figure 3.6 Shows SPM images corresponding to BaM-BTO (35/65) (a)-(d) and SrM-BTO (30/70) (e)-(h) comprising of (a)/(e) topography (deflection), (b)/(f) Vertical Piezoresponse (A·cosϕ), (c)/(g) lateral piezoresponse (A·cosϕ), and (d)/(h) MFM (phase signal) images. The images pertaining to each sample were acquired on an identical spot. The regions marked with cyan square shows the correlated features as a reference for visualizing the identity of the spots. The PFM active region in (b)/(e) as well as (f)/(g) are partially apparently inactive in the MFM images (d) and (h) respectively, highlighting a juxtaposition of the FE and FM phase/grains.

The PFM images for both systems show rather weak vertical while a strong lateral response, which simply follows from the fact that the orientation of the polar axis and hence the grain orientations of the ferroelectric phase lies mostly inclined to the sample surface, and is randomly distributed. The VPFM signal is highly unipolar, on the contrary the LPFM signal shows both negative and positive contrasts, highlighting the existence of a preferred polarization direction for the FE agglomerates, or in other word self-polarization exists in the samples.

Similar analysis on the spinel based systems (Figure 3.7) yields slightly different conclusions. Even though a complex mutual conjugation of PFM and MFM contrasts is visible, the polygonal nature of the interfaces indicates a higher grain level mixing of the two phases, unlike the partial agglomerate type distribution in the case of the hexaferrite based systems. In other words the CFO/NFO and the BTO grains juxtapose each other with a slightly lower degree of agglomeration. However, at least in the case of the CFO-BTO (60/40) sample, agglomerated phase distribution was also found at certain specific locations on the sample surface, which makes it a *partially random microstructure*. This was however not the case upon further investigation on the NFO-BTO (50/50) sample.

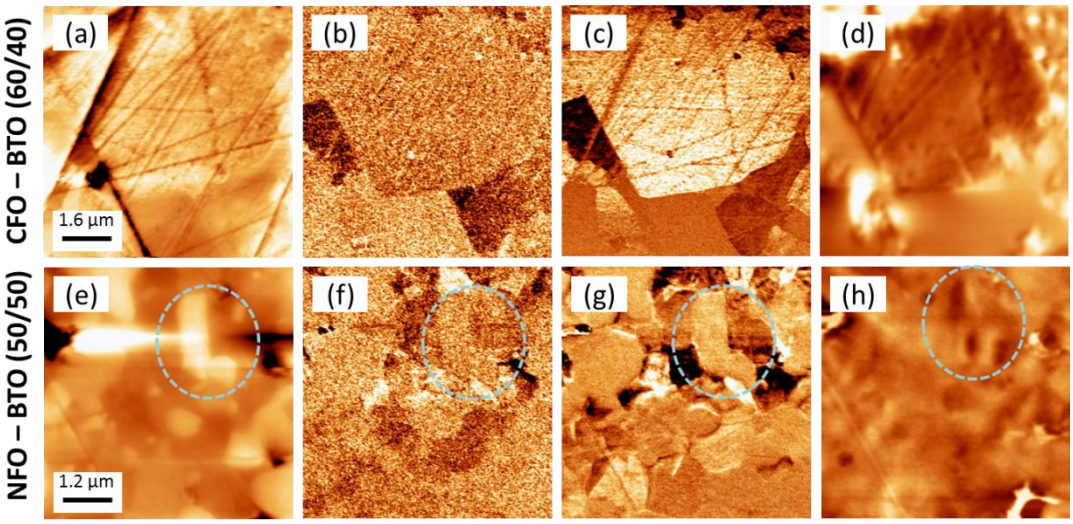

Figure 3.7 Shows SPM images corresponding to CFO-BTO (40/60) (a)-(d) and NFO-BTO (50/50) (e)-(h) comprising of (a)/(e) topography (deflection), (b)/(f) Vertical Piezoresponse (A·cosϕ), (c)/(g) lateral piezoresponse (A·cosϕ), and (d)/(h) MFM (phase signal) images. The images pertaining to each sample were acquired on an identical spot. The regions marked with cyan circle shows the correlated features as a reference for visualizing the identity of the spots. The PFM active region in (b)/(e) as well as (f)/(g) are partially apparently inactive in the MFM images (d) and (h) respectively, highlighting a juxtaposition of the FE and FM grains

Apart from the phase distribution of the spinel based systems, their piezoresponse is found to exhibit clear multipolar vertical as well as lateral components, which is in contrast with the case of hexaferrite based systems. This signifies that FE regions in the CFO/NFO-BTO systems are randomly polarized, without any effective virgin polarization, unlike the case of hexaferrite based systems where there is a self-polarization of the virgin state. This issue will be addressed as and when the key characteristics of these samples evolve over the course of this chapter. Unlike the piezoresponse, the MFM images of both systems show a bigger difference in their magnitudes. The MFM signal for CFO-BTO sample shows much stronger magnetic interaction as compared to that of the NFO-BTO sample, which simply follows from the fact that the saturation magnetization of NFO is almost 63% of that of CFO [91].

Unlike the powder processed CFO – BTO sample, the organosol processed CFO-BTO compositions show completely different morphologies. As can be seen from Figure 3.8 and Figure 3.9, the phase distribution in the organosol processed samples is highly agglomerated, with almost 0-3 type of connectivity scheme. This can be understood by taking into account the core-shell nature of the starting materials used in the organosol synthesized samples. The core-shell particles (a few 100 nm wide CFO nanoparticles form the core covered with a 50 nm thick BTO shell [143]), which are sintered to obtain the ceramic samples, tend to maintain the isolation of the CFO particles while the highly reactive nanocrystalline BTO layer tends to agglomerate with the adjacent BTO shells. Similar argument is also valid in the case of the hexaferrite systems, especially the BaM-BTO sample, where the starting BTO powder was controlled to be in the nano range, leading to an end product with highly agglomerated BTO

grains, whereas the hexaferrite phase for which the processing parameters were specifically controlled, undergoes lower agglomeration, leading to a mix between 0-3 and 3-3 type or in other words far from core-shell type connectivity scheme in the hexaferrite based systems.

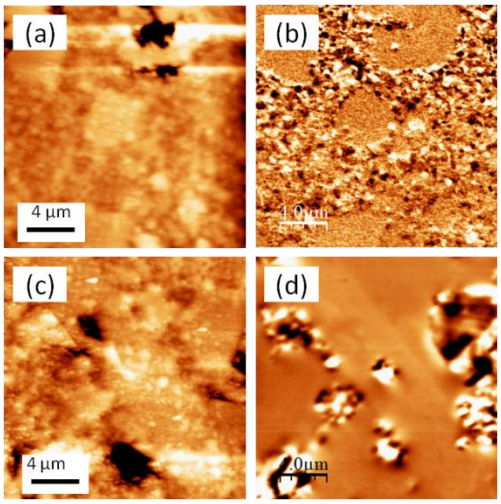

Figure 3.8 Shows topography (a)/(c), lateral piezoresponse (A·cosϕ) (b) and MFM (phase signal) (d) images on the organosol synthesized CFO-BTO(50/50) sample. The topography images (a) and (c) correspond to two different spots of acquisition for the PFM and MFM images, respectively. Overall the low roughness regions visible in the topography images correlate with the MFM active and PFM inactive regions in the respective MFM and PFM images, highlighting a correspondence to magnetic phase. Likewise the high roughness regions correspond to the ferroelectric phase.

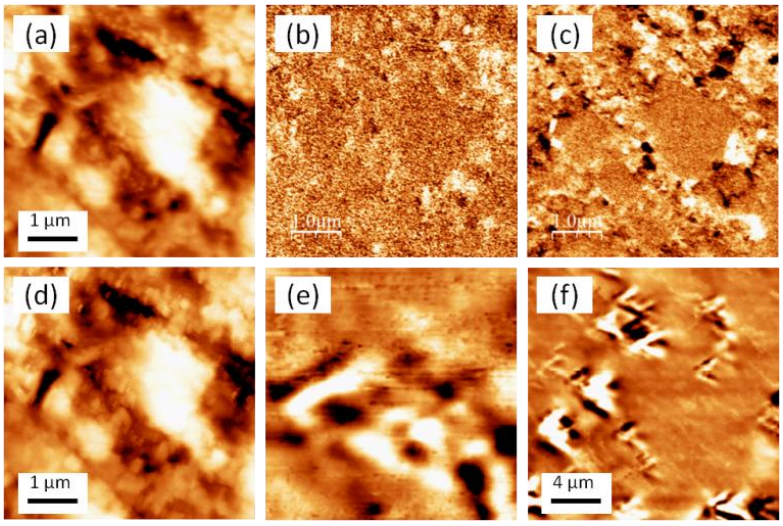

Figure 3.9 Shows topography (a)/(d),), vertical piezoresponse (A.cosϕ) (b),lateral piezoresponse (A·cosϕ) (c), and MFM (phase signal) (e) image corresponding to an identical spot on the organosol synthesized CFO-BTO (40/60) sample. The topography images (a) and (d) were simultaneously acquired during the PFM and MFM acquisitions respectively. (f) shows a higher scale MFM image at a different spot on the same sample, highlighting the distribution of magnetic regions.

A bleak idea of the constituent phase distribution in the studied samples could be obtained from the SPM images. However there is a need to sufficiently validate these distributions in terms of the actual underlying characteristic of the constituent phases, since SPM imaging is prone to cross-talk from even a non FE phase like BaM. For that matter the data-set from the Scanning Confocal Raman Microscopy, which was principally utilized to probe the local ME effect, can be considered in correlation with the SPM acquisition as a powerful reference sufficient for validating the phase distributions inferred from the SPM characterization. Raman spectroscopy is a tool which is sensitive to the chemical or structural features of the constituent phases, in other words a mapping of the Raman spectra over a spatial grid will yield the information about the distribution of the constituent phases in terms of their structural signatures. Figure 3.10 shows the data-set extracted from the CRM acquisition carried out on the BaM-BTO sample, using a specifically tailored statistical algorithm (to be discussed in later chapter 6). It shows a strong correlation between the distributions of the BTO phase and the corresponding PFM image. This corroborates the phase distribution studies carried out using SPM. Considering the identicalness of the BaM and SrM based sample, the phase distribution analysis provided above can also be extended to the SrM-BTO sample.

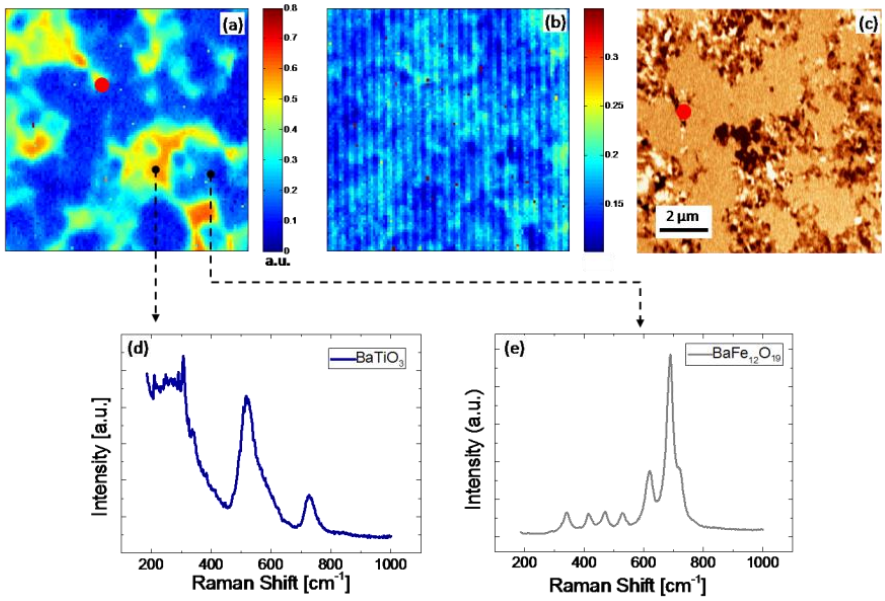

Figure 3.10 Shows concentration map (score maps) for BTO phase, extracted from the acquired CRM data set on the BaM-BTO (35/65) sample (chapter 7)(a), along with the corresponding lack of fit map (b), lateral PFM image of the same area (red dot) (c), and the extracted components/spectra corresponding to BTO (d) and BaM (e) phase.

Similar acquisition and analysis were also carried out on the powder processed spinel based systems; CFO-BTO (60/40) and NFO-BTO (50/50) (Figure 3.11).Here also, at least in the case of the CFO-BTO sample, it can be concluded that a good correlation between the SPM acquisition (PFM) and the actual chemical/structural character exist. Despite the absence of a correlated

PFM image in case of NFO-BTO sample the argument of correlation can be extended to it with confidence, taking into account the fact that the CFO and NFO based samples should share analogous experimental outcomes considering their identical structural (XRD) and morphological features.

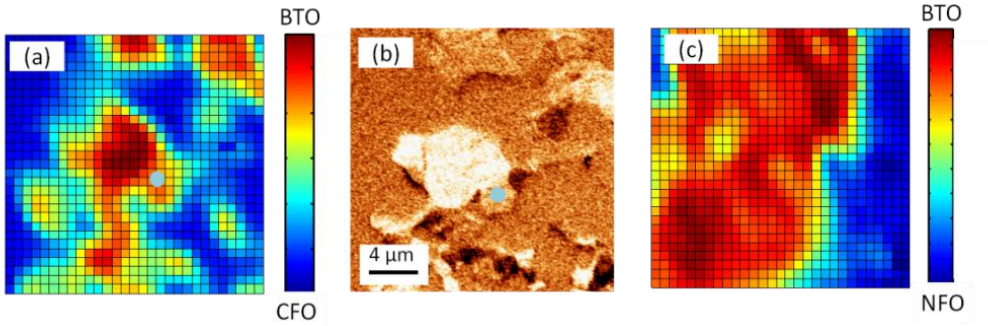

Figure 3.11 Shows concentration map (Score maps) for BTO phase, extracted from the acquired CRM data set (Chapter 7) (a),and the corresponding lateral piezoresponse image (cyan dot for reference) for the CFO-BTO (40/60) sample. (c) shows a similar BTO concentration map for the NFO-BTO (50/50) sample.

3.2.2 Grain Texture Investigations

Further microscopic investigations on the key composition, were carried out in the direction of obtaining precise information about their grain size distribution and grain orientation. For that matter, a conjunction of EBSD and SPM was utilized. The corresponding results are cross compared in terms of their corroborating features, and the outcomes are concisely discussed in this section.

In the hexaferrite based systems, unlike the spinel based systems, the distribution of grains was only partially visible in the SPM results. Hence thermal etching was carried out, in order to enhance the grain boundaries in SPM. An etching temperature of 1000^{o} C (85% of the sintering temperature, 1200^{o} C) was chosen, at which the hexaferrite based compositions dwelled for a time period of 30 minutes. Figure 3.12 shows the SPM images corresponding to the etched samples of the hexaferrite based systems. It can be seen that the BaM-BTO sample shows a larger dispersion between the average gain sizes of the BaM (~1µm) and the BTO (~200 nm) phase. On the other hand, the SrM-BTO samples do not show any dispersion, with the grain size pertaining to both centered around 1µm.

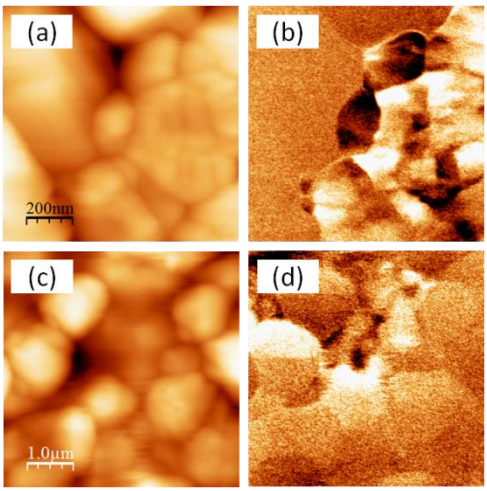

Figure 3.12 Shows pairs of topography/lateral-piezoresponse images corresponding to the BaM – BTO (35/65) (a)/(b) and the SrM – BTO (30/70) samples.

Figure 3.13 shows the EBSD images pertaining to the key samples; BaM-BTO, SrM-BTO and CFO-BTO, along with their corresponding maps of EDX intensities for Ti and Fe. It can be seen that the EBSD images are noise dominated, in other words the corresponding Kekuchi patterns are only weakly identified. EBSD is highly sensitive to surface conditions [162]. Hence, even though the samples used for EBSD acquisition, unlike the thermally etched samples, were finely polished, some amount of unevenness in the surface is inherently unavoidable, due to the existence of nuances in material removal rate on the constituent phases. However, fairly decent observations regarding the grain size distribution in the BTO phase (marked within the white boundaries) along with the grain orientation can be made. It can be seen from Figure 3.13 that the grain size distributions correlate with the EDX elemental maps which provides a concrete chemical distinction between the two phases. Also the EBSD images stand in good agreement with the grain size distribution as seen in the SPM images of the etched samples (Figure 3.12) for the hexaferrite based system. On the other hand the CFO-BTO sample shows grain sizes that are more evenly distributed amongst the two constituent phases. Also this distribution correlates to some degree with the PFM images pertaining to the CFO as well as the NFO based samples (Figure 3.7).

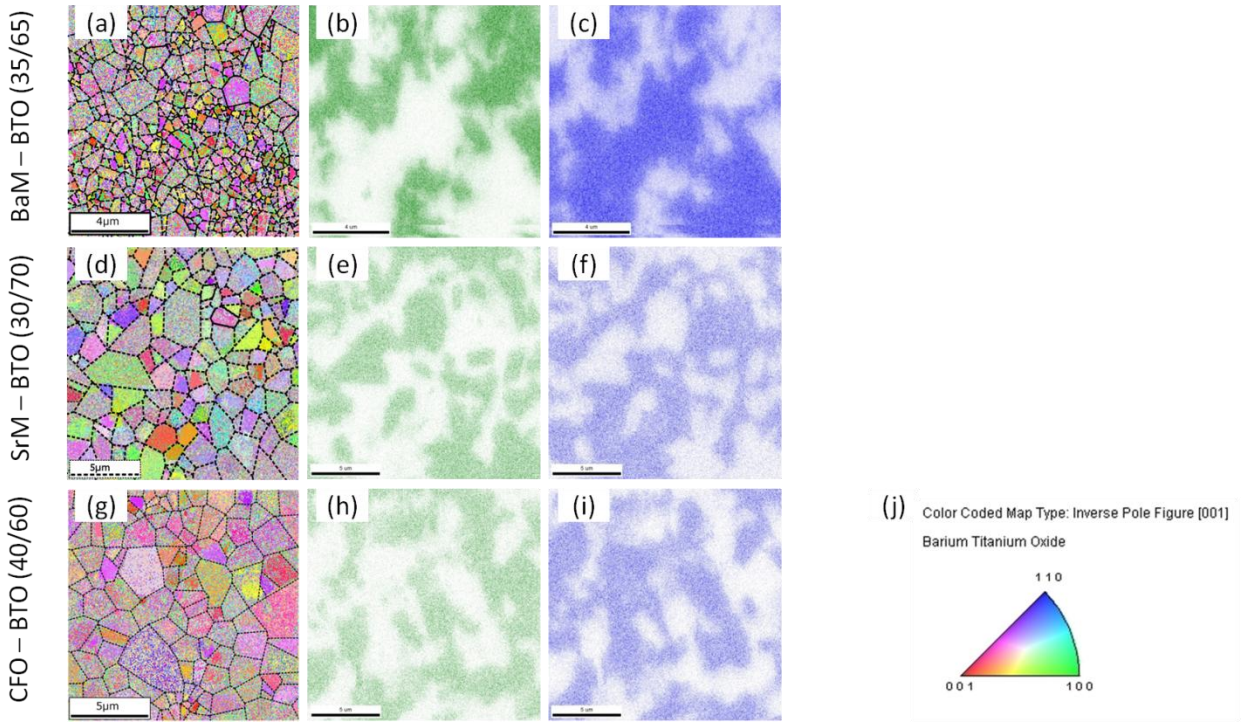

Figure 3.13 Shows the EBSD images representing the orientation of both BTO and the respective magnetic phases for the (a) BaM-BTO, (d) SrM-BTO, and (g) CFO-BTO samples along with the respective EDX elemental maps for ((b), (e), (f)) Fe and ((c), (f), (i)) Ti (The bright contrasts in each case correspond to higher element concentration and vice versa). (j) is the pole figure colormap corresponding to the BTO orientation marked in the EBSD image. The dashed lines (black) in (a), (d), and (g) are marking apparent grain boundaries.

As far as grain orientation of the BTO phase is concerned, it can be seen from Figure 3.13 that a majority of the color contrast in case of the BaM-BTO sample belongs to pink and yellow regions of the EBSD colormap, which represents out of surface orientations parallel to the (111) and (202) directions respectively. On the other hand the orientation maps SrM-BTO sample, contrast with red, orange and yellow-green shades, which correspond to the orientations close to ⟨002⟩, ⟨202⟩, and ⟨100⟩ respectively. Inferring from the directional dependence of the longitudinal piezoelectric coefficient d_{33} (Figure 1.10), the highly grainy nature of the vertical piezoresponse in the BaM-BTO sample (Figure 3.6) can be understood; the grain orientations in this case is such that there is a significant grain to grain variation of d_{33}, ranging from the maximum {(111)} to moderate values. On the other hand the SrM – BTO is not expected to have such discontinuities, as there exist no big difference between the d_{33} for the preferred grain orientations along the ⟨100⟩, and ⟨110⟩, directions. Interestingly SrM – BTO shows a fairly homogeneous vertical piezoresponse (Figure 3.6f). The grain orientations in case of the CFO – BTO sample are identical to those in case of the BaM – BTO sample, with dominating pink and yellow shades; in other words the orientations along⟨111⟩, and ⟨202⟩, directions are dominating. This is once again reflected in the PFM image corresponding to the CFO-BTO sample (Figure 3.7) in the form of big grain to grain differences in the piezoresponse. Due to the

microstructural similarities between the CFO and the NFO based samples, the grain orientation analysis made for CFO – BTO sample are hypothetically extrapolated to the NFO – BTO sample, which due to its unfavorable surface condition could not be investigated using EBSD.

3.3 Electrical and Dielectric Properties

The electrical characteristics of the composite samples is theoretically a combined contribution of both phases however since the magnetic phase is most often highly conducting, providing a mobility path to charges (short circuit), part of the contribution from the insulating BTO phase will be highly nullified. The ferrites (BaM, SrM, CFO, and NFO) are known to be low band gap semiconductors [91]. The key conduction mechanism in ferrites is of hopping type with the mixed valent Fe^{+2} and Fe^{+3} acting as hopping sites. Structurally and energetically ferrites are not expected to be conducting however it is only during the synthesis process that any deficiency or excess of iron leads to the mixed valency and hence a conducting phase [93]. Between each ferrite systems there exist differences in room temperature resistivites depending upon the structural ease in activating the electron hopping process. Normally it is found in literature that the hexagonal ferrites (BaM, and SrM) are known to have lower room temperature resistivites as compared to the spinel systems.

Table 3.1 DC resistivities of the studied samples, at ambient temperatures.

Sample	Resistivity
SrM – BTO (35/65)	180 Ω·m
BaM – BTO (30/70)	350 Ω·m
CFO – BTO (40/60)	5 MΩ·m
NFO – BTO (50/50)	30 MΩ·m

Table 3.1 lists the DC resistivities measured on the key samples, in an increasing order of their values. The resistivites of the hexaferrite based composites are in good agreement with the literature values of (2×10^2 Ω·m) of the constituent hexaferrite systems [93, 163–165], which is indicative of short circuiting of the ceramic through the magnetic phase. The trend in the resistivites of the spinel based systems are also in good agreement with literature values for CFO [55, 91, 166, 167] as well as NFO [91, 168–172] phases, with the NFO based system having higher resistivity as compared to the CFO based system.

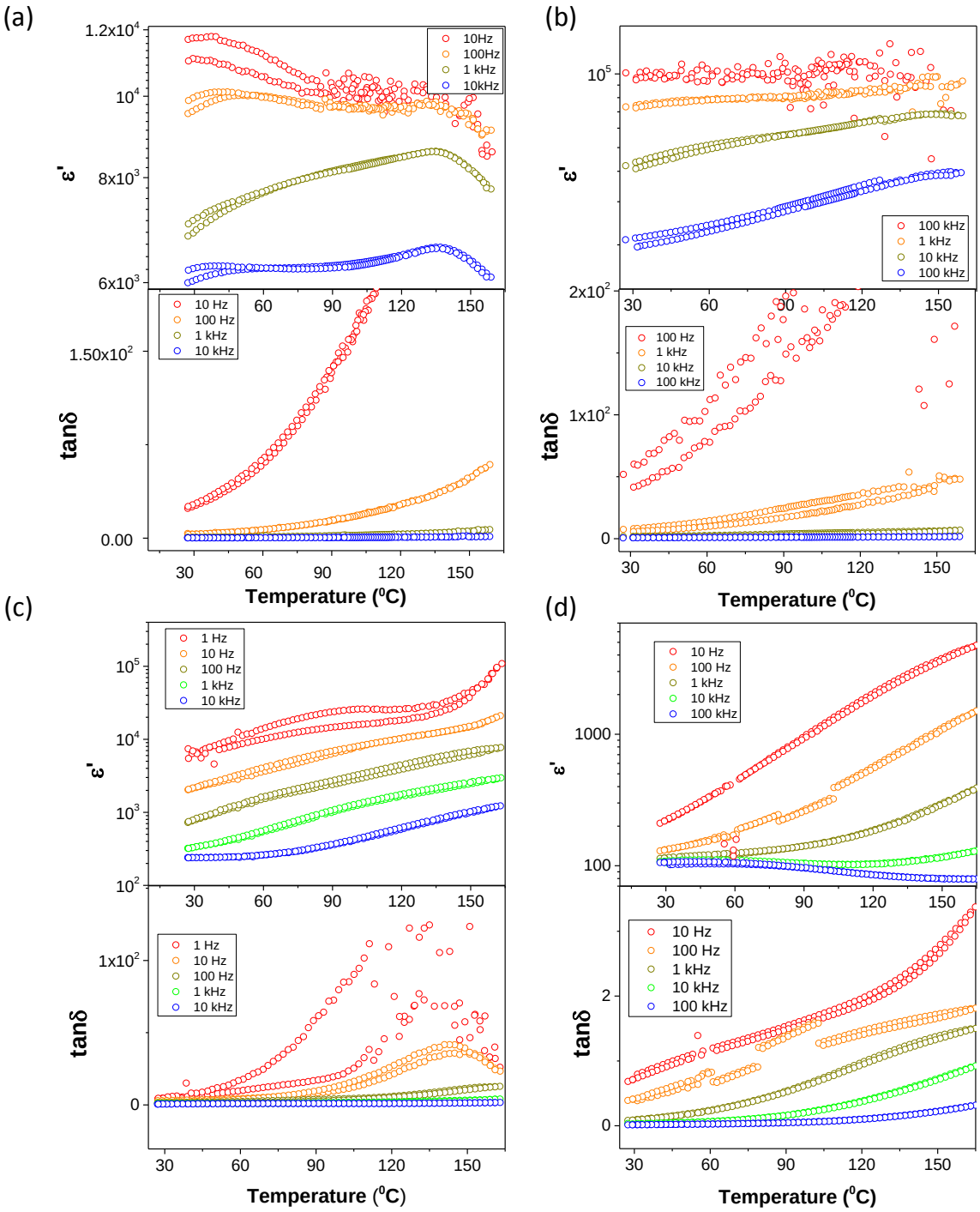

Figure 3.14 Shows logarithm of real permitivitty (upper frame) and dielectric loss; tanδ (lower frame) for BaM – BTO (35/65) (a), SrM – BTO (30/70) (b), CFO – BTO (40/60) (c), and NFO – BTO (50/50) (d) samples [Measurements courtesy to Yanling Gao, Vladimir Shvartsman, and Naveed-Ul-Haq].

Temperature dependent dielectric spectroscopy was carried out on these samples, to highlight the nuances in their macroscopic dielectric behaviour. Figure 3.14 shows the real part of dielectric

permittivity and dielectric loss (*tanδ*) as a function of temperature, for the studied samples. It can be seen that the hexaferrite based systems show high losses which increase with temperature, and simultaneously decrease with increasing frequency. Coupled with this, the unusually high dielectric values, specifically at lower frequencies, indicate a dominating transport contribution to the real permittivity. In effect, this also points toward a higher transport dominated contribution of the magnetic phases. Although in case of BaM –BTO sample, a slight hump close to the BTO cubic-tetragonal transition temperature (120^0 C) can be seen at higher frequency. This is indicative of a modicum of dielectric contributions from the BTO phase. However, this is not the case in the SrM – BTO sample which has higher conductivity as compared to the BaM – BTO sample. In case of the spinel based systems, lower dielectric losses as compared to the hexaferrite systems are seen, with the losses in CFO – BTO sample being higher as compared to the NFO – BTO system following their respective resistivity trends. Behaviour of the losses as well as the real permittivity, as a function of temperature and frequency, are identical to those in case of the hexaferrite based systems. This is once again indicative of the higher conductivity contribution to the real part of dielectric permittivity, and losses (through the magnetic phases). Interestingly, the low frequency curve of the real permittivity of the CFO – BTO sample shows a hump close to the BTO Curie temperature (120 ^{0}C) indicative of the cubic –tetragonal phase transition, which flattens with increasing frequency. This behaviour is actually opposite to what could be expected, an increasing polar dielectric response with increasing frequency. Hence the observed behaviour cannot be associated to the FE phase transition in BTO. This anomaly can be reasonably attributed to thermally activated conductivity, which should apparently be higher at low frequencies, as observed.

3.4 Magnetic Characterization

The magnetic characteristics of the composite samples are crucial in not just determining the magnetostriction in the studied sample, but also to characterize the magnetic state itself, which can in turn indicate any possible secondary effects on the magnetic phase caused due to a completely different residual stress environment. Figure 3.15a compares the M(H) hysteresis loops obtained on the studied systems. It can be seen that in case of the hexagonal ferrite based system, the remanent magnetization is at the same level for both systems (with equivalent weights), which can be easily understood considering the identical volume fractions of the magnetic constituents. Apart from this, the coercivities for BaM and SrM based composites are found to be of the order of 0.35 T and 0.2 T respectively. These values are in good agreement with literature [91, 173–178], and they also represent the theoretical nuances in the magnetocyrtalline anisotropy of the two systems. On the other hand, the coercivity of the CFO and NFO based composites (Figure 3.15b) also very well reflect the difference in the respective magnetocrystalline anisotropy, with the NFO based sample showing a softer MH loop as compared to that of the CFO based sample. However, it has to be noted that the higher value of remanent magnetization in the NFO based composite is only due to the fact that the volume fraction of NFO is higher as compared to the CFO volume fraction in the CFO based sample. Otherwise it is expected that the absolute magnetization of the CFO phase has to be higher as

compared to the NFO phase, which is actually observable from the concerned MFM images (Figure 3.7h).

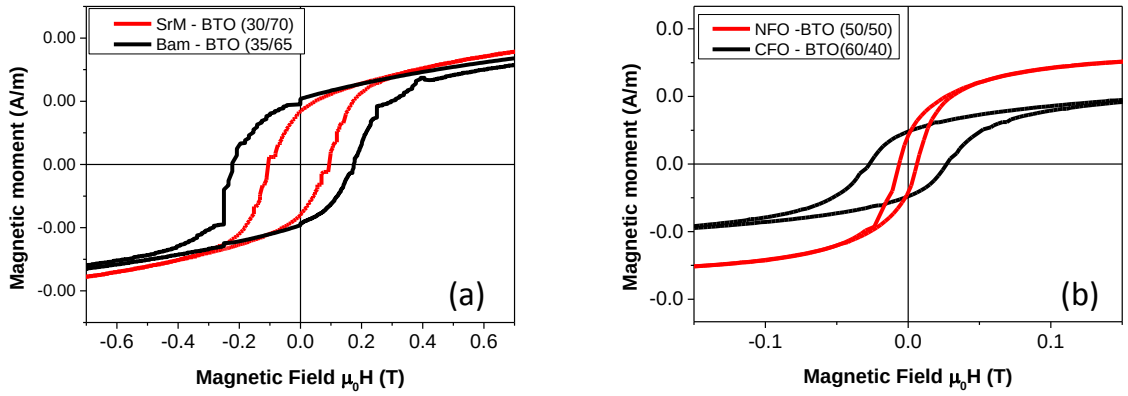

Figure 3.15 Shows MH loops corresponding to the hexaferrite (a), and the spinel (b) based systems. The saturation in both the graphs has been clipped to enhance the loop width [Measurements courtesy to Ahmadshah Nazrabi, and Soma Salamon].

The temperature dependence of magnetization (Figure 3.16a, b) for the hexaferrite based systems shows an identical magnetic transition temperature of about 700 K, which is close to the literature value of about 723 K and 733 K for BaM and SrM respectively. On the other hand the spinel based systems also show magnetic transition at temperatures which are characteristic to the respective magnetic phase with the CFO based sample having a transition temperature of 507 ^{0}C (literature value 520 ^{0}C [91]) and the NFO based sample showing a transition at 587 ^{0}C (literature value 585 ^{o}C [91]). The closeness of the transition temperatures confirms the typical ferrimagnetic characteristic of the concerned magnetic phases, without any other exchange interaction being active. There exists a huge thermal hysteresis in the hexaferrite based composites. Such a hysteresis appears due to the fact that during the heating cycle, the applied field (0.1 Tesla), which is lower than the corresponding coercive fields, is unable to magnetize the samples significantly. On the other hand, while cooling from the higher temperature, the already lowered coercivity of the samples allows generation of a relatively higher magnetization, which only further increases with decreasing temperature (field cooling). This observation is validated by the behavior of the spinel based composites (Figure 3.16c, d), where the thermal hysteresis was smaller, attributed to the fact that the applied field of 0.1 T is much larger than the corresponding coercivities. The NFO based composite which has the softest magnetic hysteresis, consequently show almost no hysteresis

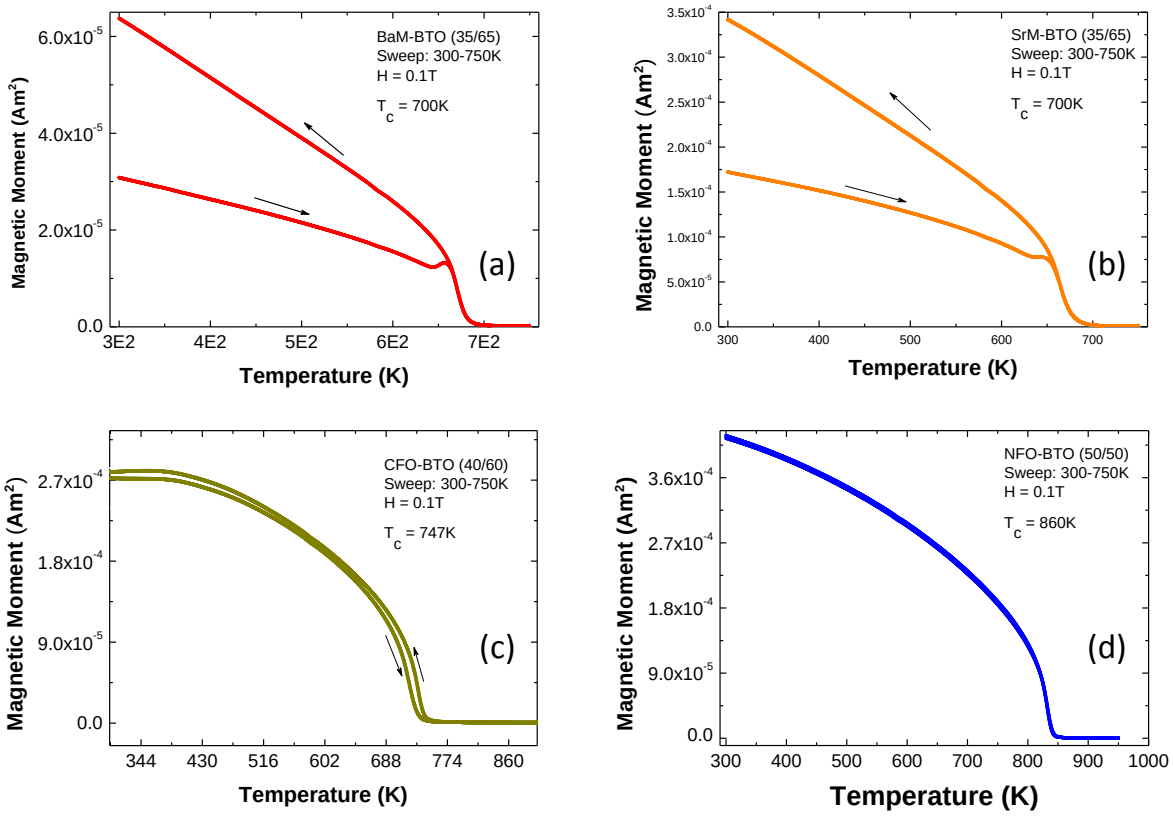

Figure 3.16 Shows magnetic moment Vs. temperature curves for BaM – BTO (35/65) (a), SrM – BTO (30/70) (b), CFO – BTO (40/60) (c), and NFO – BTO (50/50) (d) samples. The arrows represent curve sections corresponding to the heating and cooling cycles [Measurements courtesy to Soma Salamon].

3.5 Magnetoelectric Coupling

The direct magnetoelectric effect was measured on the key compositions, using the standard lock-in method [179]. A DC bias of 800 – 900 kOe was applied over an AC magnetic field which was varied from 0 – 20 Oe All the measurements were done at a constant AC field frequency of 200 Hz, in a transverse configuration (α_{E31}), where the open circuit ME voltage is measured perpendicularly to the applied magnetic field. Figure 3.17 shows the comparison of the AC field vs ME voltage along with the measured ME voltage coefficient for the key compositions. The extremely small coupling values of 0.02 mV/cm.Oe for the hexaferrite based composition can be very well associated with their extremely high RT conductivity. A higher conductivity will not allow appearance of ME induced voltage at the electrodes due to the extremely high overall conductivity. The trend in the resistivity for all the samples seems to be tightly followed by the respective trend in the ME coupling. As a consequence of this the spinel based systems which show higher resistivity simultaneously show higher ME coefficient. Interestingly the ME coefficient for NFO-BTO despite its weaker bulk magnetostriction response (Figure 3.17 ; inset) is slightly higher as compared to that of the CFO-BTO sample. This can be

attributed to the higher NFO content in the corresponding sample coupled with a higher resistivity.

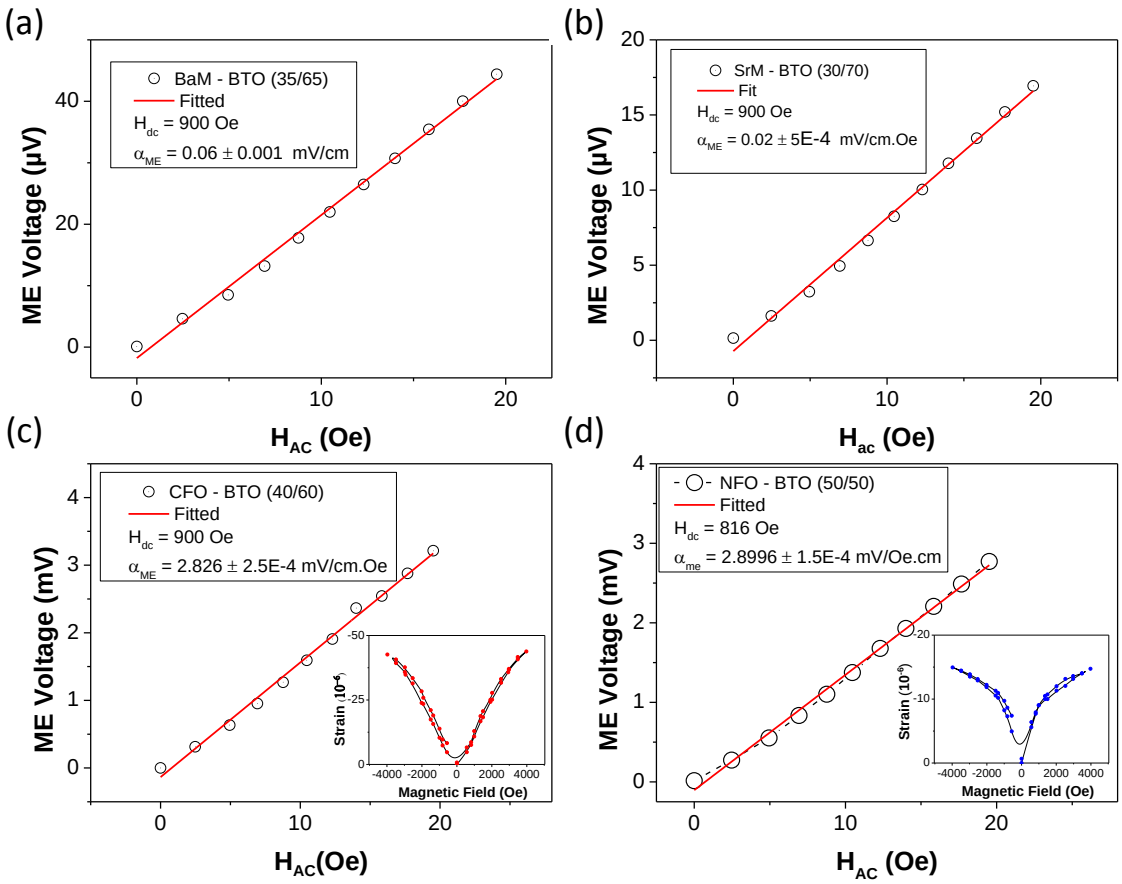

Figure 3.17 Shows ME voltage VS applied AC magnetic field for BaM – BTO (35/65) (a), SrM-BTO (30/70) (b), CFO-BTO (40/60) (c), and NFO-BTO (50/50) (d) samples.

3.6 Conclusion

All studied samples showed a wide distribution of microstructures as well as macroscopic properties. These nuances are apparently a consequence of the underlying processing parameters. However, they are important to be taken into account irrespective of their synthesis route, as the explanations concerning the investigations of local phenomena carried out in the present thesis will need a supplementary knowledge of the microstructural and the macroscopic aspects characterized. The key parameters to be considered in the present case are the microstructural aspects and the overall electrical characteristics of the studied samples. Figure 3.18 schematically classifies the studied samples in terms of the respective FE-FM phase distributions and grain size dispersion, along with their electrical resistivity trends and interface quality. As observed in the microstructural characterization the powder processed spinel based samples show a higher resistivity and simultaneously a higher degree of grain mixing. On the other hand the hexaferrite

based samples which are highly conductive, show a mixed degree of agglomeration with the SrM based sample slightly more mixed in terms of the FE and FM phases as compared to the BaM based sample. A higher degree of mixing will lead to a more homogeneously distributed magnetoelectric stresses over a semi-local scale, which due to the absence of immediate neighbor, constraints can lead to a dispersive spatial distribution of the ME parameters at the local scale. Locally, the variation of stress with fields can be different at different interfaces depending on the orientation of the grains w.r.t. to the applied field. In contrast to this a higher agglomeration will mean a highly inhomogeneous stress which is focused more at the FE-FM interface, the field dependence of which is largely homogeneous due to an aggregate response of the adjacent FE/FM agglomerates.

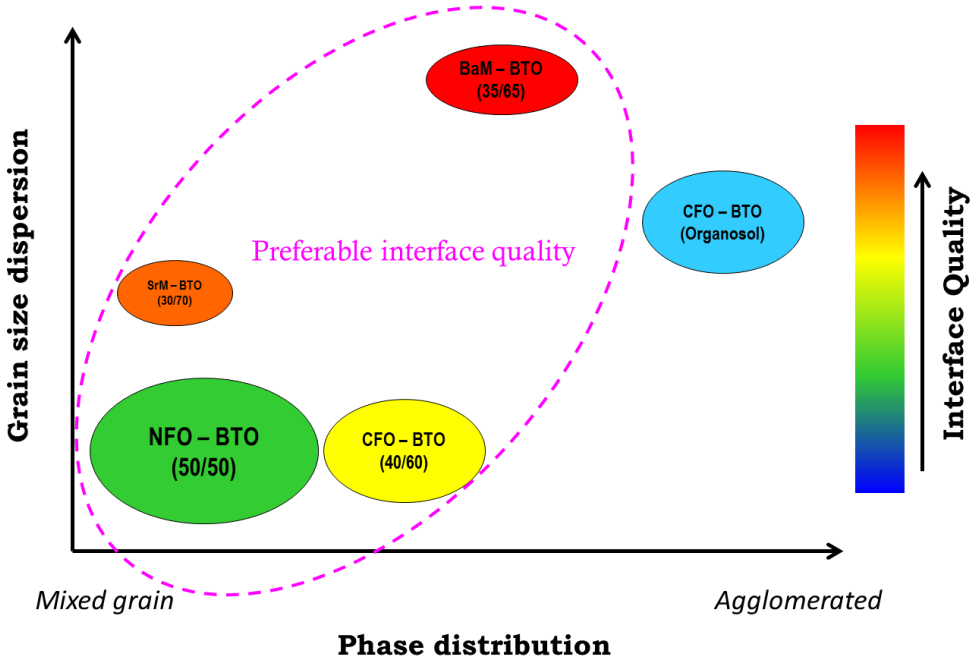

Figure 3.18 Schematically showing the phase space of the studied samples in terms of their phase distribution and grains size dispersion. The X-axis (phase distribution) shows degree of agglomeration increasing from left to right. On the other hand the Y-axis shows grain size dispersion, which refers to the difference in grain sizes corresponding to the FE and FM phases. An increasing grain size dispersion from bottom to top shows an increasing difference between the respective grain sizes. The size of the markers representing the studied samples, is fictitiously proportional to the respective RT electrical resistivity. The color of the markers is representative of the interface quality of the corresponding samples, with the quality increasing from bluish to reddish shades.

The BaM based samples show higher dispersion, with a large difference in grain size of the corresponding FE and FM phase. On the other extreme are the spinel based systems showing almost no dispersion in their respective FE/FM grain sizes, with the SrM-BTO lying in between. Apart from this, the organosol prepared CFO-BTO samples also show a large grain size dispersion similar to the BaM-BTO. However, they show a poor interface quality, and are hence

not extensively studied in the present thesis, rather just utilized for the purpose of certain qualitative analysis. A larger grain size dispersion observed is mainly associated with a smaller BTO grain size and a relatively larger BaM/CFO grain size. This means that there is a larger number of interfaces in the BTO phase as compared to the magnetic phase. As far as the converse ME effect is concerned, this large dispersion has no significance as a semi local stress distribution generated in the BTO phase in response to a macroscopically applied field will be an aggregate of individual BTO grains belonging to the neighboring aggregate with very feeble variation in the response of the magnetic phase due to their larger grain. On the other hand, in case of direct ME effect for such a sample, the stress exerted on the BTO phase will show a highly inhomogeneous distribution owing to the large number of interfaces.

These conclusions obtained from the micro/macroscopic characterizations form the basis for discussion and explanation of the local investigations in the next chapters. In addition to this, the characterizations also justify the choice of particular samples, with the interface quality as a primary factor. Although the key samples (magenta circle, Figure 3.18), with different micro/macroscopic aspects also have different chemical composition of their magnetic constituents, they are hardly considered as non-comparable as far as local investigations of direct ME effect are concerned. They can be easily divided into two groups based on their magnetic constituents: (i) uniaxial (SrM, BaM), and (ii) cubic (CFO/NFO) ME systems. With no major differences in the magnetic/magnetostriction characteristics within the uniaxial class, the BaM and SrM based samples will be considered for comparison between their respective micro/macroscopic nuances irrespective of the chemical composition of magnetic phase. On the other hand, a comparison within the cubic class will take into account identical but smaller nuances the differences of NFO and CFO phase by keeping in consideration their differences in the magnetostriction behavior (Figure 3.17). On the other hand a cross comparison between the SrM based sample of uniaxial class which has its macro and microscopic features identical to those of the cubic class with the NFO/CFO based samples will stand as a comparison between their completely different magnetostriction behaviors.

4 Converse Magnetoelectric Effect in Composites: Pseudo Real-Time Domain Dynamics

As far as composites are concerned the converse magnetoelectric effect has been seldom studied in literature [180–183], mainly due to the lack of available experimental tools. Irrespective of whether the measured coefficient is the converse ME co-efficient ($\mu_0 \Delta M/\Delta E$) or the ME flux co-efficient ($\Delta H/\Delta E$), the phenomena underlying the stress mediated coupling has a micromagnetic origin. As discussed in chapter 1, stress affects the magnetic anisotropy leading to a magnetomechanical anisotropy term (Eq(1.31), (1.32)). This means that for a uniaxial system with strong crystalline anisotropy, which will be mainly addressed in this chapter, the effect of stress is to induce motion of domains/domain walls in order to achieve a minimum energy condition. This dynamics is what defines the macroscopic change in magnetization. However a direct observation of the same has been seldom realized so far. It is precisely this aspect of magnetoelectric effect which is addressed in this chapter, where MFM based investigations are presented.

4.1 Domains and Domain Walls in Hexaferrites

As discussed in chapter 1, hexaferrites possess a uniaxial symmetry and hence the domain walls are only of 180^0 type. Also the critical grain size for a single domain in hexaferrite lies between 0.5 - 1 µm [93], hence considering the existing grain size distribution in the hexaferrite based composite samples it can be expected to encounter both, polydomain as well as single domain configurations. Figure 4.1 shows a typical polydomain state of a BaM single crystal, observed by three different methods (bitters method, Kerr microscopy, and MFM). It shows that typically the 180° domains are arranged as beveled strips.

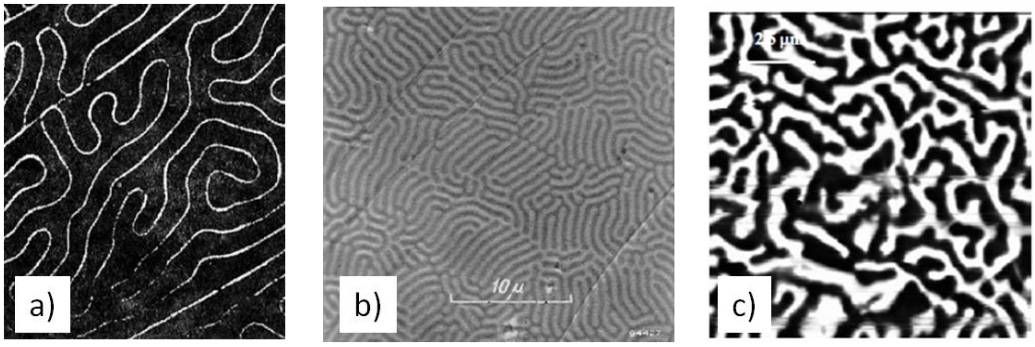

Figure 4.1 (a) Domain walls in a BaM single crystal, made visible using colloidal suspension (Bitter method)[93]. (b) Striped domain patterns in a 1µm thick BaM single crystal plate observed using Kerr effect [93, 184]. (c) MFM image on an annealed BaM thin film [184].

A primary effect of an applied mechanical stress on the magnetic inclusion is to move the domain walls as discussed in section 1.3.1. The direction and amount of the motion cannot be

pre-judged in the present case due to the extremely anisotropic nature of stresses generated. However, an estimation of aggregate domain wall motion can provide information about the net magnetization change. Associated with domain wall motion is the effect of hindrances (pinning) leading to hysteretic effects. It is known that in most of the magnetic materials including ferrites[91], the magnetization process is associated with jumps due to the pinning and de-pinning of the moving domain walls. These jumps are characterized by the famous *Barkhausen noise* [185], that is often encountered in electromagnetic devices. The magnetic power loss observed in ferrite electromagnet cores is associated with the hysteretic pinning of domain walls, hence it can be expected that also the domain wall motion induced due to stress might undergo hysteretic pinning. Recently this was studied by Carman et al. [186] where they made direct observation of domain walls in a Ni thin film grown on a piezoelectric substrate (PMN-PT). Any interaction of the magnetic domains and the residual stress that pre-exists in the material is not relevant in the case of hexaferrite based systems, since 180° domains have no misfit strain due to magnetostriction.

Another important aspect that associates itself to stress induced effects is the thickness of domain walls given by eq.(1.34). It can be seen that the anisotropy term in eq.(1.31) - (1.32) is presumed to be purely magnetocrystalline in the absence of stress, whereas in the presence of an external hydrostatic pressure a magnetoelastic contribution adds up in the new effective anisotropy term expressed as [187]:

$$K^{eff} = K_1 + K_M \tag{4.1}$$

$$K_M = (\epsilon_{xx} + \epsilon_{yy})B_{xx} + \epsilon_{zz}B_{zz} \tag{4.2}$$

$$B_{xx} = \left(\frac{\sqrt{3}}{2}B_{12} - \frac{1}{4}B_{22}\right) \tag{4.3}$$

$$B_{zz} = \left(\frac{\sqrt{3}}{2}B_{12} + \frac{1}{4}B_{22}\right) \tag{4.4}$$

Here K_M is the magnetomechanical anisotropy constant, ϵ_{ij} are the uniaxial strains in response to a hydrostatic pressure, and B_{ij} are the magnetoelastic constants. The subscripts *xx* and *zz* represent terms in a Cartesian system, whereas those which are numbered, represent terms in the symmetric irreducible representation [188]. Using tabulated values of the magnetoelastic constants [189], and by considering the exchange stiffness A (10^{-6} erg/cm) and K_1 (10^6 erg/cm^3) of the same order, an estimate of the added magnetomechanical energy can be made by substituting the observed changes in domain wall thickness into eq.(1.34). The outcomes will be discussed in section 4.5.

4.2 Electrical Poling Under the SPM Tip

In order to probe the converse ME effect via SPM, electric field under the tip was utilized to induce a momentary piezo-strain in the ferroelectric regions. As a result of this, stresses appearing in the magnetic phase can lead to irreversible micromagnetic changes. In this experiment the AFM tip scans the surface in the contact mode while applying an electric field,

the value of which can be pre-defined at different areas of the scanned frame. Often it is useful to carry out a bipolar voltage scheme as shown in Figure 4.2 (bottom centre), where two different areas of the scan are subjected to equal and opposite values of voltage. This strategy enables a convenient observation of ferroelectric switching after the scan, by comparing any correlated spatial differences in contrast.

It has to be noted that the voltage is applied by the tip which is moving at a velocity of around 10 - 20 µm/s; this translates into a rest period of about 4 milliseconds per pixel. As a consequence, the stress experienced by the magnetic regions will be extremely local, and its magnitude will vary over time as the tip hovers closer and farther from the neighboring ferroelectric domains. It is by no means feasible to model this situation in order to predefine any concrete effects on the magnetic domains. However a generalization can be made that under the influence of the continuously varying stress the magnetic domain wall will also undergo continuously varying changes with the *maximum impact* occurring when the tip voltage induces the highest piezoelectrical stress at a closest possible FE-FM interface. Since the distribution of grain orientation is random and not known a priori, it has to be assumed that statistically there are interfaces, which in terms of relative orientation of their polar axis and magnetic easy axis, are as preferably aligned as possible to give a maximum impact. This scenario will be addressed here onwards by the term *relative grain orientation*. It can be assumed that some of the changes, mostly corresponding to the *maximum impact*, will be irreversible as a consequence of domain wall hindrance (pinning). Stress acting at a particular point other than the *maximum impact* i.e. during the tip staying far away from that point will be termed as *secondary stress*. Poling by the tip by far seems to be the best alternative of studying local converse ME effect; the other possible options of patterning microelectrodes [190, 191] for applying local fields are less feasible owing to poor quality of the sintered ceramic surfaces.

Quite often such an experiment requires preferable surface conditions, in that the scanning under high voltage should not cause breakdown due to a momentary flow of high current through percolative pathways. Hence, a trial and error approach was adopted in that several spots on different hexaferrite based composite systems were investigated in order to find an optimal location. Table 4.1 summarizes the studied hexaferrite based systems, along with the characteristics of the optimal spots found.

Table 4.1 List of the hexaferrite based composite systems, along with the characteristics of the corresponding spots studied using MFM.

System	Spot reference	Electric field
$BaFe_{12}O_{19}$ – $BaTiO_3$ (83% - 17%)	Spot-1	Bipolar (± 39V,whole image)
$BaFe_{12}O_{19}$ – $BaTiO_3$ (65% - 35%)	Spot-2	Unipolar (+25V, single grain)
$BaFe_{12}O_{19}$ – $BaTiO_3$ (65% - 35%)	Spot-3	Unipolar (+35V, selected region)
$BaFe_{12}O_{19}$ – $BaTiO_3$ (65% - 35%)	Spot-4	Unipolar (+35V, selected region)
$SrFe_{12}O_{19}$ – $BaTiO_3$ (30% - 70%)	Spot-5	Unipolar (+35V, selected region)

In order to achieve a good statistical picture of the effect, attempts were made to study several spots on similar systems. The Spot-1 and Spot 2-4, imaged on BaM based composite systems, are considered identical despite of the differences in phase content, since the content doesn't play a bigg role locally. Due to unfavorable surface conditions only one spot was studied in the case of the SrM based composite. The mode of applying electric field varies from bipolar to unipolar including a single grain poling in order to examine the related effects on the micromagnetic fluctuations. Figure 4.2 shows morphologies corresponding to spot-1 along with a schematic of the poling experiment. Qualitatively it can be inferred that after poling a significant endemic change in the magnetic domain configuration takes place (Figure 4.2d, e). The effective changes observed can be associated to the pinned state of the domain walls at defect sites as discussed in the beginning of the section. The MFM images were obtained under standard operation conditions, however with a difference in the delta height. Before poling, the delta height of 68 nm was used, whereas after poling the delta height was increased to 100 nm in order to minimize cross talks due to electrical charging of the surface. However this change in delta height does not make a larger difference as far as the changes in the MFM contrast are concerned, this will be discussed in the following section. Apart from the spatial changes observed in spot 1, it was also observed that the net amplitude of the phase signal was increased by a few degrees, this can also be understood in the context of the different delta height.

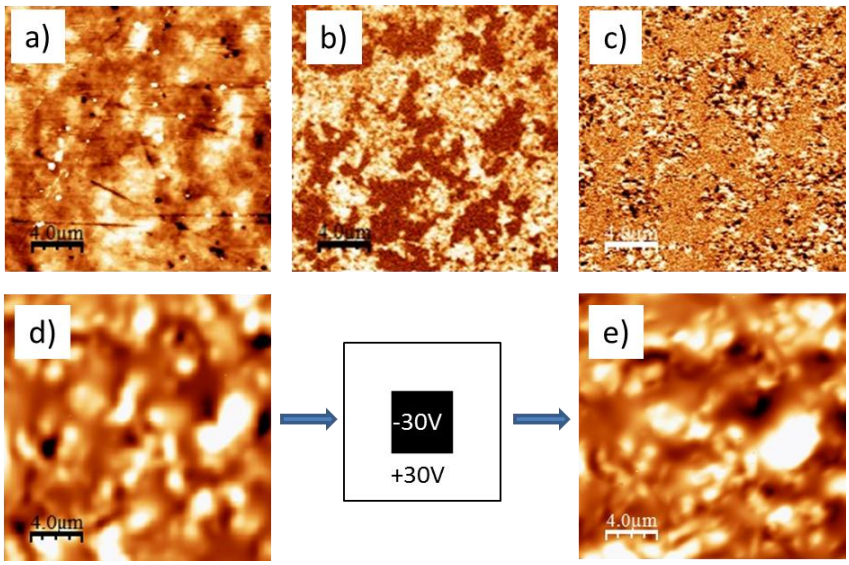

Figure 4.2 Topography (a), Vertical-PFM (b), Lateral-PFM (c) and MFM (Phase signal) (d) images corresponding to spot 1. A close and intricate distribution of the ferroelectric BaTiO3 phase can be inferred from the active areas (bright) in vertical PFM. The schematic representation of field pattern applied by the tip is shown in the bottom centre frame, followed by which is the MFM (phase signal) image (e) showing the changed state of magnetic domains after electrical poling.

Followed by the preliminary results of spot 1, poling of a single grain was explored, where the electric field is only applied to a single FE grain close to the FE-FM interface, in order to evaluate the extent of changes that can be induced by such extremely local poling. This experiment corresponds to spot-2 (Figure 4.3). Qualitatively no significant changes were observed. This indicates that the stress field generated by the straiming grain is not sufficient to induce any changes in the domain configuration close to the poled region. However, as pointed out by the cyan arrows (Figure 4.3e, f), at a region away from the poled grain, a change in domain configuration is marked. This indicates that the stress field generated by the piezostrain could only be effective at a location where possibly the grain orientation is favorable for the *maximum impact*. In other words, as compared to spot-1, where a large number of grains with statistically rich orientations were poled, spot-2 has lower probabilities of having made the *maximum impact* within the scanned area.

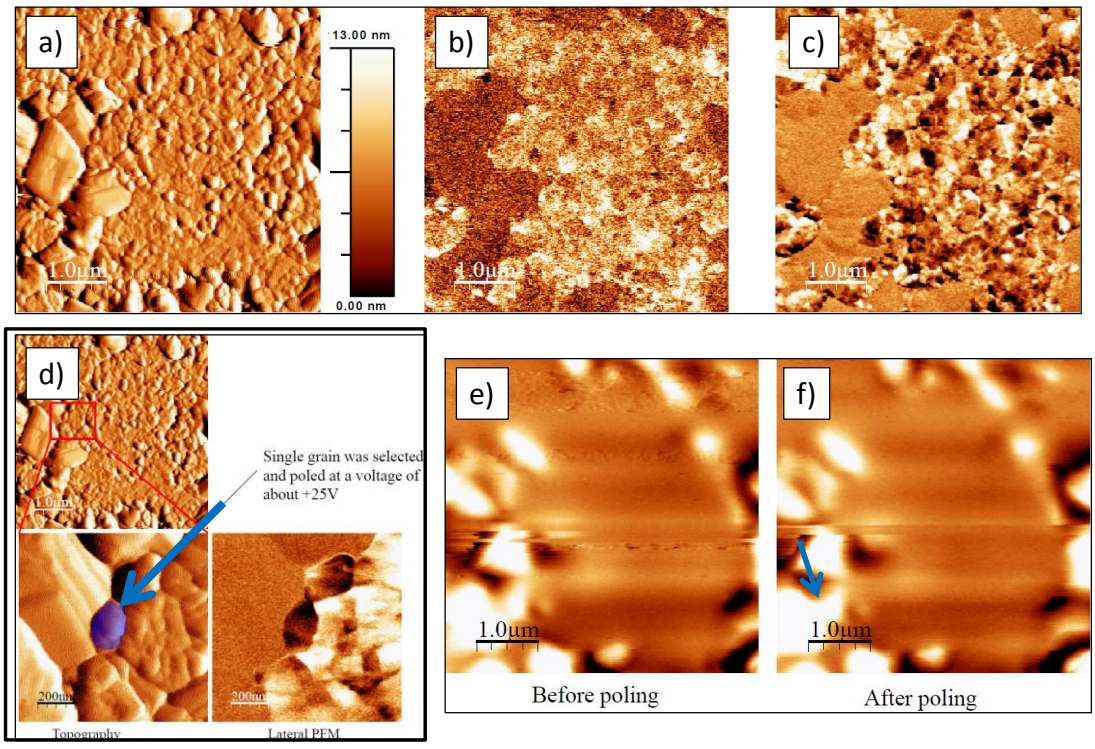

Figure 4.3 Topography (a), Vertical-PFM (b), Lateral-PFM (c) and MFM (Phase signal) (d) images corresponding to spot 2. (d) highlights the poled spot by zooming the topography image (a) the ferroelectric/piezoelectric characteristic of which is confirmed the juxtaposed lateral-PFM image. (e) and (f) shows the MFM (Phase-signal) images corresponding to spot 2 before and after the poling process respectively. The cyan arrow in (f) highlights the observed change in domain configuration.

This comparison provides the motivation of examining the effect of variability in orientation of grains on the observed domain change. For that matter spot-3 and spot-4 were measured with similar scan parameters with the aim of observing inhomogeneity in the observed domain configuration changes. Figure 4.4 shows a comparison between the morphologies and domain changes observed in spot-3 and spot 4. The cyan circle indicates the most significant spatial changes that are observed in addition to the overall increase of MFM phase amplitude corresponding to spot-4. The spatial changes are not so significant in case of spot-3 which indicates huge inhomogeneity of the stress induced micromagnetic changes, in parts due to the inhomogeneous and anisotropic stress fields and due to the random relative grain orientations of the FM and FE phases (as inferred from the single grain poling experiment).

Figure 4.5 shows the outcomes of the poling experiments on spot-5 which correspond to the SrM based hexaferrite system. Identical to spot-4, spot-5 also shows stochastic changes in domain configuration, as marked by the cyan circle. The changes within the marked area can be primarily understood as a consequence of the coincidence of the poled region, however interestingly a second evaluation suggests that in the region neighboring the poled FE area outside the cyan circle, there are interestingly no changes at all. And even within the marked

region the changes are inhomogeneous. This insinuates a bigger role of the random orientation of the relative grain orientations. A correlated comparison of grain orientation map using EBSD and the observed changes, as shown in Figure 4.6, throws more light onto the paradox pertaining to the role of the randomness of the relative grain orientations.

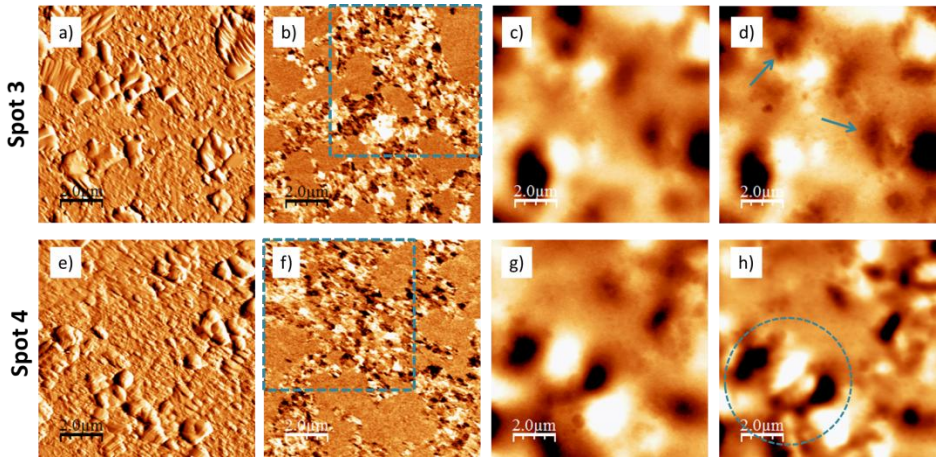

Figure 4.4 (a)-(d) shows the Topography, Vertical-PFM, Lateral-PFM, and MFM (Phase signal), images respectively corresponding to spot-3, whereas (e)-(h) shows the same for spot-4. The area marked by cyan circle shows the maximum observable changes.

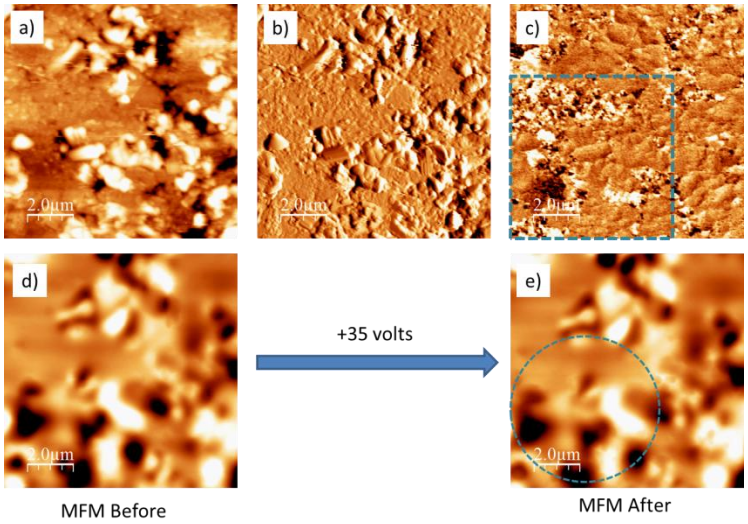

Figure 4.5 Topography (a)(b), lateral-PFM (c) and MFM (phase signal) (d) images corresponding to spot 5. A close and intricate distribution of the ferroelectric $BaTiO_3$ phase can be inferred from the active areas (black/white) in lateral-PFM. The marked square (cyan) in (c) corresponds to the area that was poled by the tip with +35 volts. (e) is the MFM (phase signal) image showing the changed state of magnetic domains after poling.

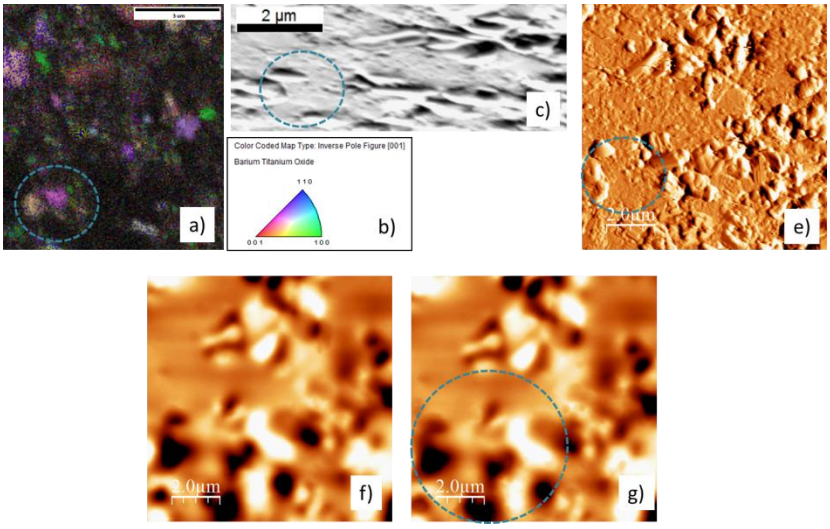

Figure 4.6 Shows an EBSD pattern overlaid on noise (a) acquired, on spot-5 along with the corresponding inverse pole colormap (b), SEM image (tilted 70° w.r.t. electron gun) (c), and the AFM topography (e). (f) and (h) are the MFM (phase signal) images before and after poling respectively, corresponding to the same spot (spot 5) as shown in Fig. 3.5. The cyan circle correlates the EBSD/SEM and the AFM/MFM images acquired in two different experiments.

The EBSD map, even though being highly noisy, shows a light brown and a pink contrast in the marked region; this means that the grains corresponding to the location have orientations somewhere between [121] and [102] directions. It is known that the tetragonal $BaTiO_3$ phase has the maximum piezoelectric effect along [111] direction, while gradually decreasing to the minimum along [100] direction (Figure 1.10). Hence the grain corresponding to brown contrast is expected to have undergone a higher out of plane, and hence in-plane strain. This can be very well attributed to the *maximum impact* observed in the vicinity of the grain.

4.3 Temperature Dependent Magnetic Force Microscopy

$BaTiO_3$, as it undergoes a structural change across its phase transition has to accommodate a large amount of strain caused by the ferroelastic straining of the unit cells. Especially the cubic-tetragonal phase transition in a bulk polycrystal leads to immense stress appearing especially at the phase boundaries [192]. Hence, during the phase transition it is expected to see large stress fields in the composites and hence a rearrangement of magnetic domains is expected. Temperature dependent MFM studies were carried out in order to directly observe related micromagnetic changes. Figure 4.7 shows the series of MFM images acquired at different temperatures ranging from RT to 200 °C with a finer interval across the cubic-tetragonal transition temperature of 120 °C before cooling back to RT.

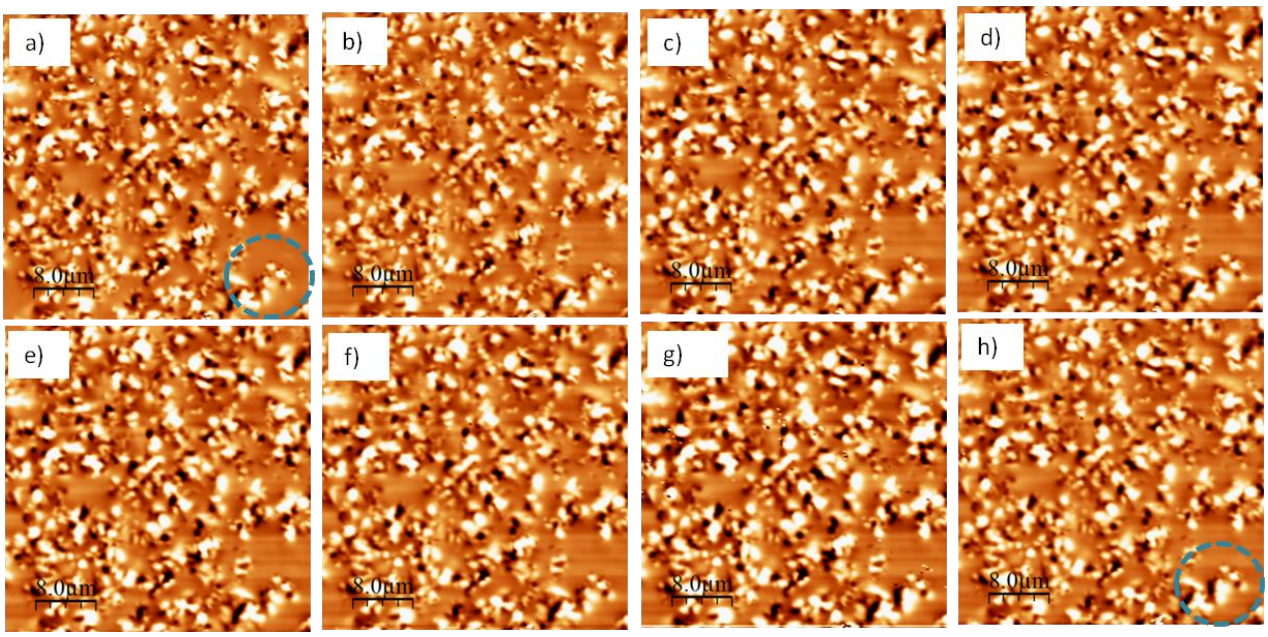

Figure 4.7 Shows MFM (Phase signal) images acquired at different temperatures starting from at 27°C (a), 100°C (b), 115°C (c), 120°C (d), 125°C (e), 150°C (f), 200°C (g), and back to 27°C (h). The marked region (cyan circle, indicates the hysteretic changes occurred during the thermal cycle.

Apart from some minor changes observed in the marked region (cyan circle), there were no significant changes observed within the scan. It has to be noted that the marked change is irreversible upon cooling, which once again insinuates existence of pinning contribution. This observation, coupled with the fact that the stress field induced upon phase transition could be inhomogeneous and anisotropic, once again points toward the hypothesis of random *relative grain orientations*. As a second observation, with increasing temperature the MFM image becomes sharper. The relative area of black and white contrast steadily increases. The increasing temperature can possibly lead to changes in the medium density, which is critical to the dynamic properties of the cantilever [193]. The medium contribution to the effective quality factor of the MFM cantilever can be related to temperature of the medium (air) as [194]

$$Q_{air} = A \cdot \sqrt{\frac{RT}{m}\frac{1}{P}} \qquad (4.5)$$

where A is a proportionality constant which depends on the cantilever characteristics, R is the ideal gas constant, m is the mass of molecules constituting the medium (air), T is temperature, and P is pressure. With this it can be inferred that an increase in temperature should lead to an increase in quality factor. In other words the phase detection slope becomes steeper. This has to be the key reason for the observed sharpening of phase contrast, because the possibility of any varying stray field distribution has to deal with an increase in magnetocrystalline anisotropy, which actually should decrease with increasing temperature [195]. Overall, a closer observation of the domain structure changes suggests that a rigorous algorithm is required to quantitatively analyze these changes in order to reveal any significant temperature dependence.

A qualitative analysis of the domain configuration changes observed in the temperature dependent as well as in the tip poling studies, establishes the following facts:

- The micromagnetic fluctuations (domain structure rearrangement) induced by the stress field, are locally pinned at defect sites. A net change in magnetization on removal of stress, if quantified, can give an idea of local pinning strength.
- The maximum impact of the stress field depends on a favorable *relative grain orientation*, resulting in extremely localized and stochastically distributed changes of the observed domain configurations.
- Temperature dependence of the micromagnetic fluctuations can be better resolved using an appropriate approach.

All these points demand for a rigorous quantitative analysis method for the micromagnetic fluctuations. In order to realize this, a custom built algorithm of image processing was developed, which relies on some basic assumptions made for the MFM contrast formation mechanism. In the next section the principles underlying MFM contrast will be discussed in the context of the observed spatial changes, followed by introduction of the developed method and discussion of the obtained results.

4.4 Contrast Mechanism in Magnetic force Microscopy

The formation of image contrast in MFM is dictated by the magnetic interaction between a magnetic tip and the sample (Section 2.1.2). The force acting on the tip, in a preliminary magnetostatic approximation, can be given as [196]

$$\vec{F} = \nabla(\overrightarrow{m_T} \cdot \vec{H}) \tag{4.6}$$

where m_T is tip magnetization and H is the surface stray magnetic field. However, in reality the tip has finite dimensions, and cannot be treated as an independent dipole unless a proper approximation is made. Simultaneously, the sample stray field H is also not trivial, as it depends on the particular micromagnetic arrangement of the magnetic domains in the vicinity of the tip. For that matter various algorithms have been suggested in literature [196, 197]. A more sophisticated way is to start expressing the force acting on a unit volume element of the tip as a consequence of the underlying stray field $H(r)$ which is then integrated over the tip volume V [196].

$$\vec{F} = \int \nabla\left(\overrightarrow{m_V}(r') \cdot \vec{H}(r + r')\right) dv \tag{4.7}$$

$$\overrightarrow{F'} = \int \vec{n} \cdot \nabla[\vec{n} \cdot \nabla\left(\overrightarrow{m_V}(r') \cdot \vec{H}(r + r')\right)]dv \tag{4.8}$$

where r is the vector corresponding to the tip position, r' is the vector corresponding to an infinitesimal volume element of the magnetic layer of the tip relative to the tip position. Hence $H(r+r')$ is the field experienced by the volume element of the tip with magnetic moment of $m_V(r')$, and n is the normal collinear to the principal axis of the tip. If the normal vector n is parallel to the z axis then eq.(**4.7**) and (**4.8**) reduce to [196]

$$\vec{F} = \int \left(m_{Vx}\frac{\partial H_x}{\partial x} + m_{Vy}\frac{\partial H_y}{\partial y} + m_{Vz}\frac{\partial H_z}{\partial z}\right) dV \tag{4.9}$$

$$\overrightarrow{F} = \int \left(m_{Vx} \frac{\partial^2 H_x}{\partial x^2} + m_{Vy} \frac{\partial^2 H_y}{\partial y^2} + m_{Vz} \frac{\partial^2 H_z}{\partial z^2} \right) dV \quad \textbf{(4.10)}$$

It can be inferred from eq.(4.10**)** that the phase shift of vertical oscillations measured in MFM, which is proportional to the z component of force gradient acting on the tip, is hence directly proportional to the second order partial derivative of the sample stray field ($\frac{\partial^2 H_z}{\partial z^2}$). Now, the classical approach [196] is to construct force gradient values by substituting the experimental results into eq.(4.10). Next an appropriate tip model (e.g. hard magnetic tip, point dipole, point monopole) is chosen for solving the inverse problem of determining the magnetic sources of the surface stray field. However this approach suffers from inherent gross error which roots in the fact that actually an average (static) interaction in the vicinity is estimated, by neglecting the finite tip oscillation amplitude (dynamic). As a result, another parametric approach is proposed [196]. In this approach a qualitative analysis of the experimental results is made followed by a comparison of the same with an appropriate domain model problem (e.g. bubble, periodic parallel domains, and cylinder domain configurations). After having chosen the best fitting model, a tip interaction model is chosen as discussed above, and the MFM image is reconstructed using initial parameters like tip geometry, magnetization, and tip sample separation. Followed by this, best fit is achieved by varying the initial parameters and the model is further refined. In the realm of the present thesis it is not useful to review this approach, since a precise knowledge of sample stray field is impossible due to the random nature of the magnetic microstructure. However, in the present case it is worthwhile to evaluate $\frac{\partial^2 H_z}{\partial z^2}$, which is proportional to the response of a hard magnetic tip, measured over a model configuration of periodic domains. Initially, a case of periodic domain can be considered, where there are domains juxtaposed with a specific period, and with opposite magnetization lying along z axis (Figure 4.8), as evaluated in literature [198]. This demonstrates the fine implications of the micromagnetic configuration on the measured response. Followed by this, an extrapolation of the qualitative observations to the case under investigation, polycrystalline hexaferrite phase will be carried out. For such a model the magnetostatic potential (only belonging to the domain structure and not the tip) can be described as [199]

$$V_m = \alpha_0 + \sum \alpha_n \sin \frac{\pi n d_1}{d_1 + d_2} \cos \frac{2\pi n x}{d_1 + d_2} \exp\left(\frac{2\pi n z}{d_1 + d_2}\right) \quad \textbf{(4.11)}$$

where α_0, and α_n are constants depending on the sample parameters like domain period, sample thickness, and anisotropy. *n* represents the number of stripes. Followed by this, the stray magnetic field *H(r)* can be calculated as

$$\vec{H}(r) = -\nabla \cdot \overrightarrow{V_m} \quad \textbf{(4.12)}$$

Further, an evaluation of the second derivative of this field along the probe oscillation direction ($\frac{\partial^2 H_z}{\partial z^2}$) provides a qualitative outlook of the experimental MFM results as it is proportional to the observed phase shift. Figure 4.8 shows ($\frac{\partial^2 H_z}{\partial z^2}$) for different ratios of the tip-height above the surface (Z_0) and domain

widths (d_1, and d_2 ; $d_1=1/3d_2$). It can be seen that with varying tip height, there is a significant change in the qualitative nature of the second derivative. Simultaneously, the micromagnetic parameters, namely the ratio of d_1 and d_2 here, are also decisive in determining the envelope of the resultant signal. In the present case, where the smallest measured feature is of the order of 320 nm (Section 4.6) and the typical tip heights are 100 nm, it can be generalized that a typical envelope will be somewhere in the middle of the ones observed in the $Z<<d_2$ and $Z=d_2$ cases (Figure 4.8). In other words the signal envelope will be qualitatively equivalent to the field envelop itself. This is also corroborated from the line section curves taken on a typical MFM image (Figure 4.9).

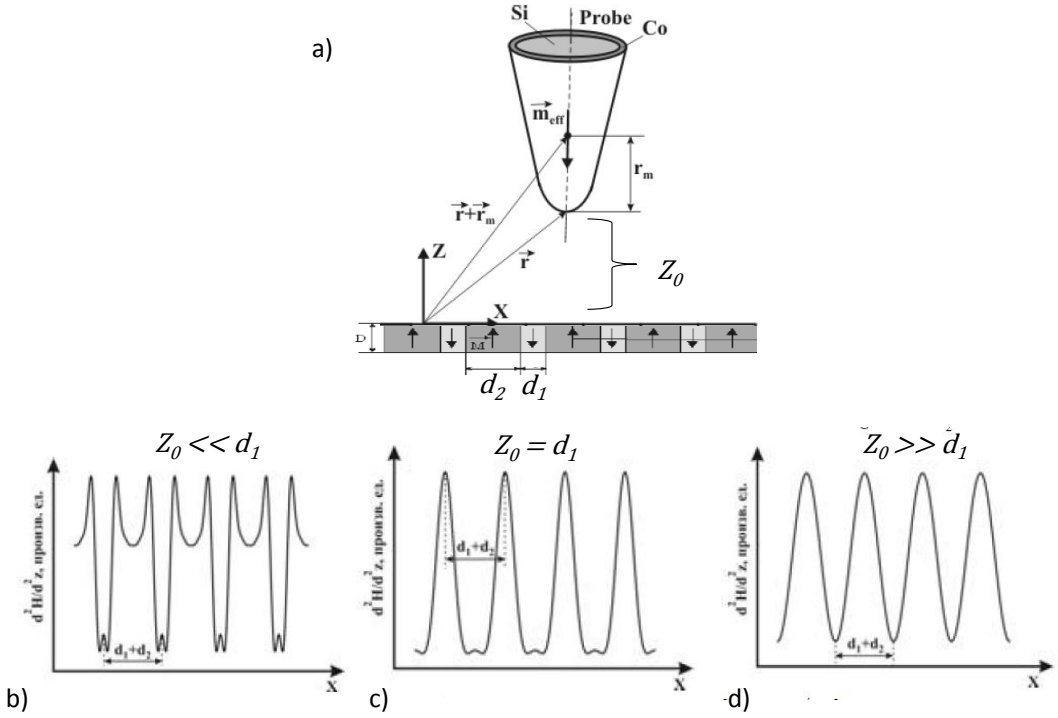

Figure 4.8 Shows the schematic arrangement of the theoretical model under consideration [198] (a). (b)-(d) shows the second order partial derivative w.r.t. the z co-ordinate, for different ratios of Z_0 and d_1.

Since the materials under study are polycrystals, a random orientation in the domain structure is expected. However, it is trivial to extrapolate the understanding discussed above in this section for cases where the orientation of the magnetic domain is randomized in 3 dimensions. Figure 4.10 shows modeled *z* components of magnetic field (H_z) in the *xy* plane above periodic domains of a magnetic inclusion embedded in $BaTiO_3$ matrix (COMSOL; see appendix-b). For the cases with domain orientation in the *xz* plane (Figure 4.10(a), (b), (d), and (e)), there is not much qualitative difference as compared to the case where the orientation is parallel to *y* the axis. The only difference in the *z* oriented domains is that with increasing x component the position of the peak field value is shifted towards the direction of the increasing *x* component (offsetting w.r.t. the domain walls). The generalization that can be made for an in-plane orientation ($x = 0$, $z = 0$) is that there are pairs of bright and dark contrast per domain, and that on increasing x and/or z component of the orientation the area of this regions increases. The ratio of intensity of these

contrasts pairs will change depending on the variation in the *z* component, simultaneously offsetting the peak value in the in-plane (*x*, *y*) direction.

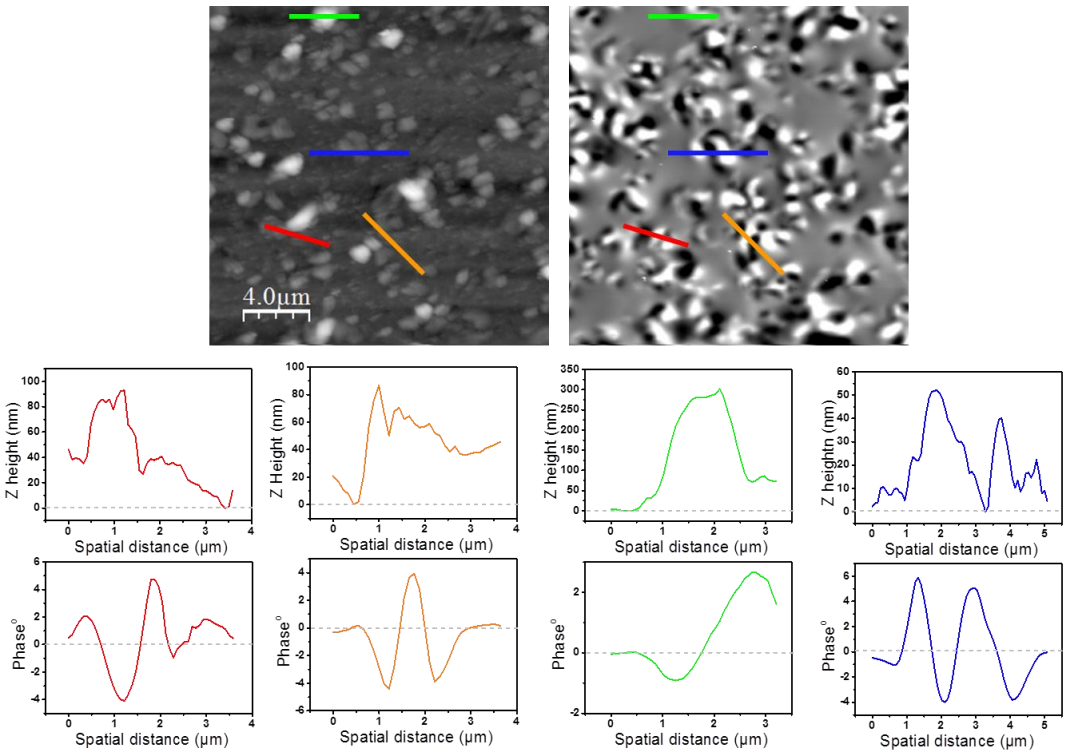

Figure 4.9 Typical topography (top; right), and MFM phase (top; left) of a BaM based composite system (BaM – BTO; 35/65 %). The corresponding cross sections (colour correlated) of the topography (middle row) as well as the MFM phase image shows the typical tip responses.

The above analysis can be extended to the case of hexaferrite grains embedded in a $BaTiO_3$ matrix, with the assumption that a smeared non-local contribution will compensate for the absence of higher repetition of domains (striped domains). This assumption is corroborated by the signal cross sections typically observed in the MFM images collected (Figure 4.9). However, the fact that there are possibilities to encounter single domains (i.e. absence of any local repetition of 180° domains), has to be handled carefully, since a generalization of such domain configurations, within the presented hypothesis of direct qualitative correlation between force gradient ($\frac{\partial^2 H_z}{\partial z^2}$) and the surface emanating fields, can only be valid if there are sufficient repetitive domains (including striped domains and/or equivalent amount of bipolar single domains) located in close proximity. However, since the probability for the grain sizes to fall within the range of critical single domains size (500 nm – 1 µm) is very weak, the above hypothesis can be extended to the studied systems without introducing any significant errors.

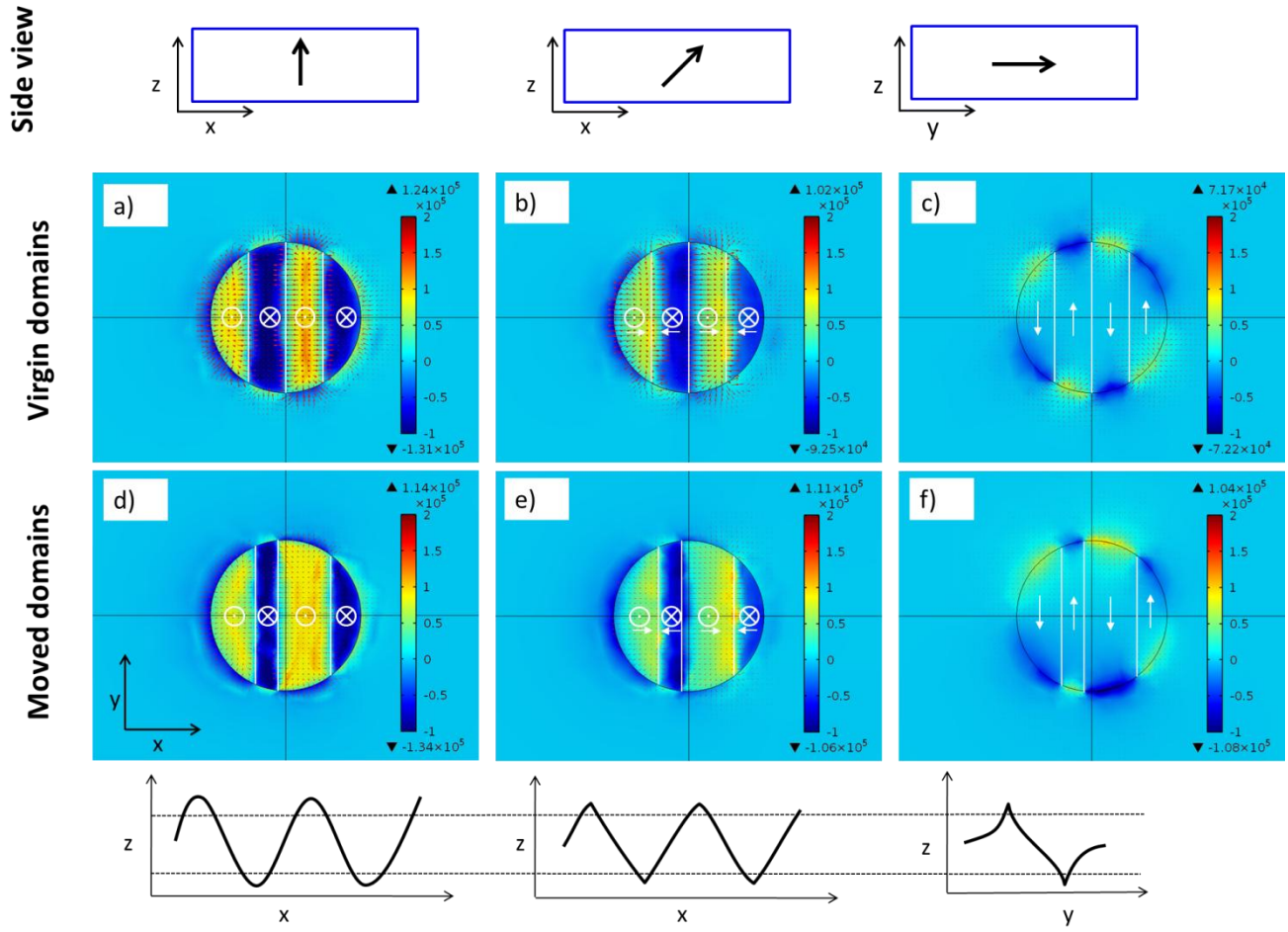

Figure 4.10 Shows the distribution of z component magnetic field (H_z) just above the plane of a modelled magnetic inclusion (half sphere; appendix-b) embedded in a $BaTiO_3$ matrix. (a)–(c) corresponds to the distribution above equally spaced domains (domain walls marked by white lines), with magnetization orientation along z axis, xz plane and y axis respectively, while (d) –(f) corresponds to the same but for domains that are moved, as if in a realistic case where the width of opposite domains are affected in equal and opposite manner. The top row indicates the magnetization orientation corresponding to the respective columns, whereas the bottom row shows a schematic cross-section of the field distribution taken along x direction for cases with $y = 0$ orientation and along y axis for the case with $y \neq 0$ orientation. The dashed line in the bottom row schematically demonstrates the area that lies between the curve and the cut-off line for different orientations. The symbols ⊙ and ⊗ represent the positive and negative directions of the out of plane component, whereas the white arrows represent the in-plane components along the respective directions.

4.5 Estimation of micromagnetic fluctuations

Considering the highly stochastic morphology of the hexaferrite phase in the composite systems, a precise correlation of the observed changes to domain dynamics is limited leading to the development of an approximation based analysis approach. Next, before proceeding to the developed analysis, the underlying assumptions are stated. As per the hypothesis presented in

section 4.4, the following points can be put forward about analyzing MFM response pertaining to a randomly distributed magnetization orientation in the hexaferrite phase.

- A direct correlation between the measured $(\frac{\partial^2 H_z}{\partial z^2})$ (in terms of phase shifts), and the surface emanating fields, can be extended in the present case. With this, a clear distinction between domains separated by domain walls can be made for the cases where the magnetization has a non-zero out of plane component.
- The portion of the measured signal, which is vertically truncated at a fixed signal height (dashed line; Figure 4.10), will be proportional to the z component of the magnetization orientation. Any in-plane movement of domains will lead to a proportional increase in the truncated part of the signals. Now, the 1D concept of the truncated portion can be easily extended to a 2D concept of contours. The contours here correspond to the image values at the fixed signal height. Apparently an increasing/decreasing portion of the truncated signal will correspond to widening/shrinking of these contours (Figure 4.11).
- The changes that might take place in domains with zero z component are not quantifiable (Figure 4.11e, f), and hence ignored. This will not affect the estimation, since any in-plane motion of domains only contributes to the in plane change of magnetization. In other words, the estimated changes will correspond only to the changes in the out of plane component of magnetization.

At this point it is necessary to return to the first section of this chapter, where the micromagnetic changes expected in a mechanical stress field were described as following:

- Domain wall motion
- Domain wall tuning (thinning/broadening)

As described in the points above, any in plane movement of the domains which represents a domain wall motion, will lead to a proportional aggregate change in the total area of bright and dark regions as marked by contours at a constant height (1/2 of the MFM signal altitudes w.r.t. to the base level, the free air phase). In other words, if circles with areas equivalent to the total area of the dark or bright contrast are constructed then the changes in the radius of this circle, owing to the changes in the area of the corresponding contrast (bright/dark), will be a measure of net domain wall motion. Figure 4.11 schematically shows the interplay of these bright and dark regions as the domain walls separating domains with different orientation undergo lateral motion. A and B are the circles with area equivalent to total area of the bright and dark regions respectively, and C and D are the corresponding circles after domain wall motion.

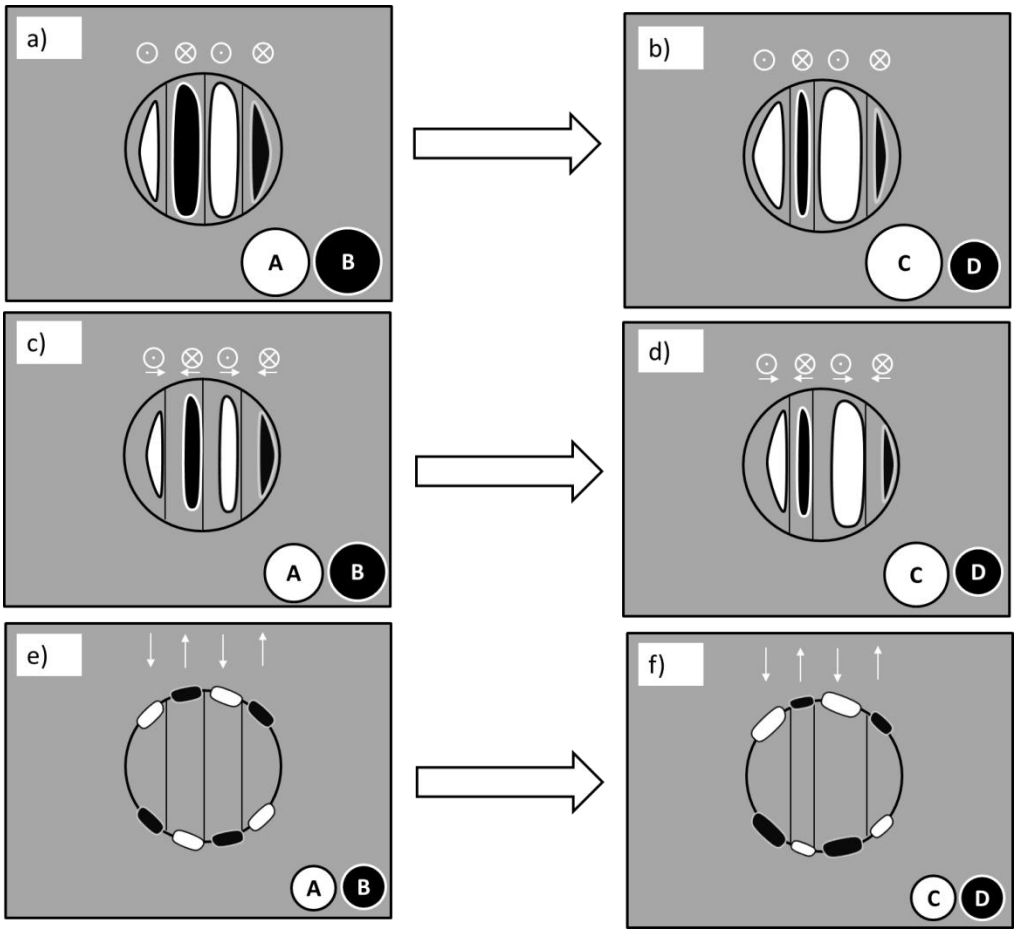

Figure 4.11 Schematically shows the contours of the signal surface taken at ½ of the peak values (positive as well as negative) corresponding to the modeled field distribution as shown in Figure 4.10. (a), (c), and (e) represent the virgin case whereas (b), (d), and (e) show the cases where the domain wall has moved. The fill inside the contours (black/white) schematically represents the signal whereas the grey area represents the base line. The symbols ⊙ and ⊗ represents the positive and negative direction of the out of plane component. The white arrows represents the in-plane components along the respective directions. The small white and black circles, insets in each frame, are the circles with area equivalent to the total white and black regions corresponding to the frame respectively.

For the first two cases with zero y-component of the magnetization orientation, there appears to be a net change in the difference of the area of the equivalent bright and dark circles. On the other hand the total changes in the equivalent bright and dark circles, for the case of completely in-plane magnetization orientation, cancel each other with no net change. For the first two cases, where there is an increase of white are over the black area, the aggregate domain wall displacement can be given as:

$$\Delta x_{domain} = |(A - B)| - (C - D) \quad \textbf{(4.13)}$$

A positive Δx_{domain} will represent the increase of dark regions over the bright ones, whereas a negative Δx_{domain} will correspond to an increase of bright over dark regions. Based on this

approach, the data from spot-1 (Section 4.2) was analyzed. Figure 4.12 shows the corresponding contours at heights chosen at ½ of the extremum signal altitudes (i.e. 0 to image maximum, and 0 to image minimum; 0 here represents the offset free air phase). These contours do not necessarily exist in pairs, like that in the model (Figure 4.10), however they represent the domains within the scanned frame and are not expected to pertain the ideal characteristic of one contour per domain, owing to the highly stochastic microstructure.

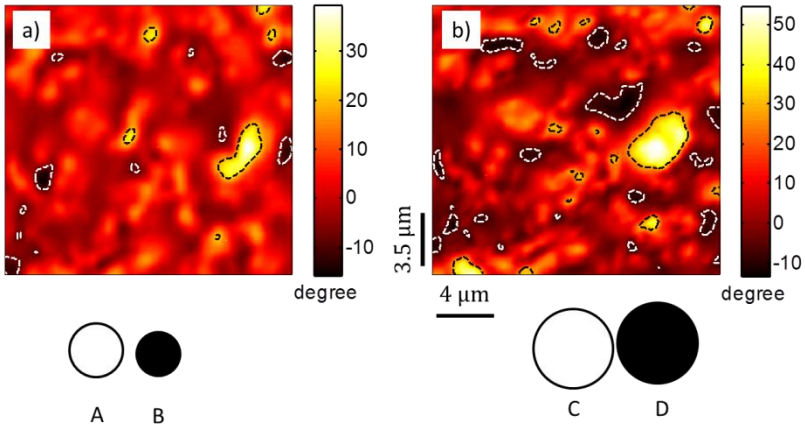

Figure 4.12 Shows the MFM (phase) images for the unpoled (a) and poled (b) states corresponding to spot 1, overlaid with the contours obtained at a height of ½ of maximum signal altitude (black dashed lines; bright contrast) and ½ of minimum signal (white dashed lines; dark contrast). The small white and black circles in the bottom of each image are the circles with area equivalent to the total bright and dark regions respectively, marked by the contour corresponding to the image above.

It can be seen from the equivalent bright and dark circles indicated in the bottom of the images (Figure 4.12), that there is a net increase in both domains, with a slight difference in the amounts of growth. This behavior is not expected from the hypothesis presented above, where an increase in one (bright domains) should rather be followed by an equal decrease in the other (dark domains). However, as will be shown later there is another effect, secondary to the domain wall motion, that might cause this anomaly. It has no effect as far as the calculation of eq.(4.13) is concerned. Applying eq.(4.13) in the case of spot-1, a domain wall motion of 270 nm was estimated. Now addressing the anomaly of simultaneous increase in bright and dark region observed in spot-1, the stress tuning of domain wall thickness {Eq.(1.34)} has to be analyzed. A widened or a shrinked domain wall can respectively increase or decrease the contour sizes at the fixed height, since the additional positive or negative contribution of the moments at the domain wall will accordingly alter the measured MFM signal intensity. Any monotonic change (a simultaneous increase or decrease) observed in the dark and bright regions, is hence associated with a change in the domain wall width. A simultaneous increase of the dark and bright regions accounts for a thinning of the domain wall separating them and likewise a simultaneous decrease in the same should correspond to a widened domain wall. A domain wall, which is defined as a gradual rotation of unit cell moments from one orientation to the other [200], thus results into an

anti-symmetric MFM phase across the domain wall region. Hence, the corresponding change in the radius of both (bright and dark) of the equivalent-circles, should be each half of the total domain wall widening/shrinking. Based on this argument a change in the width of the domain wall can be expressed as

$$\Delta x_{wall} = (A + B) - (C + D) \quad \textbf{(4.14)}$$

The value estimated from this formula needs to be divided by the average number of shapes represented by the contour, so that in the end an average change in domain wall width comes out. A negative Δx_{wall} corresponds to a thinning of a wall and a positive value shows a broadening of the wall. The value estimated for spot-1 is about 115 nm, which corresponds to an addition of magnetomechanical anisotropy energy of -3.16 × 10^6 erg/cm^3 (Appendix-c).

It is logical to think of correcting the domain wall displacement calculated from eq.(4.10), by taking into account the domain wall thinning per circle ($\Delta x_{wall}/2$), by subtracting this value from C and D. However a quick mathematical check shows that eq.(4.10) will still be valid. Now, it is useful to compute a net change in magnetization corresponding to the scanned frame. If the total difference in the radii of A and B circles is considered as a measure of the z component of net dipole moment, then a change of 270 nm corrected by the domain wall thinning leads to approximately 50% change in the z-component net, which translates to an equal amount of change in magnetization (moment per unit area of the scanned frame). And if it is assumed that the overall microstructure is comparable to that of spot-1 (even in the volume), then this change in surface magnetization can also be translated to volume magnetization. Now, considering the fact that the observed displacements are a result of a hysteretic pinning process, a 50% change in sample magnetization is unrealistic, which leads to two possible conclusions: (i) either the representative microstructure of the investigated spot cannot be homogeneously extrapolated to the whole sample (due to the often found nuances between surface and bulk characteristics), (ii) or else the defect density corresponding to the scanned frame should be relatively smaller at other microstructural points in the sample such that the overall hysteretic change in the magnetization is justified. Rigorous estimation of the associated spatial resolution limit has to be made in order to validate the arguments made so far. This will be done in section 4.6.

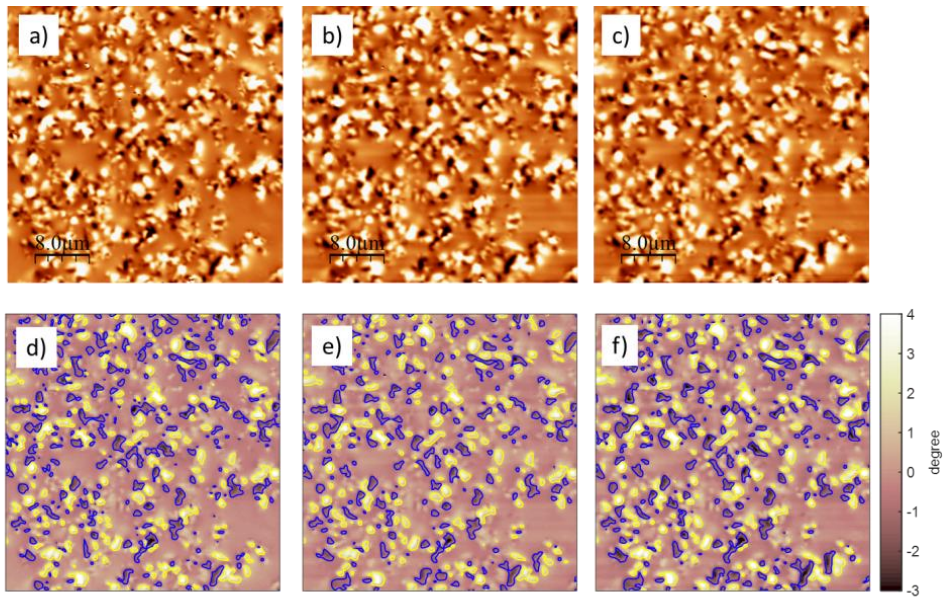

Figure 4.13 (a) –(c) shows the MFM (Phase signal) at different temperatures corresponding to Fig.3.7 (a), (c) and (h); (d)-(e) shows the same images but with overlaid contours, corresponding height of ½ of maximum signal (yellow lines; bright contrast) and ½ of minimum signal (blue lines; dark contrast)

Similar analysis was also carried out on the data pertaining to temperature dependent MFM. Figure 4.13 shows the MFM images at selected temperatures representing the temperature cycle, and the corresponding contours generated in a similar way as for spot-1. Although the MFM images by themselves do not pose any significant visual changes, calculation of Δx_{domain} and Δx_{wall} {using eq.(4.13), (4.14)} as a function of temperature (with the room temperature image as reference) reveal some interesting outcomes. Figure 4.14 shows the variation of Δx_{domain} and Δx_{wall} as a function of temperature; it can be seen that across the transition temperature of $BaTiO_3$ (120^o), there are apparent discontinuities. The domain wall displacements close to the transition temperature is of the order of 100 – 250 nm which is about two times smaller than that observed in spot-1 (under poling), despite the fact that the area of scan is almost double as compared to that for spot-1. Based on the hypothesis presented above it can be inferred that the defect density corresponding to the scanned area for the temperature dependent study is significantly lower than those estimated for spot-1. On the other hand, the maximum net change in the domain wall thickness is about 6 nm, which indicates a relatively weaker contribution of magnetomechanical anisotropy. This in turn leads to the conclusion that the strain/stress fields, generated across the ferroelectric phase transition, are much weaker than those generated by the local poling experiment.

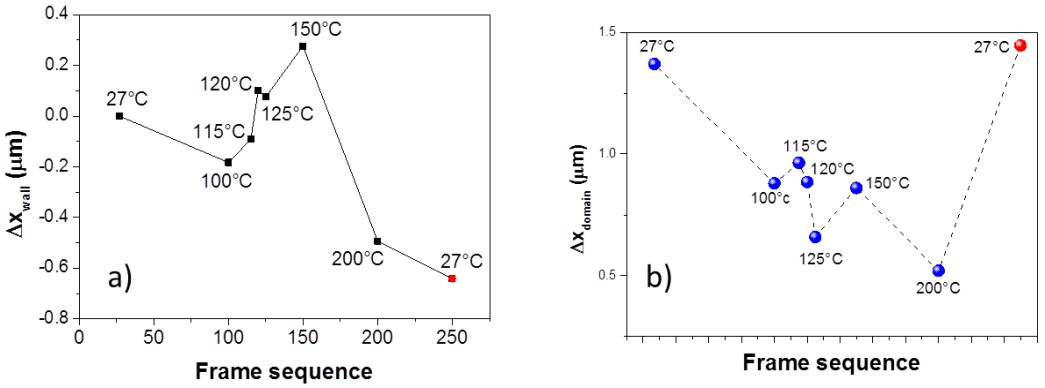

Figure 4.14 Shows the temperature dependence of the estimated Δx_{wall} (a) and Δx_{domain} (b).

The lowest measured spatial change of 6 nm is smaller than the tip radius (20nm), and much smaller than the pixel pitch (150 nm). This raises serious concerns about an effective capability of the MFM set-up to resolve such small changes. For that matter a rigorous analysis is presented in the next section, in which the observed spatial changes are rationalized.

4.6 Resolution Theory for MFM and Error in Measurement

In the present context we are interested in knowing the smallest detectable spatial change in the MFM signal. This will allow us to estimate the error in measurement of the domain wall changes estimated. The resolution theory of MFM classically addresses the problem of determining the smallest resolvable feature, in the context of experimental parameters like tip-sample separation, tip shape, and magnetization. For that matter, the image formation (force gradient along z-axis) in MFM is often considered as a convolution of an appropriate tip shape function $A(x,y,z_0)$ and a magnetic charge distribution function $h(x,y,z_0)$ at a particular tip height z_0 averaged over the sample thickness t (assuming $z_0 << t$).

$$F_z'(x,y,z_0) = \iint A(x-x',y-y',z_0)\cdot h(x',y',z_0)dx'dy' \quad \textbf{(4.15)}$$

$$F_z^{*'}(k_x,k_y) = A^*(k_x,k_y)\cdot h^*(k_x,k_y) \quad \text{(In Fourier space; } k = k_x + k_y \text{ is a wavevector)} \quad \textbf{(4.16)}$$

Here it is important to note the underlying assumption that the tip is considered as a single dipole and magnetic charges instead of dipoles are considered to be the major source of magnetic stray field [201]. The problem is now constituted in estimating an appropriate tip shape function (A^*), so as to link the fluctuations in the measurement parameters, specifically tip height (z_0), to the measured response. Quite often it is a norm to estimate a shape function experimentally, by measuring the MFM response over an extremely narrow Ni strip [202], where the strip is thin enough for the measured response to itself be like the shape function. This is difficult to achieve in the present context owing to limited experimental availabilities. However, the tip shape function has also been modeled using a Greens function based approach [201], where the representation changes from eq.(4.15) to

$$F_z^{'} = \int G(x - x^{'}, y - y^{'}, z) \cdot h(x^{'}, y^{'}, z_0) dx' dy' \quad \textbf{(4.17)}$$

Comparing eq.(4.17) with the nominal representation of force gradients in terms of the tip magnetization and sample stray field {eq.(4.15)}, the following 3D Green's functions could be provided [201]

$$G(x, y, z) = \frac{m_z}{4\pi\mu_0}\left(\frac{15z^3 \pm 9z(x^2+y^2+z^2)}{(x^2+y^2+z^2)^{7/2}}\right) \quad \textbf{(4.18)}$$

Here m_z is the tip magnetization indicating that it lies solely along Z direction. Figure 4.15 shows a cross section profile of the Green's function {eq.(4.18)} as estimated by Saito et al. [203]. It shows how the tip shape function depends on the tip sample distance (Z_0), and tip magnetization. The height of this function determines the sensitivity of the obtained image, which scales inversely with Z_0^4. However, a more important aspect to note here is the dependency of the width of this shape function on Z_0 ($1.5 \cdot Z_0$), which helps determine any corresponding spatial variations in the measured MFM response. Increasing distance Z_0 leads to a broadening of the tip shape function and hence a resultant blurring of the measured MFM image. On the premises of these relationship, the domain wall changes calculated for spot-2 are estimated to be comprising of an additional broadening of 37 nm, since the tip-surface distance uncontrollably varied from 68 nm to 100 nm after poling.

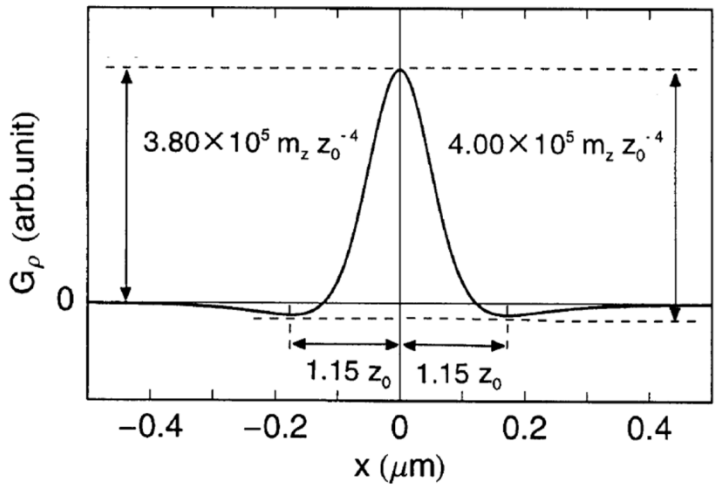

Figure 4.15 Shows the tip convolution function (shape function) as described by eq.(3.18) [203].

Next, it is aimed to determine the sensitivity of the measurement system, in order to evaluate whether or not the measured changes in domain walls are above the lower limits of the set-ups sensitivity. This problem is divided into two steps: (i) determination of the phase detection limit of the set-up, followed by (ii) linking of the spatial changes to the changes in the measured phase (transfer function), so that the instrumental error can be linked to the spatial error. The first step is not a trivial problem, since it involves a precise knowledge of measurement parameters (including those of the electronic components), and an exhaustive knowledge of various sources

of noise. For that matter, it is worthwhile to simplify the problem by assuming that the instrumental sensitivity is equivalent to the thermal noise [204]

$$F'_{zThermal} = \sqrt{\frac{4ck_bT\Delta B}{\omega_0 QA^2}} \quad \textbf{(4.19)}$$

Where c is the cantilever force constant, ΔB is the bandwidth, Q is the quality factor, k_B is the Boltzman factor, and A is the oscillation amplitude, with ω_0 being the resonance frequency. Typically for the set-up used in the present work thermal noise can be ~ 1.62 $\times 10^{-6}$ N/m which transfers {Eq.(2.7)} to a phase noise of the order of 10^{-4} degrees.

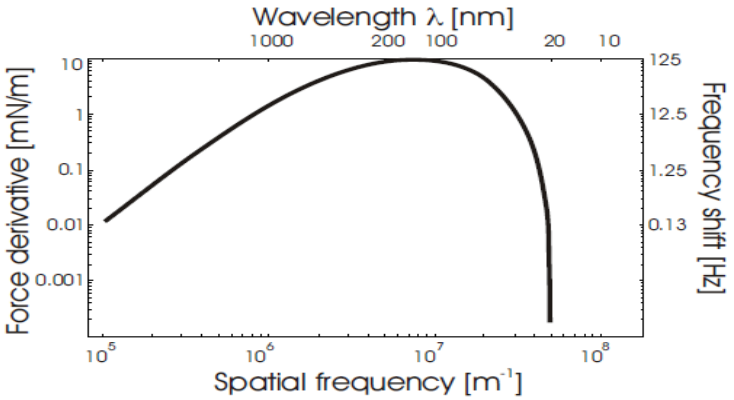

Figure 4.16 A typical response transfer function in MFM [205].

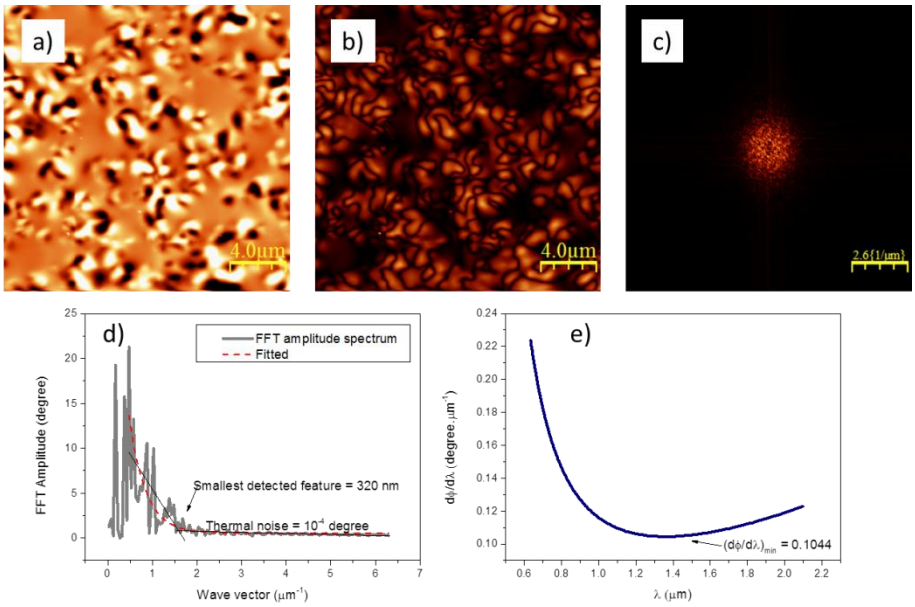

Figure 4.17 An MFM image (a), chosen for carrying out FFT analysis for resolution determination, along with an absolute transform (b), highlighting a wide distribution of domain widths and a Fourier transform (c) of the same image. (d) is the amplitude spectrum obtained by the FFT at different frequencies (wavevector k_x), whereas (e) is the differential of this spectrum w.r.t wavelength ($1/k_x$).

The second step of establishing a link between the spatial change (*x*,*y*) to the measured phase, is limited since classically a response transfer function (RTF) in Fourier space that can help correlate the measured phase to the observed spatial wavelengths (*1/K*), requires a-prior knowledge of the sample magnetic charge distribution. A response transfer function relates the tip sample interaction model (involving variables like tip-sample distance, sample thickness, tip magnetization and sample magnetic charge distribution) to the resultant force or force gradient in Fourier space. Since this function lies in the a Fourier space, it is convenient to relate spatial features (wavelengths) to the measured values of MFM phase [205]. Figure 4.16 illustrates one such response transfer function, calculated theoretically by considering the tip as a monopole. In the present case, since a-priori knowledge of the tip-sample magnetic interaction is not feasible, it is worthwhile to construct a frequency spectrum (FFT) of a typically observed MFM phase map measured on the hexaferrite based composites, especially with a wide distribution of domain sizes, assuming that this would be a good approximation to a response transfer function. Figure 4.17d shows the amplitude spectrum of the corresponding MFM image (top). Owing to the symmetry of the FFT image, the spectrum was taken only along k_x, for the sake of convenience. The amplitude was normalized by equating the maximum value obtained in FFT to the amplitude of the MFM-phase image (max –min). The smallest detected features size of 320 nm, inferred as half of the wavelength ($1/k_x$) value that could just be detected above the noise level. It can be seen that the smallest feature lies well above the estimated width of the tip shape function (78 to 115 nm). This means that any decrease in the smallest feature is reasonably detected as long as it is not larger than the lower limit of 205 nm (320 nm − 115 nm). Now, moving towards the goal of estimating the minimum measurable spatial change, the differential of the amplitude spectrum w.r.t λ was taken (Figure 4.17e only represents the part above noise level). Now, in order to set a lower limit on the spatial detection sensitivity, a minimum value of this differential is considered (0.1044 degree/μm) at which the minimum amount of spatial change (increase or decrease) is given as

$$\Delta\lambda_{min} = \frac{\Delta\phi_{min}}{(d\phi/d\lambda)_{min}} \quad \textbf{(4.20)}$$

where $\Delta\varphi_{min}$ corresponds to the thermal noise (10^{-4} degree). This yields a minimum measurable spatial change of about 1 nm. This analysis counters both arguments of larger tip radius as well as the large pixel pitch, as presented in the previous section; as per the estimated detection limit, a spatial change as small as 1 nm is capable of inducing a phase between two adjacent pixels, which is well above the assumed noise level.

At this point it needs to be re-emphasized that the aim of this analysis is to determine the minimum measurable spatial change in a single feature and not the corresponding resolution itself. Any spatial feature, smaller than the pixel pitch) is still going to be unresolved. However, if a feature, which is just above the resolution limit (>150 nm), expands by a value as low as 1 nm, the expansion at least will be traceable based on the presented analysis.

Now, what has been neglected so far is the standard 5% error that exist in the cantilever Z height control [56]. By considering this error and evaluating the error in the tip shape function from the relation $1.15Z_0$ an error of about 5.75% which is about 5.75 nm for a tip height of 100 nm, has to be expected, since it is higher than the otherwise calculated detection limit of 1 nm. By taking into consideration this error of 5.75 nm, the smallest measured change of 6 nm is still significant.

5 The Direct Magnetoelectric Effect: In-Situ Piezoresponse Force Microscopy

The direct magnetoelectric effect, which in the context of magnetoelectric composites relates to the generation of macroscopic electric charges as a consequence of magnetic field induced stresses at the microscopic FE-FM interfaces. It is thus expected to manifest distinctive and non-trivial features at the local scale. The foreground for these manifestations as laid out in chapter 1 (section), points toward existence of strain/stress gradients and a higher concentration of the same in the vicinity of interfaces. As a result of this, the stress induced effects on the ferroelectric phase are also expected to follow a similar spatial distribution.

Experimental investigations of these manifestations primarily comprise of a simple approach in that any consequential stress induced changes in FE domain patterns are non-destructively mapped. The magnetic field is applied externally to the whole sample as described in section 2.1.6. As a result a microscopic stress distribution identical to the one in the case of a typical bulk direct ME measurement will occur throughout the sample. Ideally, probing a microscopic spot on the sample can be considered equivalent to sampling out of the entire distribution of the local variations (*sample frame)*. However, in reality it has to be taken into account that the inhomogenity in microstructural features corresponding to each *sample frame* will lead to different local stress distributions. The following sections of this chapter discuss about the in-situ investigations, and later evolves on the premises of necessary data analysis using Principal Component Analysis (PCA).

5.1 Variable- Field Piezoresponse: Qualitative Analysis

Single frequency PFM imaging of the composite sample was carried out under magnetic field with the purpose of exploring any qualitative domain configuration changes. Figure 5.1 shows a sequence of PFM images acquired on the SrM-BTO (30/70) sample at magnetic field ranging from 0 – 1500 Oe. It shows slight weakening of the vertical PFM signal intensity as the magnetic field increases. On the other hand there are simultaneous but stronger changes in the Lateral PFM contras t. It has to be noted that the images show the X signal i.e. $A \cdot \sin\varphi$ hence the changes correspond to either a variation in φ or in A. A variation in φ is very unrealistic as this will mean a gradual switching of the polarization merely by the small ME stress. Hence it is presumed that the observed changes correspond to a changing PFM amplitude.

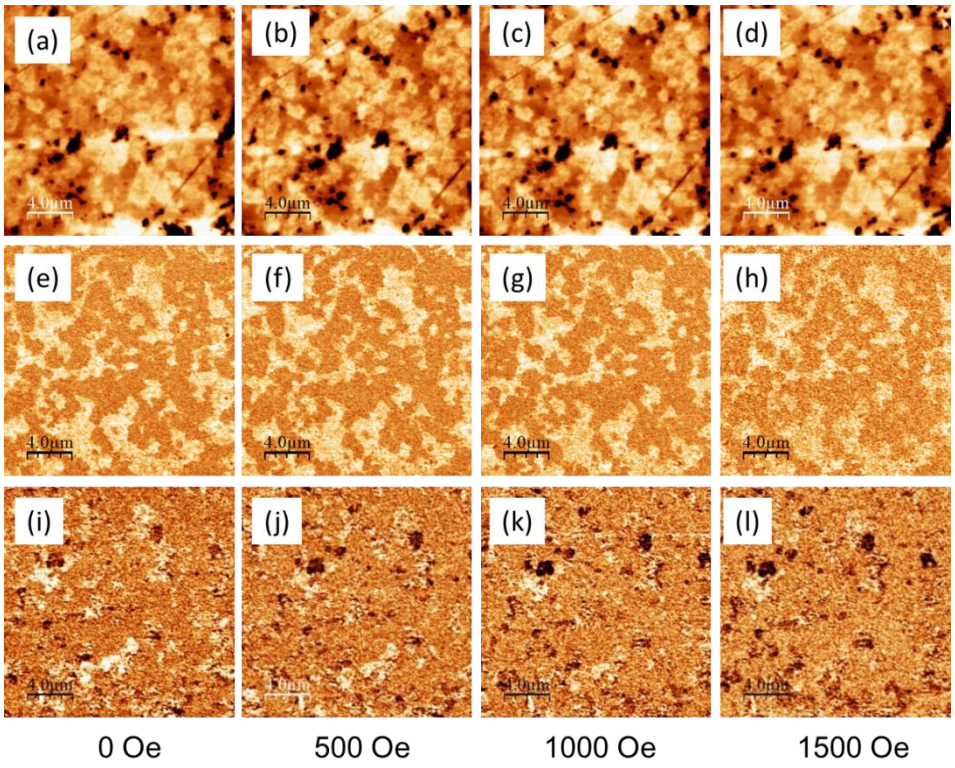

Figure 5.1 Sequence of (a) – (d) topography, (e) – (h) vertical-PFM, and (i) – (l) lateral-PFM images, acquired on the SrM-BTO sample at different magnetic field values (bottom).

Similar experiments were carried out on the spinel based organosol synthesized CFO-BTO (50/50) system (Figure 5.2). Also in this case there were some changes in PFM contrast under a magnetic field. However, in the case of the spinel based samples the nature of these changes is often different. As can be seen from Figure 5.2, the marked regions in the PFM images at higher magnetic field show changes which are in contrast with those observed in the case of the hexagonal based system (Figure 5.1), where both vertical and lateral PFM amplitude decreases with increasing magnetic field. This simply highlights a different form of magnetic field modulation of the out of plane PFM amplitude, and simultaneously corroborates the previously made hypothesis that only amplitude is modulated and not phase.

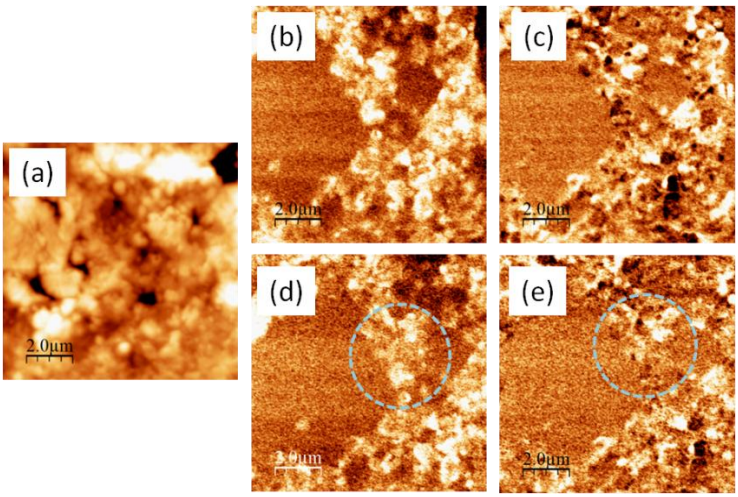

Figure 5.2 Shows (a) topography of a spot on the organosol synthesized CFO-BTO (50/50) sample, along with the corresponding vertical and lateral PFM images at magnetic field values of (b) – (c) 0 Oe, and (d) – (e) 8000 Oe respectively.

Other samples that were studied using similar experiments, showed feeble to no change in PFM amplitude as a function of magnetic field. The closeness of these other spinel and hexaferrite based samples to the studied samples (SrM -BTO, and organosol based CFO-BTO), points out that similar changes are also to be expected in this system. Hence the feeble to no response corresponds to a possible detection limit in PFM. For that matter in-situ PMF imaging close to resonance frequency can be useful, as the high sensitivity associated with imaging at cantilever resonance [206] can unravel any existing magnetic field modulation of the PFM amplitude. However, imaging at resonance has certain parasitic influences which in the form of artifacts hinder any clear qualitative analysis of the obtained images. This issue can be circumvented by integrating sophisticated statistical data analysis as discussed in chapter 2. The next few sections are devoted to this very approach along with a discussion about any possible estimation errors.

5.2 Sparse Sequential In-Situ PFM at Resonance Frequency

Sequential imaging has been widely applied in biological studies [207]. The goal of such imaging has been confined to studying morphological dynamics and has led to advancement towards high-speed atomic force microscopy [208–212]. However a semi quantitative study analogous to magneto-optic Kerr microscopy [213–217], using sequential SPM imaging has been seldom realized. For the static phenomenon in concern, the sequential nature of SPM can hardly be a problem. However, the bigger issue is the correlation of the acquired images in terms of their spatial co-ordinates as well as the fluctuation of measurement parameters. In the following, we explain the set-up and discuss the issues associated one by one.

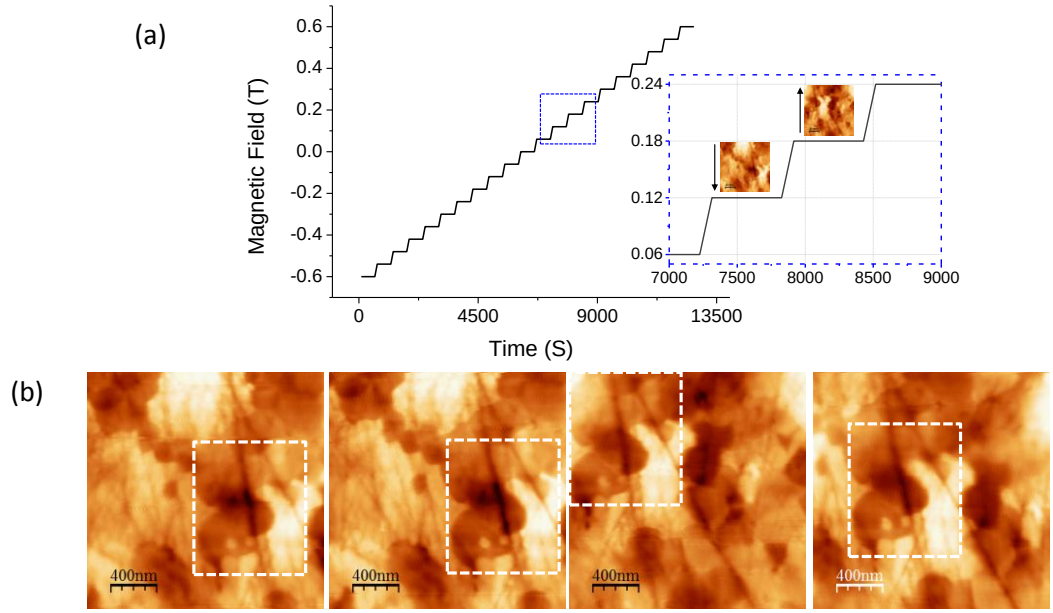

Figure 5.3(a) a time resolved magnetic field curve, describing the sparse-sequential PFM acquisition. (b) shows consecutive topography images, randomly chosen from the acquisition sequence in (a). The dashed squares in (b) marks the correlated features, demonstrating the sequential drift in the images.

The sparsely varying magnetic field was applied as shown in Figure 5.3a, where images were recorded during the rest period (steps). The change of sign in magnetic field here refers to the opposite in plane directions. In order to make the acquisition process ambient and time efficient, the whole process was automated and no manual image correction was applied during measurement. Hence the images were highly misaligned as shown in Figure 5.3. In addition it has to be noted that each consecutive image switches slow scan direction from being forward-up to forward-down (black arrow; Figure 5.3a). This makes the process continuous by avoiding the shifting of tip at the origin every time a new image begins, but simultaneously also adds an alternating skewing in the consecutive images. Although the linear drifts between consequtiveimages are corrected using the algorithm presented in Chapter 2, the skewing/rotational drifts which are caused by thermal drifts within a scan cannot be taken care of without modifying the dataset itself [218].

In addition to the spatial drift and rotations, another bigger change in sequential imaging is associated with the physical parameters determining each scan. Although PFM is sensitive to several instrumental and environmental factors, it is worthwhile to generalize a scheme of factors which concern tip-sample contact mechanics and the time dependent wear of tip and sample as a result of continuous scanning. Figure 4.4 shows this scheme of factors. Due to the stochastic topography distribution, a precise prediction of the involved wear is not possible, however it can be easily inferred that the sample (ferrites + BTO) being mechanically harder than the silicon tips would hence cast wear onto the tip. Rigorous wear investigations on silicon tips [219] show that

initial wear (up to 20 cycles of reciprocating 1.6 μm strokes) quickly removes the amorphous silicon layer exposing the crystalline silicon which than wears off steadily, flattening the tip.

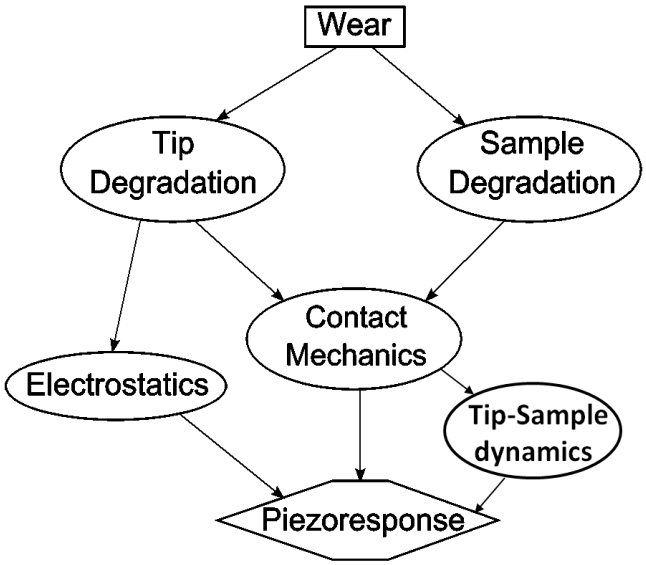

Figure 5.4 Schematics of the relationship between the tip wear, representative of the continuous scanning process, and the observed piezoresponse.

The theoretical review pertaining to various regime contributing to PFM contrast [220] suggests that for a particular set of material properties under consideration, various dominating contact regimes and hence the type of contributions, like electromechanical and/or electrostatic, to the PFM images can be delineated depending on the experimental conditions, namely, tip indentation-force and radius. Referring from this particular delineation to the present case, where a cantilever of force constant ~ 15 N/m, and radius ~ 10 nm were used at a set point deflection of ~ 100 nm (Indentation Force ~ 1.5 μN), strong (classical) indentation of the tip should be expected (neglecting the electrostatic contribution). Within this indentation regime, where the potential of the contact area is equivalent to the potential of the tip, and the vertical component of electric field (E_Z) is assumed to be zero farther from the contact point, the tip indentation (tip displacement) is given by a solution of a linear relationships between the tip force *P*, indentation depth h, and the applied potential $V_s = V_{tip}$ [221] as follow

$$h = \frac{a^2}{R} + \frac{2\beta}{3\alpha} V_{tip} \quad \textbf{(5.1)}$$

$$P = \alpha \frac{a^3}{R} - \beta a V_{tip} \quad \textbf{(5.2)}$$

Where α and β are constants depending on tip geometry, with a being the contact radius. However, presence of a thin dielectric layer between the tip and the sample cannot be ignored, which would ultimately lead to a potential at the surface attenuated by a factor γ ($V_s = \gamma V_{tip}$). Now, taking into consideration Eq.(5.1) and (5.2), together with the existence of a tip attenuation

layer, following scenario can be predicted for the present case of sequential imaging where a continuous wear of the tip leads to a steadily changing tip surface contact in addition to removal of the tip attenuation layer, and hence a steadily changing piezoresponse with increasing image sequence.

Since the tip is operated close to the resonance frequency for better sensitivity, it is necessary to take into account the contact mechanics dependence of the tip-sample dynamic behavior. It is known that factors like topographic curvature and variable local mechanical properties strongly affect the tip sample contact mechanics [222], introducing significant spatial variations of the contact resonance frequency and tip-sample dampening (quality factor Q) [206]. However, in the DART mode of operation the tip resonance is continuously tracked by the dual frequency feedback (section 2.1.4). Assuming an efficient resonance tracking, it can be inferred that it is the spatial variation of quality factor that will matter as far as the variation of piezoresponse in sequential images is concerned. The percentage of spatial variations in quality factor is often found to be relatively small as compared to those in case of the contact resonance frequency. As a result, in the present context of sequential PFM imaging, steadily changing contact mechanics due to tip wear will lead to a small but steadily changing piezoresponse.

The aimed correlated semi-quantitative study of the sequential PFM image, where each pixel corresponding to an i^{th} image is considered correlated to the same pixel of the $(i + 1)^{th}$ image ($\{x_i,y_i\} = \{x_{i+1},y_{i+1}\}$), will comprise of two different parasitic modulations of the correlated pixel values. The one corresponding to image drifts/rotations will lead to a zig-zag modulation of the correlated pixels of each consecutive image, whereas the changing contact mechanics will lead to a monotonic modulation. Both these modulations are expected to be present to some degree on top of an unknown magnetic field modulation of the piezoresponse. Since the magnetic field modulation of piezoresponse is expected to be symmetric w.r.t. zero magnetic field, owing to the identically symmetric nature of magnetostriction, it is hence distinct from the above mentioned parasitic modulations. Deciphering of precisely this modulation out of the prominent parasitic modulations and less prominent white noise, is precisely what constitutes the task of performing sophisticated statistical analysis (PCA) on the acquired data set.

5.3 Principal Component Analysis of Variable Magnetic Field PFM

The factor mentioned in section 4.2 necessitates use of sophisticated data analysis tools for such studies. Moreover the ideal goal of such experiments would be not just to extract the magnetic field modulation of piezoresponse, but to also simultaneously map the spatial distribution of the same. Like in any method of data analysis, the first step is the suitable pre-processing and data representation. The pre-processing steps to be performed include (i) drift correction, followed by (ii) line wise (area) normalization, and finally (iii) vector representation of the acquired images (Figure 5.5) using algorithms mentioned in section 2.4.3. In addition to smear the effect of in-image rotations/skewing additional step of pixelation was carried out, in which groups of pixels divided by a heuristically chosen grid

were averaged to give a new pixel. Here in the case of sequential imaging, each pixel co-ordinate (x_i, y_i) will correspond to a data-set vector with its component being the correlated-pixel values at n different magnetic field steps. These vectors are than arranged in an increasing sequence of their corresponding pixel location, to form a data-matrix (Figure 5.5c). Such choice of data-matrix scheme is specifically chosen to render the pattern or the magnetic field modulation of piezoresponse into each vector. This pattern resembles the example of mixed patterns provided in section 2.4.3, with the time replaced by the applied magnetic field in the present case. However, it has to be noted that owing to white noise the patterns captured in each vector are arbitrarily distributed. A consolidation of these patterns can be hence achieved by normalizing each vector with the maximum value occurring in it.

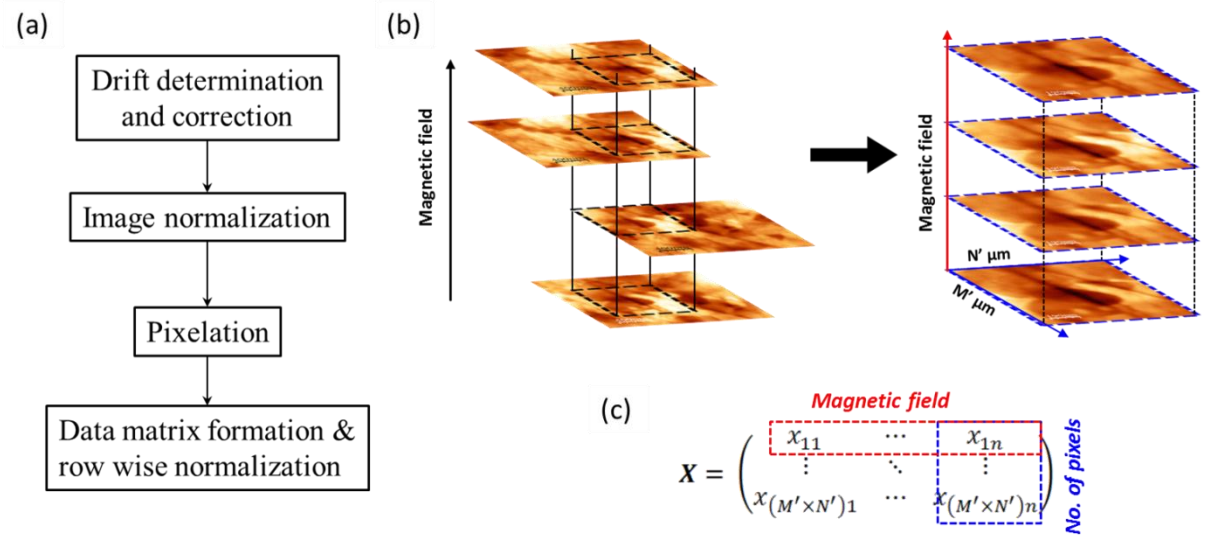

Figure 5.5 (a) shows the algorithm adopted for pre-processing the sequential PFM data-set for PCA. (b) illustrates the drift correction process, where a random section of the acquired PFM section is shown before (left) and after (right) the drift correction. (c) shows the arrangement of the data-matrix used for PCA decomposition.

As a result of such a data matrix formulation, the observed modulations of piezoresponse constitute different features in the data-set. These, as discussed in Chapter 2, correspond to the different directions in the data hyperspace along which the variances are maximum. Hence applying the non-cantered PCA on this data set using algorithms mentioned in chapter 2, will result into rotation of the whole data set such that the new data set will have maximum variance along the first vector component, and the mutual second non-central moments of each vector will be minimized. The first principal component (1st row of the rotation matrix) will correspond to the feature with highest sample variance, and likewise the next following components will represent features in decreasing order of their sample variance. The orthogonality conditions imposed in PCA have to be kept in mind before interpreting the extracted patterns. In addition to this the score matrix, as discussed in chapter 2 will be a reflection of how much of each principal

component is present in the actual data-set. Hence remapping the score matrix into the original data namely the acquired images will hence represent a spatial distribution of the extracted patterns.

Figure 5.6 shows the decomposition of components for a data set corresponding to the acquisition on BaM – BTO (35/65) sample. Out of the four patterns shown, the 1st pattern (Figure 5.6c) corresponds to the most prominent feature in the data set, followed by the less prominent features (Figure 5.6d – f). Simultaneously, the corresponding score maps represent the score of the corresponding pattern at each spatial (*x*, *y*) point. A closer look at the first pattern points toward a magnetostrictive origin as discussed in the preceding section. The correlation of the PFM amplitude image (Figure 5.6b) and the score maps for the 1st component (Figure 5.5g) is indicative of the pattern being localized to the piezoactive BTO regions. This indirectly suggests a magnetostrictive stress modulation of the measured electromechanical coupling (d^{33}_{Local}). The successive components (2 – 4) along with their respective score maps reflect the features corresponding to the image drift/rotation (zigzag type), as well as the changing contact mechanics (monotonous decrease).

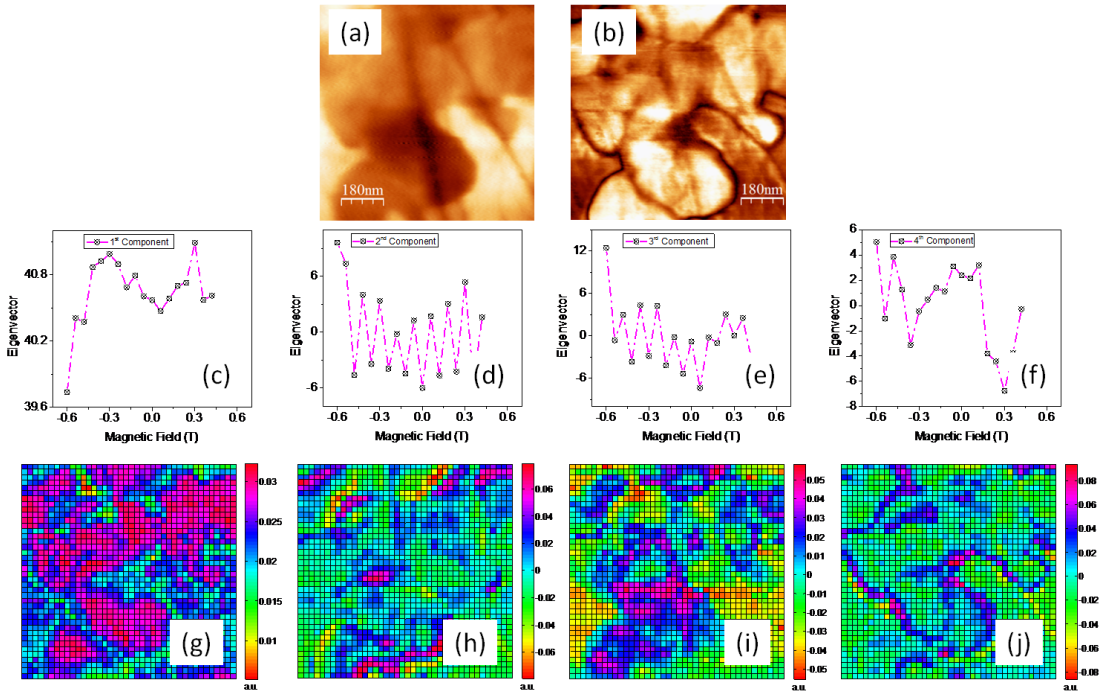

Figure 5.6 (c) – (f) the principal components, and (g) – (j) the corresponding score maps, decomposed from the sequential PFM data-set acquired on the BaM-BTO sample. (a) and (b) show the topography and vertical (DART) PFM images of the chosen spot, respectively.

A similar acquisition and decomposition was carried out on a CFO-BTO (40/60) composite system (Figure 5.7). The decomposed components in this case however have a slightly different scheme as compared to those in case of BaM-BTO (35/65), with the first two components being apparently relevant (symmetric w.r.t. zero magnetic field to some degree), while the rest still

encompasses the parasitic modulations. It can be noted that in both BaM-BTO and CFO-BTO samples the zigzag features, that correspond to the residual drift/rotation of images, are highly localized at the interfaces between regions with different contrast. This can be easily understood by considering the fact that the pixels belonging to these interfaces are highly susceptible to undergo a variation upon a drift/rotation as compared to the pixels belonging to the centre of the regions with different contrast. At this point, it is necessary to hold a speculation concerning the relevant components in case of both samples, in that the symmetrical patterns (Figure 5.5g, Figure 5.6g – h) might be a result of an additional magnetic field modulated drift/rotation of the images, which is residual to the lateral drift correction step. Such modulation would also be symmetric w.r.t. zero magnetic field. However, it is easy to check the existence of any such drifts by doing a similar PCA decomposition of the corresponding topography images, as the latter are expected to be void of any magnetic field modulations. At the same time the topography images in both BaM-BTO and CFO-BTO samples show distinct regions with different contrast levels, providing sharp interfaces that can act as efficient test sites for the speculated drifts.

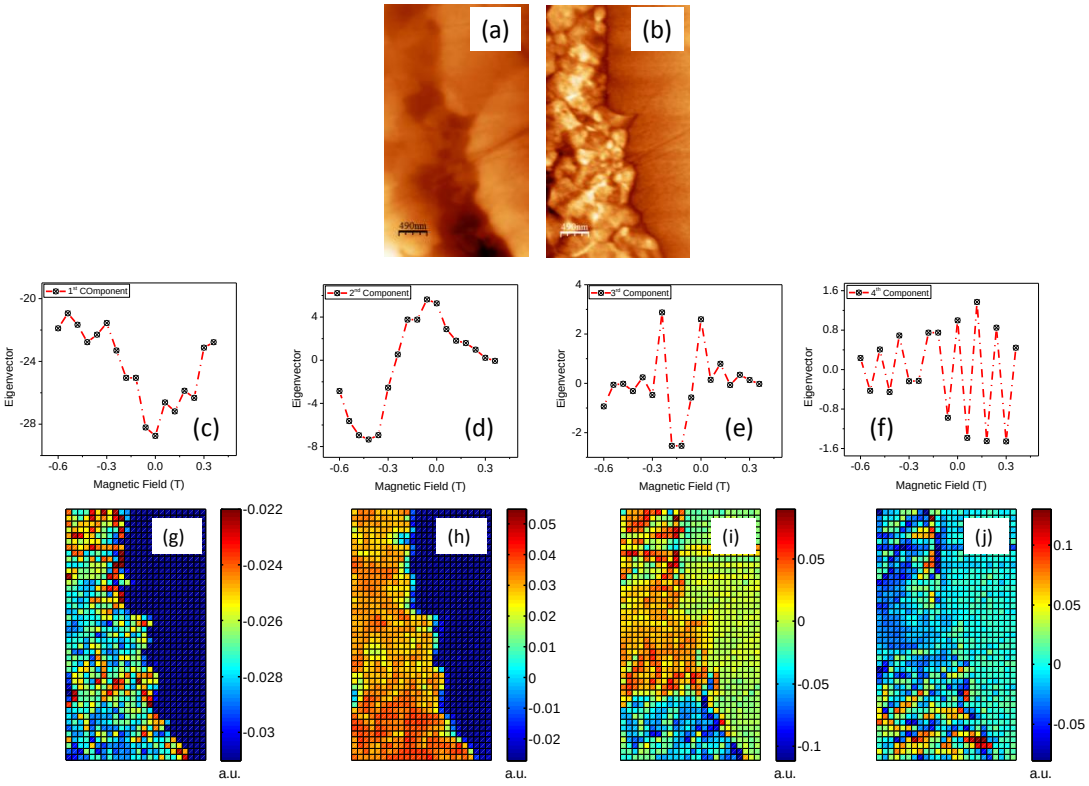

Figure 5.7(c) – (f) the principal components, and (g) – (j) the corresponding score maps, decomposed from the sequential PFM data-set acquired on the CFO-BTO sample. (a), and (b) shows the topography, and vertical (DART) PFM images of the chosen spot respectively.

Figure 5.8 shows such decomposition carried out on the topography images of BaM – BTO and CFO – BTO samples. The most prominent components (1st component) in both cases show non-existence of the magnetic field modulated drift that was suspected, and simply reiterates the

existence of the zigzag type residual drift. This increases the confidence level in the observed relevant patterns (Figure 5.5g, Figure 5.6g – h) of being magnetostrictive in origin.

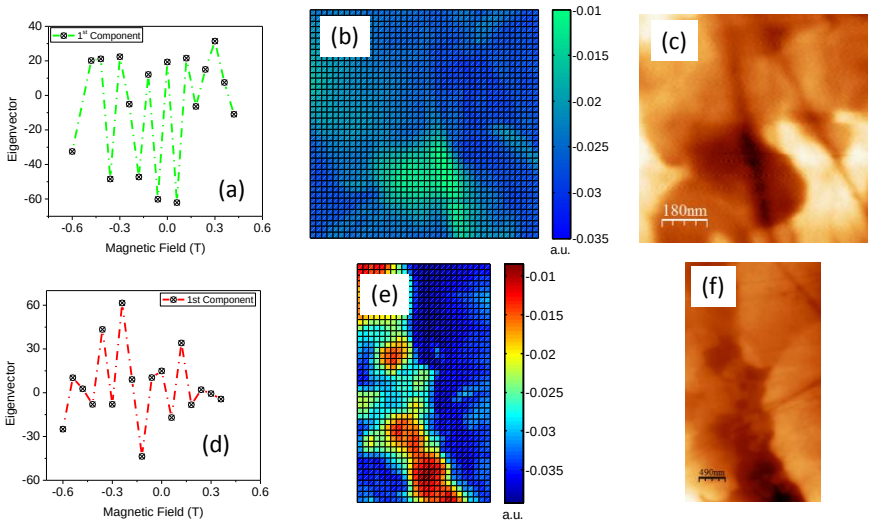

Figure 5.8 {(a), (d)} the principal components, and {(b), (e)} the corresponding score maps decomposed for the topography images {(c), (f)} acquired on the BaM-BTO, and the CFO-BTO samples respectively.

Having ruled out any possible artifacts it is worthwhile now to focus on the relevant patterns. Especially interesting are the 1st and 2nd components in case of the CFO-BTO (40/60) sample that seems to be displaying two different traits. The bright spots in score maps corresponding to the 1st and 2nd component are almost mutually conjugative, which means that the two different features are distributed exactly at two different spatial locations. The qualitative distinction between the two features, at first glance, indicates that both show a certain degree of symmetry w.r.t. zero magnetic field, with the 2nd component being non-symmetric as compared to the 1st one. Hence, both can be presumed as a first approximation to be of magnetostrictive in origin, i.e. a magnetostrictive stress modulation of the observed piezoresponse (electromechanical coupling). The qualitative difference between these two components might be associated with two different stress regimes that exist at different locations on the studied sample surface. This will be addressed in detail in the next section. The anomalous nature of the 2nd component however needs to be addressed in the context of the limitations of PCA.

As already discussed in chapter 2, PCA decomposes the high directions of variance corresponding to different features but with a limitation that each direction has to be orthogonal to all other directions. In the presence of multiple features that correspond to multiple directions of high variances, as shown in Figure 2.16 (*broken heart* problem; section 2.4.3). The decomposed principal components will hence not represent the actual features, rather there will be some degree of intermixing between the components depending on the shape of the data swarm in the *n* dimensional hyperspace. In the present case, where the dimension of the data are almost of the order of 20, it is not trivial to visualize the processed data-set in order to identify

any similarity to the *broken heart* problem. To overcome this problem, a novel approach of data visualization has been adopted, where the dimension was reduced by partitioning it such that 4 visually helpful groups of parameters can be calculated, namely position (in a 3D Cartesian system), body colour, edge colour, and size of the data markers. Figure 5.9 schematically shows the partitioned evaluation parameters. In each case, however, heuristic trial and error was carried out as far as the partitioning and scaling of the parameters is concerned in order to fit the visualization within observable limits. Followed by this, each of the data vectors (each pixel as a function of magnetic field) were projected onto a 3D scatter plot based on the calculated parameters.

Figure 5.9b and Figure 5.9c show such scatter plots for the BaM-BTO and CFO-BTO samples respectively. It can be seen that in both cases there exist a strong observable correlation in the marker characteristics, namely size, position, body colour, and edge colour. This correlation of data markers represents a distinction between different patterns (dashed arrows) presented in the data-set, which are manifested onto the 4 calculated visual parameters. Simultaneously the marker distribution also signifies directions of high data variances, which are actually identified by PCA. The data-set concerning the BaM – BTO sample (Figure 5.9b) shows a single high variance direction that is highly prominent as compared to any other possible variance directions. On the contrary, in case of the CFO – BTO data-set (Figure 5.9c) there seems to be 2 apparent directions with equally high variances. This in a rough sense signifies the existence of a *broken heart* type of data-set for the CFO – BTO sample, which can be speculated for being the origin of the observed anomaly of the corresponding 1^{st} and 2^{nd} principal components (Figure 5.7g – h). Although the generated visualization cannot perfectly characterize the shape of the data-set in an n-dimensional hyperspace, it will not be irrational to rely on it in arguing that the unidirectional nature of the data-set concerning the BaM – BTO sample is what culminates into its 1^{st} component centric nature of the PCA decomposition. Likewise, the bidirectional nature of the CFO-BTO data set results into its 1^{st} and 2^{nd} principal component being relevant. In addition, it has to be noted that out of the two prominent directions of high variances in case of the CFO – BTO data-set, one ($P1_{actual}$) has apparently a bit higher variance as compared to the other one ($P2_{actual}$). As a result, the decomposed 1^{st} component P1 is more closer to $P1_{actual}$, which means that $P1_{actual}$ and P1 both closely resembles the symmetric magnetic field modulation of PFM amplitude, whereas the 2^{nd} component P2 is slightly deviated from $P2_{actual}$ but still encompasses the magnetic field modulation up to certain degree. In contrast to this for the BaM – BTO data set, the decomposed 1^{st} component P1 exactly coincides with the corresponding $P1_{actual}$ directions as seen in the visualization (Figure 5.9b).

Another striking distinction between the cases of the BaM-BTO and CFO-BTO samples is the scale of the mapped regions, which reflects the best results of many trial and error attempts carried out at different scales. On the one hand, it can be inferred that the BaM-BTO sample manifests any identifiable magnetic field modulation only at a smaller scale (grain level interface). On the other hand, the CFO-BTO sample manifests an identifiable pattern for a

relatively larger scale (partial agglomerate interface). This means it has to do with the strength of the distribution of the magnetic field modulated features in the entire data-set. I.e. a larger scan on the BaM-BTO sample, that interestingly also happens to be highly agglomerated, would have lower number of spots that manifest a magnetic field modulation as compared to those that don't. In a way this suggests that with increasing degree of agglomeration, as the number of FE-FM interface decreases, the effect is limited to less number of interfaces, and hence is macroscopically weaker.

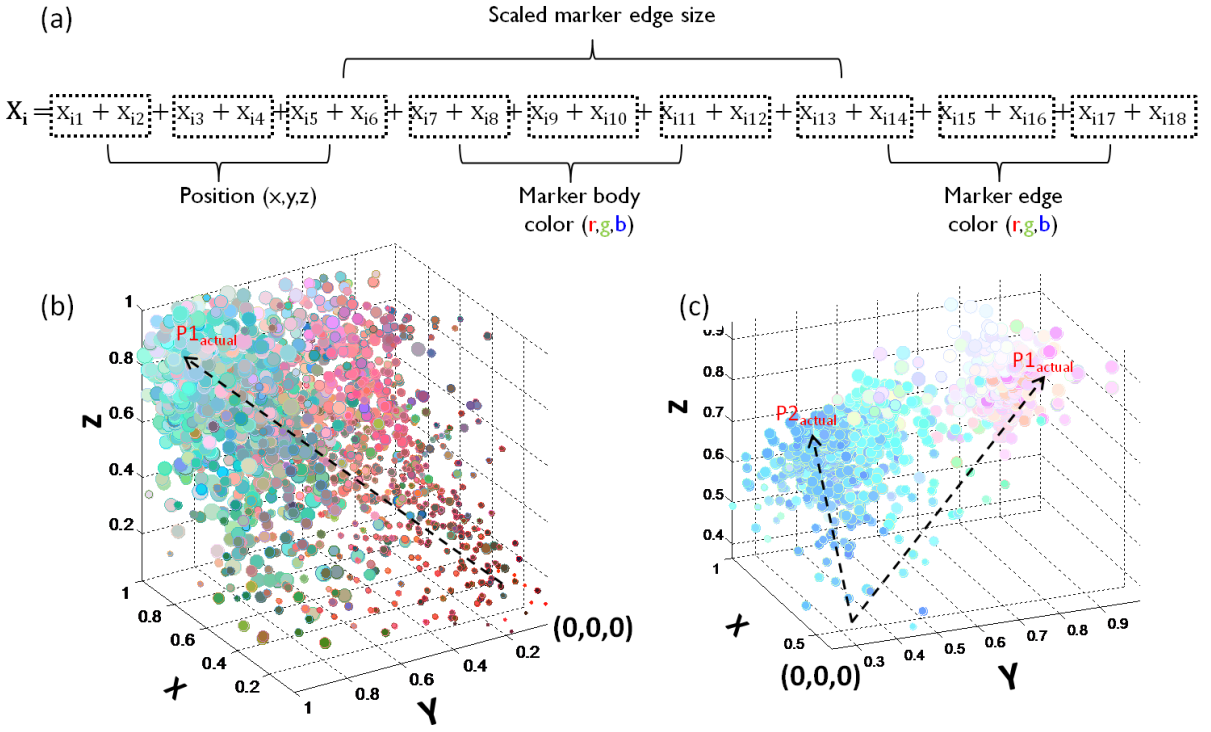

Figure 5.9 (a) shows the partitioned evaluation of the four visualization parameters, used to plot the data-sets corresponding to (b) the BaM-BTO, and (c) the CFO-BTO samples in 3D.

In addition to the studied BaM-BTO and CFO-BTO systems, the other systems SrM-BTO and NFO-BTO were also analyzed using the same approach. Fig.4.10 shows the decomposition results corresponding to the SrM-BTO and NFO-BTO samples, only the most relevant components along with their corresponding score maps are shown. It can be seen that unlike the case of the BaM-BTO and CFO-BTO systems (Figure 5.6, Figure 5.7), the SrM-BTO sample manifests a relevant pattern as a 2nd component. In addition to this, the qualitative nature of this pattern (Figure 5.10b) is anomalous, being similar to the case of CFO-BTO 2nd component (Figure 5.7d). This once again points towards the existence of a *broken heart* type data shape. In order to check this, the data-set of SrM-BTO was also projected using similar reduced dimensional representation as in the case of the BaM-BTO and CFO-BTO samples (Figure 5.11).

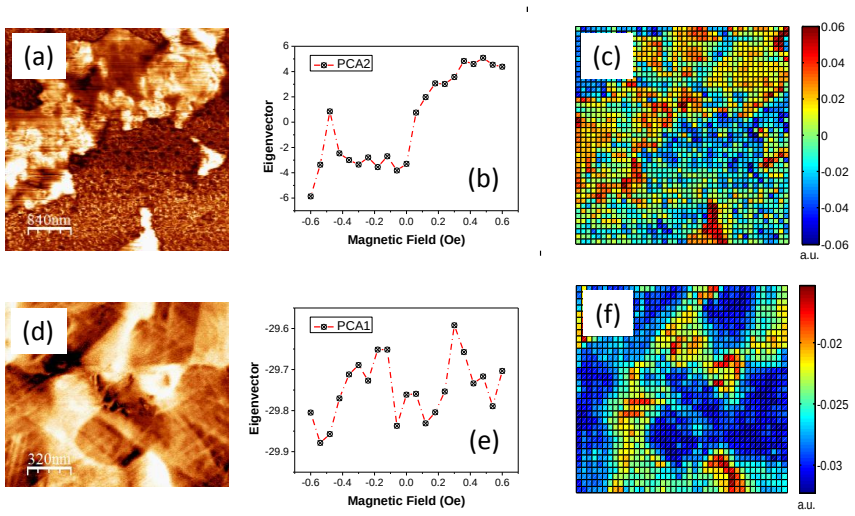

Figure 5.10 {(b), (e)} the principal components, and {(c), (f)} the corresponding score maps decomposed for the topography images {(a), (d)} acquired on the SrM-BTO, and the NFO-BTO samples respectively.

It can be seen from Figure 5.11c that indeed there exist a *broken heart* type data distribution, however it is not so distinct as compared to that in case of CFO-BTO sample (Figure 5.9b). This up to some extent can be rationalized as the cause of the anomaly in the decomposed components corresponding to the SrM-BTO sample. As shown in Figure 5.11a, the first component of SrM-BTO decomposition is not completely irrelevant, since qualitatively its envelope still shows some contributions identical to the anti-symmetric 2nd component (Figure 5.10d), in addition to the zigzag and the monotonic contributions. Which means both 1st and 2nd components show some degree of magnetic field modulation of the PFM amplitude, with the 2nd component doing that more prominently as compared to the 1st component. This fact is also corroborated from the score maps corresponding to the 1st component (Figure 5.11b) which only partially correlate with the corresponding PFM active regions in (Figure 5.10a).

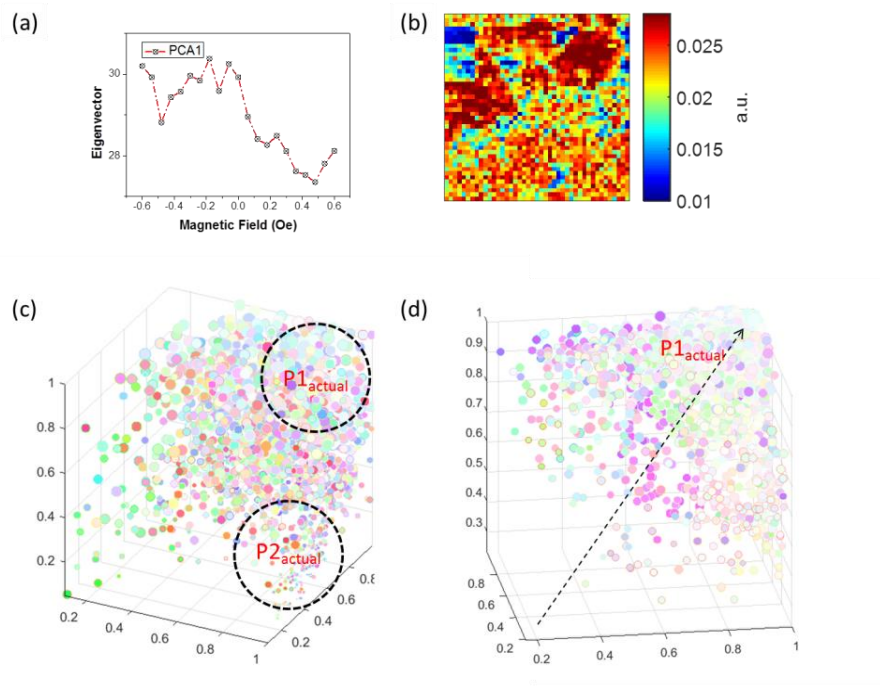

Figure 5.11 Shows the 3D plot of the PFM data-sets corresponding to the (c) SrM-BTO, and (d) the NFO-BTO samples, realized using the identical parameterization algorithm as shown in Figure 5.9a. (a), and (b) shows the first principal component, and the corresponding score maps respectively, for the PCA decomposition of SrM-BTO data set (Figure 5.10).

On the other hand, the decomposition for the case of the NFO-BTO sample shows a perfectly symmetric 1st component, which apparently relates to the magnetic field modulation of PFM amplitude. Also the corresponding data swarm (Figure 5.11b) is unidirectional in terms of maximum variance direction, identical to the case of BaM - BTO (Figure 5.9b). It is worth noting that there exist interesting similarities amongst behavior of the NFO – BTO and BaM – BTO samples. In both cases only acquisition at a very small scale showed an observable effect, which projected unidirectional variance in the corresponding data-sets. The corresponding 1st components related to the magnetic field modulation of the PFM signal are interestingly nonlinear for both cases. Simultaneously, in both cases, the spatial distributions of the relevant patterns (1st component score maps) share unique traits in that the extent of those component increases gradually from the interface to the bulk of the FE region. Considering the fact that, in both cases the observable effects concern a smaller scale imaging, one is essentially probing the effect at the grain level. On the other hand, exactly opposite similarities exist between the cases of SrM-BTO and CFO-BTO samples, where the data-sets comprise of two different features (*broken heart*), which are interestingly distributed at two different spatial locations (Figure 5.7g, g Figure 4.10c, Figure 5.11b). Based on these facts a hypothesis can be made, that investigations at the grain level (BaM-BTO, NFO-BTO) provide unique features owing to a lower microstructural inhomogenity involved. Whereas the investigations on a *partially random* (CFO-

BTO, SrM-BTO) microstructure would lead to multiple features, corresponding to the existence of multiple stress regimes due to microstructural inhomogenity within the sample frame.

Apart from the microstructural traits discussed in the paragraph above, there are also some manifestations of material properties (magnetostriction). A flying comparison of the most relevant components for each material system reflects that with decreasing magnetostriction the observed relevant patterns show equally decreasing changes in piezoresponse as a function of magnetic field. The CFO – BTO system which is associated with the highest magnetostriction shows the highest change in its piezoresponse at maximum magnetic field (Figure 5.7g), whereas the hexaferrite based systems which are both attributed to intermediate magnetostriction show a slight overlap of the noise/drift based trends (Figure 5.6g, Figure 5.10b). Likewise, the NFO-BTO system, which comprises the lowest saturation magnetostriction, shows a high degree of disturbance from the parasitic trends (Figure 5.10e).

5.4 Stress Coupled Electromechanics in $BaTiO_3$

In this section, explanations concerning the observed magnetic field modulation of the local electromechanical response are presented in context of the phenomenological theory of ferroelectrics. In ferroelectrics like $BaTiO_3$, as discussed in chapter 1, acoustic modes of crystal lattice dynamics are coupled to polar optical modes, forming the basis of coupling between the ferroelectric polarization and mechanical strain. This is phenomenologically cast into the classical expression, which relates the longitudinal piezoelectric constant with polarization {Eq.(2.12)}

Over the entire regime of applied electric field/stress the ferroelectric polarization P, as well as the piezoelectric strain ϵ are both non-linear quantities [223]. In case of displacive ferroelectrics like BTO they are linked to ionic/octahedral displacements [74]. The applied linearly varying electric field or stress that pulls the ions/octahedra in order to generate strain/dipole moment is countered by an atomic restoring force that varies non-linearly with increasing interatomic separation. This is what accounts for most of the observed non-linearities in ferroelectrics [74, 76].In the present context, it is useful to consider the scenario, where the stress applied to a BTO grains, due to magnetostriction, would lead to a static suppression/extension of the oxygen octahedral. From this stage, if any electric force (tip voltage) is applied, than it will encounter a different restoring force, as it would have been in absence of any applied stresses. Hence, every time when the AFM tip applies a small fixed AC voltage, the resultant AC displacement will be different at different applied stresses (i.e. magnetic field) due to the different restoring force. This scenario despite being valid not just in the case of the studied magnetoelectric composite but rather for any displacive ferroelectric under any form of applied stress, is sporadically addressed in literature often in the context of uniaxial [192, 224] as well as multiaxial [225] prestresssed piezoelectric device materials. Figure 5.12 summarizes results reported by Lynch et al. [192], where the applied compressive stress highly modifies the electromechanical characteristic (butterfly loop) of a PZT ceramic. As discussed here, increasing stress leads to a

non-linearly changing slope of the strain-field loop close to zero electric field, until ferroelastic switching takes place. In the absence of any DC bias in the PFM experiment, this slope is exactly what determines the observed PFM signal.

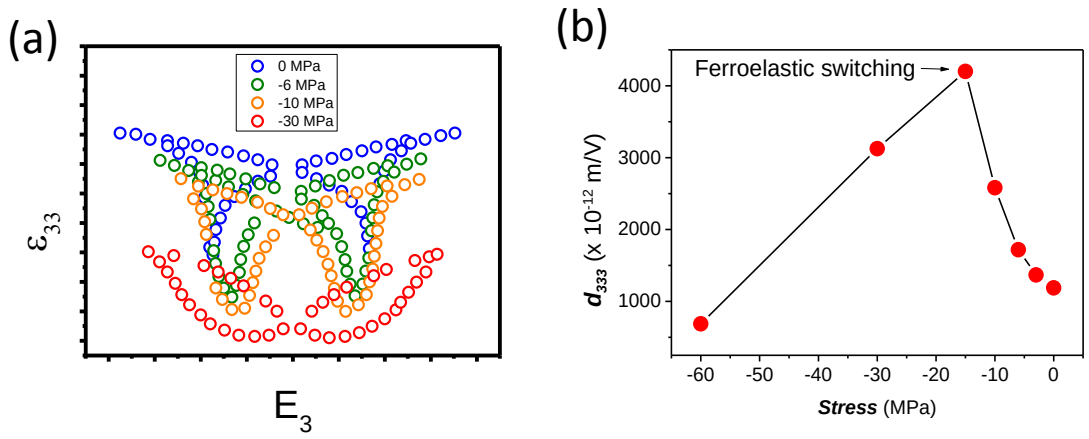

Figure 5.12 (a) shows schematic stress dependent strain-field loops reported for PZT, along with the variation of the d_{333} (slope of the strain-field curve (a) closed to zero field) w.r.t. to the applied stress [192].

As it was shown by FEM modelling of a typical inclusion-matrix case, resembling the studied magnetoelectric composites (Figure 1.23), magnetostrictive stress more that ~10 MPa is not expected in the composites, which means that the stress can be presumed to be below the ferroelastic switching limit. Hence, it can be rationalized that the linearly increasing magnetic field creates a linearly increasing stress (at least at low magnetic field) on the BTO regions, leading to a non-linearly varying PFM amplitude (Figure 5.12b). This is exactly the phenomena that is observed in the PCA decomposed components for all the studied ME systems (section 5.3).

Apart from the general non-linearity observed in the PCA components for all the samples, inflexions have been observed, specifically in the case of the BaM-BTO and NFO-BTO samples (Figure 5.6c, Figure 5.10e). For these cases, the PFM amplitude as a function of magnetic field changes non-monotonically, which cannot just be explained by the non-linearity in the variation of electromechanical coupling. Rather it has to do with the complex process of magnetostriction, which involves domain wall motion and domain rotation. As discussed in section 1.3.1, magnetostriction varies in a complex way as a function of magnetic field, in that at certain magnetic field a crossover from domain wall motion to domain rotation takes place leading to an inflexion in the magnetostriction along specific crystal directions (Figure 1.17). This phenomenon although discussed in the context of single crystals, can be equally extended to the studied ceramics where grains exist, whose orientation w.r.t. to the applied magnetic field is close to the critical directions along which such inflexion in magnetostriction occurs. This is then manifested as an aggregate effect in ceramics. It is interesting to note that though this complex magnetostrictive behaviour is to be expected in case of all the studied ME systems, it is only the

grain level PFM imaging (BaM-BTO, and NFO-BTO) that reflects it (Figure 5.6c, Figure 5.10e). Although this aspect needs rigorous theoretical investigations, it can be argued based on the experimental findings presented in this chapter that at a local scale (grain level) due to the absence of any aggregate background the complex behavior of magnetostriction is observable.

6 Mapping Fields in ME Composites: In-Situ Switching Spectroscopy Piezoresponse Force Microscopy

The essential effect of the magnetic field induced stresses in ME composites, which actually forms the basis of the direct ME effect, is to induce corresponding electric fields into the neighboring ferroelectric regions via the piezoelectric effect. Hence, the primary goal of probing local manifestations of ME effect comprise of mapping these ME fields. However, such mapping is limited in some sense due to the different electrical properties of both constituent phases. Any field that develops in the ferroelectric BTO phase, which following the findings of the previous chapters has to be significant only at the interface, should theoretically be completely screened by charge carriers from the highly conductive FM side of the interface. As a result, any experimental probe based method that relies on surface emanation of fields for their detection will be ineffective in mapping the ME fields. Figure 6.1 shows sequential KPFM images of the BaM – BTO sample, acquired at different magnetic field. Evidently, there are no significant changes in the mapped surface potential as the magnetic field increases. This primitively highlights the inefficacy of direct field observation techniques in exploring the ME generated fields. However, origins of this inefficacy still require rigorous corroborative experimental investigations.

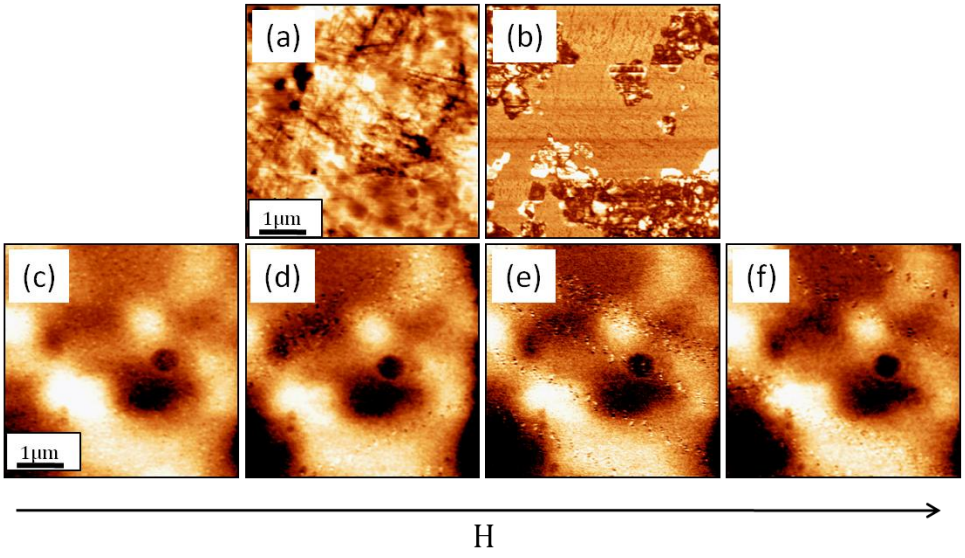

Figure 6.1 (a) Topography, (b) vertical-PFM amplitude (DART), and (c)-(f) the sequence of KPFM images acquired on an identical spot of the BaM – BTO sample, at different magnetic fields (increasing from 0 to 5000Oe, left to right).

The field distributions close to the interface still possess open questions as far as the theoretical perspective is concerned. Another theoretical argument, opted in context of the studied ME composites, is that the FE-FM interface, owing to the band gap differences in phases on either side, might actually behave as a semiconductor heterojunction. This would result in space-

charge regions at the interface. Which means that the stress generated ME fields close to the interface will only lead to either a further build up or a reduction of charges on both sides of the interface (identical to the barrier region of a biased pn-junction), in contrast to the previous argument of total screening. However, it is clear that in any case these dynamics of the fields, close to the interface, could not be resolved using a direct method unless the measurements were done in a controlled environment or vacuum. At this point the ability of PFM to probe localized ferroelectric switching dynamics (SSPFM) comes by as a useful tool for exploring the field distributions in ME composites. In this chapter, the aspects concerning localized switching of ferroelectrics under the tip are discussed in the context of in-situ magnetic field experiments carried out on two different ME composites viz. BaM-BTO and NFO-BTO.

6.1 Domain Nucleation and Growth Process in SSPFM

Switching of ferroelectric domains under a PFM tip differentiates itself from the more commonly investigated macroscopic switching. The difference lies in the fact that the field under a PFM tip is highly inhomogeneous as compared to that of macroscopic electrodes, leading to extremely localized switching. In both cases, the common aspects attached to the process of domain switching are nucleation of a domain, followed by its growth through the sample. These aspects, were comprehensively addressed for the first time in the seminal work of Abplanalp [131], followed by appropriate modifications of the same by Molotski et al. [226], Emelyanov [227], and Kalinin et al. [228]. The key focus of this theoretical development was to predict the parameters like critical size, critical field (nucleation bias), and most importantly the extent of growth.

Initially, the case of homogeneous field (macroscopic switching) is considered. Figure 6.2a shows the corresponding sample geometry with uniform top and bottom electrodes, generating a homogeneous electric field within the sample. The thermodynamics of the switching process comprises of three main components [121, 131, 226, 229–231]. The primary driving force for a purely ferroelectric 180^0 polarization switching is the change in bulk free energy

$$\Delta G_{bulk} = -\int \Delta P_i E_i dV \quad \textbf{(6. 1)}$$

This contribution is always negative and favors domain growth. Next the domain wall created between the oppositely poled domains stores an electrostatic energy density of σ_{wall} which always contribute positively to the overall free energy as

$$\Delta G_{wall} = \sigma_{wall} \Delta A \quad \textbf{(6. 2)}$$

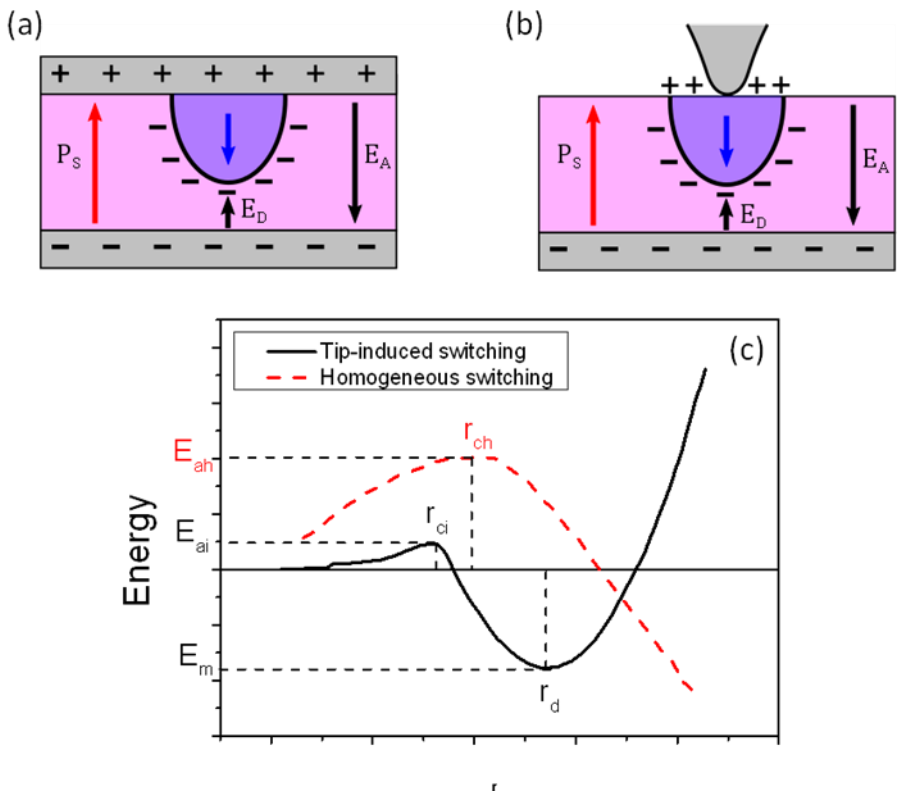

Figure 6.2 Schematic representation of ferroelectric switching under (a) homogeneous, and (b) tip induced field distributions. The coloured arrow indicates the direction of spontaneous polarizations, whereas the black arrows indicate the applied(E_A) as well as the depolarizing(E_D), fields. The proximity of the switched nuclei (blue ellipsoidal patch) to the bottom electrode is exaggerated. It should be noted that the charges in the vicinity of the tip in (b), are the uncompensated charges, bound on the surface. (c) shows the free energy of the system as a function of lateral domain size, for both cases. The homogeneous switching (red curve) is devoid of any equilibrium domain radius or energy, as the nucleation is rapidly followed by a pandemic growth [121].

Now there exists a significant depolarization field not just within the primordially switched domain, but also in the surrounding environment owing to the divergence of polarization. This depolarization field tends to oppose the nucleation of a domain and for the geometry under consideration is given as

$$\Delta G_{dep} = C\frac{r_d^4}{l_d} \quad \textbf{(6. 3)}$$

Where,

$$C = \frac{4\pi p_s^2}{3\varepsilon_{11}}\left[ln\left(\frac{2l_d}{r_d}\sqrt{\frac{\varepsilon_{11}}{\varepsilon_{33}}}\right) - 1\right] \quad \textbf{(6. 4)}$$

ε_{ij} are components of the anisotropic dielectric constant, p_s is the spontaneous polarization, whereas r_d and l_d are the radius and the penetration depth of the nucleating domain. It can be seen from eq.**(6. 3)** that the depolarization energy is minimized when the created domain has a small diameter and a high penetrating depth. The total energy calculated from the individual components is summarized in Figure 6.2c as a function of domain radius. It can be seen that as the domain radius reaches the critical radius, the domain grows indefinitely. Substituting the parameters for a typical ferroelectric like $BaTiO_3$, unrealistic critical field as well as the critical domain radius were estimated [228], suggesting that unless a very high field is applied a homogeneous nucleation is almost impossible. This explains the existence of heterogeneous domain nucleation in macroscopic switching, accounting for the experimentally observed relatively low coercive fields.

On the other hand, for the case of switching under a PFM tip (Figure 6.2b), the electric field is highly inhomogeneous and extremely localized (10^6– 10^9 V/cm) in the vicinity of the tip apex. As a result of this, the switching drive {Eq.**(6. 1)**} is only limited to a small region close to the contact point. Secondly, the depolarization field is modified from the case of macroscopic switching. As can be seen from Fig. 4.2b, in case of the tip acting as an electrode, there exist uncompensated charges on the open surface of nucleating domain, excluding the area that is in contact with the tip. Hence, the depolarization energy is now calculated in parts by considering the open surface charges and the charges present at the domain wall (apex of the spheroid in Figure 6.2). As a result of these modifications in depolarizing as well as the applied field, the switching process, as highlighted in Figure 6.2c, is associated with a relatively smaller activation energy. However, followed by the activation, the domain acquires a stable size (typically of the order of a few tens of nanometers) without undergoing indefinite growth. This is mainly due to the intense localization of the field under the tip.

From the explanation presented above, it can be concluded that there can be numerous factors, which externally affect the domain nucleation process under the tip. The theoretical work of Morozovska et al. [232, 233], has established that the surface and bulk screening conditions, which in turn determine the depolarization field, influence the nucleation barrier and can also affect the domain growth rate. This is corroborated by the experimental work reported by Maksymovych et al. [234, 235], where it was found that under different environmental/screening conditions, key characteristics of the SSPFM loops namely the nucleation biases (PNB and NNB) and the slope of the forward and reverse branches (growth rate), significantly changes. In addition to the effect of the surface screening conditions, spatial mapping of these key characteristics revealed a distinct horizontal asymmetry in the loops, which was followed with a correlated asymmetry in the slopes of forward and reverse branches. These observations were attributed to the influence of defect induced random electric fields, which apparently favor easier domain nucleation in only one direction (either forward or reverse).

In the present context, the sensitivity of localized domain switching to external parameters can be used in probing the ME generated fields. However, it has to be considered that any preexisting built-in field such as due to defects can also affect the localized switching. For that matter, it is essential to only compare the net changes, caused by changing magnetic field, and hence a statistical acquisition is required. In the present thesis, 2D mapping of localized switching parameters was carried out followed by 2D acquisition of local switching loops under SSPFM (section 2.1.5). The key parameters, like the positive and negative nucleation biases, were extracted using custom made routine (Appendix-d) based on the approach suggested by Jesse et al. [137, 236]. This will provide a statistical overview on the possible effects of the ME generated fields.

6.2 Results and Discussion

The results corresponding to SSPFM acquisition over a 16 x 16 grid on the BaM – BTO sample are shown in Figure 6.3 and Figure 6.4. The maps of the positive/negative nucleation bias are spatially filtered using a cut off value from the saturation amplitude map, such that the acquisition covering the BaM region is neglected, and the corresponding values are set to zero. Figure 6.3b and Figure 6.3c illustrate a typical PFM phase-voltage, and an amplitude-voltage hysteresis loops, respectively, corresponding to one of the grid points. "The loops measured in the absence of the magnetic field are often distorted, i.e. shifted towards either the positive or negative bias voltage. Such a shift indicates presence of internal bias fields, stabilizing energetically more favorable orientations of the polarization along their directions and resulting in an asymmetry of the switching process. This asymmetry can be quantified by comparison between the NNB and PNB. Figure 6.5a shows histograms of the nucleation bias. Analyzing the spatial distribution of the difference between PNB and NNB (PNB – $|$NNB$|$/2, or simply PNB + NNB/2), which can be considered as a measure of the strength and polarity of the internal fields, we have found that the strong asymmetry is typical for the loops measured close to the interfaces between BT and BaM grains, while the interior parts of the BT grains show more symmetric switching (Figure 6.5d)" [237].

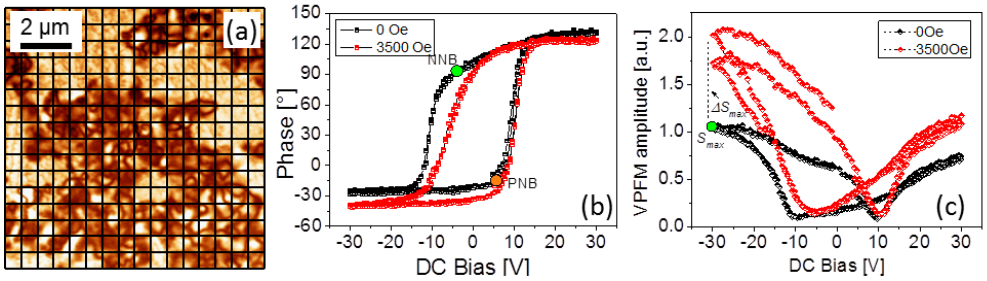

Figure 6.3DART-PFM image (a), typical local piezoresponse hysteresis loop: (b) phase and (c) amplitude signals acquired at 0 and 3500 Oe[237].

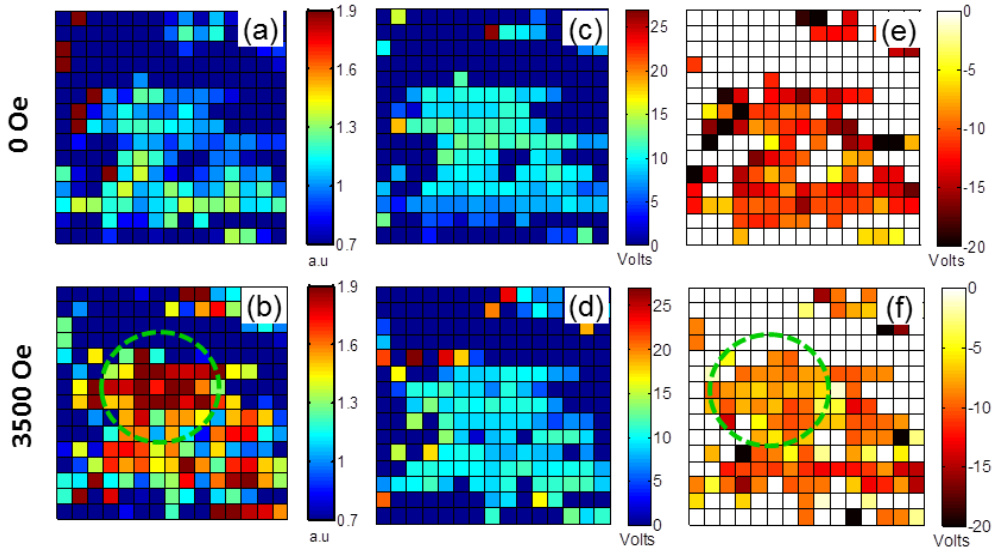

Figure 6.4 Maps corresponding to the acquisition shown in Figure 6.3a, showing (a, b) the saturation piezoresponse, (c, d) positive, and (d, e) negative nucleation bias measured at the magnetic field of 0 and 3500 Oe (all images scales 4 × 4 µm) [237].

The preexisting asymmetry in switching behavior close to interface can be primarily attributed to two possible causes: (i) modified bulk screening owing to the sides of the nucleating domain being partially shared by a relatively conductive phase, and/or (ii) preexistence of built-in fields at the interface. Both of these alter the depolarization conditions. A closer look at the possibilities makes it clear that the former contradicts the experimental observations. Assuming perfect screening at the interface due to high mobility charges on the FM side, switching in both directions (forward as well as backward) has to be equally affected. However, this is not the case with the changes observed, where switching in only favored in one direction (Figure 6.5c-d, as well as Figure 6.4e-f). Hence, the only plausible explanation is the existence of built-in fields at the interface. Interestingly, the asymmetry of the loops at the interface seems to be unipolar in nature, as indicated from the persistent negative side shift (blue contrast; Figure 6.5c) in the loops. This unipolarity of the built-in field suggests that the origin of this field has to be interface specific. This rules out the possibility of any preexisting stress generated fields, which owing to the anisotropic nature of the stresses will have to be multipolar. In addition, fields purely originating from defects will also pose a multipolar distribution along the interface, as the nature of defects can be variable (positive as well as negative). In pure BTO, the grain boundaries have been found to be dominated by a donor type impurity states [238–241], which differs from those in the bulk [242], the presence of acceptor (Fe^{+2}) doping from the neighboring phase cannot be ignored [243]. This might account for the hypothesized mixed defect state. At this point only one possible origin for the built-in fields can be rationalized, namely existence of an interfacial space-charge region with the interface acting as a semiconductor heterojunction. For formation

of a space charge region in a semiconductor heterojunction, the necessary and sufficient condition is a difference in the Fermi level [244, 245]. BTO is known to be a wide band gap semiconductor (~ 3 eV [246]), whereas BaM has the lowest band gap (~ 0.8 eV [91, 247]) amongst all the ferrites. This outlines possibility of formation of a semiconductor heterojunction at the FE-FM interface with a significant barrier height.

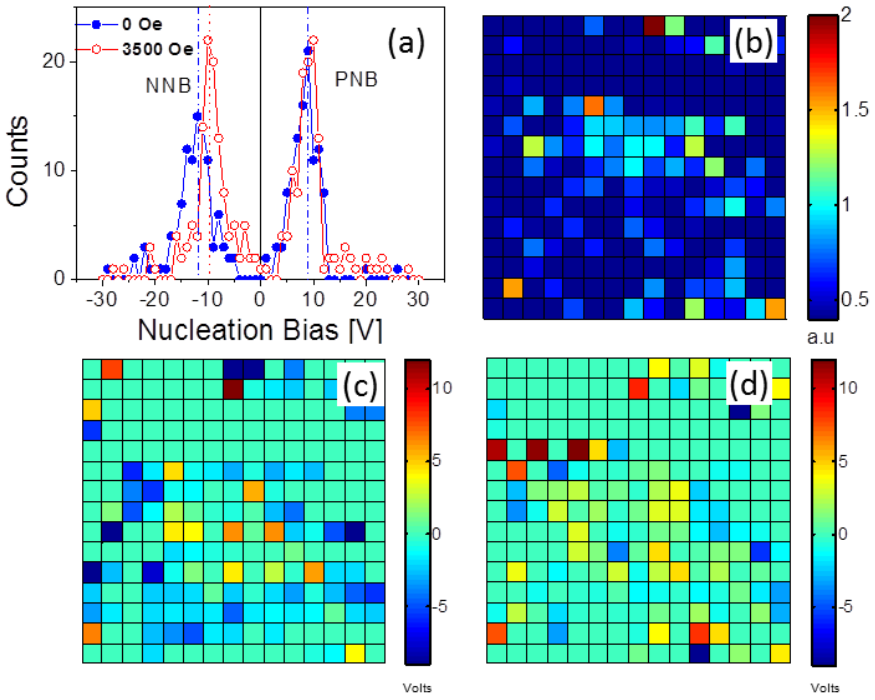

Figure 6.5 (a) histograms of the nucleation bias distributions measured with and without the magnetic field. (b) maps of the difference between the saturation PFM amplitude, ΔS_{max}, measured with and without the magnetic field. Maps of the difference between positive and negative nucleation bias, (PNB+NNB)/2, evaluated for (c) 0 Oe, and (d) 3500 Oe fields (all images scales 4 × 4 µm).

Comparison between the switching parameters, at on and off magnetic fields, reveals two apparent changes: (i) increase of the saturation amplitude of the VPFM signal (S_{max}), and (ii) reduction of the NNB. The observed changes of the nucleation bias can be considered in the following way: as discussed above, the charges trapped in the vicinity of the interface result in an internal bias field and, correspondingly, facilitate switching in one direction. Application of the magnetic field effectively lifts up the asymmetry of the domain nucleation by reducing the NNB values. Besides the change of domain nucleation bias, the domain propagation kinetics can also be affected by the magnetic field. As seen from Figure 6.3 for the negative bias (upward polarization) the maximal VPFM signal increases much more rapidly than that for the downward polarization. This indicates that the domain for the upward polarization is propagating faster through the sample, and reaches a larger volume. This can be also inferred from the illustrative loops (Figure 6.3) in which the slope for the negative switching branch reduces on application of the magnetic field. Again, such facilitated kinetics can be attributed to the ME field altering the

depolarizing condition, which comes into play after the domain is nucleated. Interestingly, the magnetic field alteration of the NNB close to the interface occurs in a stochastic manner (Figure 6.5d), which indicates that the ME field generated by the ME stress is not homogeneous. This is a rational observation, and in a sense is self-corroborative to the fact that the ME stress itself will be inhomogeneously distributed at the interface.

A similar SSPFM acquisition was also carried out on the NFO-BTO sample. Figure 6.6 shows the corresponding maps of switching parameters extracted from SSPFM acquisition on a 24 x 24 grid. The filtering of loops acquired from non-piezoactive regions was realized using the identical approach as in the case of BaM-BTO by considering, a suitable S_{max} cut off. However, in this case the filtering was not very efficient, as the PFM-amplitude corresponding to the apparently non-piezo regions was found to be anomalously equal to that of the piezo-active regions. As an initial observation it can be said that the random field parameter (PNB + NNB/2) map (Figure 6.7a) does not show any significant existence of built-in interfacial fields as in the case of BaM-BTO. Rather the loop asymmetry at the interface is stochastically distributed, indicating domination of fields from randomly distributed defects. This behavior, which is in contrast to the case of BaM-BTO, points towards a weaker space-charge layer at the interface. If it is presumed that the Fermi level difference between the constituent phases in BTO-NFO is identical to that in case of BaM-BTO, then the heterojunction of BTO and NFO can possibly form a barrier layer which has relatively lower barrier height, given the relatively wider (1.53 eV [248]) band gap in NFO. On application of the magnetic field, no significant ME field lifting of the loop asymmetry was observed (Figure 6.7b), as there are no strong unipolar interfacial fields existing in the first place.

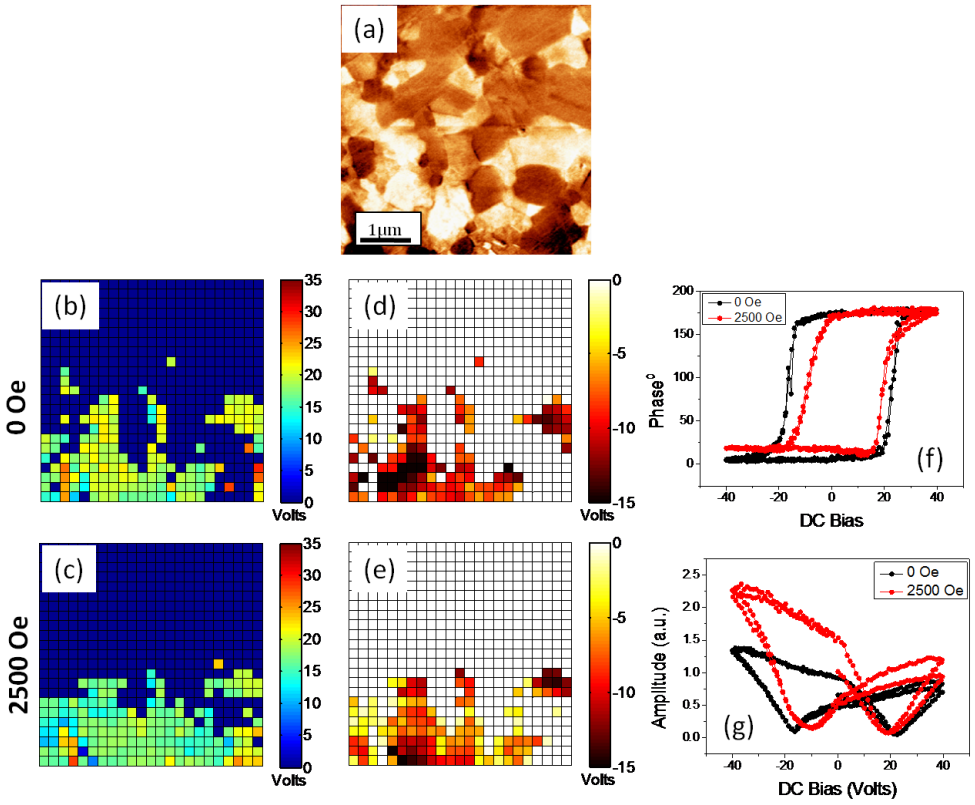

Figure 6.6 (a) vertical PFM (piezoresponse) image of the chosen spot on the NFO-BTO sample. Maps of (b, c) the positive, and the (d, e) negative nucleation bias, extracted from a 24 × 24 grid of in-situ SSPFM acquisition on spot (a). Illustrative SSPFM (f) phase, and (g) amplitude loops, chosen from a random spot on the grid.

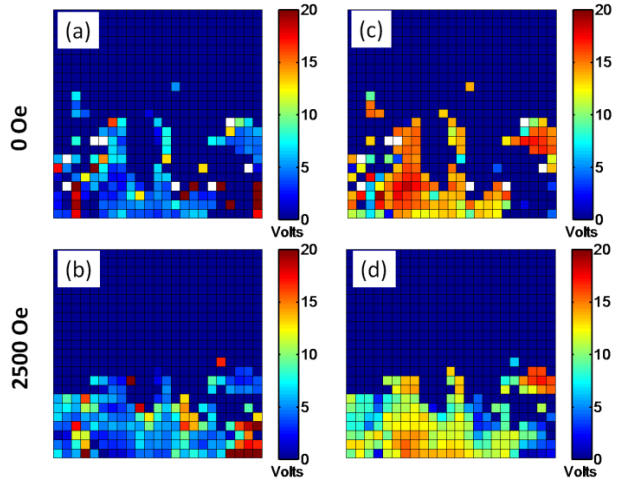

Figure 6.7 Maps of the (a, b) random field parameter (PNB + NNB/2), and (c, d) the random bond parameter (PNB - NNB/2), evaluated from the acquisition corresponding to Figure 6.6. Interestingly, instead of the random field parameters, it is the random bond parameter (a measure of loop width) that shows more significant change.

Next, upon application of a magnetic field the changes in the switching parameters are in contrast to those observed in the case of BaM-BTO. For the NFO-BTO sample, both NNB and

PNB seem to have been lowered under the influence of the ME stresses (Figure 6.7d). Although there is indeed a favored softening of the NNB (Figure 6.6f, g) which could be attributed to the appearance of ME fields, the additional reduction of nucleation biases in both switching direction is significant and points toward an origin that differentiates itself from the field based influences. The only possible explanation of this bidirectional reduction of the nucleation bias can be influence of a uniaxial component of the generated ME stress onto the switching process. This has to do with the ferroelastoelectric nature of the switching. The free energy equation now should include the stress term that was neglected in eq.**(6. 1)** as

$$\Delta G_{bulk} = -\int\left[(\Delta P_i)E_i + (\Delta d_{ijk})E_i\sigma_{jk}\right]dV \qquad \textbf{(6. 5)}$$

Eq.(6. 5) indicates that introduction of stress into the system can modify the bulk switching drive itself, either favoring or resisting the switching in both the directions. Indeed the seminal work by Abplanalp et al. [131, 249], which was specially focused on local switching thermodynamics, had demonstrated that existence of high uniaxial stress, realized by the tip, can significantly reduce the switching bias (red circle in Figure 6.8). In the present context, however, the nature of stress acting on BTO grains is unknown, which makes it difficult to precisely comprehend the observed changes in switching behavior. Interestingly, maps of the parameter (PNB − NNB/2), which actually accounts for the loop width, shows that the bidirectional reduction in the nucleation is maximal at the interface. This suggests that, the ME stress exerted is significant at the interface, in accordance with the observations made in previous chapters. In addition, the unidirectional magnetic field induced shift in the hysteresis loops observed at interface (Figure 6.5d) indicates that the stress at the interface seems to have a unique uniaxial component with minimal anisotropy. An important hypothesis that emerges at this point is as follow: since NFO possesses cubic magnetocrystalline anisotropy, it could at high magnetic fields exhibit a more isotropic stress at the FE-FM interface, irrespective of the randomness of relative grain orientations. In correlation with this argument~~s~~, in the BaM-BTO case, where anisotropic stresses are expected at interface owing to uniaxial magnetocrystalline anisotropy of BaM, the ME stress induced changes in the NNB should be more stochastic, as it was indeed observed in the experiment.

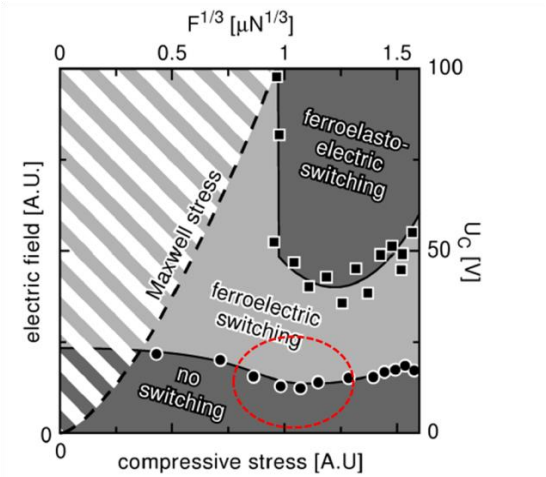

Figure 6.8 Dependence of the ferroelectric and ferroelastic switching biases (U_c), shown as a function of cube-root of the force exerted by the tip [249].

7 Direct Observation of Stress Distributions: In-Situ Scanning Confocal Raman Microscopy

Up to this point, the stress induced manifestations of the ME effect have been only observed in indirect forms. The various traits of possible underlying stress distributions hypothesized in the previous chapters can be complimented by direct observation of the resultant stress distributions. Although measuring stress in a direct sense only means making a physical contact and being able to measure the reactional force, there are tools which are known to be sensitive to stress and can accurately reflect the same in a non-destructive measurement. Various means like ultrasonic [250], optical lever strain mapping [251] and neutron diffraction [252], are widely employed to map stresses in important device components. However, such techniques lack sufficient spatial resolution, and also they seldom allow an easy instrumental access in order to apply an in-situ magnetic field.

On the other hand, Raman spectroscopy is extremely sensitive to structural changes, and hence to stress [253–258]. However in most of the cases it is not trivial to evaluate the effect of stress from Raman spectra, as the associated changes in peak widths or peak positions are ambiguous. Nevertheless, due to the recent advancements in the instrumentation and theory of Confocal Raman Microscopy (CRM) [259–262], many of its versatile applications have emerged. Of particular interest are the capabilities to carry out 2D mapping of Raman spectra over a chosen plane [263–267]. Owing to the excellent stability, sufficient resolution, and certain inherent capabilities of the Raman effect, CRM has emerged as a powerful tool for mapping functionalities in materials ranging from biomaterials [268, 269] to ferroelectrics [256, 263, 266, 270]. As a result, it is really useful to employ CRM for studying the effect of ME induced stresses on the perovskite phase (BTO) which has Raman modes that manifest interesting inter-coupling and are sensitive to an applied stress [257]. This chapter is dedicated to mapping the effect of an in-situ applied magnetic field on the Raman spectra over the ME composites.

7.1 In-situ Raman Spectra in Composites: Acquisition and Spectral Component Separation.

The acquisition of 2D Raman spectra over composite samples basically means collecting Raman spectra over a spatial grid that covers both FE and FM phases (Figure 2.12) separated by a well-defined interface. Consequently the entire 3D data set acquired will be a mix of spectra corresponding to both phases, as in all cases the phases under consideration have distinct Raman active modes. In addition to that the interface, or in general any spatial location where the beam overlaps more than one phase, will result in a convolution of the respective Raman spectra. Taking this issue into consideration, it becomes evident that a simple approach of considering raw spectra corresponding to each grid point will not yield any useful information. At this point the first goal is a qualitative determination of the spectral components present in the dataset and to factorize the whole data-set in terms of these spectral components such that it yields

information not just about constituent spectral components corresponding to individual phases, rather also provide a spatial distribution of the same.

Once again Principal Component Analysis (PCA) comes by as the most suited solution for the purpose of separating the spectral components. In the present case the features that PCA will detect are the spectra themselves. Each type of spectra constitutes different directions of high variance in the n-dimensional data hyperspace, which is then traced by PCA. Hence, in order to realize the spectral separation, the data matrix is oriented in such a way that each spectra i.e., Raman intensity values as a function of wavenumber collected at each grid point, is considered as a data vector. The data vectors corresponding to each grid point after a 3D to 2D reshaping, are arranged as rows in the data matrix.

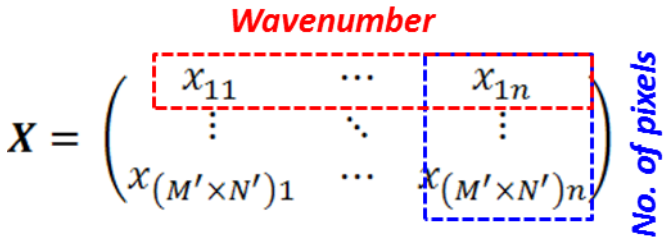

Figure 7.1 Schematic arrangement of the Raman data-matrix.

The results corresponding to the PCA decomposition of 2D CRM acquisition on BaM-BTO sample are shown in Figure 7.2. 1st and 2nd PCA components, decomposed from the acquired data set, qualitatively resembles the standard polycrystalline spectra of BTO [258] and BaM [271] phases. The PFM image taken on the same spot shows that the active regions apparently correlate with the 2nd component (BTO) score map (Figure 7.2d). This synergistically validates the approach of deconvolution of Raman spectra using PCA. These identified PCA components are, however, only qualitative in nature. In addition, the anomalous departure of the spectral envelope, in certain ranges (Figure 7.2b), insinuates the *broken heart* phenomena in the data set (Figure 2.16). However, the score maps corresponding to both components serve a more useful purpose by acting as an address book for finding raw data vectors, that actually correspond either to a purely BTO or a purely BaM spectrum.

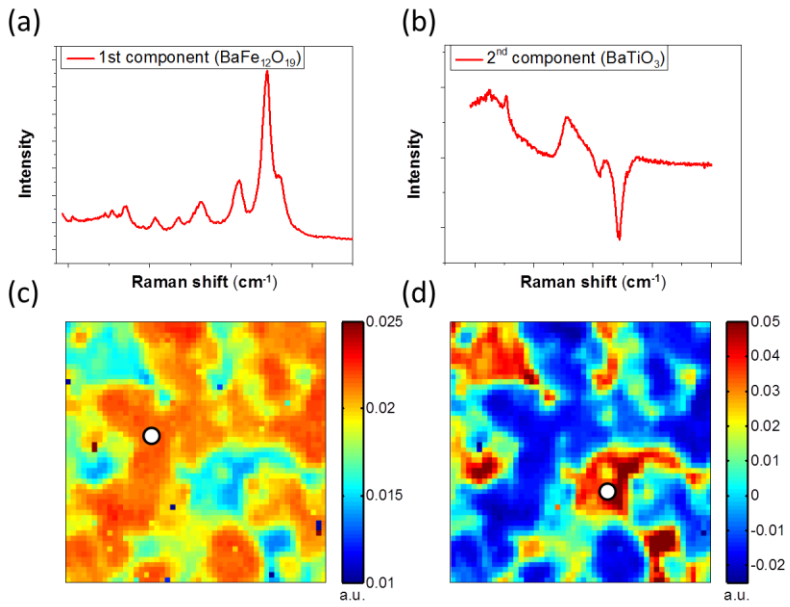

Figure 7.2 The PCA decomposition of the 3D CRM data-set of the BaM – BTO sample, showing the (a) 1st (b) and 2nd principal components, along with the respective((c), (d)) score maps.

The spectra corresponding to the grid points that belong deep within the identified (white circles) regions of 1st and 2nd component score maps (Figure 7.2) are the pure BaM and BTO spectra, respectively. These spectra are then least square fitted using appropriate models (Appendix-e) to provide initial spectra that can be further used as starting point in SMCR. As described in section 2.4.4, SMCR functions by least square fitting the initial spectra to the raw data-set (section 2.4.4), such that in the end the spectra are refined based on the actual spectral components existing in the data, and a phase concentration map is generated, which essentially comprises of the weights corresponding to the spectra of both the phases at each grid point. Finally, the BTO and BaM spectral components are separated along with their respective concentration maps (Figure 7.3d, e).

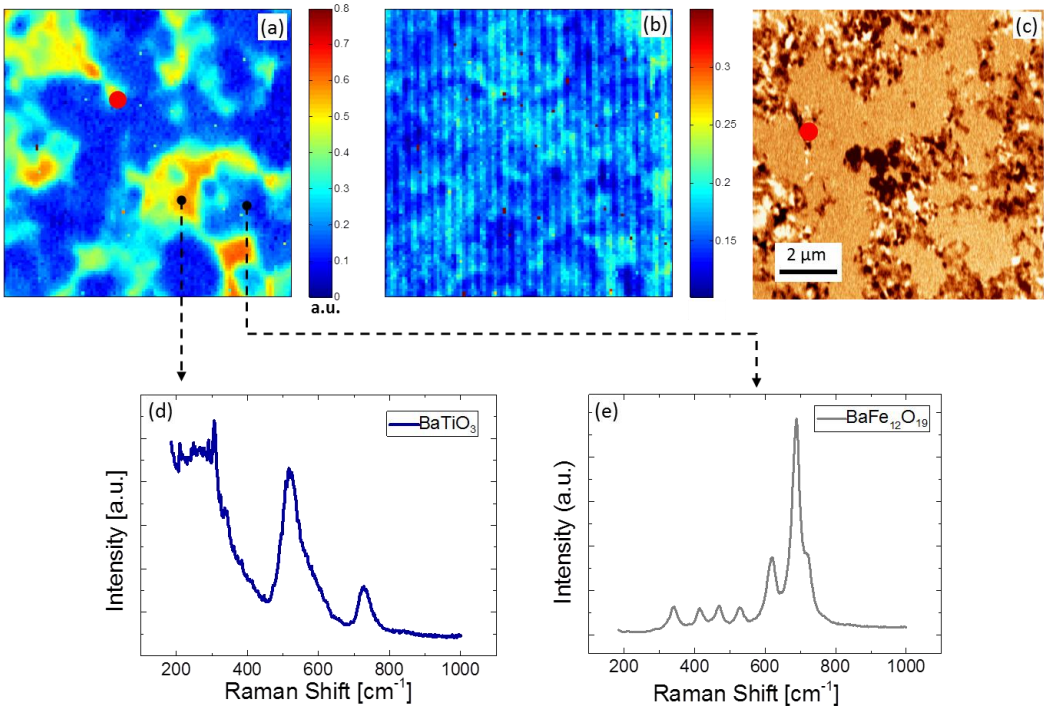

Figure 7.3 (a) the BTO concentration map (score maps) extracted using SMCR, (b) lack of fit map corresponding to SMCR, (c) lateral PFM image of the same area (Red dot is shown for correlation), and the SMCR extracted average spectra corresponding to the (d) BTO, (e) and the BaM phases [237].

Next the extracted BTO spectrum, which is an average of the BTO contributions in the entire scanned region, was fitted using an appropriate model (Appendix-e). The best fit parameters for the spectra, measured both at on and off in-situ magnetic fields, are summarized in Figure 7.4. One can see that the magnetic field of 2500 Oe induces a frequency shift of about 2.5±1.0 cm^{-1} for peaks around 520 cm^{-1} (A1 and E(TO) modes) and 720 cm^{-1} (A1 and E(LO) modes) (Figure 6). The shifts for both peaks occur in opposite directions: frequency of the phonon modes at 520 cm^{-1} decreases (mode softening), whereas for the modes at 720 cm^{-1} it increases (mode hardening). These changes are primary indicators of influence of the ME induced stresses onto the Raman active lattice vibrations in BTO. However, since the changes reflect an average of the influences on individual BTO spectra, mixed information corresponding to inhomogeneously distributed stress is what is obtained. In addition, since SMCR relies on the least square fitting based on the initial values as well as the raw data instead of a bounded realistic model, some influence of the strong 670 cm^{-1} BaM peak which is observable even in the BTO regions, can be expected. In fact this can be the reason for the observed anomaly in the peak shifting where the 520 cm^{-1} peak shows softening whereas the 720 cm^{-1} peak shows hardening. For clearer understanding, the approach has to be localized in a way that individual grid point spectra are separated and fitted, thereby yielding spatial distributions of the peak parameters. However, for the 100 x 100 CRM acquisition discussed here, localization is not useful as the individual spectra

are too noise ridden. In the coming section a strategy for improving the individual spectra quality, followed by spatial mapping of the peak parameters is presented.

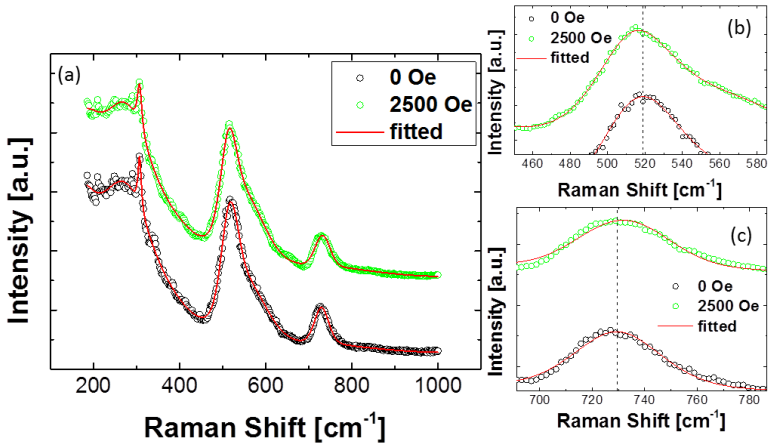

Field (Oe)	Peak -520 (cm^{-1})	Peak -730 (cm^{-1})
0	516.5 (1.1)	729.5 (0.8)
2500	513.9 (1)	731.9 (0.7)

Figure 7.4 (a) Average BTO Raman spectra extracted via the SMCR decomposition of the acquisition on the BaM-BTO composite ceramics, taken at magnetic field values of 0 Oe and 2500 Oe. Enlarged view of the spectra around (b) 520cm^{-1} (A1 and E(TO) modes) and (c) 720cm^{-1} (A1 and E(LO) modes). The bottom table summarizes the best fit parameters corresponding to the peaks shown in (b) and (c) [237].

7.2 3 Focus Distribution and Resolution

As mentioned in Section 2.2.2, the point spread function (PSF) of the detected Raman signal, also termed as the probe response function (PRF), can be assumed to be a 3D Gaussian for the sake of simplicity [272]. PRF can be expressed in terms of an arbitrarily located scattering point (x,y,z) and the incident beam location (x_0,y_0,z_0) as

$$B(x,y,z;x_0,y_0,z_0) \propto exp\left[-\frac{(x-x_0)^2+(y-y_0)^2}{2r^2}\right] \times \left[\frac{p^2}{(z-z_0)^2+P^2}\exp(-2\gamma z)\right] \quad \textbf{(7.1)}$$

Where r is the beam waist radius, p is so-called in-depth probe response parameter, and γ is the absorption coefficient of the material for the incident wavelength. In order to evaluate the finite volume that effectively emits the Raman signal from within the probe spread, the parameters r, p, and α need to be known. An approach, as reported in literature [273, 274], has proposed to calibrate the probe response function by measuring CRM scan lines in-depth as well as laterally across a sharp interface separating regions of different contrast, followed by fitting the obtained profile to the appropriate terms in eq.(1.1). As an example, in the case of a lateral calibration experiment the last term comprising vertical co-ordinates can be ignored and vice versa for the

vertical calibration [274]. However, in that approach the material ($BaTiO_3$) had the homogeneously distributed light absorption co-efficient (γ). This is not the case in ME composites: across the interface and even across the individual grains the absorption coefficients are different.

Therefore in our case it was not possible to estimate an effective Raman emitting volume using the aforementioned approach. Hence an exact resolution limit could not be determined. In this situation the incident probe size (lateral: 290 nm and vertical: 550 nm) can be considered as an upper-limit of the 3D resolution. As a result, for 2D acquisition to devoid any probe convolution, the incident beam has to be exactly juxtaposed, such that the grid pitch Δx_g (distance between two grid points) does not exceed 290 nm, casting limitations to the scan size and number of grid points per line:

$$\Delta x_g = \frac{Scan\ Size\ (\mu m)}{no.of\ grid\ points\ per\ line} \leq 290\ nm \qquad \textbf{(7.2)}$$

7.3 Spatially Mapping Stress Induced Changes

Having learned from the results discussed in section 5.1, the acquisition time was increased and the number of the grid points was decreased keeping the maximum grid pitch. The improved spectral quality has allowed carrying out SMCR factorization at local level, with BTO spectra being resolved for each grid points. This was realized in following steps:

i) Initially the PCA based recognition step was carried out, in identical manner as described in section 5.1. By this, the constituent spectral component concentration was mapped and the individual spectra samples were collected from the identified suitable grid points.
ii) The samples of the individual spectra were fitted using an appropriate model (Appendix-e). The fitted curves were used as initial values for SMCR step. In this case the SMCR step was localized: the data sample, which in section 5.1 was the entire data-set, was reduced to mere 4 spectra corresponding to the grid point under consideration along with 3 neighbouring grid points.

$$S_{local} = \begin{bmatrix} S_i \\ S_{i+1} \\ S_{i+N} \\ S_{i+N+1} \end{bmatrix} \qquad \textbf{(7.3)}$$

where S_i represents the spectra (intensity array) with the index i from 1 to the total number of spectra collected (M × N). It has to be noted that the formation of the local sample only serves the purpose of providing a just-sufficient statistical power for the separation of BTO spectrum at i^{th} grid point. Such a sample is sufficient considering the improved spectral quality. Owing to the large enough grid pitch (≥ 290 nm), no

convolution is expected between the four spectra in eq.(7.3). However, the extracted BTO spectrum can comprise some statistical influence of the rest of the neighboring spectra. Such sampling extraction was carried out for each grid point up to $(N-1)^{th}$ and $(M-1)^{th}$ grid point along the rows and the columns respectively.

iii) Next, the extracted BTO spectra were fitted using the BTO peak model, yielding a set of peak parameters corresponding to each grid point. The relevant parameters, namely the peak positions around 520 cm^{-1} and 720 cm^{-1}, were spatially mapped.

The obtained results corresponding to the BaM-BTO sample are shown in Figure 7.5. As a first observation, the distribution of peak positions correlates to the BTO concentration map, with the most reasonably accurate peak positions being in the BTO rich regions. This corroborates the effectiveness of the extraction and fit process. The maps of the peak position corresponding to the A1/E (TO) (520 cm^{-1}) and A1/E (LO) (720 cm^{-1}) bands demonstrate a weak softening with the increasing magnetic field. The shift value for the 520 cm^{-1} peak is about 0.6 cm^{-1}, whereas for the 720 cm^{-1} peak it is about ~2.5 cm^{-1} at the maximum field, as inferred from the shift of the histograms (Figure 7.6) corresponding to the maps. It is presumed here, that the hardening of the latter mode observed in the averaged spectrum (Figure 7.4) is a result of the statistical interference between the strong Raman mode around 680 cm^{-1} of BaM and the mode at 720 cm^{-1} of BT. Since SMCR is sensitive to the sampling, a drift of the scan area can result in significant changes of the average spectrum, especially with the BaM Raman mode being very strong. The field dependences of both BT Raman peaks (520 cm^{-1} and 720 cm^{-1}) reveal a monotonic and spatially persistent softening trend. The most interesting feature is that the strongest peak shift apparently occurs close to the FE-FM interface, which is again reiterating the observations made in chapter 4: the ME stress exerted is maximized at the interface and gradually decreases within the matrix, in line with Eshelby's solution [275].

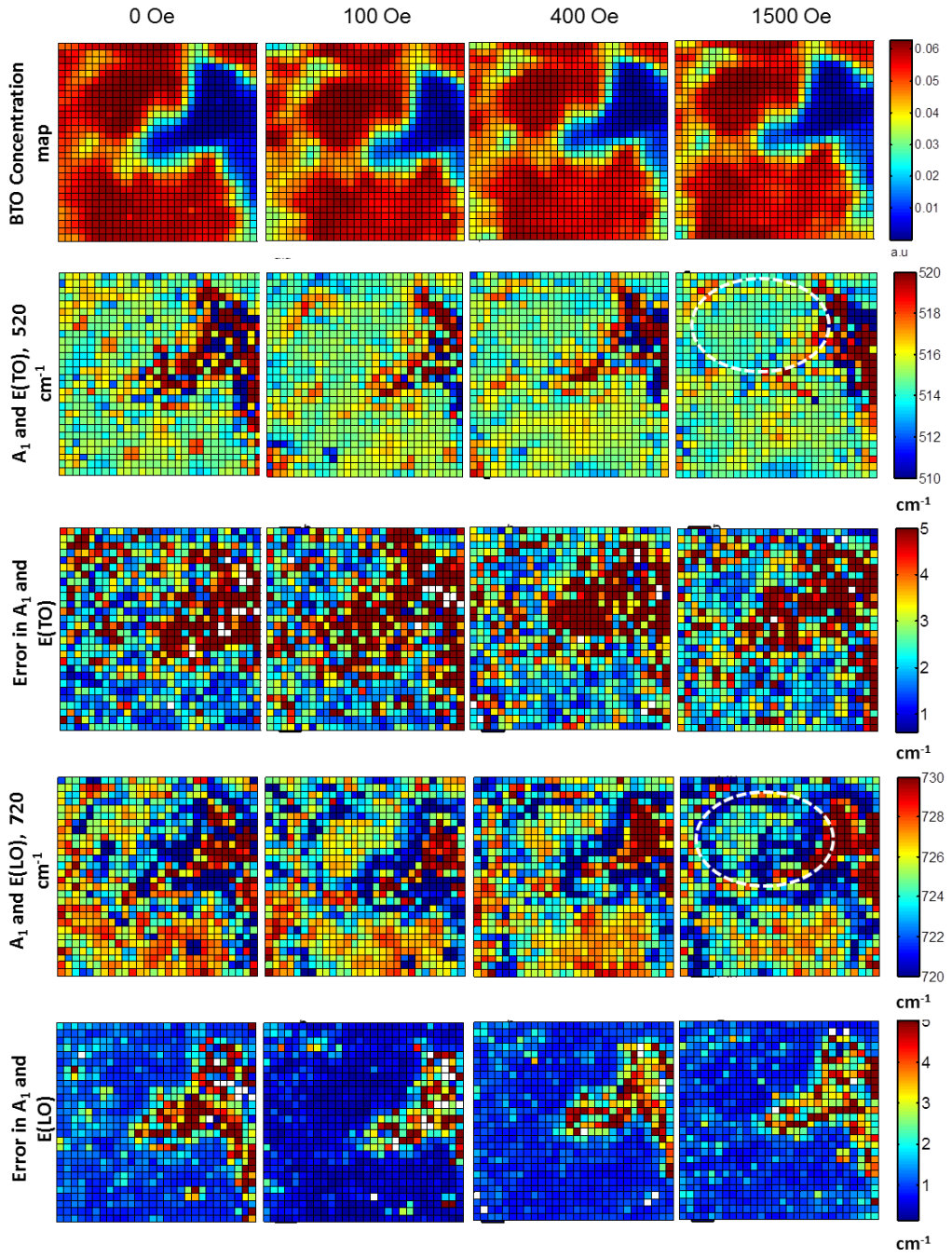

Figure 7.5 Spatial maps of fitted BTO Raman peak positions at different magnetic fields applied to the BaM-BTO sample along with their corresponding errors. The top row comprises of SMCR concentration maps that correlate the maps in each corresponding column (all images scale 7 × 7 μm).

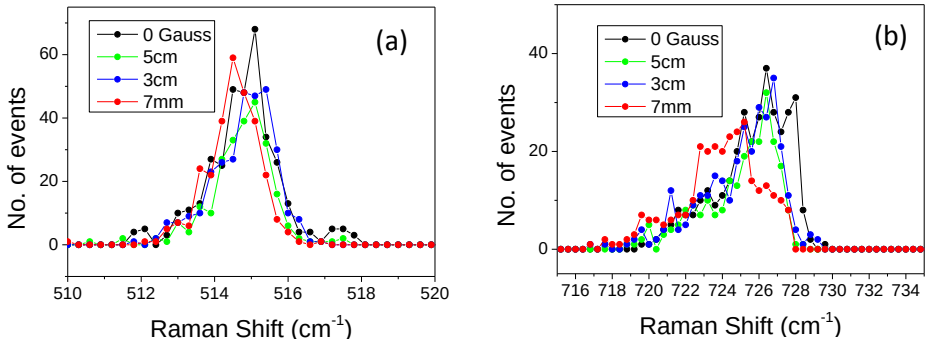

Figure 7.6 Shows the histograms corresponding to the peak parameter maps for (a) the 520 cm^{-1}, and (b) the 720 cm^{-1} bands, as shown in Figure 7.5.

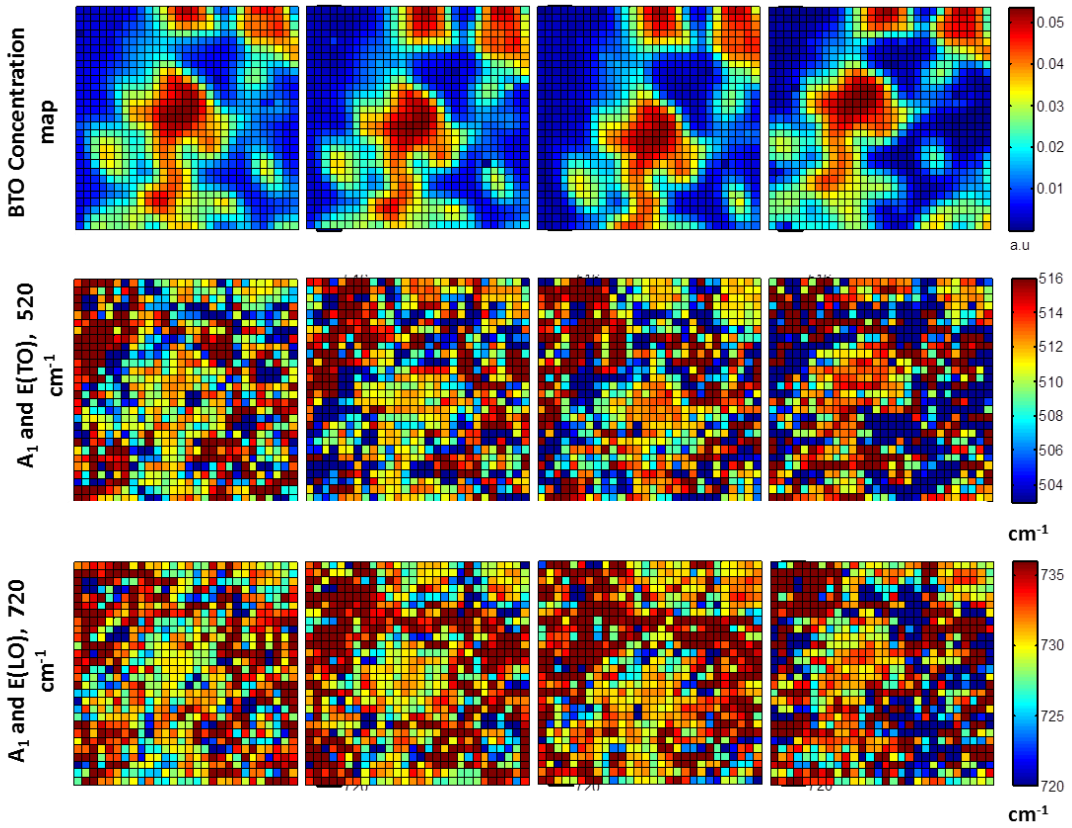

Figure 7.7 Spatial maps of fitted BTO Raman peak positions at different magnetic fields applied to the CFO-BTO sample. The top row comprises of SMCR concentration maps that correlate the maps in each corresponding column (all images scale 7 × 7 µm).

Similar results obtained on the CFO-BTO sample are summarized in Figure 7.7. Once again the correlation between the BTO concentration (Figure 7.7, top row) and the peak position maps indicate an efficient extraction and fitting process. In this case however, the peak position maps reveal a unanimous hardening in both the A1/E (TO) (520 cm-1) and the A1/E (LO) (720 cm-1) bands. This is in contrast with the observations made in the case of BaM-BTO. The primary

reason for this anomaly can be the difference between ME stress components in both cases. This, in addition, points toward the difference in magnetocrystalline anisotropy of the magnetic phase; where one is uniaxial (BaM), while the other one is cubic (CFO) in nature. A detailed discussion on possible effects of stress on BTO spectra is provided in the next section, which throws more light onto the arguments presented here.

Moreover, Figure 7.7 shows that for the studied BTO-CFO composite having the BTO region as an inclusion inside the CFO matrix, the maximum peak shifts occur within the bulk rather than at the interface. This is exactly opposite to what is observed in the case of BaM – BTO where the BTO phase morphology in the studied area is more like a continuous matrix. At this point it is worthwhile to recall the results obtained by PCA decomposition of PFM for inclusion-like BTO morphologies (the BaM – BTO and NFO – BTO samples; chapter 4), where an identical trend of bulk localized prominent ME changes was observed. A combination of these observations hence provides immense momentum for the hypothesis that the situation can be modelled as an inverse Eshelby problem, with the matrix dilating while the inclusion stays passive. Practically for such an inverse Eshelby problem, the sequence of steps followed for getting a solution will not change [275, 276]. As a result it can be imagined that for such a case, where BTO is more like an inclusion, there will be a constant distribution of stress within, identical to the dilating inclusion in a normal Eshelby problem. However the anomalous gradual decrease of the prominent change from bulk to interface can be associated to a departure of the inclusion shape from that of a perfect ellipsoid.

7.4 Stress and Raman Modes

As far as the peak shifting as a function of magnetic field is concerned, the key difference between the CRM results obtained for BaM-BTO and CFO-BTO samples is that in one case (BaM-BTO) a softening of relevant modes is observed which is stronger for the 720 cm^{-1} band, whereas in other case (CFO-BTO) a hardening of the relevant Raman modes was observed being stronger at the 520 cm^{-1} band. These nuances point towards existence of different stress components in the samples. In order to understand this argument in detail, it is essential to understand how stress affects Raman modes.

The Raman active modes which are essentially lattice vibrations of specific symmetry undergo significant influence on an externally applied stress/strain. The primary effect of strain is to modify the symmetry of vibration and induce frequency shifts [277, 278]. In most cases, as is the case of BTO, two different modes (A1(TO), and E(TO)) intrinsically lie close to each other creating a degeneracy [279, 280]. Application of strain can basically lift up such degeneracy, leading to corresponding changes in the peak parameters (position and width). Although a complete theoretical solution relating the frequency shifts to the applied strain is not available for BTO, it is worthwhile to discuss the effects of strain in the realm of the exact solutions available for the diamond structure (Sillicon) [278]. Ganesan et al. [278] were the first to theoretically comprehend the external influences (of stress and electric field) on to the Raman modes (of

silicon). They showed that the frequencies of the three Si optical modes in the presence of strain, to terms linear in the strain, can be obtained by solving the following system of simultaneous equations [277]

$$\begin{vmatrix} p\varepsilon_{11} + q(\varepsilon_{22} + \varepsilon_{33}) - \lambda & 2r\varepsilon_{12} & 2r\varepsilon_{13} \\ 2r\varepsilon_{12} & p\varepsilon_{22} + q(\varepsilon_{11} + \varepsilon_{33}) - \lambda & 2r\varepsilon_{23} \\ 2r\varepsilon_{13} & 2r\varepsilon_{23} & p\varepsilon_{33} + q(\varepsilon_{22} + \varepsilon_{11}) - \lambda \end{vmatrix} = 0 \quad \textbf{(7.4)}$$

Where p, q and r are the so called phonon deformation potentials, and λ represents the eigenvalues such that the difference between the Raman frequency of each mode in the presence (ω_j) and absence of stress (ω_{j0}) can be calculated as

$$\Delta\omega_j = \omega_j - \omega_{j0} \approx \frac{\lambda_j}{2\omega_{j0}} \quad \textbf{(7.5)}$$

Frequency change in one of the key Si Raman modes can be expressed in terms of externally acting uniaxial stress by introducing appropriate elastic compliance components

$$\Delta\omega(cm^{-1}) = \frac{1}{2\omega_0}[pS_{12} + q(S_{11} + S_{12})]\sigma \approx -2 \times 10^{-9}\sigma(Pa) \quad \textbf{(7.6)}$$

It can be seen from eq.(7.6), that to induce a change of 1 cm^{-1}, a stress of the order of 500 MPa has to be applied. This stress level is also typical for BTO as inferred from the related high pressure Raman studies in literature [257, 258]. Now as shown by the modeling result in section 1.5, the typical value of stress in ME composite created on application saturating magnetic field is of the order of 10 MPa [99], which way below the typical literature values. In contrast to this, the results presented in this chapter project changes of the order of 1 – 1.5 cm^{-1} within the statistical error. These significant changes can hence only be explained by considering existence of high shear stress components. A closer look at the linear system of equations {eq.(1.16)} suggests that under the influence of non-zero shear terms along with non-zero uniaxial terms, the solution obtained in eq.(7.4) might turn out to be rather rich with additional shear terms. Considering the fact that in BTO the shear compliance components are equally significant as the uniaxial ones ($S_{33} \sim 15.7 \times 10^{-12}$ m^2/N, and $S_{66} \sim 8.84 \times 10^{-12}$ m^2/N [76]), the central term in eq.7.6 can actually increase by mere introduction of non-zero shear stresses, resulting in increased proportionality factor between the applied stress and the resulting frequency shift. This increase in turn suggests that the threshold of stress needed to produce the experimentally observed frequency shift will actually reduce, justifying the significance of stress levels as low as 10 MPa in ME composites.

In addition, eq.(7.6) also suggests how the existence of different components of strain can lead to a sign change of the proportionality factor, thereby changing from the stress induced softening to

the stress induced hardening. Different magnetocrystalline anisotropy of the studied magnetic systems can actually lead to magnetostriction that projects different sets of stress components leading to different trends in shifting of the Raman mode frequencies. This can be an explanation to the observed anomaly where the BaM – BTO showed a mode softening whereas the CFO – BTO showed hardening.

8 Summary and Concluding Remarks

Bulk ME composites, based on combinations of $BaTiO_3$ (FE) and various spinel/hexagonal ferrites (FM), were rigorously investigated in terms of their local manifestations of the ME effect. The main focus of this work was to explore possible spatial distribution of various effects caused by the ME induced strain, especially in the vicinity of the Ferroelectric-Ferromagnetic interfaces. For that matter, the boundaries of techniques like SPM, and Confocal Raman Microscopy were pushed with the help of complimentary multivariate data-analysis techniques. The results presented in this thesis projects potential applications of the developed approaches, where they could serve as tangible sources for complimenting advanced (Texture based) modeling of ME composites. The outcomes of such a conjunction can possibly provide information for improving ME performances in polycrystalline composites, which are currently unavailable. In addition, the presented results also reveal new phenomena at the local scale, which have never been explicitly predicted in literature. The outcomes of this thesis are concisely summarized as following:

i) Local investigations of converse ME effect:

The converse ME effect was investigated by utilizing intense electric field under the SPM tip. The piezoelectric phase was poled to induce an instantaneous strain in the medium. The stress exerted on the neighboring magnetic regions lead to hysteretic changes in the magnetic domain configurations, as observed by MFM. These changes were attributed to defect pinning of the domains. Simultaneously, the EBSD analysis of SrM-BTO sample (Figure 4.6) revealed a role of *relative grain orientations*, in that a more favorable alignment of the maximum property axes of the adjacent FE and FM grains lead to a *maximum impact*. On the contrary, BaM-BTO manifested relatively homogeneous changes (Figure 4.2) in a scanned-poling experiment, but showed almost no change in a single grain poling. This nuance between the two hexaferrite based composites is attributed to the fact the constituent microstructures; the BaM-BTO, which possessed a relatively larger degree of agglomeration and grain size dispersion among the constituent phases, thus lacked grain to grain FE-FM interfaces; the SrM-BTO sample on the other hand, did showed a relatively larger amount of grain to grain interfaces. In addition, temperature dependent MFM was carried out on BaM-BTO sample, to investigate any possible influences of the significant strain induced during the tetragonal-cubic phase transition in BTO. The observed changes were very feeble and inhomogeneously distributed.

In order to quantify the observed micromagnetic fluctuations, an algorithm for image processing was developed. The algorithm yielded net domain wall displacement as well as net broadening/thinning of domain wall. The domain wall displacements revealed an anomalously large hysteretic change in magnetization, which could only be rationalized by existence of localized concentration of defects, which in turn could be possibly associated

with the fact that the analyzed spot is a surface. The induced magnetomechanical anisotropy of 3.57×10^6 erg/cm^3, from the domain wall broadening, is almost comparable to the magnetocrystalline anisotropy itself, and hence unreasonable. This signifies need to improve the developed approach, which could be achieved by better sampling in terms of scanned area (x, y) as well as the choice of height for the contours (z). The estimated micromagnetic fluctuations were rationalized in terms of resolution, using a transfer function based approach.

ii) Local investigations of direct ME effect:

Primarily, the direct ME effect was analyzed by analyzing PFM images acquired under a sparsely varying in-situ magnetic field. The application of magnetic field effectively lead to variations in the observed PFM amplitude. This was ultimately rationalized in the form of a stress modulation of the ionic restoring force in $BaTiO_3$, leading to a corresponding variation in the measured electromechanical displacement (d_{33}^{eff}). In order to precisely investigate these variations, along with a spatial mapping of the same, PCA served as a pivotal technique.

The results obtained from PCA exhibited interesting nuances amongst the studied samples, both in terms of the extracted patterns as well as the spatial distribution of the same. One of the most striking nuances was that effective changes were only observed at particular scales. The BaM-BTO sample, owing to its peculiar microstructure, showed effective magnetic field modulation of PFM-amplitude at a very small scale (Figure 5.6). The NFO-BTO sample, despite of a mixed grain type microstructure, could show an identifiable pattern only at a smaller scale, which could only be attributed to the lower magnetostriction (Figure 3.17d), and an absence of preferable phase purity/crystallinity (Figure 3.5). On the other hand, owing to their relatively higher degree of grain mixing, the SrM-BTO and CFO-BTO sample showed recognizable patterns at relatively larger scales. These observations indicate that a mixed grain microstructure, with minimal dispersion in the grain sizes of constituent phases, is necessary in order to sustain the ME induced stress across the FE phase. In addition, the qualitative nature of the extracted magnetic field variations of PFM amplitude showed similarities amongst the systems that share identical scales. The small scale of scan in case of the BaM-BTO and NFO-BTO samples apparently yielded patterns that are symmetric w.r.t. the magnetic field, signifying a unique stress regime, and hence a unique magnetostriction regime in the vicinity. On the other hand the SrM-BTO and CFO-BTO samples manifested multiple stress regimes, leading to multiple patterns that accounted for the *broken heart* shape of the corresponding data-set.

The spatial distributions (score maps) of the extracted magnetic field modulations also revealed interesting nuances, in addition to complimenting the observation made above. The distributions corresponding to the SrM-BTO and the CFO-BTO sample not just showed multiple regions corresponding to the multiple stress regimes, but also exhibited a distinct

feature in that the most prominent changes were concentrated at the interface, gradually decreasing towards the bulk. Conversely, in case of the BaM-BTO and the NFO-BTO sample, the most prominent changes were concentrated in the bulk, gradually decreasing towards the interface. Anomalously, this converse manifestation was also observed for CFO-BTO sample in the Confocal Raman study (Figure 7.7). The common feature among the samples exhibiting this anomaly was that the FE phase in the scanned regions existed in the form of inclusions in a magnetic matrix. This could possibly be hypothesized as a consequence of an inverse Eshelby problem, where the matrix dilates instead of the inclusion.

iii) ME modulation of field balances in local ferroelectric switching

Spatial distributions of effect of an applied in-situ magnetic field on the localized ferroelectric switching (SSPFM) were investigated. The results primarily suggested existence built-in fields at the FE-FM interfaces. These fields showed a consistent polarity at the interfaces, which could be rationalized by considering a material based origin. The possibility which is proposed in the present thesis is the existence of semiconductor heterojunction at the FE-FM interface, in that the persistent difference in band-gaps could lead to formation of a potential barrier. These in-built fields effectively interfered in the local ferroelectric switching process, favoring the domain nucleation process in a particular switching direction. Based on the extent and distribution of this interference, it was observed that the NFO-BTO sample possessed feeble interfacial fields in comparision to that in the BaM-BTO sample. This was attributed to the fact that band-gap difference in case of NFO-BTO is relatively smaller as compared to that in the BaM-BTO sample, possibly leading to a reduced potential barrier.

On application of magnetic field the nucleation biases, as well as the domain growth kinetics were affected. In case of the BaM-BTO sample, the application of magnetic field apparently lifts the favoring effect caused by the in-built field at the interface. Interestingly this lift-up was not uniform across the interface, suggesting existence of a highly anisotropic stress regime. On the other hand the NFO-BTO sample manifested magnetic field induced reduction of the nucleation bias in both the switching directions, which could only be explained by considering the ferroelastic contribution of the ME stress to the switching drive itself; these changes, in contrast to those in the case of the BaM-BTO sample, were uniformly distributed across the interface. These observations lead to the hypothesis that the magnetocrystalline anisotropy in each case plays a vital role in the form of degree of anisotropy in the generated stress at the FE-FM interface.

iv) Direct observation of ME stress via Raman spectroscopy

The magnetic field induced strain in the BaM-BTO and the CFO-BTO sample were observed in the form of frequency shifts of Raman modes corresponding to the $BaTiO_3$

phase. A 2D mapping of these shifts was realized by application of a self-developed algorithm, comprising of a conjunction of PCA and SMCR techniques, to the acquired 2D grid of Raman spectra.

The results, within the limits of error, showed a significant effect of the ME stress on the $BaTiO_3$ Raman spectra, which was spatially consistent. In addition, the nature of these shifts (hardening/softening) was found to be different for the two samples. However, the extent of the observed shifts was found to be inconsistent with literature in terms of its relationship with possible stress levels in the composites. This inconsistency was partially rationalized based on the premises of possible influences of high shear stresses.

In totality, these outcomes suggest that the microstructure in bulk polycrystalline ME composites plays a significant role in deciding the sustainability of the ME induced stresses throughout the sample. This could have significant consequences as far as the optimization of ME performance in polycrystalline composites is concerned. However, the carried out local investigations need further development, in terms of their credibility and feasibility. For that matter, various other techniques could be synergistically involved in order to corroborate the findings presented here. An identical set of investigations could be performed on samples with controlled morphologies and compositions; outcomes of such a study would throw more light onto the microstructure dependence of the local variations of the ME stress, and hence the ME effect. Some of the findings like the magnetic field modulation of PFM amplitude, could be further investigated using samples controlled in terms of the relative crystallographic orientations of the constituent phases (e.g. single crystal laminates, heteroepitaxial films). Moreover, the various analytical approaches opted/developed in this thesis could potentially be used in other fields.

As a natural extension of this project, further work can be carried out in close association with micromechanics based theoretical modeling. The micromechanical approaches, like the one discussed in section 1.4 [97], are in particular robust and suitable for modeling complex textures in composites. The investigations presented in this thesis form the preliminary grounds for future developments that could possibly serve as tangible sources for corroborating theoretically modeled local manifestations of the ME effect. Conversely, the theoretical models could also serve as active source suggesting new morphologies that could be experimentally investigated.

Appendix

(a) Illustration of Superparamagnetic Limit in MRAM

An MRAM comprises of juxtaposed magnetic elements, whose independently switchable magnetizations essentially serves as memory. The two possible orientation states of these elements are separated by an energy barrier, which could be thermally switched with finite probabilities at any given temperature. The mean frequency of this thermally activated flipping can be expressed using the Neel-Arrhenius relation

$$F = F_0 \exp\left(\frac{KV}{K_B T}\right) \quad \textbf{(a. 1)}$$

F_0 – Flipping frequency at 0 K
K – Total magnetic anisotropy constant (J/m^3)
V – Volume of the magnetic element (m^3)

Now, in order to increase the areal density of memory, a common strategy is to reduce the dimensions of the magnetic elements, in order to fit in more of them within a given area. If this reduction of dimensions crosses a particular limit (superparamagnetic limit) than the frequency of flipping for the elements could be very significant even at room temperature. In order to illustrate this, an example from an academic course material [86] is considered here. In this example a hypothetical material is considered, with a total magnetic anisotropy constant of 2.5×10^5 J/m^3, and an F_0 of the order of 10^9. For two different cases, where particles of this material (resembling an MRAM memory element) with diameters of 10 nm and 20 nm, the flipping frequency at room temperature can be given as

$$F_{10nm} = 10^9 exp\left(\frac{2.5\times10^5\times5.2\times10^{-25}}{1.38\times10^{-23}\times300}\right) \quad \textbf{(a. 2)}$$

$$\therefore F_{10nm} = 1.85 \times 10^{-5} Hz \quad \textbf{(a. 3)}$$

$$F_{20nm} = 10^9 exp\left(\frac{2.5\times10^5\times4.1\times10^{-24}}{1.38\times10^{-23}\times300}\right) \quad \textbf{(a. 4)}$$

$$\therefore F_{20nm} \cong 0\ Hz \quad \textbf{(a. 5)}$$

From eqs.(a. 3) and (a. 5) it can be inferred that a 20 nm of element size would virtually never flip, whereas the other element which is mere 10 nm smaller than the former one, will flip after approximately 15 hours, leading to memory loss.

(b) Model Description: A Half Space Magnetic Inclusion With Periodic Domains, Embedded in a $BaTiO_3$ Matrix

In order to simulate the stray field distributions over the magnetic phases in the ME composites, a COMSOL model was developed. Figure 8 shows the corresponding geometry, where the $BaTiO_3$ matrix was in the form of a finite slab, with the half plane inclusion continuously embedded in it. The inclusion was virtually partitioned as shown in Figure 8, such that the divided components of the same material could be assigned different magnetizetion state, thereby simulating magnetic domains. The entire assembly was than placed in a spere of air, ten times larger than the magnetic inclusion.

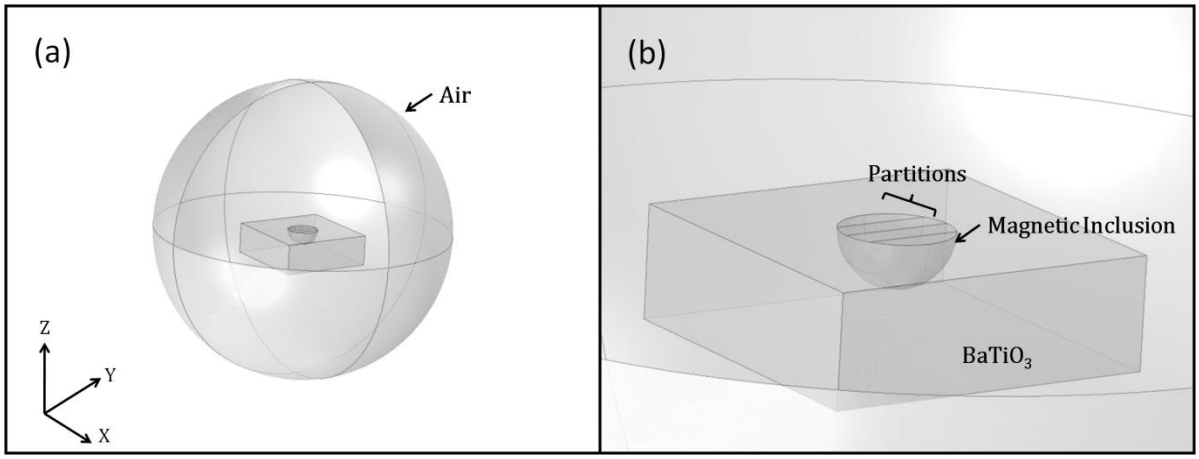

Figure b Shows (a) the entire model geometry, along with (b) a zoomed view of the same. (b) illustrates the partitioning of the magnetic inclusion, which divides the same material into different components.

A custom material was used for the magnetic inclusion, with zero conductivity, and a magnetic permeability of 157 [281]. Whereas the magnetic permeability of $BaTiO_3$ was set to 10 [281]. Later on the entire geometry was meshed with a extra fine free-tetrahedron type meshing. The model was then solved by a stationary study, and a 2D map of the z-component of the magnetic field (H_z) was obtained slightly above the inclusion-air interface (Figure 4.10). This process was repeated for different orientations of magnetization in the artificial domains.

(c) Calculation for Induced Magnetomechanical Energy Using the Experimental Domain Wall Broadening

The domain wall broadening estimated in section 4.5 was attributed to the introduction of a magnetomechanical anisotropy term {eq(4.2)} in eq.(1.34). Based on this argument following relation can be formulated

$$\pi\sqrt{\frac{A}{K_1}} - \pi\sqrt{\frac{A}{K_1+K_M}} = 115 \times 10^{-7}\ cm \qquad \textbf{(c. 1)}$$

K_1 – Magnetocrystalline anisotropy constant (erg/cm^3)
K_M – Magnetomechanical anisotropy constant (erg/cm^3)

where 115 nm is the net domain wall broadening, as estimated in section 4.5. By substituting the value of A ~ 10^6 erg/cm^3 [282] eq.(c. 1) can be reduced to

$$\frac{K_M}{K_1(K_1+K_M)} = 13.41 \times 10^{-6}\ erg/cm^3 \qquad \textbf{(c. 2)}$$

Substituting the value of K_1 ~ 3.3 × 10^6 erg/cm^3 [93] in eq.(c. 2) the value of K_C was estimated to be around 3.37 × 10^6 erg/cm^3, which is the total magnetomechanical anisotropy induced within the scanned region.

(d) Algorithm for Extracting and Mapping Key Parameters in SSPFM

The SSPFM acquisition leads to 3D data-set, consisting of arrays of amplitude and phase corresponding to each 2D grid points. This data-set is first transformed from 3D to 2D. Later, in order to extract the nucleation biases the phase arrays were used. These arrays are later divided into forward and reverse branches, based on the forward and reverse voltage sweeps, respectively (red and blue curves in Figure 9). Each branch assumes the shape of a Boltzmann type step function. Especially, fitting the reverse branch (red; Fig) with a Boltzmann type function of following form [137, 236]

$$y_{reverse} = a_1 - a_2\left[1 + exp\left(\frac{x}{a_4} - \frac{a_3}{a_4}\right)\right]^{-1} + a_5 x \qquad \textbf{(d. 1)}$$

$y_{reverse}$ – Phase values corresponding to the reverse branch
x – DC Voltage
a_1, a_2, a_3, a_4, a_5 – Fit parameters (Figure 9)

yields the negative nucleation bias (NNB) in the form of $a_3 - a_4$ (Figure 9). However, repeating the same procedure for the forward branch would artifactually lead to the point of maximum DC bias, rather than the positive nucleation bias (PNB). Hence, the forward branch was inverted, both vertically as well as horizontally, and then fitted using eq.(d. 1); the estimated values were carefully extrapolated to the original horizontal axis (voltage), giving the actual PNB.

Before each fitting, the initial values were determined for the arrays as follows:

- a_1: Max(y)
- a_2: Max(y) – Min(y)
- a_3: The inflexion point of second derivative of each branch
- a_4: Heuristically chosen to be 4

These initial values were fed into the nonlinear fitting algorithms in MATLAB. The entire procedure was automated in the form of a MATLAB routine, which was then looped over each grid point, yielding 1D arrays of PNB and NNB values. These values were then 1D to 2D transform, yielding the 2D maps shown in section 6.2.

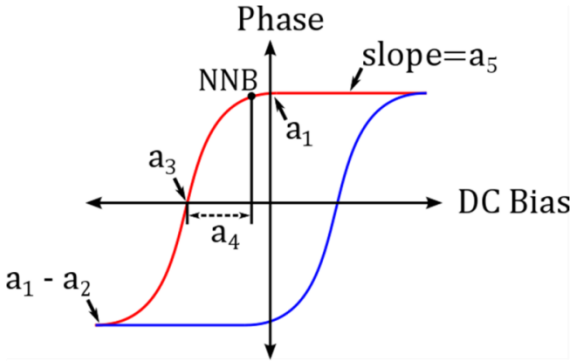

Figure d labeling of the fit parameters of a typical SSPFM loop, also highlighting the division of the phase array into reverse (red) and forward (blue) branches.

(e) Fit Model for $BaTiO_3$ Raman Spectrum

The obtained Raman spectra corresponding to $BaTiO_3$ were consistently assigned a unique set of peaks. Different bands observed in the spectra were assigned to the standard modes in $BaTiO_3$ (Figure 10), by considering a literature report [274] as basis.

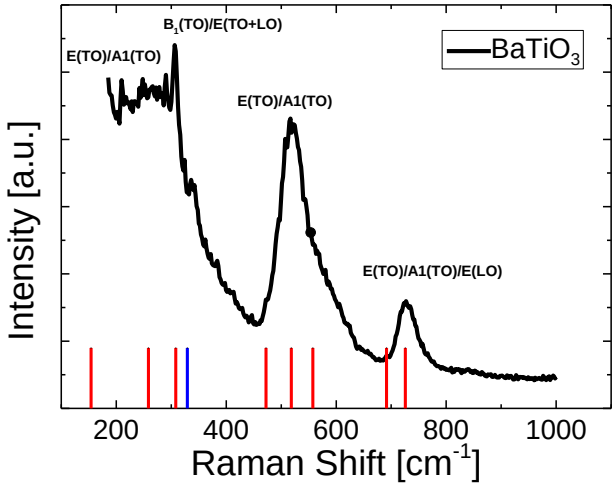

Figure e Shows an average Raman spectrum of $BaTiO_3$, marked with the 9 peak positions (drop lines) used for the fit model. The blue line corresponds to the peak position which was not identified as per the standard $BaTiO_3$ spectrum used [274].

The peaks, marked in Figure 10 were used as initial values in a 9-peak Gaussian-Lorentzian peak function, with following basis

$$y = y_0 + m_L\left[\frac{0.63A.W}{(x-x_p)^2+W^2}\right] - m_G\left[\frac{0.79A}{W}\exp\left\{-\frac{2(x-x_p)^2}{W^2}\right\}\right] \quad \textbf{(e. 1)}$$

y – Raman intensity
x – Raman shift
y_0 - Background
m_L – Weight of Lorentzian function

m_G – Weight of Gaussian function
A – Area under the peak
W – Width of the peak
x_p – Peak position

The second and third terms in eq.(e. 1) are the Lorentzian and Gaussian peak functions respectively. The weight of these functions were included in the fit parameters, along with *A*, *W*, and x_p. Before each fitting step, the non linear background was determined by truncating the active portion of the spectrum (as shown in Figure 10). This background was then subtracted from the original spectrum. Only the truncated active portion of the spectrum was utilized for fitting. The statistical error in fitting was also estimated.

The entire procedure was automated in the form of MATLAB routine, and looped over spectra corresponding to each grid points. The list of fitting parameters, and similarly the list of corresponding errors were arranged as columns in a matrix. The parameters of interest (peak positions; section 7.3) were extracted from this matrix as arrays, and later 1D to 2D transformed to yield the parameter maps, as shown in section 7.3.

References

[1]. R.W. Cahn, *The coming of materials science* (New York; Pergamon, Amsterdam, 2001)

[2]. N.G. Park, *Perovskite solar cells,* Materials Today **18,** 2, 65 (2015)

[3]. W.J. Yin, J.H. Yang, J. Kang, Y. Yan, S.-H. Wei, *Halide perovskite materials for solar cells,* J. Mater. Chem. A **3,** 17, 8926 (2015)

[4]. R. Marschall, *Semiconductor Composites,* Adv. Funct. Mater. **24,** 17, 2421 (2014)

[5]. R.R. Jitta, R. Gundeboina, N.K. Veldurthi, R. Guje, V. Muga, *Defect pyrochlore oxides,* J. Chem. Technol. Biotechnol., **90,** 11, 1937 (2015)

[6]. J.S. Meena, S.M. Sze, U. Chand, T.-Y. Tseng, *Overview of emerging nonvolatile memory technologies,* Nanoscale research letters **9,** 1, 526 (2014)

[7]. J.M. Slaughter, *Materials for Magnetoresistive Random Access Memory,* Annu. Rev. Mater. Res. **39,** 1, 277 (2009)

[8]. R.E. Newnham, *Properties of materials: Anisotropy, symmetry, structure: Anisotropy, symmetry, structure* (Oxford University Press, Oxford, New York, 2005)

[9]. J.F. Nye, *Physical properties of crystals: Their representation by tensors and matrices: Their representation by tensors and matrices* (Clarendon Press; Oxford University Press, Oxford [Oxfordshire], New York, 1985)

[10]. P. Greengard, *The neurobiology of slow synaptic transmission,* Science (New York, N.Y.) **294,** 5544, 1024 (2001)

[11]. J. Clarke, A.I. Braginski, *The SQUID handbook* (Wiley-VCH, Weinheim, Cambridge, (2006)

[12]. H. Greve, E. Woltermann, H.-J. Quenzer, B. Wagner, E. Quandt, *Giant magnetoelectric coefficients in* $(Fe_{90}Co_{10})_{78}Si_{12}B_{10}$*-AlN thin film composites,* Appl. Phys. Lett. **96,** 18, 182501 (2010)

[13]. R. Jahns, A. Piorra, E. Lage, C. Kirchhof, D. Meyners, J.L. Gugat, M. Krantz, M. Gerken, R. Knöchel, E. Quandt, D.J. Green, *Giant Magnetoelectric Effect in Thin-Film Composites,* J. Am. Ceram. Soc. **96,** 6, 1673 (2013)

[14]. M.I. Bichurin, V.M. Petrov, G. Srinivasan, *Theory of low-frequency magnetoelectric effects in ferromagnetic-ferroelectric layered composites,* J. Appl. Phys. **92,** 12, 7681 (2002)

[15]. M. Bichurin, D. Filippov, V. Petrov, V. Laletsin, N. Paddubnaya, G. Srinivasan, *Resonance magnetoelectric effects in layered magnetostrictive-piezoelectric composites,* Phys. Rev. B: Condens. Matter Mater. Phys. **68,** 13 (2003)

[16]. T. Maiti, *Ferroelectric, Antiferroelectric and Relaxor materials* (2011)

[17]. Manuel Bibes and Agnès Barthélémy, *Towards a magnetoelectric memory,* Nat. Mater. **7** (2008)

[18]. H. Béa, M. Gajek, M. Bibes, A. Barthélémy, *Spintronics with multiferroics,* J. Phys.: Condens. Matter **20,** 43, 434221 (2008)

[19]. Adrian Proctor, *Non-Volatile Memory & its use in Enterprise Applications (White paper)* (2012)

[20]. Kristijan Glas, *MRAM – The Birth of the Super Memory*, http://thefutureofthings.com/3037-mram-the-birth-of-the-super-memory/

[21]. I. Dzyaloshinskii, *Magnetoelectric to multiferroic phase transitions,* EPL **96,** 1, 17001 (2011)

[22]. D. N. Astrov, Sov. Phys. JETP **11** (1960)

[23]. T. Zhao, A. Scholl, F. Zavaliche, K. Lee, M. Barry, A. Doran, M.P. Cruz, Y.H. Chu, C. Ederer, N.A. Spaldin, R.R. Das, D.M. Kim, S.H. Baek, C.B. Eom, R. Ramesh, *Electrical control of antiferromagnetic domains in multiferroic BiFeO3 films at room temperature,* Nat. Mater. **5,** 10, 823 (2006)

[24]. T. Kimura, T. Goto, H. Shintani, K. Ishizaka, T. Arima & Y. Tokura, *Magnetic control of ferroelectric polarization,* Nature **426**, 55 (2003)

[25]. V. Laukhin, V. Skumryev, X. Martí, D. Hrabovsky, F. Sánchez, M. García-Cuenca, C. Ferrater, M. Varela, U. Lüders, J. Bobo, J. Fontcuberta, *Electric-Field Control of Exchange Bias in Multiferroic Epitaxial Heterostructures,* Phys. Rev. Lett. **97,** 22 (2006)

[26]. G. Lawes, A. Harris, T. Kimura, N. Rogado, R. Cava, A. Aharony, O. Entin-Wohlman, T. Yildirim, M. Kenzelmann, C. Broholm, A. Ramirez, *Magnetically Driven Ferroelectric Order in Ni3V2O8,* Phys. Rev. Lett. **95,** 8 (2005)

[27]. Y. Choi, H. Yi, S. Lee, Q. Huang, V. Kiryukhin, S.W. Cheong, *Ferroelectricity in an Ising Chain Magnet,* Phys. Rev. Lett. **100,** 4 (2008)

[28]. van den Brink, Jeroen, D.I. Khomskii, *Multiferroicity due to charge ordering,* Journal of Physics: Condensed Matter **20,** 43, 434217 (2008)

[29]. C.A. Vaz, J. Hoffman, C.H. Ahn, R. Ramesh, *Magnetoelectric coupling effects in multiferroic complex oxide composite structures,* Adv. Mater. **22,** 26-27, 2900 (2010)

[30]. R.E. Newnham, R.P. Santoro, P.F. Seal, G.R. Stallings, *Antiferromagnetism in $Mn_3B_2O_6$, $Co_3B_2O_6$, and $Ni_3B_2O_6$,* phys. stat. sol. (b) **16,** 1, K17-K19 (1966)

[31]. M. Avellaneda, G. Harshe, *Magnetoelectric Effect in Piezoelectric/Magnetostrictive Multilayer (2-2) Composites,* J. Intell. Mater. Syst. Struct **5,** 4, 501 (1994)

[32]. W.F. Brown, *Upper Bound on the Magnetoelectric Susceptibility,* Phys. Rev. **168,** 2, 574 (1968)

[33]. J. Wang, J.B. Neaton, H. Zheng, V. Nagarajan, S.B. Ogale, B. Liu, D. Viehland, V. Vaithyanathan, D.G. Schlom, U.V. Waghmare, N.A. Spaldin, K.M. Rabe, M. Wuttig, R. Ramesh, *Epitaxial BiFeO3 multiferroic thin film heterostructures,* Science (New York, N.Y.) **299,** 5613, 1719 (2003)

[34]. L.W. Martin, S.P. Crane, Y.H. Chu, M.B. Holcomb, M. Gajek, M. Huijben, C.H. Yang, N. Balke, R. Ramesh, *Multiferroics and magnetoelectrics,* J. Phys. Condens. Matter. **20,** 43, 434220 (2008)

[35]. C.H. Yang, J. Seidel, S.Y. Kim, P.B. Rossen, P. Yu, M. Gajek, Y.H. Chu, L.W. Martin, M.B. Holcomb, Q. He, P. Maksymovych, N. Balke, S.V. Kalinin, A.P. Baddorf, S.R. Basu, M.L. Scullin, R. Ramesh, *Electric modulation of conduction in multiferroic Ca-doped BiFeO3 films,* Nat. Mater. **8,** 6, 485 (2009)

[36]. M. Gajek, M. Bibes, S. Fusil, K. Bouzehouane, J. Fontcuberta, A. Barthelemy, A. Fert, *Tunnel junctions with multiferroic barriers,* Nat. Mater. **6,** 4, 296 (2007)

[37]. A.F. Devonshire, *Theory of ferroelectrics,* Advances in Physics **3,** 10, 85 (1954)

[38]. D.C. Lupascu, H. Wende, M. Etier, A. Nazrabi, I. Anusca, H. Trivedi, V.V. Shvartsman, J. Landers, S. Salamon, C. Schmitz-Antoniak, *Measuring the magnetoelectric effect across scales,* GAMM-Mitteilungen **38,** 1, 25 (2015)

[39]. M. Etier, V.V. Shvartsman, Y. Gao, J. Landers, H. Wende, D.C. Lupascu, *Magnetoelectric Effect in (0–3) $CoFe_2O_4$ –$BaTiO_3$ (20/80) Composite Ceramics Prepared by the Organosol Route,* Ferroelectrics **448,** 1, 77 (2013)

[40]. M. Etier, C. Schmitz-Antoniak, S. Salamon, H. Trivedi, Y. Gao, A. Nazrabi, J. Landers, D. Gautam, M. Winterer, D. Schmitz, H. Wende, V.V. Shvartsman, D.C. Lupascu,

Magnetoelectric coupling on multiferroic cobalt ferrite–barium titanate ceramic composites with different connectivity schemes, Acta Materialia **90**, 1 (2015)

[41]. G. Srinivasan, E. Rasmussen, R. Hayes, *Magnetoelectric effects in ferrite-lead zirconate titanate layered composites: The influence of zinc substitution in ferrites,* Phys. Rev. B **67,** 1 (2003)

[42]. C. Deng, Y. Zhang, J. Ma, Y. Lin, C.-W. Nan, *Magnetic-electric properties of epitaxial multiferroic $NiFe_2O_4$–$BaTiO_3$ heterostructure,* J. Appl. Phys. **102,** 7, 74114 (2007)

[43]. F. Zavaliche, H. Zheng, L. Mohaddes-Ardabili, S. Y. Yang, Q. Zhan, P. Shafer, E. Reilly, R. Chopdekar, Y. Jia, P. Wright, D. G. Schlom, Y. Suzuki, and R. Ramesh, *Electric Field-Induced Magnetization Switching in Epitaxial Columnar Nanostructures,* Nano Lett. **5,** 9, 1793 (2005)

[44]. S.H. Xie, Y.M. Liu, Y. Ou, Q.N. Chen, X.L. Tan, J.Y. Li, *Magnetoelectric coupling of multilayered $Pb(Zr_{0.52}Ti_{0.48})O_3$-$CoFe_2O_4$ film by piezoresponse force microscopy under magnetic field,* J. Appl. Phys. **112,** 7, 74110 (2012)

[45]. S. Xie, F. Ma, Y. Liu, J. Li, *Multiferroic $CoFe_2O_4$-$Pb(Zr(0.52)Ti(0.48))O_3$ core-shell nanofibers and their magnetoelectric coupling,* Nanoscale **3,** 8, 3152 (2011)

[46]. A.M.J.G. Van Run, D.R. Terrel, J.H. Scholing, *An insitu growth eutectic magnetoelectric composite material,* J. Mater. Sci. **9**, 1710 (1974)

[47]. G. Srinivasan, V.M. Laletsin, R. Hayes, N. Puddubnaya, E.T. Rasmussen, D.J. Fekel, *Giant magnetoelectric effects in layered composites of nickel zinc ferrite and lead zirconate titanate,* Solid State Communications **124,** 10-11, 373 (2002)

[48]. J. Ryu, S. Priya, K. Uchino, H.-E. Kim, Journal of Electroceramics **8,** 2, 107 (2002)

[49]. S. Dong, J.F. Li, D. Viehland, *Giant magnetoelectric effect in laminate composites,* Philosophical Magazine Letters **83,** 12, 769 (2003)

[50]. N. Cai, C.W. Nan, J. Zhai, Y. Lin, *Large high-frequency magnetoelectric response in laminated composites of piezoelectric ceramics, rare-earth iron alloys and polymer,* Appl. Phys. Lett. **84,** 18, 3516 (2004)

[51]. Y. Wang, S.W. Or, Chan, Helen Lai Wa, X. Zhao, H. Luo, *Enhanced magnetoelectric effect in longitudinal-transverse mode Terfenol-D/$Pb(Mg_{1/3}Nb_{2/3})O_3$–$PbTiO_3$ laminate composites with optimal crystal cut,* J. Appl. Phys. **103,** 12, 124511 (2008)

[52]. J. Van Den Boomgaard, D.R. Terrell, R. A. J. Born, H. F. J. I. Giller, *An in situ growth eutectic magnetoelectric composite material,* J. Mater. Sci. **9**, 1705 (1974)

[53]. Girish Rajaram Harshe, *Magnetoelectric Effect in Piezoelectric-Magnetostrictive Composites*. PhD (The Pennsylvania State University, 1991)

[54]. V. Corral-Flores, D. Bueno-Baques, D. Carrillo-Flores, J.A. Matutes-Aquino, *Enhanced magnetoelectric effect in core-shell particulate composites,* J. Appl. Phys. **99,** 8, 08J503 (2006)

[55]. M.E. Botello-Zubiate, D. Bueno-Baqués, De Frutos Vaquerizo, J., Fuentes Cobas, L. E., J.A. Matutes-Aquino, *Magnetoelectric Measurements by Two Different Methods of Cobalt Ferrite-Barium Titanate Composites,* Ferroelectrics **338,** 1, 247 (2006)

[56]. F. Bai, H. Zhang, J. Li, D. Viehland, *Magnetic and magnetoelectric properties of as-deposited and annealed $BaTiO_3$–$CoFe_2O_4$ nanocomposite thin films,* J. Phys. D: Appl. Phys. **43,** 28, 285002 (2010)

[57]. H. Zheng, *Multiferroic $BaTiO_3$-$CoFe_2O_4$ Nanostructures,* Science **303,** 5658, 661 (2004)

[58]. Y. Zhang, C. Deng, J. Ma, Y. Lin, C.-W. Nan, *Enhancement in magnetoelectric response in $CoFe_2O_4$–$BaTiO_3$ heterostructure,* Appl. Phys. Lett. **92,** 6, 62911 (2008)

[59]. J. Van Den Boomgaard, R. A. J. Born, *A sintered magnetoelectric composite material $BaTiO_3$ -Ni(Co, Mn)Fe_2O_4,* J. Mater. Sci. **13**, 1538 (1978)

[60]. G. Sreenivasulu, V.H. Babu, G. Markandeyulu, B.S. Murty, *Magnetoelectric effect of $(100-x)BaTiO_3$–$(x)NiFe_{1.98}O_4$ (x=20–80 wt %) particulate nanocomposites,* Appl. Phys. Lett. **94,** 11, 112902 (2009)

[61]. R.S. Devan, B.K. Chougule, *Effect of composition on coupled electric, magnetic, and dielectric properties of two phase particulate magnetoelectric composite,* J. Appl. Phys. **101,** 1, 14109 (2007)

[62]. J.P. Zhou, L. Lv, Q. Liu, Y.X. Zhang, P. Liu, *Hydrothermal synthesis and properties of $NiFe_2O_4$-$BaTiO_3$composites with well-matched interface,* Sci. Technol. Adv. Mater. **13,** 4, 45001 (2012)

[63]. Y. Jia, S.W. Or, J. Wang, Chan, Helen Lai Wa, X. Zhao, H. Luo, *High magnetoelectric effect in laminated composites of giant magnetostrictive alloy and lead-free piezoelectric ceramic,* J. Appl. Phys. **101,** 10, 104103 (2007)

[64]. J.Y. Zhai, N. Cai, L. Liu, Y.H. Lin, C.W. Nan, *Dielectric behavior and magnetoelectric properties of lead zirconate titanate/Co-ferrite particulate composites,* Materials Science and Engineering: B **99,** 1-3, 329 (2003)

[65]. J.P. Zhou, H.C. He, Z. Shi, G. Liu, C.-W. Nan, *Dielectric, magnetic, and magnetoelectric properties of laminated $PbZr_{0.52}Ti_{0.48}O_3/CoFe_2O_4$ composite ceramics,* J. Appl. Phys. **100,** 9, 94106 (2006)

[66]. S.G. Lu, Z.K. Xu, Y.P. Wang, S.S. Guo, H. Chen, T.L. Li, S.W. Or, *Effect of $CoFe_2O_4$ content on the dielectric and magnetoelectric properties in $Pb(ZrTi)O_3/CoFe_2O_4$ composite,* J. Electroceram. **21,** 1-4, 398 (2007)

[67]. Y. Wu, J.G. Wan, J.M. Liu, G. Wang, *Significant enhancement of magnetoelectric output in multiferroic heterostructural films modulated by electric polarization cycles,* Appl. Phys. Lett. **96,** 15, 152902 (2010)

[68]. M. Zeng, *Resonance magnetoelectric effect in bulk composites of lead zirconate titanate and nickel ferrite,* J. Appl. Phys. **95,** 12, 8069 (2004)

[69]. R.A. Islam, V. Bedekar, N. Poudyal, J.P. Liu, S. Priya, *Magnetoelectric properties of core-shell particulate nanocomposites,* J. Appl. Phys. **104,** 10, 104111 (2008)

[70]. G. Srinivasan, E.T. Rasmussen, J. Gallegos, R. Srinivasan, Y.I. Bokhan, V.M. Laletin, *Magnetoelectric bilayer and multilayer structures of magnetostrictive and piezoelectric oxides,* Phys. Rev. B **64,** 21 (2001)

[71]. H. Miao, X. Zhou, S. Dong, H. Luo, F. Li, *Magnetic-field-induced ferroelectric polarization reversal in magnetoelectric composites revealed by piezoresponse force microscopy,* Nanoscale **6,** 15, 8515 (2014)

[72]. W. Cochran, *Crystal stability and the theory of ferroelectricity,* Advances in Physics **9,** 36, 387 (1960)

[73]. R.H. Lyddane, R.G. Sachs, and E. Teller, *On the Polar Vibrations of Alkali Halides,* Phys. Rev. **59**, 673 (1941)

[74]. ME. Lines, A.M. Glass, *Principles and applications of ferroelectrics and related materials* (Oxford University Press, 2001)

[75]. D. Damjanovic, *Ferroelectric, dielectric and piezoelectric properties of ferroelectric thin films and ceramics, Rep. Prog. Phys. **61**, 9, 1267* (1996)

[76]. Don Berlincourt and Hans Jaffe, *Elastic and Piezoelectric Coefficients of Single-Crystal Barium Titanate*, Phys. Rev. **111,** 1, 143 (1958)

[77]. D. Damjanovic, F. Brem, N. Setter, *Crystal orientation dependence of the piezoelectric d_{33} coefficient in tetragonal $BaTiO_3$ as a function of temperature*, Appl. Phys. Lett. **80,** 4, 652 (2002)

[78]. D. G. Schlom, *Visualizing the Anisotropy of Crystals: Nye Plus 3-D Graphics*, Journal of Materials Education **20**, 77 (1998)

[79]. J.P. Srivastava, *Elements of Solid State Physics* (PHI Learning, New Delhi, 2011)

[80]. R.M. EISBERG, R. Resnick, *Quantum physics of atoms, molecules, solids, nuclei, and particles* (John Wiley and Sons, New York, etc., 1974)

[81]. P.W. Anderson, *Antiferromagnetism. Theory of Superexchange Interaction*, Phys. Rev. **79**, 2, 350 (1950)

[82]. J.B. Goodenough, *Theory of the Role of Covalence in the Perovskite-Type Manganites [La, M(II)]MnO_3*, Phys. Rev. **100**, 2, 564 (1955)

[83]. J. Kanamori, *Superexchange interaction and symmetry properties of electron orbitals*, Journal of Physics and Chemistry of Solids **10,** 2-3, 87 (1959)

[84]. J.C. Slater, *Ferromagnetism and the Band Theory*, Rev. Mod. Phys. **25**, 1, 199 (1953)

[85]. B.D. Cullity, C.D. Graham, *Introduction to magnetic materials* (Wiley, Hoboken, N.J., Chichester, 2009)

[86]. D.C. Agrawal, *Introduction To Nanotechnology (MS 617)* (Kanpur, India, 2010)

[87]. S.P. Kuntsevich, V.P. Palekhin, *Influence of Ba^{+2}, Sr^{+2}, and Pb^{+2} ions on the magnetoelastic properties of hexaferrites of structural type M*, Soviet Physics Journal **19,** 7, 956 (1976)

[88]. Earl Callen and Herbert B. Callen, *Magnetostriction, Forced Magnetostriction, and Anomalous Thermal Expansion in Ferromagnets*, Phys. Rev. **139**, 2A, 455 (1965)

[89]. F.S. Galasso, N. Kurti, R. Smoluchowski, *Structure and Properties of Inorganic Solids: International Series of Monographs in Solid State Physics* (Elsevier Science, 2013)

[90]. J. Teillet, F. Bouree, R. Krishnan, *Magnetic structure of $CoFe_2O_4$*, Journal of Magnetism and Magnetic Materials **123,** 1-2, 93 (1993)

[91]. J. Smit, H.P.J. Wijn, *Ferrites* (Philips Technical Library, 1959)

[92]. R.M. Bozorth, *Anisotropy and Magnetostriction of Some Ferrites,* Phys. Rev. **99,** 6, 1788 (1955)

[93]. R.C. Pullar, *Hexagonal ferrites,* Progress in Materials Science **57,** 7, 1191 (2012)

[94]. C.W. Nan, *magnetoelectric effect in composites of piezoeelctric and piezomagnetic phases,* Phys. Rev. B **50,** 9, 6082 (1994)

[95]. V. Petrov, G. Srinivasan, M. Bichurin, A. Gupta, *Theory of magnetoelectric effects in ferrite piezoelectric nanocomposites,* Phys. Rev. B: Condens. Matter Mater. Phys. **75,** 22 (2007)

[96]. G. Srinivasan, E. Rasmussen, R. Hayes, *Magnetoelectric effects in ferrite-lead zirconate titanate layered composites: The influence of zinc substitution in ferrites,* Phys. Rev. B **67,** 1 (2003)

[97]. M. Labusch, M. Etier, D.C. Lupascu, J. Schröder, M.-A. Keip, *Product properties of a two-phase magneto-electric composite: Synthesis and numerical modeling,* Comput Mech **54,** 1, 71 (2014)

[98]. J. Schröder, M.A. Keip, *Two-scale homogenization of electromechanically coupled boundary value problems,* Comput Mech **50,** 2, 229 (2012)

[99]. A. Raval, *Modeling of Local Stress in Magnetoelectric Composite*. Master (University of Duisburg-Essen)

[100]. Y. Geng, H. Das, A.L. Wysocki, X. Wang, S.W. Cheong, M. Mostovoy, C.J. Fennie, W. Wu, *Direct visualization of magnetoelectric domains,* Nat. Mater. **13,** 2, 163 (2014)

[101]. F. Yan, G. Chen, L. Lu, P. Finkel, J.E. Spanier, *Local probing of magnetoelectric coupling and magnetoelastic control of switching in $BiFeO_3$-$CoFe_2O_4$ thin-film nanocomposite,* Appl. Phys. Lett. **103,** 4, 42906 (2013)

[102]. M. Pan, S. Hong, J.R. Guest, Y. Liu, A. Petford-Long, *Visualization of magnetic domain structure changes induced by interfacial strain in $CoFe_2O_4$/$BaTiO_3$ heterostructures,* J. Phys. D: Appl. Phys. **46,** 5, 55001 (2013)

[103]. Gabriel caruntu, Amin Yourdkhani, Marian Vosaroiu, and Gopalan Srinivasan, *cn,* Nanoscale **4**, 3218 (2012)

[104]. Y. Zhou, M.G. Chen, Z.J. Feng, X.Y. Wang, Y.J. Cui, J.C. Zhang, *High Magnetoelectric Coupling in Nano—Microscale Particulate Composites at Low Frequency,* Chin. Phys. Lett **28,** 10, 107503 (2011)

[105]. M.B. Holcomb, L.W. Martin, A. Scholl, Q. He, P. Yu, C.-H. Yang, S.Y. Yang, P.-A. Glans, M. Valvidares, M. Huijben, J.B. Kortright, J. Guo, Y.-H. Chu, R. Ramesh, *Probing the evolution of antiferromagnetism in multiferroics,* Phys. Rev. B **81,** 13 (2010)

[106]. Q. He, E. Arenholz, A. Scholl, Y.-H. Chu, R. Ramesh, *Nanoscale characterization of emergent phenomena in multiferroics,* Current Opinion in Solid State and Materials Science **16,** 5, 216 (2012)

[107]. J. Schaab, I.P. Krug, F. Nickel, D.M. Gottlob, H. Doğanay, A. Cano, M. Hentschel, Z. Yan, E. Bourret, C.M. Schneider, R. Ramesh, D. Meier, *Imaging and characterization of conducting ferroelectric domain walls by photoemission electron microscopy,* Appl. Phys. Lett. **104,** 23, 232904 (2014)

[108]. M. Fiebig, T. Lottermoser, D. Fröhlich, A.V. Goltsev, R.V. Pisarev, *Observation of coupled magnetic and electric domains,* Nature **419,** 6909, 818 (2002)

[109]. M. Fiebig, *Magnetoelectric phase control in multiferroic manganites,* Phase Transitions **79,** 12, 947 (2006)

[110]. T. Lottermoser, M. Fiebig, *Magnetoelectric behavior of domain walls in multiferroic HoMnO3,* Phys. Rev. B **70,** 22 (2004)

[111]. M. Matsubara, S. Manz, M. Mochizuki, T. Kubacka, A. Iyama, N. Aliouane, T. Kimura, S.L. Johnson, D. Meier, M. Fiebig, *Multiferroics. Magnetoelectric domain control in multiferroic $TbMnO_3$,* Science (New York, N.Y.) **348,** 6239, 1112 (2015)

[112]. D. Meier, J. Seidel, A. Cano, K. Delaney, Y. Kumagai, M. Mostovoy, N.A. Spaldin, R. Ramesh, M. Fiebig, *Anisotropic conductance at improper ferroelectric domain walls,* Nature materials **11,** 4, 284 (2012)

[113]. Gerd K. Bennig, *Atomic force microscope and method for imaging surfaces with atomic resolution* (1986)

[114]. K. E. Carr, *Applications of scanning electron microscopy in biology,* International review of cytology **30**, 183 (1971)

[115]. H. Fujisawa, M. Shimizu, H. Niu, T. Horiuchi, T. Shiosaki, K. Matsushige, *Simultaneous observation of the surface topography and current flow of PZT thin films using an atomic force microscope,* Integrated Ferroelectrics **18,** 1-4, 71 (1997)

[116]. M. Nonnenmacher, M.P. O'Boyle, H.K. Wickramasinghe, *Kelvin probe force microscopy,* Appl. Phys. Lett. **58,** 25, 2921 (1991)

[117]. B. Bhushan, V.N. Koinkar, *Nanoindentation hardness measurements using atomic force microscopy,* Appl. Phys. Lett. **64,** 13, 1653 (1994)

[118]. R. Garcia, R. Proksch, *Nanomechanical mapping of soft matter by bimodal force microscopy,* European Polymer Journal **49,** 8, 1897 (2013)

[119]. P. Grütter, D. Rugar, H.J. Mamin, *Magnetic force microscopy of magnetic materials,* Ultramicroscopy **47,** 4, 393 (1992)

[120]. R.B. Proksch, T.E. Schäffer, B.M. Moskowitz, E.D. Dahlberg, D.A. Bazylinski, R.B. Frankel, *Magnetic force microscopy of the submicron magnetic assembly in a magnetotactic bacterium,* Appl. Phys. Lett. **66,** 19, 2582 (1995)

[121]. A. Gruverman, S.V. Kalinin, *Piezoresponse force microscopy and recent advances in nanoscale studies of ferroelectrics,* J. Mater. Sci. **41,** 1, 107 (2006)

[122]. N. Balke, S. Jesse, Y. Kim, L. Adamczyk, A. Tselev, I.N. Ivanov, N.J. Dudney, S.V. Kalinin, *Real space mapping of Li-ion transport in amorphous Si anodes with nanometer resolution,* Nano letters **10,** 9, 3420 (2010)

[123]. S. Kalinin, A. Gruverman (eds), *Scanning Probe Microscopy* (Springer New York, New York, NY, 2007)

[124]. A. Ehresmann, I. Krug, A. Kronenberger, A. Ehlers, D. Engel, *In-plane magnetic pattern separation in NiFe/NiO and Co/NiO exchange biased bilayers investigated by magnetic force microscopy,* J. Magn. Magn. Mater. **280,** 2-3, 369 (2004)

[125]. T. Zhao, C. Hou, H. Fujiwara, H. Cho, J.W. Harrell, A. Khapikov, *Study of 360° domain walls in NiFe/NiO film by tip–sample interaction on magnetic force microscope,* J. Appl. Phys. **87,** 9, 6484 (2000)

[126]. S.H. Liou,R.F. Sabiryanov,S.S. Jaswal,J.C. Wu,Y.D. Yao, *Magnetic domain patterns of rectangular and Magnetic domain Patterns of rectangular and elliptic arrays of small permalloy elements,* J. Magn. Magn. Mater. **226-230**, 1270 (2000)

[127]. D.A. Bonnell, S.V. Kalinin, A.L. Kholkin, A. Gruverman, *Piezoresponse Force Microscopy,* MRS Bulletin **34,** 09, 648 (2011)

[128]. H.O. Jacobs, H.F. Knapp, A. Stemmer, *Practical aspects of Kelvin probe force microscopy,* Rev. Sci. Instrum. **70,** 3, 1756 (1999)

[129]. L. Collins, J.I. Kilpatrick, M. Bhaskaran, S. Sriram, S.A.L. Weber, S.P. Jarvis, B.J. Rodriguez, in *2012 Joint 21st IEEE ISAF/11th IEEE ECAPD/IEEE PFM (ISAF/ECAPD/PFM)* , p. 1

[130]. S.V. Kalinin, E. Karapetian, M. Kachanov, *Nanoelectromechanics of piezoresponse force microscopy,* Phys. Rev. B **70,** 18 (2004)

[131]. M. Abplanalp, *Piezoresponse scanning force microscopy of ferroelectric domains* (Zürich, 2001)

[132]. A.L. Kholkin, S.V. Kalinin, A. Roelofs, A. Gruverman, in *Scanning Probe Microscopy*, ed. by S. V. Kalinin, A. Gruverman (Springer New York, 2007), p. 173

[133]. Brian J Rodriguez and Clint Callahan and Sergei V Kalinin and Roger Proksch, *Dual-frequency resonance-tracking atomic force microscopy,* Nanotechnology **18,** 47, 475504 (2007)

[134]. S. Jesse, S.V. Kalinin, *Band excitation in scanning probe microscopy: sines of change,* J. Phys. D: Appl. Phys. **44,** 46, 464006 (2011)

[135]. An Oxford Instrument company, *Piezo Force Microscopy (PFM) using Dual AC Resonance-Tracking (Whitepaper)* (US, 2011)

[136]. S. Jesse, B.J. Rodriguez, S. Choudhury, A.P. Baddorf, I. Vrejoiu, D. Hesse, M. Alexe, E.A. Eliseev, A.N. Morozovska, J. Zhang, L.Q. Chen, S.V. Kalinin, *Direct imaging of the spatial and energy distribution of nucleation centres in ferroelectric materials,* Nature materials **7,** 3, 209 (2008)

[137]. S. Jesse, H.N. Lee, S.V. Kalinin, *Quantitative mapping of switching behavior in piezoresponse force microscopy,* Rev. Sci. Instrum. **77,** 7, 73702 (2006)

[138]. I.R. Lewis, H.G.M. Edwards, *Handbook of Raman spectroscopy: From the research laboratory to the process line: From the research laboratory to the process line* (Marcel Dekker, New York, 2001)

[139]. C.N. Banwell, E.M. McCash, *Fundamentals of molecular spectroscopy* (McGraw-Hill Book, London, New York, 1994)

[140]. Princeton Instruments, *Confocal Raman Microscopy General Overview (Whitepaper)*

[141]. T. Dieing, O. Hollricher, J. Toporski, *Confocal Raman microscopy* (Springer, Heidelberg, London, 2011)

[142]. M. Minsky, *Memoir on inventing the confocal scanning microscope,* Scanning **10,** 4, 128 (1988)

[143]. M. Etier, Y. Gao, V.V. Shvartsman, A. Elsukova, J. Landers, H. Wende, D.C. Lupascu, *Cobalt Ferrite/Barium Titanate Core/Shell Nanoparticles,* Ferroelectrics **438,** 1, 115 (2012)

[144]. D.V. Karpinsky, R.C. Pullar, Y.K. Fetisov, K.E. Kamentsev, A.L. Kholkin, *Local probing of magnetoelectric coupling in multiferroic composites of $BaFe_{12}O_{19}$–$BaTiO_3$,* J. Appl. Phys. **108,** 4, 42012 (2010)

[145]. J.I. Goldstein, D.E. Newbury, P. Echlin, D.C. Joy, C.E. Lyman, E. Lifshin, L. Sawyer, J.R. Michael, *Scanning Electron Microscopy and X-ray Microanalysis* (Springer US, Boston, MA, 2003)

[146]. G.V. Duong, R. Groessinger, *Effect of preparation conditions on magnetoelectric properties of $CoFe_2O_4$–$BaTiO_3$ magnetoelectric composites,* J. Magn. Magn. Mater. **316,** 2, e624-e627 (2007)

[147]. H. Shinzawa, K. Awa, W. Kanematsu, Y. Ozaki, *Multivariate data analysis for Raman spectroscopic imaging,* J. Raman Spectrosc. **40,** 12, 1720 (2009)

[148]. R.Y. Sato-Berrú, E.V. Mejía-Uriarte, C. Frausto-Reyes, M. Villagrán-Muniz, H.M. S, J.M. Saniger, *Application of principal component analysis and Raman spectroscopy in the analysis of polycrystalline $BaTiO_3$ at high pressure,* Spectrochimica acta. Part A, Molecular and biomolecular spectroscopy **66,** 3, 557 (2007)

[149]. E.V. Mejía-Uriarte , R.Y. Sato-Berrú , M. Navarrete , O. Kolokoltsev , J. M. Saniger (ed), *Determination of Phase Transition by Principal Component Analysis Applied to Raman Spectra of Polycristalline $BaTiO_3$ at Low and High Temperature* (Journal of Apllied Research and Technology, 2012)

[150]. O. Abu Omar, S. Nouranian, R. King, J.L. Bouvard, H. Toghiani, T.E. Lacy, C.U. Pittman, *Data mining and knowledge discovery in materials science and engineering,* Advanced Engineering Informatics **27,** 4, 615 (2013)

[151]. A.V. Ceguerra, A.J. Breen, L.T. Stephenson, P.J. Felfer, V.J. Araullo-Peters, P.V. Liddicoat, X. Cui, L. Yao, D. Haley, M.P. Moody, B. Gault, J.M. Cairney, S.P. Ringer, *The rise of computational techniques in atom probe microscopy,* Current Opinion in Solid State and Materials Science **17,** 5, 224 (2013)

[152]. S. Jesse, S.V. Kalinin, *Principal component and spatial correlation analysis of spectroscopic-imaging data in scanning probe microscopy,* Nanotechnology **20,** 8, 85714 (2009)

[153]. Paul Honeine, *An eigenanalysis of data centering in machine learning* (Troyes, France, 2014)

[154]. Daniel D. Lee, H. Sebastian Seung, *Algorithms for Non-negative Matrix Factorization,* Adv. Neural Info. Proc. Syst. **13**, 556 (2001)

[155]. K. Awa, T. Okumura, H. Shinzawa, M. Otsuka, Y. Ozaki, *Self-modeling curve resolution (SMCR) analysis of near-infrared (NIR) imaging data of pharmaceutical tablets,* Anal. Chim. Acta **619,** 1, 81 (2008)

[156]. D. V. Karpinsky, E. K Selezneva, I. K Bdikin, F. Figueiras, K. E. Kamentsev, Y. K Fetisov, *Development of Novel Multiferroic Composites Based on $BaTiO_3$ and Hexagonal Ferrites,* Mater. Res. Soc. Symo. Proc. **1161** (2009)

[157]. M.E. Buttner R.H., *Structural Parameters and Electron Difference density in $BaTiO_3$,* Acta Crystallographica, Section B: Structural Science **48**, 764 (1992)

[158]. X. Obradors, A. Collomb, M. Pernet, D. Samaras, J. Joubert, *X-ray analysis of the structural and dynamic properties of $BaFe_{12}O_{19}$ hexagonal ferrite at room temperature,* Journal of Solid State Chemistry **56**, 171 (1985)

[159]. Z.F. Zi, Y.P. Sun, X.B. Zhu, Z.R. Yang, J.M. Dai, W.H. Song, *Structural and magnetic properties of $SrFe_{12}O_{19}$ hexaferrite synthesized by a modified chemical co-precipitation method,* J. Magn. Magn. Mater., 2008, 2746 (320)

[160]. G.D. Rieck, J. Thijssen, *The cation distribution in Co Fe2 O4,* Acta Crystallographica B **24,** 982-983 (1968)

[161]. E.J. Palin, R.J. Harrison, *A Monte Carlo investigation of the thermodynamics of cation ordering in 2-3 spinels,* American Mineralogist **92**, 1334 (2007)

[162]. M.M. Nowell, R.A. Witt, B. True, *EBSD Sample Preparation,* MAM **11,** S02 (2005)

[163]. D. Ravinder, P. Shalini, P. Mahesh, K. Koteswara Rao, M. Vithal, B. Boyanov, *Electrical conductivity of Ba–Co–Ti hexagonal ferrites,* Journal of Alloys and Compounds **364,** 1-2, 17 (2004)

[164]. M. El Hiti, A. Abo El Ata, *Semiconductivity in $Ba_2Ni_{2-x}Zn_xFe_{12}O_{22}$ Y-type hexaferrites,* Journal of Magnetism and Magnetic Materials **195,** 3, 667 (1999)

[165]. G. Asghar, M. Anis-ur-Rehman, *Structural, dielectric and magnetic properties of Cr–Zn doped strontium hexa-ferrites for high frequency applications,* Journal of Alloys and Compounds **526**, 85 (2012)

[166]. M.A. Ahmed, S.F. Mansour, M.A. Abdo, *Electrical properties of Cu substituted Co nano ferrite,* Phys. Scr. **86,** 2, 25705 (2012)

[167]. M.S. Khandekar, R.C. Kambale, J.Y. Patil, Y.D. Kolekar, S.S. Suryavanshi, *Effect of calcination temperature on the structural and electrical properties of cobalt ferrite synthesized by combustion method,* Journal of Alloys and Compounds **509,** 5, 1861 (2011)

[168]. P.A. Shaikh, R.C. Kambale, A.V. Rao, Y.D. Kolekar, *Structural, magnetic and electrical properties of Co–Ni–Mn ferrites synthesized by co-precipitation method,* Journal of Alloys and Compounds **492,** 1-2, 590 (2010)

[169]. T.K. Kundu, S. Mishra, N. Karak, P. Barik, *Effect of Ti^{+4} ions doping on microstructure and dc resistivity of nickel ferrites,* Journal of Physics and Chemistry of Solids **73,** 4, 579 (2012)

[170]. Y. Zhou, F.G. Shin, *Magnetoelectric effect of mildly conducting magnetostrictive/piezoelectric particulate composites,* J. Appl. Phys. **100,** 4, 43910 (2006)

[171]. B.K. Bammannavar, L.R. Naik, R.K. Kotnala, *Study of electrical properties and the magnetoelectric effect in $Ni_{0.2}Co_{0.8}Fe_2O_4$+$PbZr_{0.8}Ti_{0.2}O_3$ particulate composites,* Smart Mater. Struct. **20,** 4, 45005 (2011)

[172]. G. Srinivasan, V.M. Laletsin, R. Hayes, N. Puddubnaya, E.T. Rasmussen, D.J. Fekel, *Giant magnetoelectric effects in layered composites of nickel zinc ferrite and lead zirconate titanate,* Solid State Communications **124,** 10-11, 373 (2002)

[173]. J. J. Went, G. W. Rathenau, E. W. Gorter, and G. W. van Oosterhout, *Hexagonal Iron-Oxide Compounds as Permanent-Magnet Materials*

[174]. J. Dho, E.K. Lee, J.Y. Park, N.H. Hur, *Effects of the grain boundary on the coercivity of barium ferrite $BaFe_{12}O_{19}$,* Journal of Magnetism and Magnetic Materials **285,** 1-2, 164 (2005)

[175]. D.J. Craik, E.W. Hill, *Coercivity mechanisms in oxide magnets,* J. Phys. Colloques **38,** C1, 39-41 (1977)

[176]. J. Dufour, R. Latorre, C. Negro, E.M. Alcalá, A. Formoso, F. López-Mateos, *Protocol for the synthesis of Ba-hexaferrites with prefixed coercivities,* Journal of Magnetism and Magnetic Materials **172,** 3, 308 (1997)

[177]. L. Jahn, H.G. Müller, *The Coercivity of Hard Ferrite Single Crystals*, phys. stat. sol. (b) **35,** 2, 723 (1969)

[178]. A. Cochardt, *Modified Strontium Ferrite, a New Permanent Magnet Material*, J. Appl. Phys. **34,** 4, 1273 (1963)

[179]. G.V. Duong, R. Groessinger, M. Schoenhart, D. Bueno-Basques, *The lock-in technique for studying magnetoelectric effect,* J. Magn. Magn. Mater. **316,** 2, 390 (2007)

[180]. S. Geprägs, A. Brandlmaier, M. Opel, R. Gross, Goennenwein, S. T. B., *Electric field controlled manipulation of the magnetization in Ni/$BaTiO_3$ hybrid structures,* Appl. Phys. Lett. **96,** 14, 142509 (2010)

[181]. Hong, Nguyen Thi Minh, P.D. Thang, N.H. Tiep, V. Le Cuong, N.H. Duc, *Voltage-controllable magnetic behavior in PZT/NiFe/CoFe nanocomposites,* Adv. Nat. Sci.: Nanosci. Nanotechnol. **2,** 1, 15015 (2011)

[182]. Y. Jia, S.W. Or, Chan, Helen Lai Wa, X. Zhao, H. Luo, *Converse magnetoelectric effect in laminated composites of PMN–PT single crystal and Terfenol-D alloy*, Appl. Phys. Lett. **88,** 24, 242902 (2006)

[183]. W. Eerenstein, M. Wiora, J.L. Prieto, J.F. Scott, N.D. Mathur, *Giant sharp and persistent converse magnetoelectric effects in multiferroic epitaxial heterostructures,* Nat Mater **6,** 5, 348 (2007)

[184]. A. Lisfi, J.C. Lodder, *Magnetic domains in epitaxial BaFe12O19 thin films with perpendicular anisotropy,* J. Phys. Condens. Matter. **14**, 12339 (2002)

[185]. H.J. Williams, *A Simple Domain Structure in an Iron Crystal Showing a Direct Correlation with the Magnetization,* Phys. Rev. **75,** 1, 178 (1949)

[186]. J.L. Hockel, S.D. Pollard, K.P. Wetzlar, T. Wu, Y. Zhu, G.P. Carman, *Electrically controlled reversible and hysteretic magnetic domain evolution in nickel film/Pb($Mg_{1/3}Nb_{2/3}$)O_3]0.68-[$PbTiO_3$]0.32 (011) heterostructure,* Appl. Phys. Lett. **102,** 24, 242901 (2013)

[187]. H. Klimker and M. Rosen, *Effect of Hydrostatic Pressure on the Elastic and Inelastic Behavior of Gadolinium in the Spin-Reorientation Region*, Phys. Rev. **139,** 2A, A455 (1965)

[188]. Earl Callen and Herbert B. Callen, *Magnetostriction, Forced Magnetostriction, and Anomalous Thermal Expansion in Ferromagnets*

[189]. A.G. Chesnokov and E.P. Na, *Influence of Diamagnetic Cations Sc^{+3} on the Magnetoelastic Energy of M-Type Hexaferrites*, Phys. Solid State **43**, 9, 1728 (2001)

[190]. J. Cui, C.-Y. Liang, E.A. Paisley, A. Sepulveda, J.F. Ihlefeld, G.P. Carman, C.S. Lynch, *Generation of localized strain in a thin film piezoelectric to control individual magnetoelectric heterostructures,* Appl. Phys. Lett. **107,** 9, 92903 (2015)

[191]. J. Cui, J.L. Hockel, P.K. Nordeen, D.M. Pisani, G.P. Carman, C.S. Lynch, *Giant electric-field-induced magnetic anisotropy reorientation with patterned electrodes on a Ni thin film/lead zirconate titanate heterostructure,* J. Appl. Phys. **115,** 17, 17C711 (2014)

[192]. C.S. Lynch, *The effect of uniaxial stress on the electro-mechanical response of 8/65/35 PLZT,* Acta Materialia **44,** 10, 4137 (1996)

[193]. S. Weigert, M. Dreier, M. Hegner, *Frequency shifts of cantilevers vibrating in various media,* Appl. Phys. Lett. **69,** 19, 2834 (1996)

[194]. J. Lübbe, M. Temmen, H. Schnieder, M. Reichling, *Measurement and modelling of non-contact atomic force microscope cantilever properties from ultra-high vacuum to normal pressure conditions,* Meas. Sci. Technol. **22,** 5, 55501 (2011)

[195]. J. Wang, F. Zhao, W. Wu, G.-M. Zhao, *Unusual temperature dependence of the magnetic anisotropy constant in barium ferrite $BaFe_{12}O_{19}$,* J. Appl. Phys. **110,** 9, 96107 (2011)

[196]. NT-MDT, *Magnetic Force Microscopy: Quantitative Results Treatment (Whitepaper)* (Moscow, Russia)

[197]. U. Hartmann, *Magnetic Force Microscopy,* Annu. Rev. Mater. Sci. **29**, 53 (1999)

[198]. T. Lakvekheliany, *Magnetic Force Microscopy: Quantitative Results Treatment (White Paper)*

[199]. U.E.C. Kooy, Phillips Res. Repts. **15**, 7 (1960)

[200]. B.D. Cullity, C.D. Graham, *Introduction to magnetic materials* (Wiley, Hoboken, N.J., Chichester, 2009)

[201]. H. Saito, J. Chen, S. Ishio, *Description of magnetic force microscopy by three-dimensional tip Green's function for sample magnetic charges,* Journal of Magnetism and Magnetic Materials **191,** 1-2, 153 (1999)

[202]. T. Chang, M. Lagerquist, J.H. Judy, Jian-Gang Zhu, in *1992. Digests of Intermag. International Magnetics Conference* , p. 419

[203]. H. Saito, J. Chen, S. Ishio, *Description of magnetic force microscopy by three-dimensional tip Green's function for sample magnetic charges,* Journal of Magnetism and Magnetic Materials **191,** 1-2, 153 (1999)

[204]. Z. Li, X. Li, D. Dong, D. Liu, H. Saito, S. Ishio, *AC driven magnetic domain quantification with 5 nm resolution,* Sci Rep **4**, 5594 (2014)

[205]. Leon Abelmann, Arnout van den Bos, Cock Lodder, *Towards higher resolution in Magnetic Force Microscopy*

[206]. S. Jesse, B. Mirman, S.V. Kalinin, *Resonance enhancement in piezoresponse force microscopy,* Appl. Phys. Lett. **89,** 2, 22906 (2006)

[207]. Tilman E. Schäffer, in *Force microscopy*, ed. by B.P. Jena, Hörber, J. K. Heinrich (Wiley-Liss Hoboken, N.J., 2006), p. 222

[208]. T. Ando, N. Kodera, E. Takai, D. Maruyama, K. Saito, A. Toda, *A high-speed atomic force microscope for studying biological macromolecules,* Proceedings of the National Academy of Sciences of the United States of America **98,** 22, 12468 (2001)

[209]. N. Kodera, D. Yamamoto, R. Ishikawa, T. Ando, *Video imaging of walking myosin V by high-speed atomic force microscopy,* Nature **468,** 7320, 72 (2010)

[210]. T. Ando, T. Uchihashi, N. Kodera, D. Yamamoto, A. Miyagi, M. Taniguchi, H. Yamashita, *High-speed AFM and nano-visualization of biomolecular processes,* Pflügers Archiv : European journal of physiology **456,** 1, 211 (2008)

[211]. T. Uchihashi, R. Iino, T. Ando, H. Noji, *High-speed atomic force microscopy reveals rotary catalysis of rotorless F_1-ATPase,* Science (New York, N.Y.) **333,** 6043, 755 (2011)

[212]. G.E. Fantner, R.J. Barbero, D.S. Gray, A.M. Belcher, *Kinetics of antimicrobial peptide activity measured on individual bacterial cells using high-speed atomic force microscopy,* Nature nanotechnology **5,** 4, 280 (2010)

[213]. W.Y. Lee, S. Gardelis, B.-C. Choi, Y.B. Xu, C.G. Smith, Barnes, C. H. W., D.A. Ritchie, E.H. Linfield, Bland, J. A. C., *Magnetization reversal and magnetoresistance in a lateral spin-injection device,* J. Appl. Phys. **85,** 9, 6682 (1999)

[214]. M.R. Freeman, J.F. Smyth, *Picosecond time-resolved magnetization dynamics of thin-film heads,* J. Appl. Phys. **79,** 8, 5898 (1996)

[215]. G.P. cameron, W.J. Eberle, *Characterization of chevron-shaped permalloy magnetic memory elements by 4 magnetic imaging techniques,* Scanning **13,** 6, 419 (1991)

[216]. H.G. Min, S.H. Kim, M. Li, J.B. Wedding, G.C. Wang, *Thickness-dependent coercivity of ultrathin Co films on a rough substrate: Cu-buffered Si(111),* Surface Science **400,** 1-3, 19 (1998)

[217]. W. Kleemann, J. Rhensius, O. Petracic, J. Ferré, J.P. Jamet, H. Bernas, *Modes of Periodic Domain Wall Motion in Ultrathin Ferromagnetic Layers,* Phys. Rev. Lett. **99,** 9 (2007)

[218]. P. Rahe, R. Bechstein, and A. Kühnle, *Vertical and lateral drift corrections of scanning probe microscopy images,* J. Vac. Sci. Technol. B **28,** 3, C4E31 - C4E38 (2010)

[219]. K.H. Chung, Y.H. Lee, D.E. Kim, *Characteristics of fracture during the approach process and wear mechanism of a silicon AFM tip,* Ultramicroscopy **102,** 2, 161 (2005)

[220]. S. Kalinin, D. Bonnell, *Imaging mechanism of piezoresponse force microscopy of ferroelectric surfaces,* Phys. Rev. B: Condens. Matter Mater. Phys. **65,** 12 (2002)

[221]. S.S. A.E. Giannakopoulos, *Theory of indentation of piezoelectric materials,* Acta Mater. **47,** 7, 2153 (1999)

[222]. B. Mirman, S.V. Kalinin, *Resonance frequency analysis for surface-coupled atomic force microscopy cantilever in ambient and liquid environments,* Appl. Phys. Lett. **92,** 8, 83102 (2008)

[223]. C.S. Lynch, *The effect of uniaxial stress on the electro-mechanical response of 8/65/35 PLZT,* Acta Materialia **44,** 10, 4137 (1996)

[224]. H. Cao, A.G. Evans, *Nonlinear Deformation of Ferroelectric Ceramics,* J American Ceramic Society **76,** 4, 890 (1993)

[225]. W. Chen, C.S. Lynch, *Multiaxial Constitutive Behavior of Ferroelectric Materials,* J. Eng. Mater. Technol. **123,** 2, 169 (2001)

[226]. M. Molotskii, *Generation of ferroelectric domains in atomic force microscope,* J. Appl. Phys. **93,** 10, 6234 (2003)

[227]. A.Y. Emelyanov, *Coherent ferroelectric switching by atomic force microscopy,* Phys. Rev. B **71,** 13 (2005)

[228]. S.V. Kalinin, A. Gruverman, B.J. Rodriguez, J. Shin, A.P. Baddorf, E. Karapetian, M. Kachanov, *Nanoelectromechanics of polarization switching in piezoresponse force microscopy,* J. Appl. Phys. **97,** 7, 74305 (2005)

[229]. A. Gruverman, O. Auciello, H. Tokumoto, *Imaging and control of domain structures in ferroelectric thin films via scanning force microscopy 1,* Annu. Rev. Mater. Sci. **28,** 1, 101 (1998)

[230]. O. Kolosov, A. Gruverman, J. Hatano, K. Takahashi, H. Tokumoto, *Nanoscale Visualization and Control of Ferroelectric Domains by Atomic Force Microscopy,* Phys. Rev. Lett. **74,** 21, 4309 (1995)

[231]. T. Tybell, P. Paruch, T. Giamarchi, J.-M. Triscone, *Domain Wall Creep in Epitaxial Ferroelectric $Pb(Zr_{0.2}Ti_{0.8})O_3$ Thin Films,* Phys. Rev. Lett. **89,** 9 (2002)

[232]. A.N. Morozovska, S.V. Kalinin, E.A. Eliseev, S.V. Svechnikov, *Local Polarization Switching in Piezoresponse Force Microscopy,* Ferroelectrics **354,** 1, 198 (2007)

[233]. A.N. Morozovska, E.A. Eliseev, S.V. Kalinin, *Domain nucleation and hysteresis loop shape in piezoresponse force spectroscopy,* Appl. Phys. Lett. **89,** 19, 192901 (2006)

[234]. P. Maksymovych, N. Balke, S. Jesse, M. Huijben, R. Ramesh, A.P. Baddorf, S.V. Kalinin, *Defect-induced asymmetry of local hysteresis loops on BiFeO3 surfaces,* J Mater Sci **44,** 19, 5095 (2009)

[235]. P. Maksymovych, S. Jesse, M. Huijben, R. Ramesh, A. Morozovska, S. Choudhury, L.-Q. Chen, A.P. Baddorf, S.V. Kalinin, *Intrinsic Nucleation Mechanism and Disorder Effects in Polarization Switching on Ferroelectric Surfaces,* Phys. Rev. Lett. **102,** 1 (2009)

[236]. S. Jesse, A.P. Baddorf, S.V. Kalinin, *Switching spectroscopy piezoresponse force microscopy of ferroelectric materials,* Appl. Phys. Lett. **88,** 6, 62908 (2006)

[237]. H. Trivedi, V.V. Shvartsman, D.C. Lupascu, Medeiros, Marco S. A., R.C. Pullar, A.L. Kholkin, P. Zelenovskiy, A. Sosnovskikh, V.Y. Shur, *Local manifestations of a static magnetoelectric effect in nanostructured $BaTiO_3$ –$BaFe_{12}O_9$ composite multiferroics,* Nanoscale **7**, 4489 (2015)

[238]. B. Huybrechts, K. Ishizaki, M. Takata, *The positive temperature coefficient of resistivity in barium titanate,* J Mater Sci **30,** 10, 2463 (1995)

[239]. G.V. Lewis, C.R.A. Catlow, R.E.W. Casselton, *PTCR Effect in $BaTiO_3$,* J American Ceramic Society **68,** 10, 555 (1985)

[240]. G. V. Lewis, C. R. A. Catlow, *The PTCR effect in $BaTiO_3$,* Br. Ceram. Proc. **36**, 187 (1985)

[241]. H.M. Chan, M.R. Harmer, D.M.L. Smyth, *Compensating Defects in Highly Donor-Doped $BaTiO_3$,* J American Ceramic Society **69,** 6, 507 (1986)

[242]. T. Naoyama, Y. Sakioka, M. Noda, M. Okuyama, K. Saito, *A Low Temperature Preparation of $BaTiO_3$Thin Film by Sol-Gel-Hydrothermal Treatment below 210°C,* Jpn. J. Appl. Phys. **44,** 9B, 6873 (2005)

[243]. N.H. Chan, R.K. Sharma, D.M. Smyth, *Nonstoichiometry in Undoped $BaTiO_3$,* J American Ceramic Society **64,** 9, 556 (1981)

[244]. W. Schockely, *Circuit element utilizing semiconductive material,* U.S. Patent **2569347** (1951)

[245]. S. M. Sze, *Physics of Semiconductor Devices* (Jhon Wiley & Sons, New York, 1981)

[246]. S.H. Wemple, *Polarization Fluctuations and the Optical-Absorption Edge in $BaTiO_3$,* Phys. Rev. B **2,** 7, 2670-2689 (1970)

[247]. A. Meftah, J.M. Costantini, N. Khalfaoui, S. Boudjadar, J.P. Stoquert, F. Studer, M. Toulemonde, *Experimental determination of track cross-section in $Gd_3Ga_5O_{12}$ and comparison to the inelastic thermal spike model applied to several materials,* Nucl. Instrum. Methods Phys. Res., Sect. B **237,** 3-4, 563 (2005)

[248]. M. Meinert, G. Reiss, *Electronic structure and optical band gap determination of $NiFe_2O_4$,* Journal of physics. Condensed matter : an Institute of Physics journal **26,** 11, 115503 (2014)

[249]. M. Abplanalp, J. Fousek, P. Günter, *Higher Order Ferroic Switching Induced by Scanning Force Microscopy,* Phys. Rev. Lett. **86,** 25, 5799 (2001)

[250]. Eva Drescge-Krasicka, J. R. Willis, *Mapping stress with ultrasond,* Nature **384,** 7, 52 (1996)

[251]. S. Panarello, C. Triolo, A. Testa, S. Patane, D. Patti, S. Russo, in *2014 IEEE 26th International Symposium on Power Semiconductor Devices & IC's (ISPSD)* , p. 321

[252]. P.J. Withers, *Mapping residual and internal stress in materials by neutron diffraction,* Comptes Rendus Physique **8,** 7-8, 806 (2007)

[253]. I.D. Wolf, *Micro-Raman spectroscopy to study local mechanical stress in silicon integrated circuits,* Semicond. Sci. Technol. **11,** 2, 139 (1996)

[254]. S. Ganesan, A. A. Maradudin, J. Oitmaa, *A Lattice Theory of Morphic Effects in Crystals of the Diamond Structure,* Annals Of Physics **56**, 556 (1970)

[255]. J.A. Sanjurjo, E. López-Cruz, G. Burns, *High-pressure Raman study of zone-center phonons in $PbTiO_3$,* Phys. Rev. B **28,** 12, 7260 (1983)

[256]. I.A. Kornev, L. Bellaiche, P. Bouvier, P.E. Janolin, B. Dkhil, J. Kreisel, *Ferroelectricity of Perovskites under Pressure,* Phys. Rev. Lett. **95,** 19 (2005)

[257]. A.K. Sood, N. Chandrabhas, and D.V.S. Muthu, A Jayaram, *Phonon interference in $BaTiO_3$: High-Pressure Raman study,* Phys. Rev. B: Condens. Matter Mater. Phys. **51,** 14, 8892 (1995)

[258]. Uma D. Venkateswaran, Vaman M. Naik, and Ratna Naik, *High-pressure Raman studies of polycrystalline $BaTiO_3$,* Phys. Rev. B: Condens. Matter Mater. Phys. **58,** 21, 14256 (1998)

[259]. Thomas Dieing, Olaf Hollricher, Jan Toporski, *Confocal Raman Microscopy* (Springer-Verlag Berlin Heidelberg, 2011)

[260]. W.H. Weber, R. Merlin, *Raman scattering in materials science* (Springer, Berlin, New York, 2000)

[261]. Princeton Instruments, *Confocal Raman Microscopy General Overview (Whitepaper)*

[262]. N.J. Everall, *Confocal Raman microscopy: performance, pitfalls, and best practice,* Applied spectroscopy **63,** 9, 245A-262A (2009)

[263]. V.Y. Shur, V.A. Shikhova, A.V. Ievlev, P.S. Zelenovskiy, M.M. Neradovskiy, D.V. Pelegov, L.I. Ivleva, *Nanodomain structures formation during polarization reversal in uniform electric field in strontium barium niobate single crystals,* J. Appl. Phys. **112,** 6, 64117 (2012)

[264]. V. Ya. Shur, P.S. Zelenovskiy, *Micro- and nanodomain imaging in uniaxial ferroelectrics: Joint application of optical, confocal Raman, and piezoelectric force microscopy,* J. Appl. Phys. **116,** 6, 66802 (2014)

[265]. P.S. Zelenovskiy, V.Y. Shur, P. Bourson, M.D. Fontana, D.K. Kuznetsov, E.A. Mingaliev, *Raman Study of Neutral and Charged Domain Walls in Lithium Niobate,* Ferroelectrics **398,** 1, 34 (2010)

[266]. V.Y. Shur, P.S. Zelenovskiy, M.S. Nebogatikov, D.O. Alikin, M.F. Sarmanova, A.V. Ievlev, E.A. Mingaliev, D.K. Kuznetsov, *Investigation of the nanodomain structure formation by piezoelectric force microscopy and Raman confocal microscopy in $LiNbO_3$ and $LiTaO_3$ crystals,* J. Appl. Phys. **110,** 5, 52013 (2011)

[267]. A.C. Ferrari, J.C. Meyer, V. Scardaci, C. Casiraghi, M. Lazzeri, F. Mauri, S. Piscanec, D. Jiang, K.S. Novoselov, S. Roth, A.K. Geim, *Raman Spectrum of Graphene and Graphene Layers,* Phys. Rev. Lett. **97,** 18 (2006)

[268]. C. Xie, D. Chen, Y.-q. Li, *Raman sorting and identification of single living micro-organisms with optical tweezers,* Opt. Lett., OL **30,** 14, 1800 (2005)

[269]. F.-C. von Rundstedt, S.P. Lerner, *New imaging techniques for nonmuscle invasive bladder cancer,* Current opinion in urology **24,** 5, 532 (2014)

[270]. V. Ya. Shur, P.S. Zelenovskiy, *Micro- and nanodomain imaging in uniaxial ferroelectrics: Joint application of optical, confocal Raman, and piezoelectric force microscopy,* J. Appl. Phys. **116,** 6, 66802 (2014)

[271]. J. Kreisel, G. Lucazeau, and H. Vincent, *Raman study of substituted barium ferrite single crystals,* J. Raman Spectrosc. **30**, 115 (1999)

[272]. A. Atkinson, S. C. Jain, *Spatially resolved stress analysis using Raman spectroscopy,* J. Raman Spectrosc. **30**, 885 (1999)

[273]. A. Atkinson, S.C. Jain, *Spatially resolved stress analysis using Raman spectroscopy,* J. Raman Spectrosc. **30,** 10, 885 (1999)

[274]. G. Pezzotti, A. Matsutani, W. Zhu, *Spectroscopic Assessments of Domain Texture in Barium Titanate,* Journal of the American Ceramic Society **93,** 1, 256 (2010)

[275]. Eshelby, J. D., *The Determination of the Elastic Field of an Ellipsoidal Inclusion, and Related Problems,* Proceedings of the Royal Society of London. Series A, Mathematical and Physical Sciences **241,** 1226, 376 (1957)

[276]. S. Li, G. Wang, *Introduction to micromechanics and nanomechanics* (World Scientific, Singapore, Hackensack, NJ, 2008)

[277]. Ingrid de Wolf, *Micro-Raman spectroscopy to study local mechanical stress in silicon integrated circuits,* Semicond. Sci. Technol. **11**, 139 (1996)

[278]. S. Ganesan, A. Maradudin, J. Oitmaa, *A lattice theory of morphic effects in crystals of the diamond structure,* Annals of Physics **56,** 2, 556 (1970)

[279]. R. Loudon, *Theory of the resonance Raman effect in crystals,* J. Phys. France **26,** 11, 677 (1965)

[280]. G. Pezzotti, A. Matsutani, W. Zhu, *Spectroscopic Assessments of Domain Texture in Barium Titanate: I. Confocal Raman Polarization Analysis,* Journal of the American Ceramic Society **93,** 1, 256 (2010)

[281]. R. Wang, Q. Han, E. Pan, *An analytical solution for a multilayered magneto-electro-elastic circular plate under simply supported lateral boundary conditions,* Smart Mater. Struct. **19,** 6, 65025 (2010)

[282]. Y.A. Mamluĭ, *Hexagonal ferrite,* Low Temp. Phys. **31,** 3, 268 (2005)